2015-02-25

Propagation Model and Performance Analysis for Mobility Constrained Indoor Wireless Environments

Dey, Indrakshi

UNIVERSITY OF CALGARY

Propagation Model and Performance Analysis for Mobility Constrained Indoor Wireless Environments

by

Indrakshi Dey

A THESIS

SUBMITTED TO THE FACULTY OF GRADUATE STUDIES

IN PARTIAL FULFILLMENT OF THE REQUIREMENTS FOR THE

DEGREE OF DOCTOR OF PHILOSOPHY

DEPARTMENT OF GRADUATE PROGRAM IN ELECTRICAL ENGINEERING

CALGARY, ALBERTA

FEBRUARY, 2015

Abstract

In an indoor wireless environment like an open office or laboratory, there are not enough large obstacles to reflect or refract the main waves contributed by the scattering clusters visited by the mobile user. Moreover, mobile WLAN users generally restrict their movements to a small area due to the inability of most WLAN standards to accommodate hand-offs. As a result, users visit at most one or two scattering clusters and experience only a handful of different shadowing values.

This thesis proposes the first ever appropriate composite fading / shadowing channel model, that characterizes the combination of small scale fading and large scale shadowing for users confined to small coverage areas in a large office environment described above. Based on a detailed indoor measurement campaign, a joint distribution called the Joint fading and Two-path Shadowing (JFTS) distribution is proposed that combines the Rician fading and the two wave with diffuse power (TWDP) shadowing models.

This thesis also presents the first ever analysis of different performance metrics like outage probability, error rate performances and spectral efficiencies of existing high throughput communication techniques like error control coding, fixed and adaptive modulation in a mobility constrained indoor wireless environment, where the propagation scenario can be appropriately characterized by the newly developed JFTS model. Performance evaluation is done both in presence or absence of perfect channel state information.

Acknowledgments

Firstly and importantly, I am truly grateful to my dearest supervisor Prof. Geoffrey Messier for his generous help and being always supportive. His broad knowledge and wonderful personality impressed me and is having and will have a significant impact on me.

Secondly, I would like to thank my co-supervisor Dr. Sebastian Magierowski, whose encouragement, supervision and support from the introductory to the concluding level enabled me to develop a deep understanding of the subject. His guidance and assistance helped me traverse through the difficult phases of the entire accomplishment.

Lastly, I want to thank my husband, for always being supportive and encouraging, and comforting me whenever I face difficulties.

Table of Contents

List of Tables

List of Figures and Illustrations

List of Abbreviations and Nomenclature

Acronyms	Expansions
WLAN	Wireless Land Area Network
AP	Access Point
LMS	Land Mobile Satellite
BER	Bit Error Rate
ABER	Average Bit Error Rate
TBER	Target Bit Error Rate
CBER	Conditional Bit Error Rate
SNR	Signal-to-Noise Ratio
CSNR	Carrier Signal-to-Noise Ratio
AM	Adaptive Modulation
ACM	Adaptive Coded Modulation
PDF	Probability Density Function
CDF	Cumulative Distribution Function
CCDF	Complementary Cumulative Distribution Function
TWDP	Two-Wave with Diffused Power
CSI	Channel State Information
JFTS	Joint Fading and Two-path Shadowing
QAM	Quadrature Amplitude Modulation
RQAM	Rectangular Quadrature Amplitude Modulation
XQAM	Cross Quadrature Amplitude Modulation
SQAM	Square Quadrature Amplitude Modulation
PSK	Phase Shift Keying
BPSK	Binary Phase Shift Keying
QPSK	Quadrature Phase Shift Keying
FSK	Frequency Shift Keying
BFSK	Binary Frequency Shift Keying
AWGN	Additive White Gaussian Noise
MGF	Moment Generating Function
PSAM	Pilot Symbol Assisted Modulation
VNA	Vector Network Analyzer
SISO	Single Input Single Output
GPIB	General Purpose Interface Bus
SER	Symbol Error Rate
ASER	Average Symbol Error Rate
LCR	Level Crossing Rate

AF	Amount of Fading
MLE	Maximum Likelihood Estimation
FEC	Forward Error Correction
CC	Convolutional Coding
HC	Hamming Coding
VD	Viterbi Decoding
HD	Hamming Decoding
HDD	Hard Decision Decoding
SDD	Soft Decision Decoding
LDPC	Low Density Parity Check
iid	independent and identically distributed
RSC	Recursive Systematic Convolutional
PEP	Pairwise Error Probability
GA	Gaussian Approximation
LLR	Log-Likelihood Ratio
CCMC	Continuous Input Continuous Output Memoryless Channel
DCMC	Discrete Input Continuous Output Memoryless Channel
OPRA	Optimal Power and Rate Adaptation
ORA	Optimal Rate Adaptation
CIFR	Channel Inversion with Fixed Rate
ACR	Adaptive Continuous Rate
ADR	Adaptive Discrete Rate
ASE	Average Spectral Efficiency
TCM	Trellis Coded Modulation

Chapter 1

Introduction

The high density and individual data rate requirements of present-day indoor wireless users have made high capacity wireless communication systems a priority for indoor wireless environments. Though the use of indoor pico-cells is going to grow in the future, presently this demand is primarily served by indoor wireless access points. Hence it is essential to find out accurately what high throughput wireless communication system can achieve when implemented on densely deployed indoor wireless access points.

It is well known that indoor wireless links are affected by both small scale fading and shadowing effects. In an indoor wireless environment like an open office or laboratory, there are not enough large obstacles to reflect or refract the main waves contributed by the scattering clusters visited by the mobile user. Moreover, mobile WLAN users generally restrict their movements to a small area due to the inability of most WLAN standards to handle hand-offs. However, assuming a constant shadowing value is also not accurate since it is possible for a user to still visit a small handful of scattering clusters within the coverage area of a Wifi access point. This will result in the user experiencing a small subset of the shadowing variations observed for more mobile users.

The primary goal of this thesis is two-fold. The first is to accumulate measurements and derive a propagation model for mobility constrained densely deployed indoor wireless LAN (WLAN) scenarios based on the measured data. The second contribution is to analyze outage probability, error rate performances and spectral efficiencies of existing high throughput communication techniques like error control coding, fixed and adaptive modulation over the newly developed propagation model.

The rest of this chapter is organized as follows. Section 1.1 presents the key research problems that are analyzed and solved in this thesis. Section 1.2 provides a brief summary of the key results and insights obtained from the works done in this thesis and Section 1.3 provides a brief outline of the contents of this thesis.

1.1 The Research Problem

The Wireless Propagation Challenge :

There are few things in nature more unwieldy than the power-limited, space-varying, time-varying, frequency-varying indoor wireless channels. Radiowaves propagating through indoor wireless environments suffer from small scale fading (caused by transmission via different reflectors resulting in a large variety of propagation path delays), shadowing (caused by obstacles of size much greater than the radio wavelength), scattering (caused by the interaction of the radiowaves with objects of dimension on the order of a wavelength or less), diffraction (caused by bending of the radiowaves around an obstacle) and the change in pathloss due to variation in the relative distance between the transmitter and the receiver.

In outdoor wireless channels, where the obstacles are large, variations in the average received power of the signal due to shadowing are assumed to be constant over hundreds of wavelengths. Variations due to shadowing in dense urban environments are assumed to be constant over tens of wavelengths [1, 2]. However, in an indoor environment, shadowing variations exhibit a spatial correlation of only ten wavelengths or less [3]. As a result, the time scale of indoor shadowing variations begin to approach that of small scale fading, and hence, it is not accurate to assume a constant shadowing value when evaluating wireless system performance.

Attempts to model the combined effect of small scale fading and shadowing were primarily developed to characterize outdoor land mobile satellite (LMS) and macro-cellular channels, the entire set of which can be broadly classified in two groups.The first group attempts to model propagation channels where the channel statistics remain approximately constant in a small area over a certain period of time and therefore are characterized using a single statistical distribution. The second group characterizes communication channels where the signal statistics vary considerably over a large area and hence are modeled using the weighted summation of several statistical distributions. A summary of both these groups of narrow-band LMS channel models has been tabulated in [4].

The first group of channel models can again be divided in two sub-groups depending on the type of shadowing considered. The first sub-group considers environments where only the LOS components that experience shadowing due to complete or partial blockage by buildings, trees, mountains etc., while the scattered components caused by multipath fading have a constant power level [5]. The second sub-group considers environments where both the LOS and the scattered components suffer from random variations in the power level resulting in multiplicative shadow fading [6]. In both [5] and [6], multipath fading is characterized by the Rician distribution and the log-normal distribution is used to model shadowing. The channel model in [5] is extended in [7] by assuming that the power of the scattered components is a log-normal variable, irrespective of the LOS component. The channel model in [5] is generalized in [8] by including an extra additive scatter component.

The second group of LMS channel models consist of at least two distributions, where each distribution corresponds to a particular channel state in which the channel statistics remain constant over a certain time period of interest. The model of [9] consists of the weighted sum of two distribution, while that of [10] consists of three distributions.

The propagation model proposed in this thesis differs from the above mentioned composite channel models in two fundamental ways. Firstly, our model characterizes indoor WLAN communication scenarios in an open concept office or laboratory layout, while the LMS channel models attempt to model the communication channel between satellites and mobile land users in an outdoor dense urban, sub-urban or rural environment. As a result, the main waves that form the shadowing signal component in our scenario are not reflected or refracted by large obstacles. Secondly, outdoor LMS users can be considered mobile enough to visit many scattering clusters over a certain time period of interest. However, as most WLAN standards are incapable of handling hand-offs, mobile WLAN users restrict their movements to a small neighborhood. As a result, users can only visit at most one or two scattering clusters and will experience only one or two discrete shadowing values.

The Performance Analysis Challenge :

The wide variety of applications of indoor wireless communication has resulted in the increased demand of exact theoretical analysis for such systems. For example, expressions for the average bit error rate (ABER) and outage probability are absolutely necessary for designing effective signaling and error control coding schemes. This is because these analytical expressions provide insights into how system parameters affect performance and are more computationally efficient for analyzing system performance. Another example is the dependence of the choice of the optimum carrier signal-to-noise ratio (CSNR) region boundaries on the analytical expression of the BER of an Adaptive Coded Modulation (ACM) technique.

A further consequence is the large demand for radio channel spectrum and high information data rates which can only be ensured using modulation techniques with larger constellation sizes yielding higher bandwidth efficiency. An accurate picture of what high throughput wireless communications systems can achieve when implemented on densely deployed indoor access points is provided by Shannon channel capacity. With the introduction of capacity achieving coding schemes [11], Shannon capacity is now of both theoretical and practical interest. In case of wireless links, Shannon channel capacity characterizes the long-term achievable information rate and therefore is termed as the ergodic capacity [12]. However, the ergodic Shannon capacity estimates are only as good as the channel model upon which they are based.

Of the bulk of the composite fading/shadowing models available, Suzuki [13] and Nakagami - log-normal [4] channel models are widely used.The major drawback of these two models is that the probability density functions (PDF) of these fading models do not have closed form. A more practical closed form composite fading model is the $\mathcal{K}$-distribution [14], where log-normal shadowing is approximated by Gamma shadowing and therefore the received envelope can be expressed in terms of zero mean complex Gaussian random variables with different shape factors. Hence in all of these cases, at higher received CSNR, the received signal envelope approaches zero mean complex Gaussian distribution with a shape factor of 1. As a result, the achievable ergodic channel capacity starts approaching the Shannon bound as the received CSNR increases.

The propagation model proposed in this thesis is a convolution of the Rician fading distribution and the two-wave with diffused power (TWDP) shadowing model. The Rician distribution can be expressed in terms of circular bivariate Gaussian random variable with potentially non-zero mean, while the TWDP [15] distribution is the sum of two half-Ricians. Hence, the distribution of the received signal envelope in this case can only be expressed in terms of bi-variate non-centralized chi-squared distribution and therefore can never be described using Gaussian random variables.

Unlike the $\mathcal{K}$-fading model, the channel model proposed here has been verified using a practical measurement campaign. The new channel model also has a closed form PDF expression as opposed to the Suzuki or Nakagami-log-normal channel models. The parameters of this proposed distribution can also be varied to represent a wide variety of channel conditions like no-fading (infinitely high fading parameter), no-shadowing (infinitely high shadowing parameter), heavy fading (low fading parameter) or heavy shadowing (low shadowing parameter). Hence, the expressions for different performance metrics evaluated over this channel model will provide us with the achievable performance measures over a large variety of practical channel conditions, without assuming that the propagation environment is complex Gaussian distributed.

If perfect channel state information (CSI) is not available at the receiver, the estimated signal envelope over traditional fading models like Rayleigh or Nakagami-m [16, 17] is a sum of two zero-mean complex Gaussian random variables, the transmitted signal envelope and the additive white Gaussian noise (AWGN). As a result, the estimated signal envelope is itself complex Gaussian distributed with zero mean. Hence, the estimated instantaneous CSNR will follow the same distribution as the true instantaneous CSNR. But in case of the propagation model proposed here, the true and the estimated received envelopes will not follow the same distribution. Hence, this thesis will also analyze the statistical properties of the CSNR estimation error as this analysis will enable us to predict the range of acceptable amount of error in CSNR over which a system can operate, when the the true and the estimated CSNR do not necessarily follow the same distribution.

1.2 Summary of Results and Insights

Measurement Campaign : A detailed measurement campaign is conducted consisting of over 30 thousand individual channel measurements for capturing the impact of spatio-temporal variations in the received signal envelope in an open-concept office or laboratory indoor wireless environment. From the measured data, individual distributions of small scale fading and shadowing are extracted. Rician distribution is found to offer the best fit to the small scale fading distributions while Two-wave with Diffused Power (TWDP) distribution offers best possible fit to the shadowing distributions.

Propagation Model : The first ever propagation model that combines small scale fading and large scale shadowing for mobility constrained indoor wireless LAN users is proposed. Rician distribution is combined with TWDP distribution to derive the joint PDF for the large and the small scale channel effects. The new propagation model is coined as Joint Fading and Two-path Shadowing (JFTS) model. Based on the recorded Q-values of the incomplete Gamma function, it can be concluded that the JFTS PDF offers a god fit to the experimentally extracted received signal envelope over a time window larger than the coherence time of large scale shadowing. The JFTS distribution is found to offer better fit to the measured envelopes even in comparison to the Nakagami-m - log-normal composite fading/shadowing distribution.

Physical Meaning of Model Parameters : This thesis is the first to explore and map JFTS model parameters to real world propagation scenarios. The fundamental parameters of the JFTS distribution are the fading parameters, K, the shadowing parameter, S_h and the shape parameter, Δ. Numerical values for each of these parameters can be mapped to any propagation scenario depending on the relative position of the indoor mobile WLAN user and the access point. For example, if the user and the access point are in the same room, the K-factor will vary from 9 dB to 11 dB, the S_h-factor will vary from 9 dB to 12 dB, while the Δ-parameter will vary from 0.6 to 0.95. On the other hand, if the user and the access point are in different rooms separated by two to three sets of drywalls, the K-factor will have values between 6 dB and 7 dB, the S_h-factor will vary from - 4.5 dB to - 0.5 dB, while the Δ-parameter will vary from 0.2 to 0.3.

Fixed Modulation and Coding : This thesis developed the first ever expressions for average bit error rate of different fixed modulation techniques over a practical measurement-based indoor composite fading/shadowing propagation model. Performance degrades as the fading parameter and/or the shadowing factor decreases and the shape parameter increases. If non-iterative coding techniques are used, convolutional coding offers a 3 dB improvement in performance over linear block codes like Hamming codes in presence of deep fading and shadowing. Soft decision decoding offers another 3 dB enhancement in performance over hard decision decoding for a fixed set of JFTS parameters.

Adaptive Coded Modulation : This thesis derives the first ever analytically tractable expressions for ergodic capacity under different adaptive transmission schemes over an indoor composite fading/shadowing propagation model. If perfect CSI is available at the receiver, achievable spectral efficiency with adaptive coded modulation over a JFTS faded/shadowed channel decreases with the decrease in the fading and/or shadowing parameters. Discrete-rate adaptive coded M-QAM obtains both a large spectral efficiency and a small target BER because it is able to exploit the time-varying nature of the instantaneous received CSNR. It is found that ACM achieves an improvement of around 20 dB in BER performance over fixed modulation and coding techniques. For satisfactory operation, both the adaptive variable-rate encoder and variable-rate decoder must use the same code at any instant. A fast and error-free feedback channel is therefore essential to ensure error-free signaling between the encoder and decoder. During periods of low CSNR, the throughput may be low. A buffer is therefore required at the transmitter. The appropriate size of this buffer is a subject for further research.

Impact of Channel Estimation : This thesis has derived the first ever expressions for distribution of estimation error for non-Gaussian joint faded/shadowed random variables. The statistical properties of the estimation error like PDF, Cumulative Distribution Function (CDF) and moments is dependent on the JFTS parameters, average received CSNR and the variance of the corrupting additive white Gaussian noise (AWGN). Numerical results demonstrate that the estimation error variance increases with the increase in the small scale fading and/or shadowing parameters of the JFTS distribution, and decreases with the decreases in AWGN variance. The error variance also decreases with the increase in the mean-squared voltages of the scattered components. However, the estimation error is independent of the correlation coefficient between the true and the estimated CSNR.

1.3 Outline of the Thesis

This thesis is conveniently divided into two parts. Chapters 2 and 3 present the measurement campaign and the propagation model for an indoor WLAN scenario in an open office-type environment. Chapters 4 to 6 present analysis of performance of existing fixed and adaptive modulation and coding techniques over a JFTS faded/shadowed communication channel in presence of perfect or estimated CSI. The following subsections summarize the contents of each chapter.

1.3.1 Propagation Modeling

Chapter 2 presents the measurement campaign and the derivation of the analytical channel model for an indoor WLAN scenario that represents a large open office or laboratory layout with few obstacles to reflect or refract the transmitted signal. Most mobile WLAN users generally restrict their movements to a small area due to the inability of most WLANs to accommodate hand-offs. As a result, users travel through at most one or two scattering clusters and experience only one or two shadowing values. Moreover in an indoor environment shadowing varies quickly enough to require some channel estimation algorithms to account for both small scale and large scale statistics. Therefore this chapter will present a distribution that jointly models variations due to both small scale fading and shadowing. An analytical expression for the PDF of the joint distribution will be derived through distribution fitting to the experimental propagation data.

Chapter 3 presents an intuitive understanding of the characteristics of the JFTS distribution and dependence of its behavior on its fundamental parameters. The accuracy of distribution fitting using the JFTS distribution to the joint fading and shadowing PDFs extracted from the measurement campaign is analyzed. New expressions for the joint moments, mean, variance, CDF and Amount of Fading (AF) of the JFTS distribution are derived in this chapter. The derived expressions for the theoretical mean, variance and CDF are shown to agree with the experimental results. The AF expression is used for comparing the severity of fading imparted by the JFTS distribution to the fading severity of other common small scale fading and composite fading/shadowing distributions.

1.3.2 Performance Analysis

The primary contribution of Chapter 4 is to derive expressions for the error probability, spectral efficiency and outage probability of different fixed modulation techniques with or without iterative error control coding over a JFTS channel. In order to do that, let us assume that $s(t)$ represents a signal with symbol energy E_s that is transmitted over a composite slow shadowed and flat faded wireless communication channel with JFTS statistics. The received signal $y(t)$ over the symbol duration τ_s can then be expressed as,

$$y(t) \; = \; z(t) \, e^{\jmath\phi(t)} \, s(t) \; + \; n(t) \tag{1.1}$$

where $n(t)$ is the complex AWGN with one-sided power spectral density of N_0, $\phi(t)$ is the instantaneous phase and $z(t)$ denotes the composite fading/shadowing envelope which is JFTS distributed. The system block diagram can be represented as in Fig. 1.1.

Chapter 4 uses two sets of approaches for the error probability analysis : firstly, the Moment Generating Function (MGF) - based approach using the PDF of the instantaneous CSNR and secondly, the CDF - based approach using the CDF of the instantaneous CSNR. Finally performances of different fixed modulation and coding are simulated over JFTS fading/shadowing channels and compared with analytical expressions to establish the validity of the derived expressions.

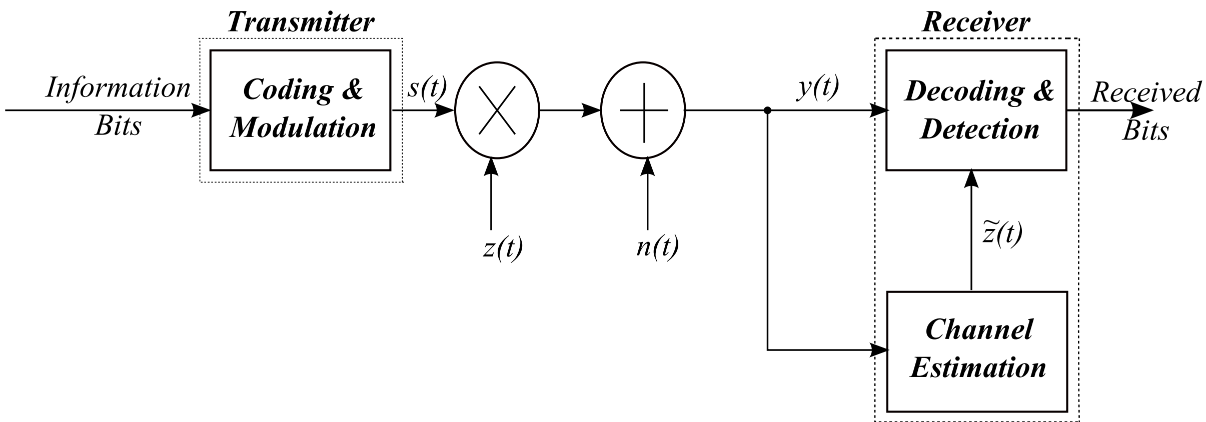

Figure 1.1: System Block Diagram.

Chapter 5 studies the optimum design of adaptive modulation techniques based on M-QAM with or without iterative error control coding over a JFTS channel, where perfect CSI is available at the receiver. The data rate and in some variants the transmit power are adapted to maximize the spectral efficiency subject to average power and bit error rate constraints. The key issues studied here are how the JFTS parameters will affect the optimized transmission properties, such as the CSNR boundaries that determine when to apply different modulation rates and power and to what extent it affects the spectral efficiency. Optimal solutions for the rate and transmit power are derived based on the received instantaneous CSNR. Trellis-coded M-QAM is used as a candidate for improvement in spectral efficiency at a given average received CSNR.

The principal contribution of Chapter 6 is to derive expressions for the error probability performance of different fixed modulation techniques without iterative coding in a JFTS channel in presence of imperfect channel estimates. As a result, the impact of estimation error in the estimation of received CSNR on the decision regions of the demodulator and the amount of degradation in performance over a JFTS channel are analyzed. In turn, statistical properties of the estimated instantaneous CSNR are derived and studied, where pilot symbol assisted modulation (PSAM) is used for fading estimation. The expressions for BER are computed as functions of the JFTS and PSAM parameters, using CDF of the estimated instantaneous CSNR. Finally intuitive conclusions regarding the range of acceptable amount of error in CSNR estimation over which the system can operate correctly in a JFTS channel are made from the expressions.

Chapter 2

Measurement Campaign

2.1 Background

In an indoor environment, shadowing variations exhibit a spatial correlation of only ten wavelengths and, as a result, the time scale of indoor shadowing variations begin to approach that of small scale multipath fading. Hence, assuming a constant shadowing value will not render accurate evaluation wireless system performance in an indoor wireless propagation scenario. An appropriate channel model that characterizes the transition from local small scale fading to global shadowing statistics is necessary for this purpose.

Composite small scale fading and shadowing models for characterizing land mobile satellite (LMS) and macro-cellular channels are well known. In bulk of those literatures, the log-normal distribution is used to model shadowing. This is done because LMS and macro-cellular communication users are highly mobile in an outdoor environment. As the mobile user travels a considerable distance, it visits many scattering clusters and a range of main waves arrive at the mobile as it visits these clusters. The strengths of each of these main waves can be drawn from the log-normal distribution. A brief summary of the competing joint models related to this work is provided in Subsection 2.1.1.

On the other hand, in an indoor environment like an open office or laboratory, there are not enough large obstacles to reflect and refract the main waves for the power of those waves to be accurately characterized using the log-normal distribution. Moreover, mobile WLAN users generally restrict their movements to a small area due to the inability of most WLAN standards to handle hand-offs. As a result, users visit at most one or two scattering clusters and experience only one or two discrete shadowing values. A detailed explanation on the mechanics of shadowing in different propagation scenarios is provided in Subsection 2.1.2.

This chapter uses propagation measurements collected for a signal bandwidth of 10 MHz, to develop a statistical channel model suitable for the indoor WLAN scenario discussed above. The transmit antenna is fixed and mounted at a height of 4 m. The receive antenna is mounted on a cart that is moved along a path within an area representative of a typical access point coverage area. This technique of accumulating measurement is fundamentally different from other more recent studies of indoor propagation, a brief discussion of which is detailed in Subsection 2.1.3.

The rest of this section is organized as follows. Subsection 2.1.1 summarizes competing joint models. Subsection 2.1.2 explains the general mechanics of shadowing while a summary of related indoor measurement campaigns and techniques is provided in Subsection 2.1.3.

2.1.1 **Composite Fading/Shadowing Models**

Attempts to model the combined effect of small scale fading and shadowing were first proposed in [13], where small scale fading was characterized by the Rayleigh distribution and the log-normal distribution was used to model shadowing. This channel model was proposed for appropriately describing land mobile and macro-cellular channels, where line-of-sight (LOS) communication is rare. A variation to this model was proposed in [8] by combining non-selective Rician fading and log-normal shadowing. It assumes an additive shadowing-fading model, where only the direct LOS component is affected by log-normal shadowing, while the scattered components have constant average power levels. This model was found to be adequate for rural land mobile satellite (LMS) channels and was later modified in [18] by assuming a multiplicative shadowing-fading model, where log-normal shadowing affects both the direct and diffuse components. This modified channel model was found to be suitable for both urban and rural environments.

Another extension of [8] is found in [4], where the power of the scattered components is assumed to be a log-normal variable, irrespective of the LOS component. The channel model in [18] is generalized in [8] by including an extra additive scatter component. The Rician fading model was replaced by the Nakagami-m fading model in [18] yielding a joint Nakagami-m - log-normal channel model for LMS communication. In order to derive a closed form solution for second order statistics of combined small scale fading and shadowing in LMS channels, a new shadowed Rician channel model was introduced in [4] where the amplitude of the LOS component is characterized by the Nakagami-m distribution.

The work presented in this chapter is fundamentally different from the LMS channel modeling [13]-[18]. This chapter proposes a composite fading/shadowing model that characterizes indoor WLAN communication scenarios in an open concept office or laboratory layout, while the LMS channel models attempt to model the communication channel between satellites and mobile land users in an outdoor dense urban, sub-urban or rural environment. As a result, the main waves that form the shadowing signal component in our scenario are not reflected or refracted by large obstacles for it to be accurately characterized using the log-normal distribution.

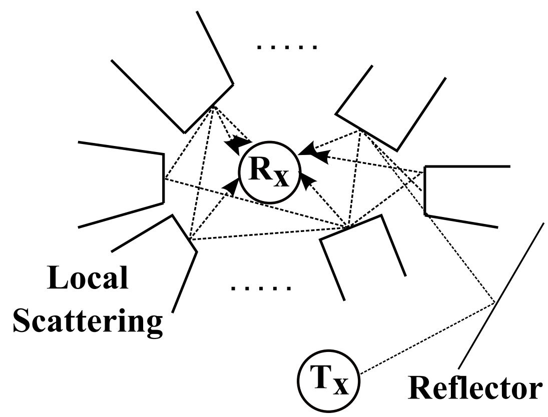

Figure 2.1: Outdoor LMS and Macro-cellular Propagation Scenario

2.1.2 Mechanics of Shadowing

The transition from the local Rayleigh distribution to the global log-normal distribution was first explained by Suzuki in [13]. Let us assume that a mobile station transits between several local neighborhoods, each of which contain different clusters of scattering objects. If a few main waves arrive at each cluster after being attenuated by several multiplicative reflections and refractions, the main waves can be modeled by a log-normal distribution with a standard deviation of σ, due to these multiplicative factors.

If multiple reflections and refractions due to each scatterer are assumed to have approximately equal amplitudes and random uniformly distributed phases, the envelope sum of these components has a Rayleigh distribution. It is noted in [13], that the received power of the main waves will remain approximately constant for several hundred wavelengths. However, as the mobile travels a considerable distance, it will visit many scattering clusters. Therefore, a range of main waves will arrive at the mobile as it visits these clusters, the strengths of each of which can be drawn from the log-normal distribution for each scattering cluster that is visited. A schematic diagram

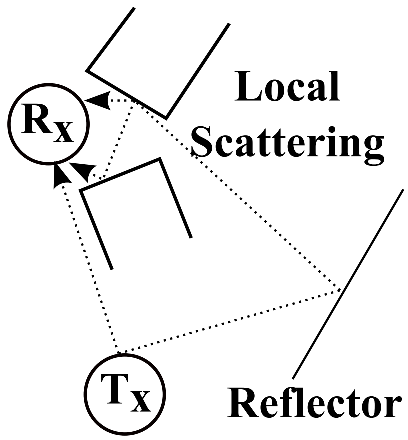

Figure 2.2: Indoor Mobility Constrained Propagation Scenario

of such a propagation scenario is presented in Fig. 2.1.

In an indoor environment, mobile WLAN users generally restrict their movements to a small area due to the inability of most WLAN standards to handle hand-offs. As a result, users will visit at most one or two scattering clusters and will experience only one or two discrete shadowing values. A schematic diagram of such a scenario is presented in Fig. 2.2.

To model the above-mentioned scenario, let us assume that each user will visit at most two scattering clusters and will therefore encounter two discrete shadowing values. In this case, the shadowing envelope can be characterized by the Two-Wave with Diffuse Power (TWDP) distribution [19]. The Δ-parameter of the TWDP distribution will represent the transition from one scattering cluster to the next and will thereby determine the shape of the distribution. The value of Δ will range between 0 and 1. When the magnitude of shadowing values contributed by two consecutive scattering clusters will become equal, $\Delta = 1$, while the absence of one shadowing cluster will render $\Delta = 0$. Within each scattering cluster, each scatterer will contribute to multiple reflection and refraction and the envelope sum of these components will be characterized by the Rician distribution. Since the considered measurement scenario is an indoor environment where the WLAN access points antennas are elevated, at least one direct LOS component will be present between the access point and the user. Hence, the small scale fading envelope will have a Rician distribution.

2.1.3 Related Measurement Techniques

The channel models developed using indoor propagation measurements can be broadly classified in two groups, depending on the way the measurements are collected. The first group [20]-[23], captures many channel impulse response measurements within a small area that is centered at each measurement location (generally a square of the order of 1 meter by 1 meter). The receiver is kept stationary during the acquisition of each impulse response. The second group [24]-[26] collects a series of channel impulse responses while moving the receiver along a fixed path at an approximately constant velocity. For both measurement methods, the transmitter is kept stationary.

One crucial factor in indoor propagation measurements is the antenna height. Measurements are conducted by either keeping both the transmit and receive antennas at the same height like [20, 21, 22, 26, 27], or by installing the transmit antenna much higher than that of the receive antenna like [23, 24, 25, 28]. For example in [27] the receive antenna is mounted on a plastic pole, 1.9 m high on the floor, while the transmit antenna is mounted on a similar 1.6 m high plastic pole fixed on a wooden circular platform, thus keeping both the antennas almost at the same height. On the other hand in [28] the transmitters are placed at a height of 2.5 m near the ceiling while the reception points are kept at a height of 1.2 m.

This chapter presents a measurement campaign intended to capture propagation conditions for a typical open office WLAN scenario. The transmit antenna is fixed and mounted at a height of 4 m which is intended to model a ceiling mounted access point. The receive antenna is mounted on a cart that is moved along a path within an area representative of a typical access point coverage area. The measurements are replicated for a variety of transmit antenna locations. The receiver cart is moved at an average velocity of 1 m/s in order to replicate the normal walking speed of human beings, acting either as receivers or scatterers.

The rest of this chapter is organized as below. The detailed measurement set-up is presented in Section 2.2, followed by details on the measurement scenario considered, in Section 2.3. The procedures followed to accumulate measurement data and to extract parameters from the measurement data are explained in Section 2.4 and Section 2.5. Section 2.6 presents the derivation of the analytical channel model and distribution fitting. The concluding remarks are made in Section A.1.

2.2 Measurement Apparatus

The main components of the measurement campaign is an Agilent E5071B Vector Network Analyzer (VNA) connected to either a pair of 900 MHz 5 dBi L-Com Rubber Duck antennas or a pair of $2.4 - 2.5/4.9 - 5.3/5.7 - 5.8$ GHz Tri-band L-Com Rubber Duck antennas. Both kinds of antenna are vertically polarized and exhibit omni-directional radiation patterns. The VNA is used to measure the sampled frequency response of the channel by capturing complex S_{21} measurements for the channel between the transmit and receive antennas. These channel responses are determined by scanning over a bandwidth of 10 MHz. The values of $|S_{21}|$ and $\angle(S_{21})$ represent the magnitude and the argument or phase of the ratio P_r/P_t respectively, where, P_r is the received

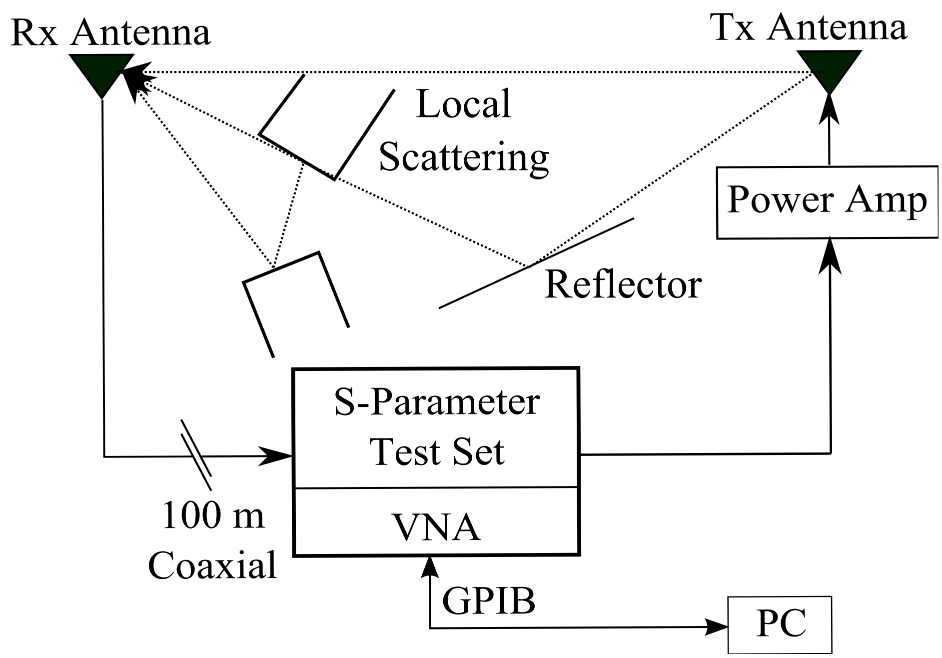

Figure 2.3: Measurement Apparatus

signal power and P_t is the transmitted signal power.

An amplifier for the VNA signal is also sometimes used depending on the distance between the transmitter and receiver. When the distance between the transmitter and receiver is between 0 m and 10 m, no transmit amplifier is used. In this case, a transmit power of 0 dBm is transmitted from the VNA, maintaining a noise floor of -96 dBm. When the distance between the transmitter and the receiver is varied from 10 m to 120 m, a 30 dB RF amplifier is used on the transmit side. A maximum transmit power of 25 dBm is transmitted, with a noise floor maintained at -85 dBm. The effect of the cables and amplifier on the measurements is calibrated out using the Agilent 85033E 3.5 mm calibration kit. Separate calibrations are used for the scenarios with and without the transmit amplifier.

For each set of measurements, single input single output (SISO) transmission is used. The transmitter is kept stationary and the transmit antenna is mounted on top of a tripod at the height of 4 m. The receiving antenna is mounted at a height of 1.4 m. The receiving antenna is connected back to the VNA using a low loss coaxial cable. The measured data at the VNA is accumulated back in a PC for further analysis. A block diagram of the measurement set-up is presented in Fig. 2.3.

2.3 Measurement Scenario

Several fixed transmit locations and moving receiver routes have been chosen intentionally in several different rooms and corridors, so that our measurement environment best reflects an "open concept" office environment. Measurements have been collected overnight in order to avoid the presence of people moving inside the offices. All the measurements have been done on the second floor of the ICT building at the University of Calgary main campus.

The exact transmit positions and their corresponding receiver routes are depicted in Fig. 2.4. The first step when conducting the measurements is to fix the transmitter position at one of the locations indicated on the figure. For example, the first round of measurements fixed the transmit antenna at $T1$. Then the receiver is moved through all the receiver routes, from $R1$ to $R9$ respectively. For each pairing of a transmit position and receiver route, a separate measurement file is generated. For example, while the transmitter is fixed at $T1$, 9 different measurement files are generated corresponding to 9 different receiver routes, which henceforth are denoted by, $T1 : R1$, $T1 : R2$, $\ldots$, $T1 : R9$. The same procedure is repeated for $T2$, $T3$, $T4$, $T5$ and $T6$ respectively. For further reference, each transmit location and each receiver route will be denoted by Td and Rd, respectively, where d is the numerical counter mentioned in the diagram.

2.4 Measurement Accumulation

To characterize the time varying nature of the communication channel, the coherence time of the propagation channel is calculated from,

$$T_c = \frac{9\lambda}{16\pi v} = \frac{9c}{16\pi v f_c} \tag{2.1}$$

where, f_c is the carrier frequency or frequency of operation, v is the mean velocity of the moving receiver and the moving scatterers and λ is the corresponding wavelength [29]. In our case, the selected f_cs are 900 MHz, 2450 MHz and 5000 MHz. Coherence time for frequencies of operation of 900 MHz, 2450 MHz and 5000 MHz are 61 ms, 23 ms and 11 ms, respectively.

The time required by the VNA to measure the frequency domain transfer function of the channel must be kept much below the coherence time. Hence, the VNA is triggered every 800 μs to sweep across a band of 10 MHz that is centered at f_c and data is accumulated over 11 equally spaced sample points. The $|S_{21}|$ and $\angle(S_{21})$ measurements are automatically appended and stored in the controlling PC after every sweep of 800 μs, through a General Purpose Interface Bus (GPIB) connection. In this way, for each frequency band and for each route of the moving receiver, a new measurement file is generated and stored for further processing. The same procedure is repeated for each transmit location.

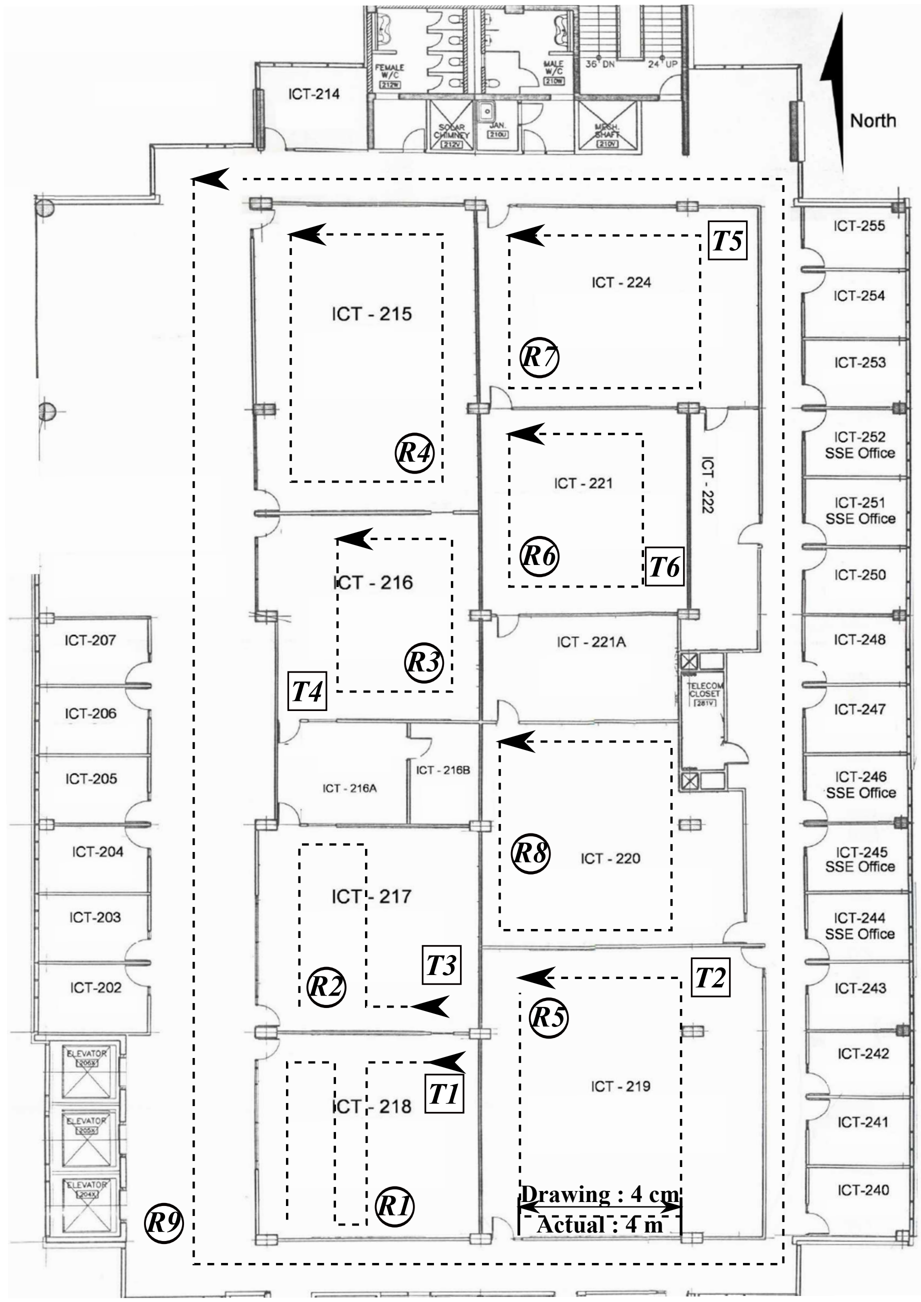

Td →**Transmit Locations** **Rd** → **Receiver Routes** **Scale - 1: 100**

Figure 2.4: Measurement scenario with different transmit locations, Td and receiver routes Rd

2.5 Parameter Extraction

In order to model the combined effect of small scale fading and shadowing, it is necessary to separate large scale channel effects from small scale fading in the measurement data. Extracted large scale fading components will be further analyzed to separate out propagation pathloss components from the variations in mean signal level due to shadowing. The small scale fading components and the large scale shadowing components will then be used to derive the individual distributions of small scale fading and large scale shadowing, respectively. The individual distributions will be utilized, in turn, to derive the joint distribution for the mixture of small scale fading and large scale shadowing, in an indoor wireless propagation environment.

The rest of this section is organized as follows. Subsection 2.5.1 explains the procedure followed to separate out small scale fading effects and large scale channel effects from the accumulated set of $|S_{21}|$ values. A few graphical samples of measurement analyses, collected in different scenarios, are also presented. Finally Subsection 2.5.2 presents a discussion on the appropriate choice of the time window for separating small and large scale effects.

2.5.1 Extraction of Fading and Shadowing Envelopes

The first step is to analyze the accumulated measurement files. Here each measurement file corresponds to the accumulated $|S_{21}|$ values collected over one complete receiver route. Each 10 MHz frequency band is sampled 11 times. Each set of corresponding 11 $|S_{21}|$ values are concatenated to form a vector where, the n^{th} 11 element vector from a file is denoted by $\mathbf{s}'_n$. For example, the total distance covered by the receiver in $R1$ is 19.5 m, at a constant speed of 1 m/s. Hence, the total time required to traverse the total distance is approximately 20 s. If the total number of measured sample points in route, $R1$ is 275000, then we are left with 25000 $\mathbf{s}'_n$ vectors in $R1$.

Each measurement file can be considered a concatenation of P $\mathbf{s}'_n$ vectors, $\mathbf{s}_n = [\mathbf{s}'_1, \mathbf{s}'_2, \ldots \mathbf{s}'_n, \ldots \mathbf{s}'_P]$. For example, for $R1$, $P = 25000$. The next step is to remove the large scale channel effects from $\mathbf{s}_n$. To accomplish that, the set of 11 $|S_{21}|$ values of each of $\mathbf{s}'_n$ are first squared and then linearly averaged over the measurement frequency band, to generate average received energy components, e'_n. In each measurement file, all the e'_n values are then concatenated to form another vector, $\mathbf{e}_n = [e'_1, e'_2, \ldots e'_n, \ldots e'_P]$. Large scale variations in the average received energy is determined by filtering signal energy $|\mathbf{e}_n|$ with a moving average low pass filter operating on a small time window of 4λs, over which large scale fading will remain stationary, as is done in [30].

The moving average filtering process produces a P-element vector $\mathbf{f}_n = [f_1, f_2, \ldots f_n, \ldots f_P]$. The square root of each component of the filter output is used to normalize $\mathbf{s}_n$, to get the small scale fading components.

$$\mathbf{s}_{n,nrm} = \left[\frac{\mathbf{s}'_1}{\sqrt{f_1}}, \frac{\mathbf{s}'_2}{\sqrt{f_2}}, \ldots , \frac{\mathbf{s}'_P}{\sqrt{f_P}} \right] \tag{2.2}$$

Note that the vector, $\mathbf{s}_{n,nrm}$ in (2.2) contains the small scale fading variations that we will later be modeling as a small scale fading random process, X. The entire procedure is repeated for each f_c. A few samples of small scale fading envelopes at different transmit positions and receiver routes with $f_c = 2.45$ GHz, are presented in Fig. 2.5.

Next, a long averaging window of 150λs is used for moving average filtering of the previous filtered output, $\mathbf{f}_n$. The new filter output, $\mathbf{f}'_n$ represents the pathloss components or variation due to distance and is used to normalize $\mathbf{f}_n$ to obtain the shadowing variations $\mathbf{s}_{\mathbf{h}n,nrm}$, which will later

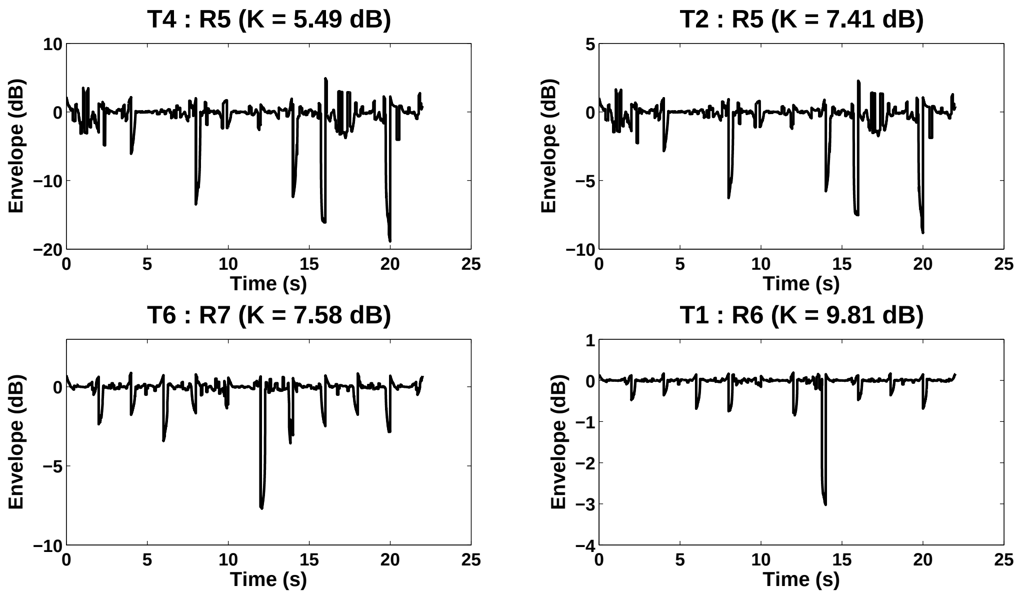

Figure 2.5: Small Scale Fading Envelope at $f_c = 2450$ MHz

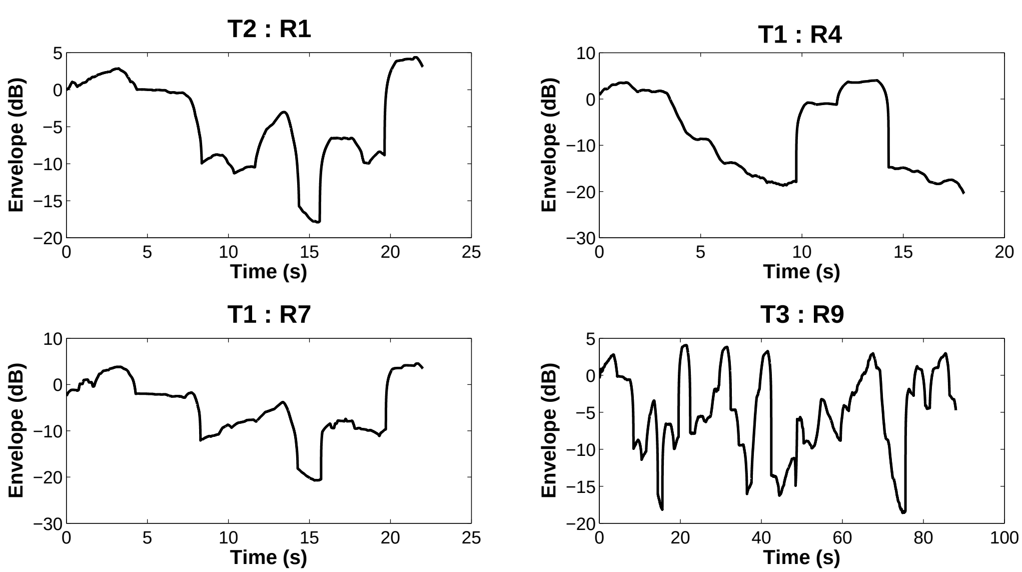

Figure 2.6: Large Scale Shadowing Envelope at $f_c = 2450$ MHz

be modeled as a large scale shadowing random process, Y.

$$\mathbf{s}_{\mathbf{h}n,nrm} = \left[\frac{f_1}{f'_1}, \frac{f_2}{f'_2}, \ldots, \frac{f_P}{f'_P}\right] \tag{2.3}$$

This is done to ensure that the average value of the large scale shadowing envelope is same from one measurement file to the next. However, since the values contained in $\mathbf{s}_{\mathbf{h}n,nrm}$ are given by the ratio of the moving average filter coefficients, a few of the shadowing envelope values can be expected to be negative. The filter window in this case, is chosen long enough so that the effects of user motion on large scale attenuation are preserved in the measurements. A few samples of shadowing envelopes at different transmit positions and receiver routes with $f_c = 2.45$ GHz, are depicted in Fig. 2.6. The corresponding PDFs of small scale fading and shadowing components will be used further, to derive the joint distribution of the mixture of small scale and large scale channel effects.

2.5.2 Separation of Large and Small Scale Channel Effects

The choice of the time window of the moving average filter used to extract the large scale channel variation is crucial. An appropriate selection depends on the time scale of shadowing. In outdoor wireless channels, where the obstacles are large, variations in the average received power of the signal due to shadowing are assumed to be constant over hundreds of wavelengths. Variations due to shadowing in dense urban environments are assumed to be constant over tens of wavelengths [19, 20]. However in an indoor environment, shadowing variations exhibit a spatial correlation of only 10 wavelengths or less and have a correlation distance of around $1 - 2$ m, as established in [13]. This correlation distance can then be translated to wavelengths. Wavelengths at 900 MHz, 2.45 GHz and 5 GHz are 33 cm, 12 cm and 6 cm respectively. In these cases, the choice of a 10 wavelength subinterval to remove small scale fading variation, as mentioned in [21] - [23], is too long and will distort the shadowing experienced in an indoor environment. A better choice is a filter window of 4λs which corresponds to a correlation distance of approximately 1 m.

2.6 Analytical Derivation

In order to characterize the mixture of small scale and large scale channel effects, this section devises an analytical model and expression for the joint distribution of combined small scale fading and large scale shadowing. This is accomplished in three consecutive steps. Firstly, distribution fitting is employed to the extracted PDFs of the small scale fading process, X, which in turn is used to derive the distribution, $f_X(x)$, in Subsection 2.6.1. Secondly, distribution fitting is employed to the extracted PDFs of the large scale shadowing process, Y, which in turn is used to derive the distribution, $f_Y(y)$, in Subsection 2.6.2. Finally, in Subsection 2.6.3, $f_X(x)$ and $f_Y(y)$ are used to derive the joint distribution $f_Z(z)$, where $Z = XY$.

2.6.1 Derivation of $f_X(x)$

An analytical PDF, $f_X(x)$, for the small scale fading process, X, is determined by fitting an analytical distribution to the measured data. On observation, the distributions of small scale fading can be approximated by a Rician distribution. Hence, it can be written,

$$f_X(x) \;=\; f_X(x; K, P_1) \;=\; \frac{x}{P_1}\exp\left(\frac{-x^2}{2P_1} - K\right) I_0\left(x\sqrt{\frac{2K}{P_1}}\right) \tag{2.4}$$

where, $I_0(.)$ is the zeroth order modified Bessel function of the first kind and the Rician K-factor, K is given by,

$$K = \frac{\text{Specular Power}}{\text{Diffused Power}} = \frac{{V_1}^2}{2P_1}$$

Next Chi-Squared distribution fitting is used to estimate the parameters K and P_1 that offer best fit to each extracted distribution of small scale fading. A statistical measure of the goodness-of-fit is also calculated for each case. This measure is based on the incomplete Gamma function, $Q(\frac{N-2}{2}, \frac{{\chi_1}^2}{2})$, where ${\chi_1}^2$ is the Chi-Squared merit function [25] and can be written as,

$$ {\chi_1}^2(K, P_1) \;=\; \sum_{i=1}^{N} \left[\frac{f_{X_i}(x_i) - \frac{x_i}{P_1}\exp\left(\frac{-{x_i}^2}{2P_1} - K\right) I_0\left(x_i\sqrt{\frac{2K}{P_1}}\right)}{u_i} \right]^2 \tag{2.5} $$

where N is the number of data points in each measurement file and u_i denotes the measurement errors. Chi-Squared distribution fitting is chosen for our application, because it is one of the most popular non-parametric statistical procedure. A non-parametric statistical method does not rely on data belonging to any particular distribution and does not assume that the structure of a model is fixed. Hence, Chi-Squared distribution fitting technique does not require normal distribution or variance assumptions about the populations from which the samples are drawn.

In order to determine K and P_1 values, (2.5) is to be minimized with respect to K and P_1, respectively. For simplification, let, $A_i = f_{X_i}(x_i) - \frac{x_i}{P_1}\exp\left(\frac{-{x_i}^2}{2P_1} - K\right) I_0\left(x_i\sqrt{\frac{2K}{P_1}}\right)$. At its minimum, derivatives of ${\chi_1}^2(K, P_1)$ with respect to K and P_1 will vanish.

$$ 0 = \frac{\partial {\chi_1}^2}{\partial K} = 2\sum_{i=1}^{N} \frac{A_i}{{u_i}^2}\left(\frac{\partial A_i}{\partial K}\right) \tag{2.6} $$

$$ 0 = \frac{\partial {\chi_1}^2}{\partial P_1} = 2\sum_{i=1}^{N} \frac{A_i}{{u_i}^2}\left(\frac{\partial A_i}{\partial P_1}\right) \tag{2.7} $$

Detailed calculation of $\frac{\partial A_i}{\partial K}$ and $\frac{\partial A_i}{\partial P_1}$ is presented in Appendix A. Using, (2.6) and (2.7), numerical solution for the values of K and P_1 are obtained, that offer best fit to each distribution. An example set of extracted PDFs and their best fit Rician distributions are shown in Fig. 2.7.

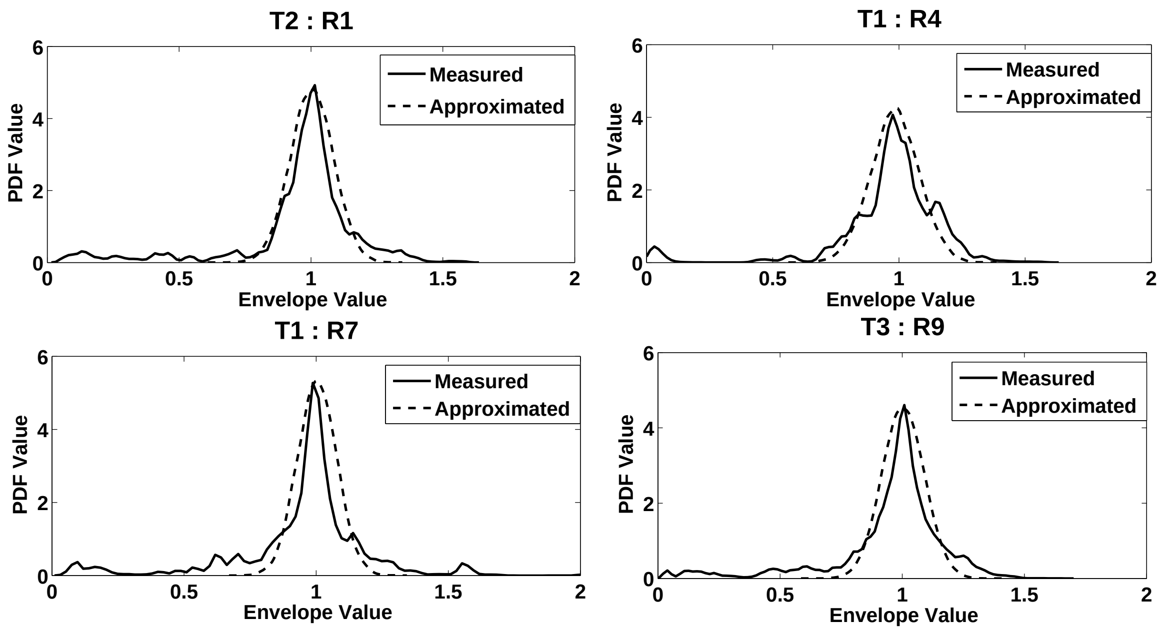

Figure 2.7: Measured and Approximated PDFs for Small Scale Fading at $f_c = 2450$ MHz

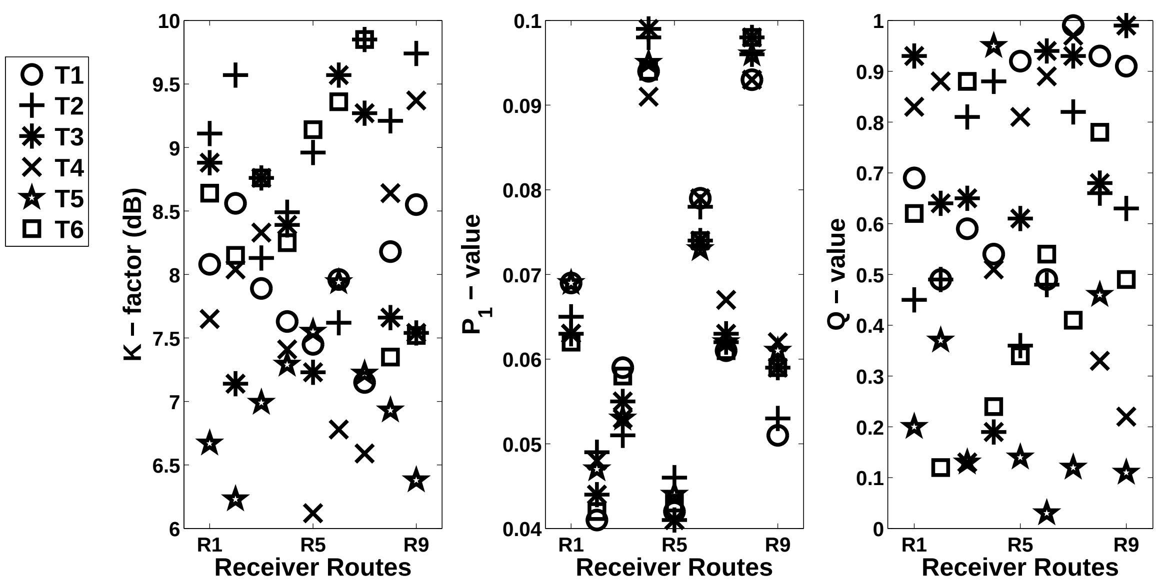

Figure 2.8: Calculated values of K, P_1 and Q over all receiver routes and transmit locations at $f_c = 900$ MHz

Next, the goodness-of-fit measure is estimated by the incomplete Gamma function [25],

$$Q\left(\frac{N-2}{2}, \frac{{\chi_1}^2}{2}\right) = \frac{1}{\Gamma\left(\frac{N-2}{2}\right)} \int_{\frac{{\chi_1}^2}{2}}^{\infty} e^{-t} t^{\left(\frac{N-2}{2}\right)-1} \mathrm{d}t \tag{2.8}$$

where, Q is the probability that a value of chi-square as poor as the value (2.5) should occur by chance. If the Q-value is larger than 0.1, the distribution fitting is fine under any condition. When it is smaller than 0.1 but larger than 0.001, the distribution fitting is fine if the measurement errors are non-normal or have been moderately underestimated. If Q-value is less than 0.001, then the model and / or the estimation procedure is questionable. Fig. 2.8 presents the calculated values of K, P_1 and their corresponding goodness-of-fit, Q values over all receiver routes and transmit locations at $f_c = 900$ MHz while, Fig. 2.9 represents calculated values at $f_c = 2450$ MHz. All the calculated Q-values lie between 0.08 and 0.97, which establishes the fact that our approximated PDFs offer a good fit to the extracted PDFs, with the distribution of measurement errors being non-normal.

2.6.2 Derivation of $f_Y(y)$

The PDF, $f_Y(y)$, for the shadowing process, Y, is also determined by fitting the analytical distribution to the measured data. On visual inspection of the measurement data, it is assumed that a Two-Wave with Diffuse Power (TWDP) distribution [15] can be used for the approximation. Though TWDP has been used by the authors of [15], to characterize small scale fading, it will be used here to approximate shadowing. Hence, it can be written,

$$f_Y(y) = f_Y(y; S_h, P_2, \Delta) = \frac{y}{P_2}\exp\left(\frac{-y^2}{2P_2} - S_h\right)\sum_{j=1}^{M} a_j\ D\left(\frac{y}{\sqrt{P_2}}; S_h, \Delta\cos\frac{\pi(j-1)}{2M-1}\right) \tag{2.9}$$

where,

$$D(\alpha; u, \beta) = \frac{1}{2}\exp(\beta u)I_0\left(\alpha\sqrt{2u(1-\beta)}\right) + \frac{1}{2}\exp(-\beta u)I_0\left(\alpha\sqrt{2u(1+\beta)}\right)$$

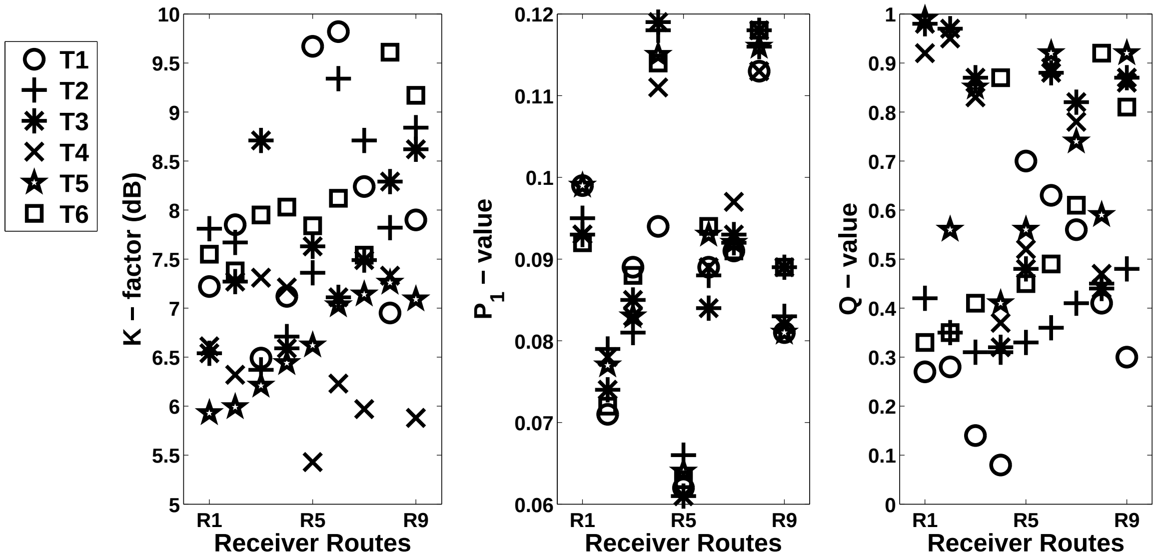

Figure 2.9: Calculated values of K, P_1 and Q over all receiver routes and transmit locations at $f_c = 2450$ MHz

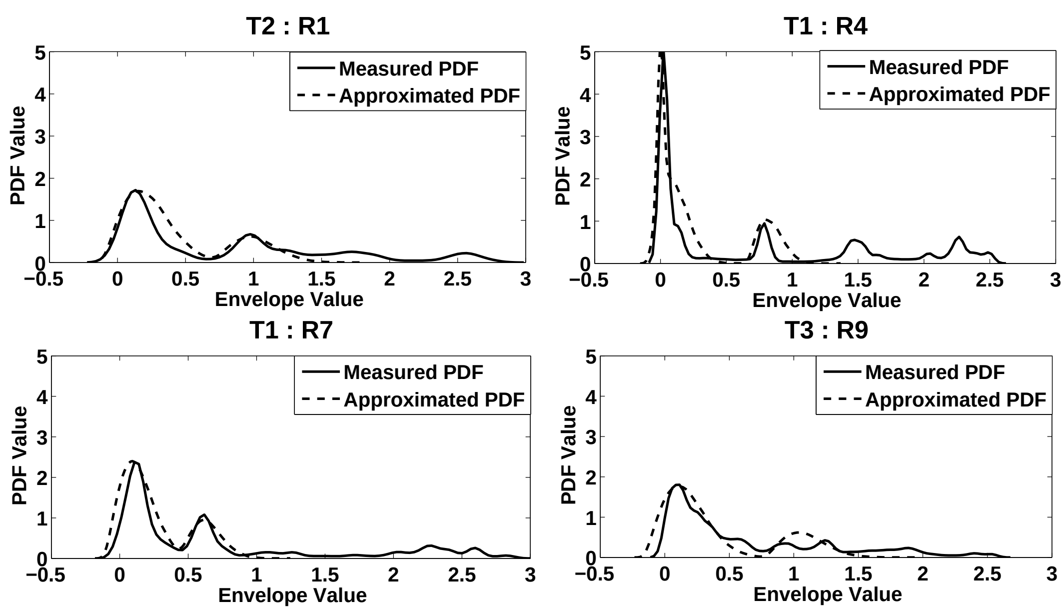

Figure 2.10: Measured and Approximated PDFs for Large Scale Shadowing at $f_c = 2450$ MHz

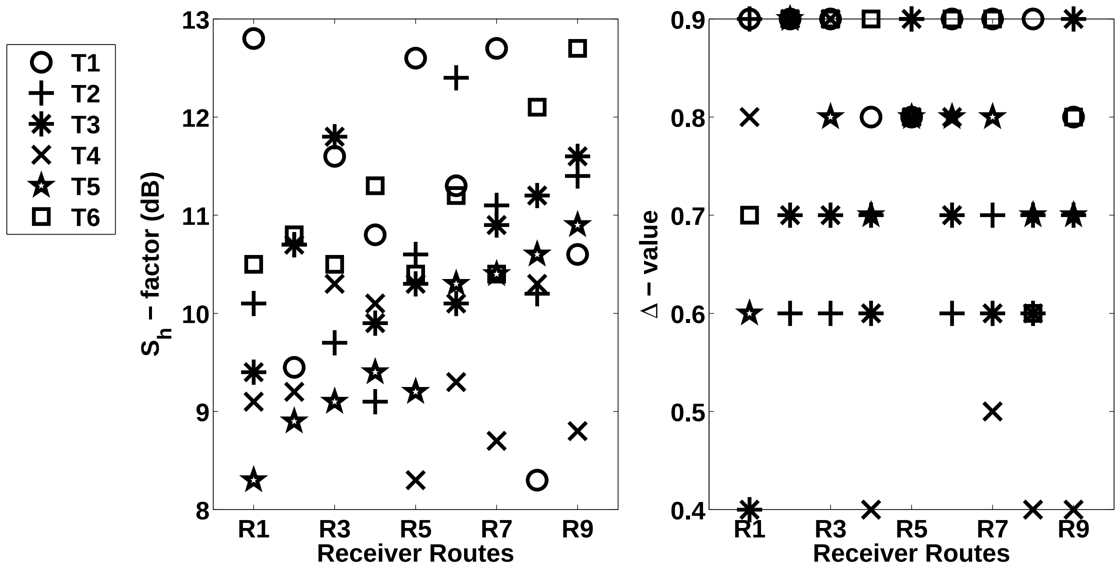

Figure 2.11: Calculated values of S_h and Δ over all receiver routes and transmit locations at $f_c = 2450$ MHz

The shadowing parameter, S_h-factor physically represents the range of discrete shadowing values experienced by a user while traveling through different scattering clusters. The Δ-parameter is the shape parameter of the shadowing distribution and represents the transition, as the user travels from one scattering cluster to the next one. An order, M of 4 is used for this set of distribution fitting. Using the Chi-Squared merit function to estimate the parameters S_h, Δ and P_2, that offer best fit to the distributions, the following expression can be obtained,

$$\chi_2{}^2(S_h, \Delta, P_2) = \sum_{i=1}^{N} \left[\frac{f_{Y\,i}(y_i) - \frac{y_i}{P_2}\exp\left(\frac{-y_i{}^2}{2P_2} - S_h\right) \sum_{j=1}^{M} a_j D\left(\frac{y}{\sqrt{P_2}}; S_h, \Delta \cos\frac{\pi(j-1)}{2M-1}\right)}{v_i} \right]^2 \tag{2.10}$$

where v_i denotes the measurement errors. Minimizing $\chi_2{}^2$ with respect to S_h, Δ and P_2, three sets of equations are obtained,

$$0 = \frac{\partial \chi_2{}^2}{\partial S_h} = 2\sum_{i=1}^{N} \frac{G_i}{v_i{}^2}\left(\frac{\partial G_i}{\partial S_h}\right) \tag{2.11}$$

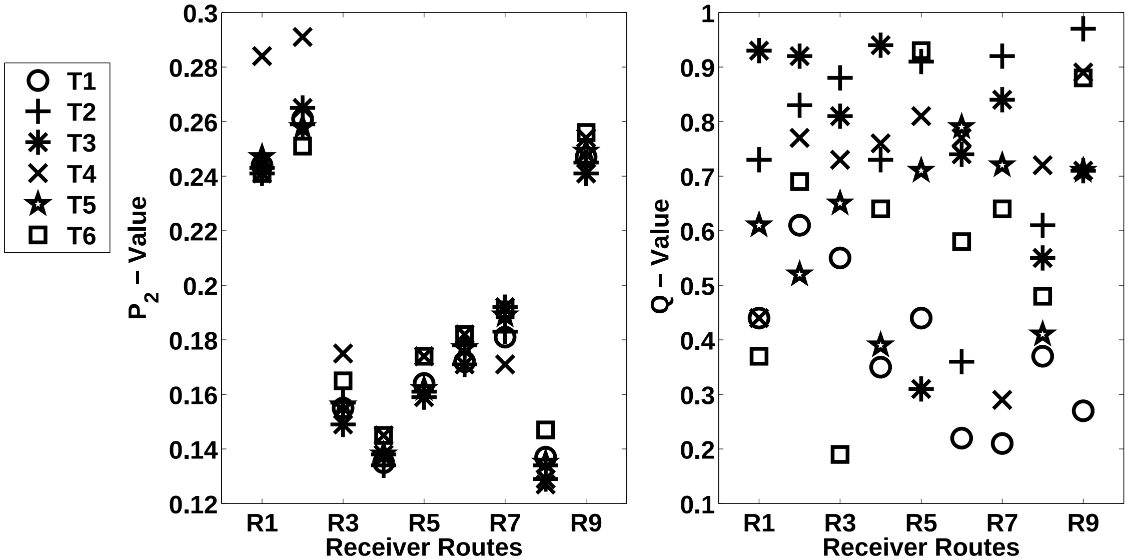

Figure 2.12: Calculated values of P_2 and Q over all receiver routes and transmit locations at $f_c = 2450$ MHz

$$0 = \frac{\partial {\chi_2}^2}{\partial \Delta} = 2\sum_{i=1}^{N} \frac{G_i}{{v_i}^2}\left(\frac{\partial G_i}{\partial \Delta}\right) \tag{2.12}$$

$$0 = \frac{\partial {\chi_2}^2}{\partial P_2} = 2\sum_{i=1}^{N} \frac{G_i}{{v_i}^2}\left(\frac{\partial G_i}{\partial P_2}\right) \tag{2.13}$$

where,

$$G_i \ = \ f_{Y\,i}(y_i) - \frac{y_i}{P_2}\exp\left(\frac{-{y_i}^2}{2P_2} - S_h\right)\sum_{j=1}^{M} a_j D\left(\frac{y}{\sqrt{P_2}}; S_h, \Delta\cos\frac{\pi(j-1)}{2M-1}\right)$$

Detailed calculation of $\frac{\partial G_i}{\partial S_h}$, $\frac{\partial G_i}{\partial \Delta}$ and $\frac{\partial G_i}{\partial P_2}$ is presented in Appendix A. Using, (2.11), (2.12) and (2.13), numerical solution for the values of S_h, Δ and P_2 are obtained, that offer best fit to each distribution. An example set of extracted PDFs and their approximated PDFs for large scale

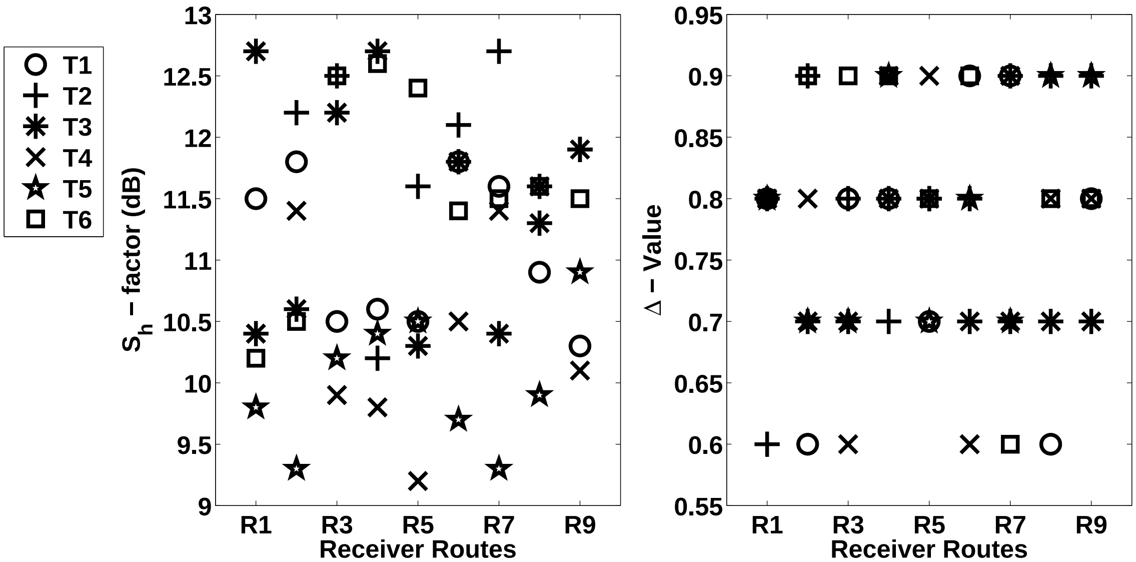

Figure 2.13: Calculated values of S_h and Δ over all receiver routes and transmit locations at $f_c = 5000$ MHz

shadowing is presented in Fig. 2.10.

Next, the goodness-of-fit measure is estimated by (2.8). Fig. 2.11 presents the calculated values of S_h, and Δ, while Fig. 2.12 depicts the calculated values of P_2 and goodness-of-fit, Q values over all receiver routes and transmit locations at $f_c = 2450$ MHz. Fig. 2.13 and Fig. 2.14 present the calculated values of S_h, Δ, P_2 and their corresponding goodness-of-fit, Q values, respectively over all receiver routes and transmit locations at $f_c = 5000$ MHz . All the calculated Q-values lie between 0.3 and 0.98, which establishes the fact that, our approximated PDFs offer a good fit to the extracted PDFs, with the distribution of measurement errors being non-normal.

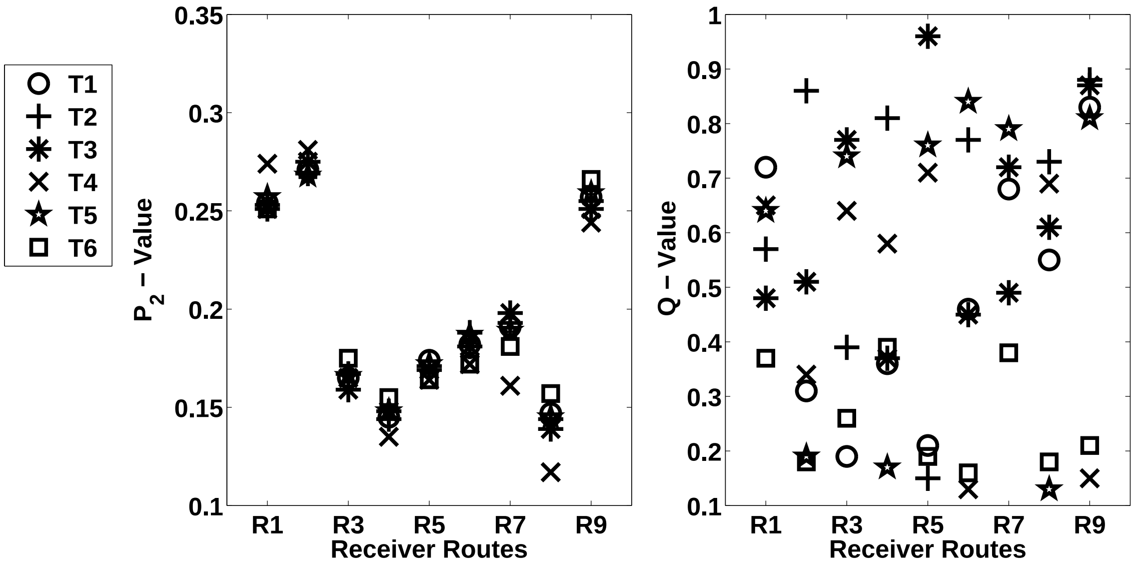

Figure 2.14: Calculated values of P_2 and Q over all receiver routes and transmit locations at $f_c = 5000$ MHz

2.6.3 Derivation of $f_Z(z)$

The envelope of the mixture of small scale and large scale channel effects is denoted as Z where $Z = XY$. In order to derive the analytical PDF $f_Z(z)$ of Z, the joint distribution $f_{XY}(x, y)$ will be derived, which in turn will be mapped to $f_Z(z)$ using a linear transformation. However the distribution fitting of $f_Z(z)$ to the measured data will be done in the next chapter to determine how well it captures the combined effect of indoor fading and shadowing. Based on the assumption of independent fading and shadowing, small scale fading distribution, $f_X(x)$, (2.4) derived in Subsection 2.5.1 is combined with shadowing distribution, $f_Y(y)$, (2.9) derived in Subsection 2.5.2 to derive the joint distribution $f_{XY}(x, y)$. Next, the term $D(\alpha; u, \beta)$ of (2.9) is expanded using

(A.5) presented in Appendix 2.A and hence, the joint distribution $f_{XY}(x,y)$ can be written as,

$$\begin{aligned} f_{XY}(x,y) =& \frac{xy}{P_1P_2}\exp\left(-\frac{x^2}{2P_1}-\frac{y^2}{2P_2}-K-S_h\right) \\ & I_0\left(x\sqrt{\frac{2K}{P_1}}\right)\left[\frac{751}{17280}T_1+\frac{3577}{17280}T_2+\frac{49}{640}T_3+\frac{2989}{17280}T_4\right] \end{aligned} \tag{2.14}$$

Now the term, $\frac{751}{17280}T_1I_0\left(x\sqrt{\frac{2K}{P_1}}\right)$ can be calculated using infinite series expansion of Modified Bessel Function as,

$$\frac{751}{17280}T_1I_0\left(x\sqrt{\frac{2K}{P_1}}\right) = b_1D\left(xy\sqrt{\frac{2K}{P_1P_2}};S_h,\Delta\right) \tag{2.15}$$

the detailed calculation of which is presented in Appendix A. Similarly,

$$\begin{aligned} \frac{3577}{17280}T_2I_0\left(x\sqrt{\frac{2K}{P_1}}\right) &= b_2D\left(xy\sqrt{\frac{2K}{P_1P_2}};S_h,0.9\Delta\right) \\ \frac{49}{640}T_3I_0\left(x\sqrt{\frac{2K}{P_1}}\right) &= b_3D\left(xy\sqrt{\frac{2K}{P_1P_2}};S_h,0.6\Delta\right) \\ \frac{2989}{17280}T_4I_0\left(x\sqrt{\frac{2K}{P_1}}\right) &= b_4D\left(xy\sqrt{\frac{2K}{P_1P_2}};S_h,0.2\Delta\right) \end{aligned} \tag{2.16}$$

where, $b_1 = \frac{751}{8640}I_0(1)$, $b_2 = \frac{3577}{8640}I_0(1)$, $b_3 = \frac{49}{320}I_0(1)$ and $b_4 = \frac{2989}{8640}I_0(1)$.

Next the distribution function, $F_Z(z)$ of z is obtained as,

$$F_Z(z) = \mathbf{P}\{XY \le Z\} \;=\; \int_{y=-\infty}^{\infty}\int_{x=-\infty}^{z/y} f_{XY}(x,y)\mathrm{d}x\mathrm{d}y \tag{2.17}$$

and, hence, $f_Z(z) = \frac{\mathrm{d}F_Z(z)}{\mathrm{d}z}$. Using linear transformation, 2.17 can be written as,

$$f_{ZR}(z,r) = |\mathbf{J}(z,r)|f_{XY}(r,z/r) \;=\; \frac{1}{|r|}f_{XY}(r,z/r) \tag{2.18}$$

where $XY = Z$, $X = R$ and $\mathbf{J}$ represents the Jacobian matrix. Hence 2.18 can be expressed as,

$$f_Z(z) = \int_{-\infty}^{\infty}\frac{1}{|r|}f_{XY}(r,z/r)\mathrm{d}r \tag{2.19}$$

Solving the integration in (2.19), the final expression for the joint distribution is obtained as,

$$
\begin{aligned}
f_Z(z) =& \frac{z}{P_1 P_2} \exp\left(-K - S_h\right) \sum_{j=1}^{4} b_j D\left(z\sqrt{\frac{2K}{P_1 P_2}}; S_h, \Delta \cos\frac{\pi(j-1)}{2M-1}\right) \\
&\cdot \sum_{h=1}^{m} w_h \left[\frac{1}{|r_h|} \exp\left(\frac{{r_h}^2(2P_1-1)}{2P_1} - \frac{z^2}{2P_2 {r_h}^2}\right)\right]
\end{aligned}
\tag{2.20}
$$

where, K is the small scale fading Rician K-factor and is given as the ratio of the specular power to the diffused power contributed by multiple reflections and refractions due to individual scatterers within a scattering cluster. The parameter S_h is defined as the range of shadowing values experienced, while traveling through different scattering clusters and Δ, as the shape parameter of the joint fading and shadowing distribution. The value of Δ ranges between 0 and 1 representing the transition from one scattering cluster to the next. When the magnitude of shadowing values contributed by two consecutive scattering clusters become equal, $\Delta = 1$, while the absence of one shadowing cluster results in $\Delta = 0$. The expression in (2.20) will be referred to as the Joint Fading and Two-path Shadowing (JFTS). The detailed calculation of $f_Z(z)$ is shown in Appendix A. An example set of measured PDFs that contain both shadowing and fading along with their best fit JFTS distributions will be presented in the next chapter along with the discussion on how well the JFTS model fits the joint fading and shadowing PDFs extracted from the measurements described in Section 2.4.

2.7 Summary

A detailed measurement campaign is conducted for capturing the impact of spatio-temporal variations in the received signal envelope over an indoor wireless channel. From the measured data, individual distributions of small scale fading and shadowing are extracted. Next Rician distribution is used to approximate the small scale fading distribution and the TWDP distribution to approximate shadowing. Then both the distributions are combined to yield a joint distribution, which analytically models the combined effect of small scale multipath fading and large scale shadowing in an indoor environment. The newly developed model is coined as the Joint Fading and Two-path Shadowing (JFTS) distribution.

The JFTS distribution consists of three fundamental parameters, K, S_h and Δ. The parameter, K, is the small scale fading Rician K-factor and is given by the ratio of the specular power to the diffused power contributed by multiple reflections and refractions due to individual scatterers within a scattering cluster. The parameter, S_h, is defined as the range of shadowing values experienced, while traveling through different scattering clusters, and Δ, as the shape parameter representing the transition from one scattering cluster to the next one.

Chapter 3

Propagation Model

3.1 Background

In an indoor wireless environment like an open office or laboratory, there are not enough large obstacles to reflect or refract the main waves contributed by the scattering clusters. Moreover, due to the inability of most WLAN standards to accommodate hand-offs, mobile WLAN users have to limit their movements within a small area traveling between at most one or two scattering clusters. In order to characterize the transition from local small scale fading to global shadowing statistics in such an indoor wireless environment, a detailed measurement campaign was conducted over signal bandwidths of 10 MHz, the description of which is presented in Chapter 2. A joint distribution that combines Rician fading and the TWDP shadowing model was derived based on the collected measurement data. However, the work in Chapter 2 is limited only to the derivation of the JFTS PDF.

The JFTS propagation model differs fundamentally from other more recent studies of indoor propagation. Recent efforts in modeling indoor wireless communication scenarios can be broadly classified in to two groups. The first group [31] - [33] aims at formulation of numerical techniques that can rigorously capture the underlying physics of wireless links. The second group [34] - [36] concentrates on modeling the stochastic or temporal variations in its power spectral density. However, JFTS accounts for both the small scale and large scale channel effects over a small neighborhood of at most two scattering clusters within a time window larger than the coherence time of large scale shadowing. Hence, JFTS propagation model is neither site-specific like the first group, nor it only examines the local fading statistics like the second group.

The first contribution of this chapter therefore is to examine the breadth of the application of the JFTS model and its capability of modeling a wide variety of indoor wireless communication scenarios. In order to do that the derived PDF expression for JFTS will be fit to measured distributions that capture the combined effect of indoor fading and shadowing. Based on the distribution fitting, some ranges of numerical values of each parameter of the distribution will be suggested depending on the relative position of the mobile WLAN user and the access point.

Statistical characterization of the received signal envelope in terms of its moments, like mean and variance, and CDF is useful in the design of a mobile radio communication system and the analysis of its performance. On one hand, moments of the fading and shadowing distribution are used to develop the PDF and the Moment Generating Function (MGF) of the instantaneous received signal-to-noise ratio (SNR) over the communication channel. These PDF and MGF expressions are in turn used to derive analytical expressions for performance measures like average SNR, average bit error rate (BER) and average symbol error rate (SER). On the other hand, the expression for CDF can used to analyze the outage probability performance of communication systems. CDF expressions can also be used to calculate higher order statistics like Level Crossing Rate (LCR) or Amount of Fading (AF), as is done in [37].

Expressions for BER and SER do not capture all the benefits of diversity combining, as mentioned in [38]. In this case, another performance measure called AF is used that take into account higher moments of the combiner output SNR. The AF is a unified measure of the severity of fading and is expressed in terms of moments of the fading distribution itself. Therefore, it can be used as numerical basis for comparing severity of fading contributed by the JFTS distribution to that imparted by other commonly used fading and composite fading/shadowing distributions.

Hence, the second contribution of this chapter is to derive new expressions for the joint moments, CDF and AF of the JFTS distribution. The expression for AF will be used to compare the severity of fading imparted by the JFTS distribution with the fading severity of Rayleigh, Nakagami-m, K-distribution [14] and Nakagami-m - log-normal distribution [18]. This will also enable us to calculate the values of the JFTS parameters for which the amount of JFTS fading will be approximately equivalent to the AF contributed by the above mentioned conventional channel distributions.

The rest of this chapter is organized as follows. Section 3.2 illustrates the application and accuracy of the JFTS model while the analytical derivation of joint moments, CDF and AF is presented in Section 3.3. The concluding remarks are made in Section 3.4.

3.2 PDF Characterization and Distribution Fitting

The PDF of the JFTS distribution is given by (refer to (2.20) in Chapter 2),

$$f_Z(z) = \frac{z}{P_1 P_2}\, e^{(-K-S_h)} \sum_{j=1}^{4} b_i D\left(z\sqrt{\frac{2K}{P_1 P_2}}; S_h, \Delta \mathsf{M}_j \right) \sum_{h=1}^{\mathsf{m}} \left[\frac{w_h}{|r_h|}\, e^{\left(\frac{{r_h}^2 (2P_1 - 1)}{2P_1} - \frac{z^2}{2P_2 {r_h}^2} \right)} \right] \tag{3.1}$$

where Z is the composite faded/shadowed received signal envelope, $I_0(\cdot)$ is the zeroth order modified Bessel function of the first kind, $\mathsf{M}_j = \cos((j-1)\pi/7)$ and $b_j = a_j I_0(1)$, where $a_1 = 751/17280$, $a_2 = 3577/17280$, $a_3 = 49/640$ and $a_4 = 2989/17280$ for $j = 1, 2, 3, 4$ respectively. The parameter K is the Rician K-factor, S_h is the range of discrete shadowing values experienced by a user as it transits through different scattering clusters, Δ represents the transition from one scattering cluster to the next one, P_1 is the mean-squared voltage of the diffused components and P_2 is the mean squared voltage of the shadowed components. The variable, m is the quadrature order (determining approximation accuracy) and the multiplier w_h are the Gauss-Hermite quadrature weight factors which is tabulated in [39] and is given by,

$$w_h = \frac{2^{\mathsf{m}-1}\mathsf{m}!\sqrt{\pi}}{\mathsf{m}^2[H_{\mathsf{m}-1}(r_h)]^2}$$

where $H_{\mathsf{m}-1}(.)$ is the Hermite polynomial with roots r_h for $h = 1, 2, \ldots, m$ and, $b_i = a_i I_0(1)$. For our analysis, we have chosen $\mathsf{m} = 20$, as is done for parameter estimation of composite gamma - log-normal fading channels in [40].

The rest of this section is organized as follows. Subsection 3.2.1 discusses the behavior of the JFTS distribution and presents an intuitive understanding of how its characteristics depend on its three main parameters, K, S_h and Δ. Subsection 3.2.2 demonstrates how well the JFTS model fits to the joint fading and shadowing PDFs extracted from the measurements described in Chapter 2 - Section 2.3.

3.2.1 Behavior of the JFTS Distribution

An example set of JFTS distributions is plotted in Fig. 3.1 and Fig. 3.2, for three different combinations of K and S_h. Correspondingly, Δ is kept constant for each plot, but changed from one plot to the next. The most predominant feature of the JFTS distribution is the existence of the two humps, the dominant bell-shaped peak and narrow spike-shaped peak. As each of the parameter of the three main parameters, K, S_h and Δ, are varied the distance between the two peaks as well as the width of each peak changes. For example, when K and Δ are varied the distance between the humps changes, while when K and S_h are varied the width of the individual humps changes.

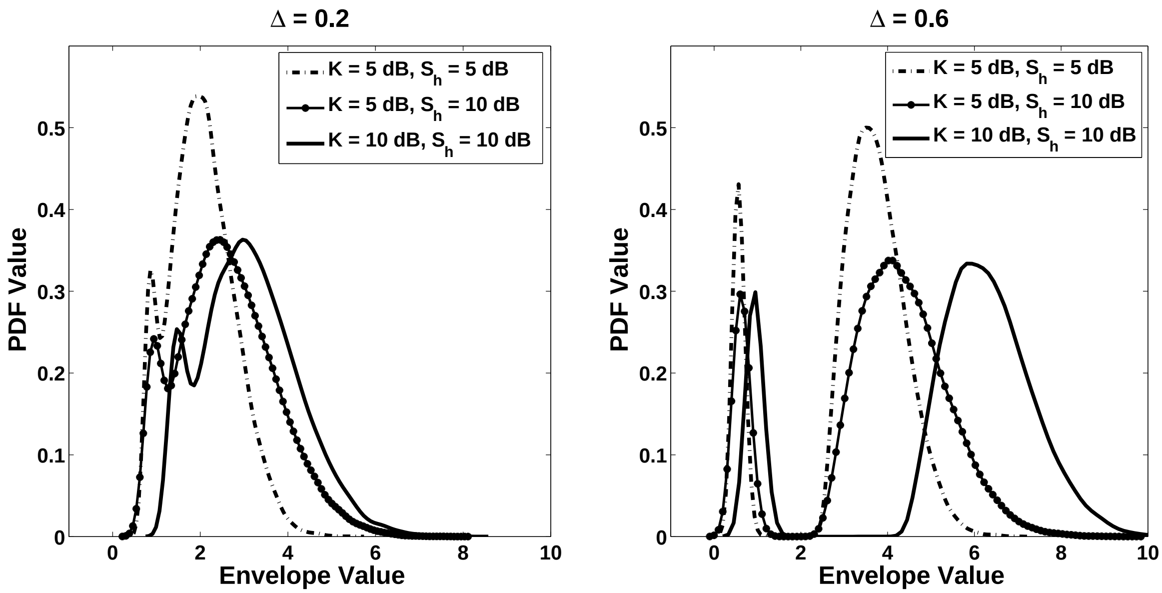

Figure 3.1: PDF of JFTS generated by varying values of Δ, K from 5 dB to 10 dB and S_h from 5 dB to 10 dB.

In case of both Fig. 3.1 and Fig. 3.2, K-value is increased from 5 dB to 10 dB. As K increases, the peaks of the distribution gets shifted due to the fact that once $K \geq 5$ dB the shadowing factor essentially determines the shape of the distribution. This represents a typical indoor wireless environment where Rician fading K-factor varies from 4 dB to 12 dB. Higher K-factor established presence of a dominant LOS component between the transmitter and the receiver. Moreover in an indoor environment, a group of strong reflected specular components will always exist between the transmitter and the receiver due to the light construction of the office interior walls. As a result, the power contributed by the specular components will always exceed that contributed by the diffused components resulting in a positive K-factor.

In case of Fig. 3.1, S_h is increased from 5 dB to 10 dB, while in case of Fig. 3.2, it is increased from -10 dB to -5 dB. As S_h increased, the peaks of the PDF widen. This represents scenarios

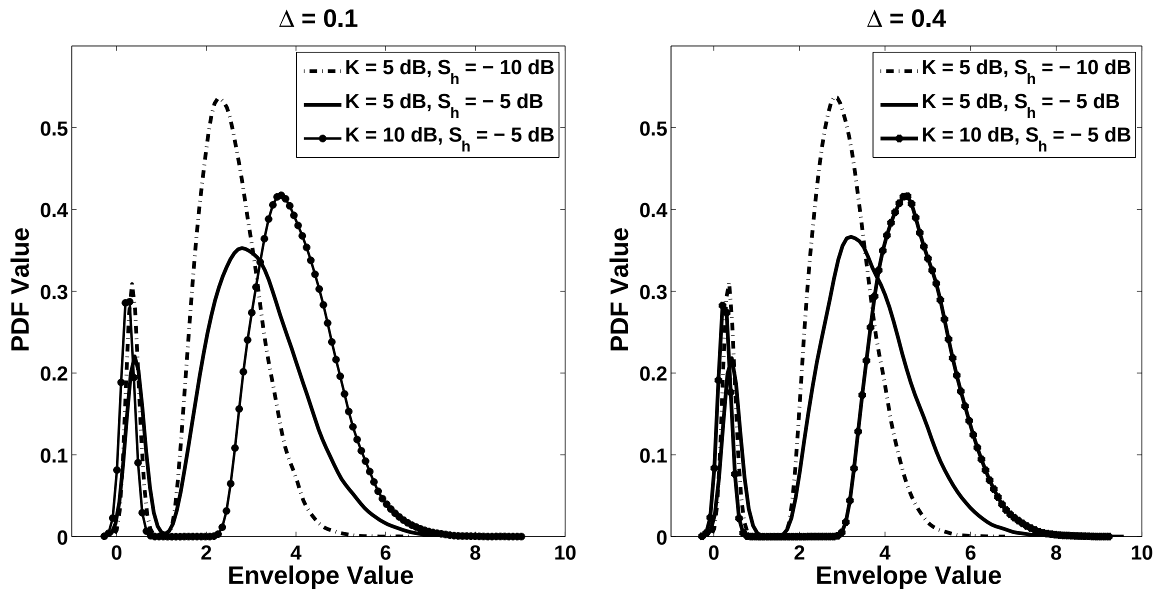

Figure 3.2: PDF of JFTS generated by varying values of Δ, K from 5 dB to 10 dB and S_h from -10 dB to -5 dB.

where each scattering neighborhood presents a larger range of shadowing values. A low shadowing parameter represents the scenario where each scattering cluster contributes a very small range of discrete shadowing values, that are encountered repeatedly. In that case S_h can assume values between 0 and 1 resulting in negative values in the decibel scale.

As mentioned before, Δ parameter is the shape parameter of the JFTS distribution. The value of Δ ranges between 0 and 1 representing the transition from one scattering cluster to the next. When the magnitude of shadowing values contributed by two consecutive scattering clusters become equal, $\Delta = 1$, while the absence of one shadowing cluster results in $\Delta = 0$. Hence, when Δ is increased, the magnitude of the shadowing values contributed by two consecutive scattering clusters get closer to each other. As a result, the distribution exhibits two distinct peaks and the distance between the humps of the distribution increases, as is evident from Fig. 3.1 and Fig. 3.2.

3.2.2 Application to Measured Data

The JFTS distribution of $f_Z(z)$ is used for distribution fitting of the extracted joint PDFs with the help of Chi-squared merit function. Distribution of the variations in the received signal envelope are extracted over a time scale exceeding the coherence time of large scale shadowing. Hence, it can be written as,

$$\chi^2(K, S_h, \Delta, P_1, P_2) = \sum_{i=1}^{N} \left[\frac{F_{3i} - \sum_{h=1}^{20} \frac{z_i}{P_1 P_2} e^{-K - S_h - \frac{z_i^2}{2P_2 r_h^2}} \mathcal{R} \sum_{j=1}^{4} D\left(z_i \sqrt{\frac{2K}{P_1 P_2}}; S_h, \Delta \mathsf{M}_j\right)}{q_i} \right]^2 \tag{3.2}$$

where $\mathcal{R} = \frac{w_h}{|r_h|} e^{\frac{{r_h}^2 (2P_1 - 1)}{2P_1}}$, $F_{3i} = f_{Z_i}(z_i)$ with individual standard deviations of q_i. In order to determine the values of K, S_h, P_1, P_2 and Δ, that best fit each fast variation envelope distribution, (3.2) is to minimized with respect to K, S_h, P_1, P_2 and Δ respectively. Following the same procedures as in Subsection 2.5.1 and Subsection 2.5.2, the values for K, S_h, P_1, P_2 and Δ are calculated.

Next, the goodness-of-fit measure is estimated by the incomplete Gamma function [41]. Fig. 3.3 presents the calculated values of K, S_h and Δ, while Fig. 3.4 depicts the calculated values of P_1, P_2 and their corresponding goodness-of-fit, Q values over all receiver routes and transmit locations at $f_c = 900$ MHz. Fig. 3.5 and Fig. 3.6 present the calculated values of K, S_h, Δ, P_1, P_2 and corresponding goodness-of-fit, Q values, respectively over all receiver routes and transmit locations at $f_c = 2450$ MHz . All the Q-values lie between 0.2 and 0.95, which establishes the fact that, our approximated PDFs offer a good fit to the extracted PDFs. The set of measured PDFs with their fitted approximated PDFs, with $f_c = 2.45$ GHz, is presented in Fig. 3.7.

In order to increase confidence that JFTS offers the best possible fit to the collected measurement

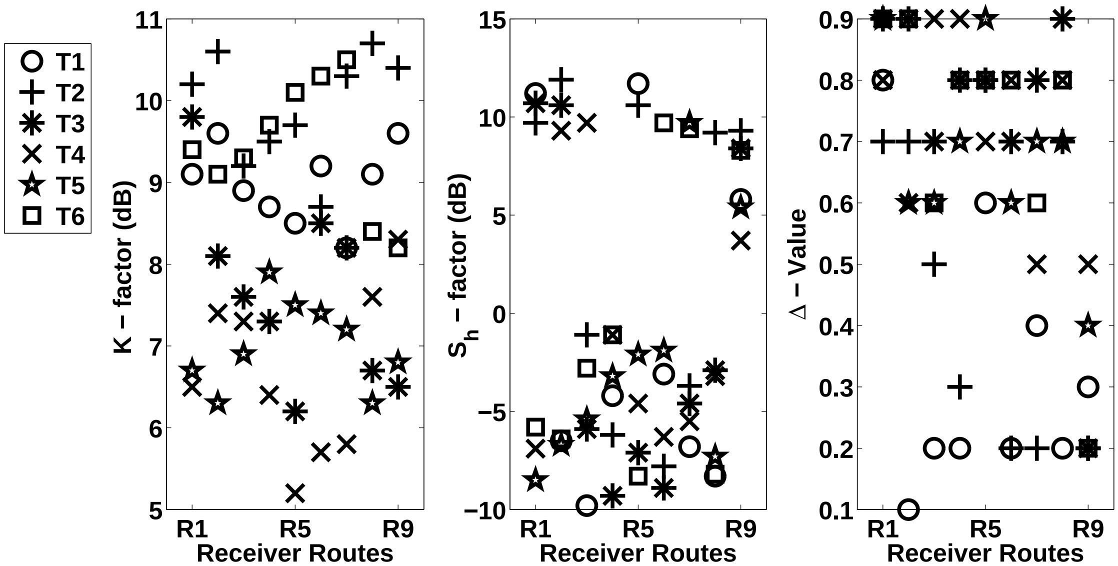

Figure 3.3: Calculated values of K, S_h and Δ over all receiver routes and transmit locations at $f_c = 900$ MHz

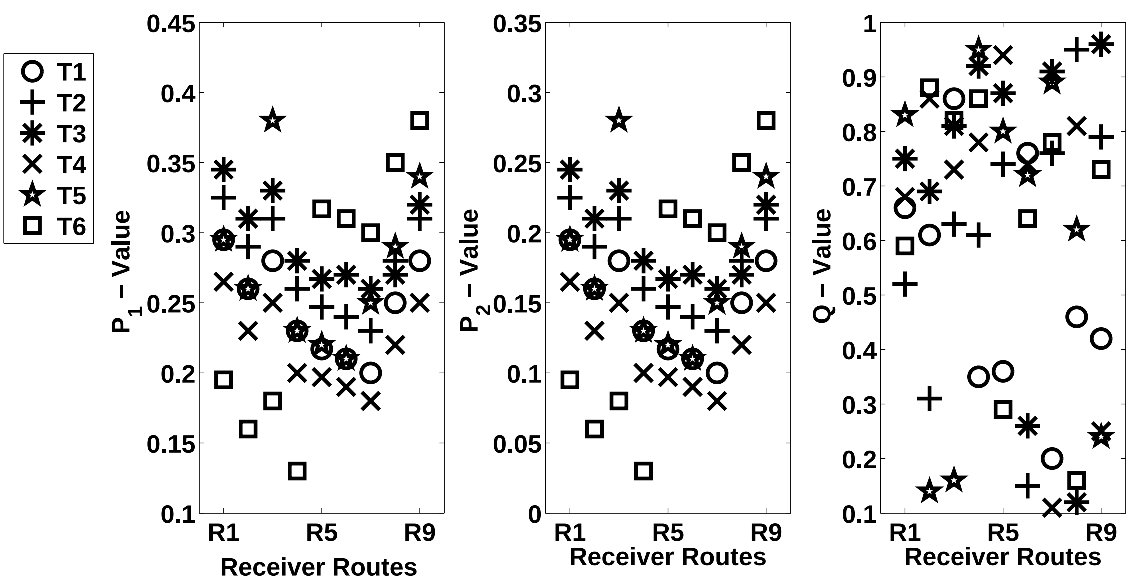

Figure 3.4: Calculated values of P_1, P_2 and Q over all receiver routes and transmit locations at $f_c = 900$ MHz

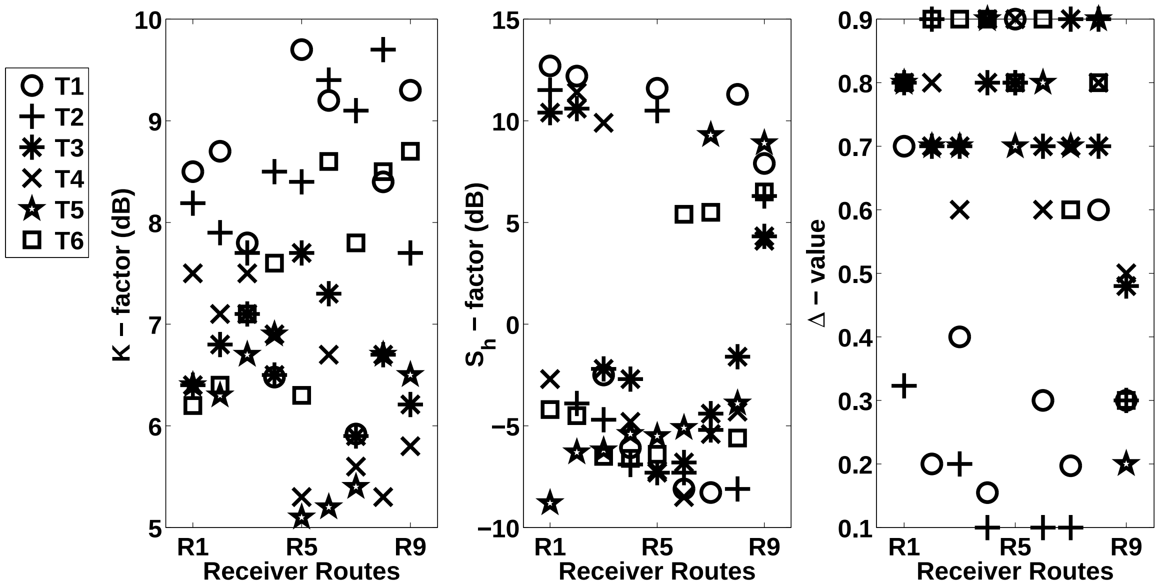

Figure 3.5: Calculated values of K, S_h and Δ over all receiver routes and transmit locations at $f_c = 2450$ MHz

set, a comparative distribution fitting of the joint Nakagami-m - log-normal [18] distribution and the JFTS distribution to the measurement data set is also presented. Nakagami-m - log-normal channel model is our preferred choice for comparison because the Nakagami-m factor can be varied to characterize both Rician and Rayleigh fading and the log-normal distribution is used to model shadowing in the bulk of the available composite fading/shadowing models.

The PDF of the received signal power over a log-normal shadowed Nakagami-m fading communication channel is given by,

$$\begin{aligned} f_\Xi(\xi) &= f_\Xi(\xi; m, \mu, \sigma^2) \\ &= \int_0^\infty \frac{m^m \xi^{m-1}}{\omega^m \Gamma(m)}\, e^{-\frac{m\xi}{\omega}}\, \frac{4.3429}{\sqrt{2\pi}\sigma\omega}\, e^{-\frac{(10\log_{10}\omega - \mu)^2}{2\sigma^2}}\, \mathrm{d}\omega \end{aligned} \tag{3.3}$$

where m is the Nakagami m factor and μ (dB) and σ (dB) are the mean and standard deviation of

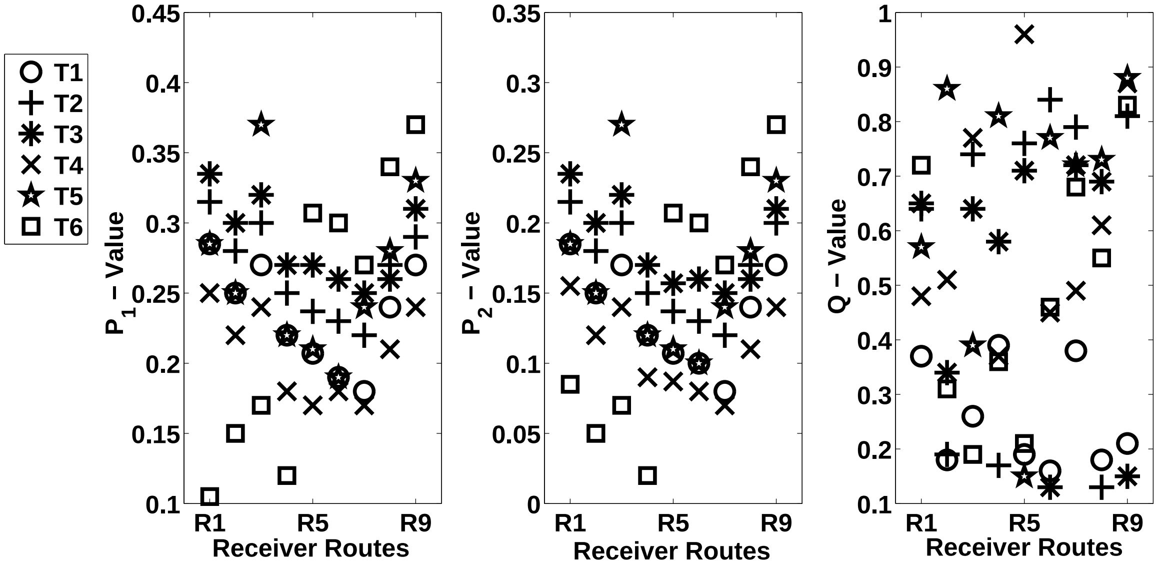

Figure 3.6: Calculated values of P_1, P_2 and Q over all receiver routes and transmit locations at $f_c = 2450$ MHz

the log-normal shadowing distribution respectively. The Newton - Raphson method [42] has been used for maximum likelihood estimation (MLE) of the composite shadowing/fading distribution parameters, m and σ (dB) for distribution fitting to the measured PDF. The sample set of approximated PDFs using Nakagami-m - log-normal distribution is also presented in Fig. 3.7. The best fit parameters of both the distributions are tabulated in Table 3.1.

It is evident from Table 3.1 that distribution fitting using the Nakagami-m - log-normal distribution yields Q-values lower than that of the JFTS distribution in the case of each of the four scenarios considered. Particularly in the case of $T1 : R7$ and $T3 : R9$, distribution fitting with the Nakagami-m - log-normal distribution yields Q-values lower than 0.1. As mentioned in Chapter. 2, if the Q-value is lower than 0.1, the distribution fitting is fine under the constraint that the measurement either are non-normal or have been moderately under-estimated. For both of

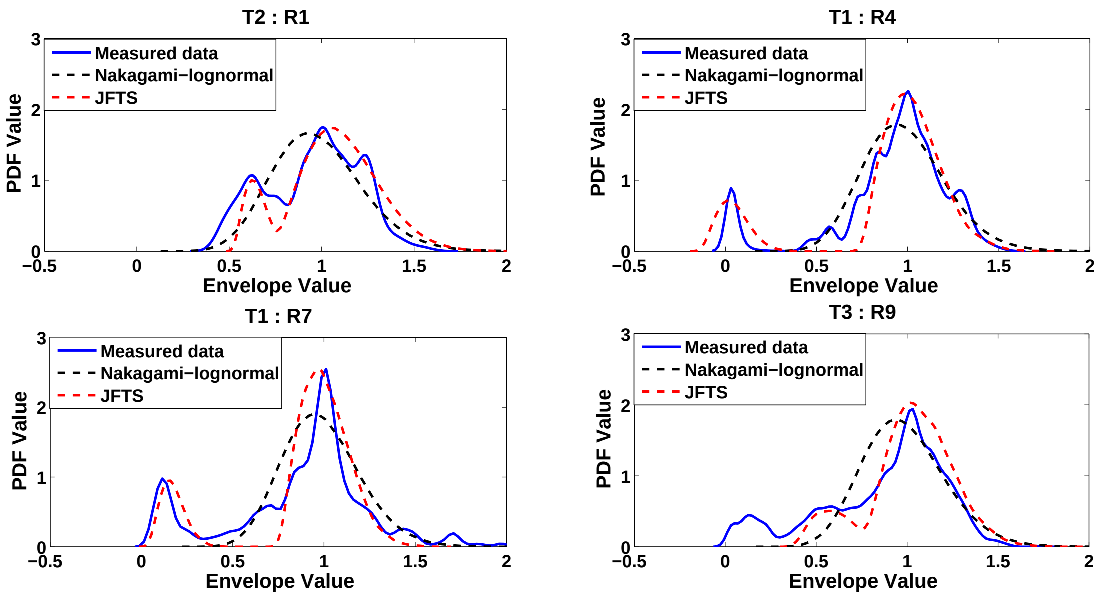

Figure 3.7: Comparative distribution fitting using Nakagami-m - log-normal and JFTS distributions with the approximated PDFs for $f_c = 2450$ MHz

these communication scenarios, distribution fitting using JFTS model yields Q-values higher than 0.1, which renders fitting to be fine without any constraint. In addition, visual inspection of the distributions in Fig. 3.7 indicate that Nakagami-m - log-normal distribution fails to adequately characterize the two peaks commonly seen in the fading distributions generated using the measurement data presented in this thesis.

For the $T2 : R1$ scenario of Fig. 3.7, the calculated JFTS parameters are $K = 8.19$ dB, $S_h = 11.51$ dB and $\Delta = 0.323$. The measurements are taken when the transmitter is located in an open lab room, with smaller obstacles like low tables, cabinets and equipment. The receiver is moved through another room cluttered with large obstacles like book-shelves, equipment and file-cabinets, soft cubicle walls, lab benches as well as small obstacles like work tables, hairs and several pieces

Table 3.1: Parameters used for distribution fitting

Transmit Position : Receive Position	Nakagami-m - log-normal parameters	JFTS parameters
$T2 : R1$	$m = 5$, $\sigma = 0$ dB, Q-value $= 0.1474$	$K = 8.19$ dB, $S_h = 11.51$ dB, $\Delta = 0.323$, Q-value $= 0.626$
$T1 : R4$	$m = 2$, $\sigma = 2$ dB, Q-value $= 0.227$	$K = 6.48$ dB, $S_h = -6.08$ dB, $\Delta = 0.155$, Q-value $= 0.396$
$T1 : R7$	$m = 2$, $\sigma = 2$ dB, Q-value $= 0.091$	$K = 5.92$ dB, $S_h = -8.28$ dB, $\Delta = 0.372$, Q-value $= 0.372$
$T3 : R9$	$m = 4$, $\sigma = 0$ dB, Q-value $= 0.046$	$K = 6.21$ dB, $S_h = 4.32$ dB, $\Delta = 0.48$, Q-value $= 0.168$

of electronic equipment. The two rooms are separated by walls constructed of two thin sheets of dry-walls with no insulation between the sheets. As a result, larger variations in the main wave amplitudes are obtained for each scattering neighborhood, yielding a high S_h-factor. The Δ factor is neither very high nor very low. This represents a scenario, where there exists at least two scattering clusters and the physical scattering conditions are similar over adjacent neighborhoods. On the other hand, as the transmitter and the receiver are close to each other, there exists a group of strong reflected specular components that arrive with relatively little attenuation due to the light construction of the office interior walls. This has resulted in high small scale fading K-factor.

For the $T1 : R4$ and $T1 : R7$ scenarios of Fig. 3.7, the calculated JFTS parameters are $K = 6.48$ dB, $S_h = -6.08$ dB, $\Delta = 0.155$ and $K = 5.92$ dB, $S_h = -8.28$ dB, $\Delta = 0.1973$ respectively. These measurements are taken when the transmitter is located in a lab room cluttered with large obstacles. The receivers are moved through open lab rooms with smaller objects like low tables and cabinets. The two rooms in concern in both cases, are very far from each other, separated by several drywalls, doors and other in-building structures. As a result, very low S_h-factors are

Table 3.2: Generalized range of values for the parameters of JFTS distribution

User / Access Point (AP) Positions	K (dB)	S_h (dB)	Δ
Same room	9 to 11	9 to 12	0.6 to 0.95
Different rooms separated by 1 wall or partition	7 to 9	6 to 11	0.3 to 0.58
Different rooms separated by 2 to 3 walls or partitions	6 to 7	- 4.5 to - 0.5	0.2 to 0.3
Different rooms separated by more than 3 walls or partitions	5 to 6	- 5 to - 9.8	0.1 to 0.2

obtained. This represents a scenario where, each scattering cluster contributes a very small range of discrete shadowing values, that are encountered repeatedly. The Δ factor is also very low. This is due to the fact that although there exists at least two scattering clusters, the magnitude of the shadowing values encountered in one is much larger than that of the other. However, there still exist a small group of strong specular components between the transmitter and the receiver. this resulted in a high small scale fading K-factor, but lower than that of the first plot.

For the $T3 : R9$ scenario, the calculated JFTS parameters are $K = 6.21$ dB, $S_h = 4.32$ dB and $\Delta = 0.48$. These measurements are taken when the transmitter is located in a lab room cluttered with large obstacles. The receive dis moved through the entire corridor. Hence, at some points the transmitter and the receiver are very close to each other. As a result, a large range of shadowing values are contributed by each scattering neighborhood, yielding a high S_h factor. In this case, the product $S_h\Delta \approx 2$. According to the properties of the TWDP distribution mentioned in [15], the TWDP PDF resembles a Rician PDF in shape for $S_h\Delta \leq 2$. Therefore, the joint distribution, in this case, can be approximated by a bivariate Rician distribution.

After extensive data fitting, it is possible to recommend JFTS model parameters that are suitable for different scenarios within the indoor office environment. The different ranges of values of K, S_h and Δ have been compiled in Table 3.2 for these scenarios.

3.3 Statistical Properties

In this section, the expression for the joint PDF of the JFTS distribution will be used to derive the expressions for different statistical properties like joint moments, CDF and AF of the distribution. Subsection 3.3.1 derives the nth joint moment of the JFTS distribution which will be subsequently used to derive the expression for AF in Subsection 3.3.2. Finally the expression for CDF is derived in Subsection 3.3.3.

3.3.1 Joint Moments

The JFTS distribution combines Rician fading and TWDP shadowing models. Assuming mutually independent fading, $X(t)$, and shadowing, $Y(t)$, processes, the received signal envelope over a JFTS faded/shadowed channel can be given by $Z = XY$. In this case, the distribution of the fading process can be expressed using the Rician distribution as,

$$f_X(x) \;=\; \frac{x}{P_1}\, e^{-\frac{x^2}{2P_1}-K}\; I_0\!\left(x\sqrt{\frac{2K}{P_1}}\right) \tag{3.4}$$

and the distribution of the shadowing process can be expressed using the TWDP distribution as,

$$f_Y(y) \;=\; \frac{y}{P_2}\, e^{-\frac{y^2}{2P_2}-S_h}\; \sum_{j=1}^{4} a_j D\!\left(\frac{y}{\sqrt{P_2}}; S_h, \Delta\mathsf{M}_j\right) \tag{3.5}$$

The joint probability density function, $f_{XY}(x, y)$ of $X(t)$ and $Y(t)$ will then be given by,

$$f_{XY}(x,y) \;=\; \frac{xy}{P_1P_2}\, e^{-\frac{x^2}{2P_1}-\frac{y^2}{2P_2}-K-S_h}\; I_0\!\left(x\sqrt{\frac{2K}{P_1}}\right)\,\left[a_1\mathsf{T}_1 + a_2\mathsf{T}_2 + a_3\mathsf{T}_3 + a_4\mathsf{T}_4\right] \tag{3.6}$$

where,

$$\mathsf{T}_j \;=\; e^{S_h \Delta \mathsf{M}_j}\; I_0\bigg(y\sqrt{2S_h(1-\Delta\mathsf{M}_j)/P_2}\bigg) + e^{-S_h\Delta\mathsf{M}_j}\; I_0\bigg(y\sqrt{2S_h(1+\Delta\mathsf{M}_j)/P_2}\bigg) \tag{3.7}$$

To calculate the nth moment of $f_Z(z)$, the following integral is needed to be solved,

$$\mathrm{E}\{Z^n\} \;=\; \int_{-\infty}^{\infty} z^n\; f_Z(z)\mathrm{d}z \tag{3.8}$$

Given two independent random variables X and Y and a function $g(x,y)$, where $Z = g(x,y) = XY$, $\mathrm{E}\{Z^n\}$ can be expressed directly in terms of the function $g(x,y)$ and the joint density, $f_{XY}(x,y)$ [43]. Hence, (3.8) can then be written as,

$$\mathrm{E}\{(g(X,Y))^n\} \;=\; \int_{-\infty}^{\infty}\int_{-\infty}^{\infty} [g(x,y)]^n f_{XY}(x,y)\mathrm{d}x\mathrm{d}y. \tag{3.9}$$

Inserting (3.4) in (3.9), (3.9) can be written as,

$$\begin{aligned}\mathrm{E}\{(g(X,Y))^n\} \;=\; & \int_{-\infty}^{\infty} \frac{(y)^{n+1}}{P_2}\; e^{-\frac{y^2}{2P_2}-S_h}\; \Big(a_1\mathsf{T}_1 + a_2\mathsf{T}_2 + a_3\mathsf{T}_3 + a_4\mathsf{T}_4\Big) \\ & \cdot \left[\int_{-\infty}^{\infty} \frac{(x)^{n+1}}{P_1}\; e^{-\frac{x^2}{2P_1}-K} I_0\bigg(x\sqrt{\frac{2K}{P_1}}\bigg)\mathrm{d}x\right]\mathrm{d}y. \end{aligned} \tag{3.10}$$

The integration in (3.10) can be solved by separating the integrand into two parts, $\mathcal{A}$ and $\mathcal{B}$, which can be evaluated as,

$$\begin{aligned}\mathcal{A} \;&=\; \int_{-\infty}^{\infty} \frac{(x)^{n+1}}{P_1}\; e^{-\frac{x^2}{2P_1}-K} I_0\bigg(x\sqrt{\frac{2K}{P_1}}\bigg)\mathrm{d}x \\ &= (2P_1)^{n/2}\; \Gamma(1+n/2)\; L_{n/2}(-K)\end{aligned} \tag{3.11}$$

and

$$
\begin{aligned}
\mathcal{B} &= \sum_{j=1}^{4} a_j \int_{-\infty}^{\infty} \mathsf{T}_j \, \frac{(y)^{n+1}}{P_2} \, e^{-\frac{y^2}{2P_2} - S_h} \mathrm{d}y \\
&= \sum_{j=1}^{4} a_j \, (2P_2)^{n/2} \, \Gamma(1+n/2) \, \big[L_{n/2}(-(1-\Delta\mathsf{M}_j)S_h) + L_{n/2}(-(1+\Delta\mathsf{M}_j)S_h) \big] \qquad (3.12)
\end{aligned}
$$

where the Laguerre polynomial $L_\beta(\alpha)$ can be defined by the Rodrigues formula, $L_\beta(\alpha) = \frac{e^\alpha}{\beta!} \frac{\mathrm{d}^\beta}{\mathrm{d}\alpha^\beta}(\alpha^\beta \, e^{-\alpha})$ [44] and $\Gamma(\alpha') = (\alpha' - 1)!$ [45]. The detailed derivations of (3.11) and (3.12) are provided in Appendix B. Combining (3.11) and (3.12), the final expression for joint moments of JFTS distribution is obtained as,

$$
\mathrm{E}\{(g(X,Y))^n\} = (4P_1P_2)^{n/2} \, \{\Gamma(1+n/2)\}^2 \, L_{n/2}(-K) \sum_{j=1}^{4} a_j \, G^{(n)}(S_h, \Delta\mathsf{M}_j) \qquad (3.13)
$$

where a new function $G^{(n)}(\beta', \delta')$ is introduced for simplification of notation and is defined as,

$$
G^{(n)}(\beta', \delta') = [L_{n/2}(-(1-\delta')\beta') + L_{n/2}(-(1+\delta')\beta') \qquad (3.14)
$$

Next the expression for joint moments (3.13) will be used to derive the mean, second moment and variance of the JFTS distribution.

Mean : The mean of the JFTS distribution can be obtained by putting $n = 1$ in (3.13),

$$
\begin{aligned}
\mu_z^1 &= \mathrm{E}\{(g(X,Y))\} = \mathrm{E}\{Z\} \\
&= \frac{\pi}{2} \sqrt{P_1P_2} \, L_{1/2}(-K) \sum_{j=1}^{4} a_j \, G^{(1)}(S_h, \Delta\mathsf{M}_j) \qquad (3.15)
\end{aligned}
$$

Second Moment : The second moment of the JFTS distribution can be obtained by putting $n = 2$ in (3.13),

$$
\begin{aligned}
\mu_z^2 &= \mathrm{E}\{(g(X,Y))^2\} = \mathrm{E}\{Z^2\} \\
&= 8P_1P_2 \, (1+K) \sum_{j=1}^{4} a_j \, (1+S_h) \qquad (3.16)
\end{aligned}
$$

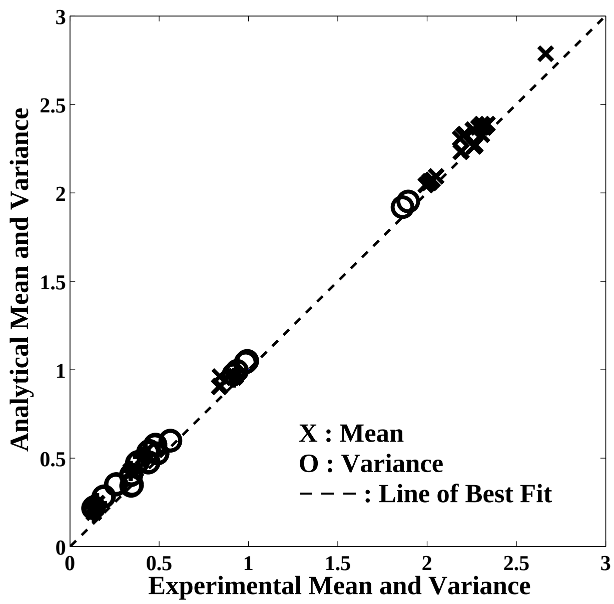

Figure 3.8: Analytical and Experimental means and variances

Variance : The second central moment or the variance of the JFTS distribution can be calculated as,

$$\begin{aligned} \sigma_z^2 &= \mathrm{E}\{Z^2\} - (\mathrm{E}\{Z\})^2 \\ &= 8P_1P_2\ (1+K)\ \sum_{j=1}^{4} a_j\ (1+S_h) - \frac{\pi^2}{4}\ P_1P_2\ L_{1/2}^2(-K)\ \sum_{j=1}^{4} a_j^2\ \{G^{(1)}(S_h, \Delta\mathsf{M}_j)\}^2 \end{aligned} \tag{3.17}$$

In order to verify the validity of the derived expressions for mean and variance of the JFTS distribution, all the measurement files collected over the center frequency of 2.45 GHz are chosen for analysis. The theoretical and experimental means and variances for each measurement data set are plotted on Fig. 3.8, where experimental mean and variance are plotted on the x-axis and the theoretical mean and variance are plotted on the y-axis. In the case of the theoretical expressions, the JFTS parameters used are the best fit values for each measurement file. In is evident from Fig. 3.8, that the theoretical results agree with the experimental results. For example, for the measurement file of $T2 : R5$, the ratio of the theoretical mean to the experimental one is -0.2 dB, while for $T3 : R4$, the ratio of the means is approximately equal to -0.3 dB. Similarly, the ratio of the theoretical variance to the experimental variance for $T1 : R9$ is -0.03 dB.

3.3.2 Amount of Fading (AF)

Amount of Fading (AF) is a common performance metric of wireless communication systems, where both the first and second moments of the fading distribution are taken into consideration for evaluating the metric. For the JFTS distribution, AF can be calculated as,

$$\mathrm{AF} \;=\; \frac{\mathrm{Var}\{Z^2\}}{(\mathrm{E}\{Z^2\})^2} \;=\; \frac{\mathrm{E}\{Z^4\} - (\mathrm{E}\{Z^2\})^2}{(\mathrm{E}\{Z^2\})^2} \tag{3.18}$$

where $\mathrm{E}\{Z^4\}$ is the 4th moment of the JFTS distribution and can be calculated by putting $n = 4$ in (3.13)

$$\mathrm{E}\{Z^4\} \;=\; 16P_1^2P_2^2\ (K^2 + 4K + 2) \sum_{j=1}^{4} a_j\ (S_h^2 + 4S_h + 2 + S_h^2\Delta^2\mathsf{M}_j^2) \tag{3.19}$$

The square of the second moment of the JFTS distribution $(\mathrm{E}\{Z^2\})^2$ can be calculated as,

$$(\mathrm{E}\{Z^2\})^2 \;=\; 64P_1^2P_2^2\ (K^2 + 2K + 1) \sum_{j=1}^{4} a_j^2\ (S_h^2 + 2S_h + 1) \tag{3.20}$$

Hence the final expression for AF can be obtained by combining (3.19) and (3.20) as,

$$\mathrm{AF} \;=\; \frac{(K^2 + 4K + 2)\ \sum_{j=1}^{4} \left({S_h}^2 + 4S_h + 2 + {S_h}^2\Delta^2{\mathsf{M}_j}^2\right)}{4\ (K^2 + 2K + 1)\ \sum_{j=1}^{4} a_j\ \left({S_h}^2 + 2S_h + 1\right)} \;-\; 1 \tag{3.21}$$

The new expression for AF is now used to quantify the severity of fading experienced over the channel measured in Chapter 2. Assuming that the communication channel is JFTS faded, the theoretical amounts of fading contributed by different ranges of JFTS parameters are compiled in Table 3.3. The values for each set of parameters used in the AF expressions are chosen from the ranges of their numerical values proposed in Table 3.2, depending on the relative position of the

Table 3.3: Theoretical AFs for JFTS distribution

AP/User Proximity	K (dB)	S_h (dB)	Δ	AF
Same Room	9 to 11	9 to 12	0.6 to 0.95	1.19 to 1.82
1 Wall Separation	7 to 9	6 to 11	0.3 to 0.6	1.29 to 1.93
2 - 3 Wall Separation	6 to 7	- 4.5 to - 0.5	0.2 to 0.3	2.61 to 3.08
> 3 Wall Separation	5 to 6	- 9.8 to - 5	0.1 to 0.2	3.09 to 3.45

mobile LAN user and the access point.

It is evident from Table 3.3 that the AF contributed by JFTS fading can vary from 1.2 to 3.45 depending on the relative position of the mobile WLAN user and the access point. It can also be concluded that the AF of the JFTS distribution increases with a decrease in K-factor and/or the S_h-factor. This is due to the fact that as K decreases, the power contributed by the strong specular components decreases in comparison to that contributed by the diffused and the scattered components. The result is an increase in fading severity. On the other hand, a low S_h factor depicts a scenario where each scattering cluster contributes a very small range of discrete shadowing values that are higher in magnitude and encountered repeatedly. This condition results in an increased severity in shadowing.

The JFTS distribution has a very different PDF from common small scale fading distributions like the Rayleigh or Nakagami-m distributions or other composite fading/shadowing distributions like the Nakagami-m - log-normal or $\mathcal{K}$-distribution. However, the AF expressions for these conventional models can be used to determine the conventional channel conditions that would yield similar AF values to Table 3.3. For example, when the AP and the user are in the same room, the AF contributed by the JFTS fading varies between 1.19 and 1.82, which is equivalent to the

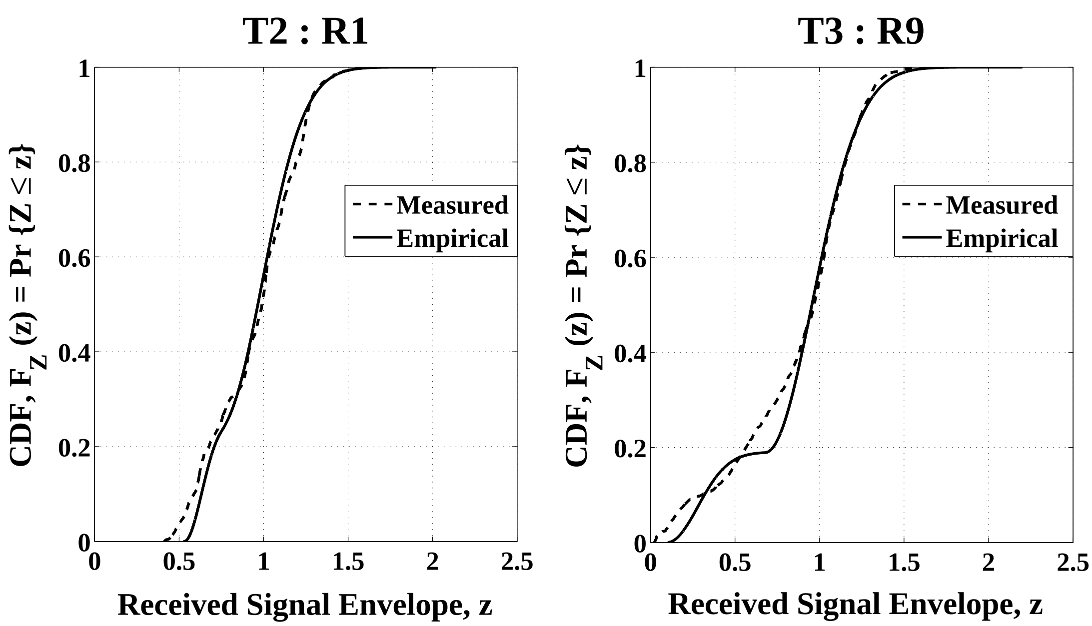

Figure 3.9: Set 1 : Measured and Empirical CDFs for JFTS at $f_c = 2450$ MHz.

AF contributed by the Nakagami-m distribution with $m = 0.55$ to 0.84, the $\mathcal{K}$-distribution with $\nu = 2.44$ to 10.53 and the Nakagami-m - log-normal distribution with $m = 1$ and $\sigma = 1.31$ to 2.55. Similarly, when the AP and the user are in different rooms separated by more than 3 partitions, the AF contributed by JFTS fading varies between 3.09 and 3.45, which is equivalent to the AF contributed by the Nakagami-m with $m = 0.29$ to 0.32, the K-distribution with $\nu = 0.82$ to 0.96 and the Nakagami-m - log-normal distribution with $m = 1$ and $\sigma = 3.67$ to 3.88.

3.3.3 Cumulative Distribution Function (CDF)

The Cumulative Distribution Function (CDF) of the composite fading/shadowing process, $Z(t)$ can be defined as $F_Z(z) \triangleq \Pr\{Z \leq z\}$ and the complimentary CDF (CCDF) of that process can be written as, $\bar{F}_Z(z) \triangleq \Pr\{Z \leq z\} = 1 - F_Z(z)$. By definition, the expression for JFTS CDF can be determined by solving,

$$F_Z(z) \;=\; \int_{-\infty}^{z} f_{\mathsf{U}}(\mathsf{u})\mathrm{d}\mathsf{u} \tag{3.22}$$

where U is the JFTS distributed received signal envelope with the PDF given by (3.1). Putting (3.1) in (3.22)and rearranging, the following is obtained,

$$F_Z(z) \;=\; \mathcal{C}_1 \sum_{j=1}^{4} \frac{b_j}{2} \sum_{h=1}^{20} \mathcal{R} \int_{-\infty}^{z} \mathsf{u}\; e^{-\mathcal{C}_2 \mathsf{u}^2}\; \big[\mathcal{D}_3 I_0(2\mathsf{u}\mathcal{D}_1) + \mathcal{D}_4 I_0(2\mathsf{u}\mathcal{D}_2)\big]\mathrm{d}\mathsf{u} \tag{3.23}$$

where, $\mathcal{C}_1 \;=\; e^{-K-S_h}/P_1P_2$, $\mathcal{C}_2 \;=\; 1/P_2r_h^2$, $\mathcal{D}_1 \;=\; 2\sqrt{KS_h(1-\Delta\mathsf{M}_j)/P_1P_2}$, $\mathcal{D}_3 \;=\; e^{S_h\Delta\mathsf{M}_j}$, $\mathcal{D}_2 \;=\; 2\sqrt{KS_h(1+\Delta\mathsf{M}_j)/P_1P_2}$ and $\mathcal{D}_4 \;=\; e^{-S_h\Delta\mathsf{M}_j}$. Using the infinite series expansion of the modified Bessel function and the integral solution from [39] we can obtain the final expression of the CDF of the JFTS distribution as,

$$\begin{aligned} F_Z(z) \;=\; & \sum_{j=1}^{4} \frac{b_j}{2} \sum_{h=1}^{20} \mathcal{R}\; e^{-K-S_h} \sum_{\mathsf{k}=0}^{\infty} \frac{K^{\mathsf{k}} S_h^{\mathsf{k}}}{(\mathsf{k}!)^2 P_1^{\mathsf{k}} P_2^{\mathsf{k}}} \left[(1-\Delta\mathsf{M}_j)^{\mathsf{k}}\; e^{S_h\Delta\mathsf{M}_j} + (1+\Delta\mathsf{M}_j)^{\mathsf{k}}\; e^{-S_h\Delta\mathsf{M}_j}\right] \\ & \cdot \left[1 - 2^{\mathsf{k}}(P_2r_h^2)^{\mathsf{k}+1}\Gamma\left(\mathsf{k}+1, \frac{z^2}{2P_2r_h^2}\right)\right]. \end{aligned} \tag{3.24}$$

For simplicity of analysis, the CDF expression can also be expressed in a easy-to-compute format using Marcum Q-function, as is done while representing CDF of any non-centralized chi-squared distribution like Rician distribution [46] In that case, the final expression for the CDF of the JFTS distribution will be given by,

$$\begin{aligned} F_Z(z) \;=\; & \sum_{j=1}^{4}\sum_{h=1}^{20} \frac{b_j}{2} \frac{\mathcal{R}r_h}{P_1\sqrt{P_2}}\; e^{-K-S_h} \Big[e^{S_h\Delta\mathsf{M}_j}\; Q_1(\sqrt{KS_h(1-\Delta\mathsf{M}_j r_h)/P_1}, z) \\ & + e^{-S_h\Delta\mathsf{M}_j}\; Q_1(\sqrt{KS_h(1+\Delta\mathsf{M}_j r_h)/P_1}, z)\Big] \end{aligned} \tag{3.25}$$

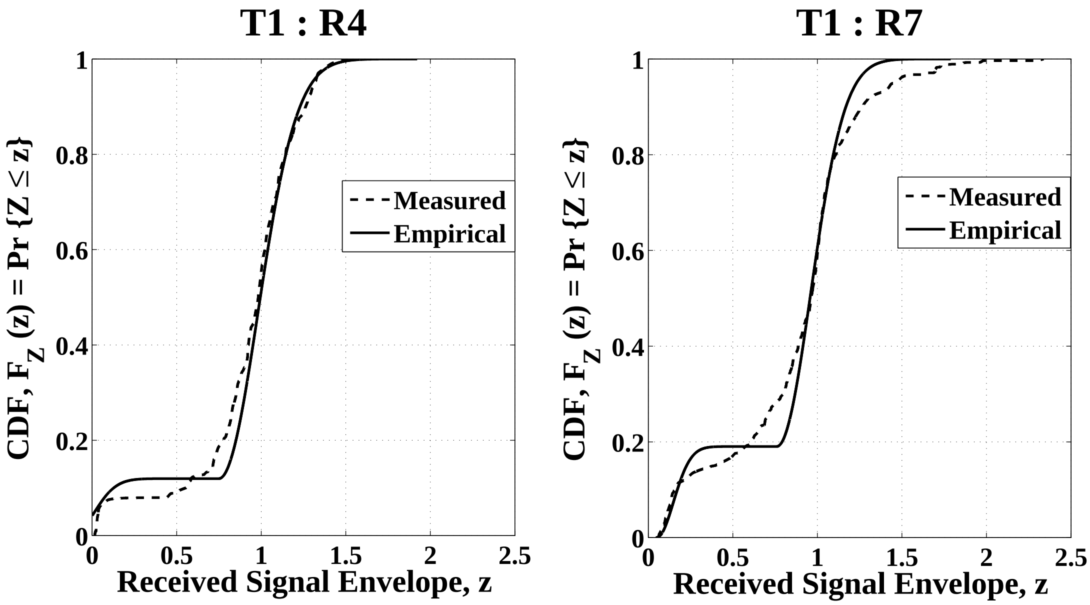

Figure 3.10: Set 2 : Measured and Empirical CDFs for JFTS at $f_c = 2450$ MHz.

where $\mathcal{R}$ and r_h are constants and can be obtained from the Gauss-Hermite polynomial table used in [40] and Q_1 is the Marcum Q-function, monotonic and log-concave in statistical characteristics.

Next the validity of the expression in (3.25) will be evaluated by comparing it with CDF curves generated using the measured data reported in Chapter 2. For the first set of figures in Fig. 3.9, measurements collected over the $T2 : R1$ and $T3 : R9$ scenarios are used for a measurement band of center frequency of 2.45 GHz. The best fit JFTS parameters for these two scenarios are found to be $K = 8.19$ dB, $S_h = 11.51$ dB, $\Delta = 0.323$ and $K = 6.21$ dB, $S_h = 4.32$ dB, $\Delta = 0.48$, respectively. The same set of parameters are used for CDF curve fitting. The expression is also verified over $T1 : R4$ and $T1 : R7$ scenarios.

In order to measure the goodness-of-fit between the CDF of the measured data, $F_{\mathsf{X}}(\mathsf{x})$ and the derived analytical CDF, $F_Z(z)$, we used the Kolmogorov-Smirnov (K-S) test, which can be defined as,

$$\mathsf{D} \overset{\triangle}{=} \max |F_Z(z) - F_{\mathsf{X}}(\mathsf{x})| \tag{3.26}$$

Let H_0 be defined as the null hypothesis that the measured data X belongs to the derived analytical CDF of the JFTS distribution, as is done in [47]. The K-S test is used to compare D to a critical level $\mathsf{D}_{\max} = 0.04301$ and a significance level $\delta = 0.05$. Any H_0 for which, $\mathsf{D} < \mathsf{D}_{\max}$ is accepted with a significance level of $1-\delta$. For all the measurement data sets considered in both Set 1 and Set 2, the null hypothesis is accepted with 95% significance, which establishes the fact that the derived expression for CDF offers a good fit to the CDFs of the measured data, with the distribution of the measurement errors being non-normal.

3.4 Summary

The first contribution of this chapter is to examine the appropriateness of the JFTS distribution in modeling mobility constrained indoor wireless environments through distribution fitting to measured PDFs of the variations in the received signal envelope. Next new expressions for the joint moments, mean, variance and CDF of the JFTS distribution are derived. It is also established that theoretical mean, variance and CDF of the JFTS distribution offer good agreements with the experimental results. Next the closed-form expression for the AF of the JFTS distribution is also derived and found that AF increases with the decrease in K - factor and/or S_h - factor. Finally the new AF expression is used for comparing the severity of fading imparted by the JFTS distribution with that by other common small scale fading and composite fading/shadowing distributions.

Chapter 4

Fixed Modulation and Coding

4.1 Background

Indoor wireless communication has resulted in new technologies and applications ranging from communications between individuals inside cars, homes, flights, boats or ferries to impersonal communications between wireless sensors, industrial equipments, indoor machineries and home appliances. This has resulted in the increased demand of exact theoretical analysis for such systems. For example, expressions for the average bit error rate (ABER) and outage probability are absolutely necessary for designing effective signaling and error control coding schemes. A further consequence is the large demand for radio channel spectrum and high information data rates which can only be ensured using modulation techniques with larger constellation sizes yielding higher bandwidth efficiency. In light of these considerations, this chapter provides an analytical approach to study the performance of such communication systems in an indoor wireless environment that can be characterized by the JFTS propagation model.

The rest of this section is organized as follows. Subsection 4.1.1 summarizes the techniques used for performance evaluation of different fixed modulation techniques. Subsection 4.1.2 provides a brief summary of performance evaluation techniques of different iterative and non-iterative coding techniques respectively while the discussion on channel capacity analysis is provided in Subsection 4.1.3.

4.1.1 **Fixed Modulation**

M-ary Quadrature Amplitude Modulation (M-QAM) and M-ary Phase Shift Keying (M-PSK) are the preferred modulation techniques for digital communication systems due to their high bandwidth efficiency and hence they find applications in many WLAN and Wifi standards. Different variants of the QAM and PSK techniques like Square QAM (SQAM), Binary Phase Shift Keying (BPSK), Quadrature Phase Shift Keying (QPSK), Orthogonal Binary Frequency Shift Keying and multi-level Amplitude Shift Keying modulation are all grouped as special cases under Rectangular QAM (RQAM) [38]. On the other hand, Cross QAM (XQAM) is an optimal QAM constellation for odd number of bits per symbol as it has a lower average symbol energy than RQAM [49]. XQAM finds application with constellations from 5 bits to 15 bits and has been used in ADSL and VDSL standards. Moreover M-QAM has been been found to be useful in blind equalization [50] and adaptive modulation [51], [52] and therefore, is adapted in DVB-C standard.

Several techniques for theoretical performance evaluation of M-QAM and M-PSK over different fading, shadowing and composite fading/shadowing channel models have been proposed in literature. For example, generalized Average Symbol Error Rate (ASER) expression for RQAM over fading channels is presented in [53], while that for XQAM is given in [54]. A general closed-form Average Bit Error Rate (ABER) expression for coherent M-PSK is derived in [55], where Gray coded bit mapping is employed. In all these cases [53] - [55], PDF of the received instantaneous CSNR is used to deduce the nth order MGF of the instantaneous CSNR, which in turn is utilized to obtain the expressions for ASER and ABER. However, in case of some channel models [56], [57], MGF of the instantaneous CSNR involves higher transcendental functions which are laborious to calculate when used for performance evaluation of higher-order modulation techniques. In those cases, CDF of the received instantaneous CSNR is used to derive expressions for ABER utilizing the method proposed in [57].

The first objective of this chapter is to derive analytical expressions for the error probability performance of a wireless communication system using fixed modulation techniques over a JFTS joint faded/shadowed channel. This is accomplished in two steps. Firstly, expressions for error probability of uncoded coherent M-PSK and M-QAM are deduced using PDF and nth order MGF of the received instantaneous composite CSNR. Secondly, expressions for bit error rate of uncoded M-PSK and M-QAM techniques are derived using CDF of the received instantaneous CSNR.

4.1.2 Error Correction Coding

Forward Error Correction (FEC) coding schemes in combination with fixed modulation techniques like M-PSK [58], [59] are found to be effective in minimizing the impairment caused by burst errors in the delivery of high speed data traffic over fading, shadowing or composite fading/shadowing communication channels. The history of FEC coding dates back to Shannon's work [60], in which he showed that it is possible to design a communication system with any desired small probability of error, whenever the rate of transmission is smaller than the capacity of the channel. This motivated the search for codes that would produce arbitrarily small probability of error. Specifically, Hamming [61] and Golay [62] were the first to develop practical error control codes. Convolutional codes [63] were later introduced by Elias, while Viterbi [64] invented a maximum likelihood sequence estimation algorithm for efficiently decoding convolutional codes. Bahl proposed the more complex Maximum A-Posteriori (MAP) algorithm in [65], which is capable of achieving the minimum achievable BER.

During the last decade major research efforts have been devoted to the construction and performance analysis of capacity-approaching low-complexity codes, in particular Turbo and Low Density Parity Check (LDPC) codes [66] - [68]. In their most basic forms, Turbo and LDPC codes employ convolutional coding as the component codes and MAP algorithm as the decoding technique. The results in [66] - [68] proved that a performance close to the Shannon limit can be achieved in practice with the aid of binary codes. Particularly, Turbo codes offer impressive performances over fading channel conditions and hence, has recently been standardized in the ratified third-generation (3G) mobile radio systems [69].

Performance evaluation in terms of deriving closed-form ABER expressions for Turbo and LDPC coding is exhaustive and laborious. Hence, for Turbo codes, bulk of the existing literature [70], [71] resort to bounding techniques based on computationally complex maximum likelihood (ML) decoding, most of which uses the tight upper bounds provided by [71] for the AWGN and Rician fading channel cases. While in case of LDPC codes, the analysis has been restricted to simulations and density evolution (DE) due to the complex iterative decoding process [72] - [75].

As an alternative, the works introduced in [76] and [77] used a probability distribution to derive the pairwise error probability of Turbo codes and Gaussian Approximation (GA) - based BER of LDPC codes respectively, over Rayleigh fading channels. In particular, [76] showed that this approach led to computationally efficient results. A similar approach is also used in [78] and [79] to derive exact and efficient expressions for pairwise error probability (PEP) of Turbo codes and approximate BER of LDPC codes respectively, over fully interleaved Nakagami-m fading channels. The derived expressions for error probability in [76] - [79] are also approximated to yield tight upper bounds which stay close to the exact expressions.

The second objective of this chapter is to evaluate the error probability performance of a wireless communication system using FEC techniques over a JFTS joint faded/shadowed channel in presence or absence of channel interleavers and de-interleavers. Error rate performance of iterative coding techniques like Turbo and LDPC-coded BPSK are analyzed using PDF of the sum of the squared independent and identically distributed (iid) JFTS random variables. Error probability performance of non-iterative coding schemes is evaluated using simulation results only.

4.1.3 **Channel Capacity**

Another important performance measure for wireless communication systems is the determination of the channel capacity, which quantifies the maximum achievable transmission rate of a system communicating over a bandlimited channel, while maintaining an arbitrarily low probability of error. Given the fact that the available bandwidth of all transmission media is limited, it is desirable to transmit information as bandwidth efficient as possible. In recent years, the available wireless communications frequency bands have been auctioned by the American, British, German and other governments to service provider companies at a high price and therefore it is of great commercial interest to exploit the available bandwidth as best as possible.

Quantifying these information theoretic limits for the JFTS faded/shadowed channel is the final objective of this chapter. Calculating these limits, the rest of this thesis will attempt at quantifying the ability of various fixed and adaptive modulation and coding techniques to perform as close to the limits as possible. Bandwidth efficiency over a JFTS faded/shadowed channel will also be calculated by normalizing the channel capacity with respect to the bandwidth occupied. A lower bound to the channel capacity referred to as the channel's cut-off rate will also be derived for a JFTS channel in this chapter.

The rest of this chapter is organized as follows. Section 4.2 describes the statistics of the instantaneous received CSNR over the JFTS channel model. The error performance analysis and the channel capacity analysis are presented in Section 4.3 and Section 4.4 respectively. Numerical results and discussions are given in Section 4.5 and the concluding remarks are provided in Section 4.6.

4.2 Statistics of Instantaneous CSNR

Let $s(t)$ represents a signal with symbol energy E_s that is transmitted over a composite slow shadowed and flat faded wireless communication channel with JFTS statistics. The received signal $\bar{y}(t)$ over the symbol duration τ_s can be expressed as,

$$\bar{y}(t) \ = \ z(t)\ e^{\jmath\phi(t)}\ s(t) \ + \ n(t) \tag{4.1}$$

where $n(t)$ is the complex AWGN with one-sided power spectral density of N_0, $\phi(t)$ is the instantaneous phase and $z(t)$ denotes the composite fading/shadowing envelope which is JFTS distributed.

The first order statistics of the channel fading stochastic process, $z(t)$, can be represented by the random variable Z, which has a PDF given by (refer to (2.20) in Chapter 2),

$$f_Z(z) \ = \ \sum_{j=1}^{4} \sum_{h=1}^{20} \frac{z\ b_j\ \mathcal{R}}{P_1 P_2}\ e^{-K-S_h-\frac{z^2}{2P_2 r_h^2}}\ D\Big(z\sqrt{\frac{2K}{P_1P_2}}; S_h, \Delta\mathsf{M}_j\Big) \tag{4.2}$$

and a CDF given by,

$$\begin{aligned} F_Z(z) \ = \ \sum_{j=1}^{4} \sum_{h=1}^{20} \frac{b_j\ \mathcal{R}\ r_h}{2P_1\sqrt{P_2}}\ e^{-K-S_h}\ \Big[& e^{S_h\Delta\mathsf{M}_j}\ Q_1\Big(\sqrt{KS_h(1-\Delta\mathsf{M}_j r_h)/P_1}, z\Big) \\ & + \ e^{-S_h\Delta\mathsf{M}_j}\ Q_1\Big(\sqrt{KS_h(1+\Delta\mathsf{M}_j r_h)/P_1}, z\Big)\Big] \end{aligned} \tag{4.3}$$

where K is the fading parameter given by K = Specular Power / Diffused Power. The value of the shadowing parameter, S_h, is set based on the range of shadowing values experienced by a user while traveling through different shadowing clusters. The Δ - parameter is the shape parameter of the shadowing distribution and represents the transition from one scattering cluster to the next one. The parameters P_1 and P_2 are the mean-squared voltages of the diffused components and the shadowed components respectively. In the remainder of this section, Subsection 4.2.1 presents the PDF of the received instantaneous composite CSNR. Subsection 4.2.2 presents the CDF of the instantaneous CSNR and expression for the nth order MGF of the instantaneous CSNR is derived in Subsection 4.2.3.

4.2.1 PDF of Instantaneous CSNR

Let the mean-squared value of the joint faded and two-path shadowed envelope, Z, be given by, $\Omega = \mathrm{E}\{Z^2\}$. The value for Ω can be obtained from Chapter 3 as, $\Omega = 8P_1P_2(1+K)\sum_{j=1}^{4} a_j(1+S_h)$. However, since $a_1 = \frac{751}{17280}$, $a_2 = \frac{3577}{17280}$, $a_3 = \frac{49}{640}$ and $a_4 = \frac{2989}{17280}$, we can arrive at the final value of the summation $\sum_{j=1}^{4} a_j = a_1 + a_2 + a_3 + a_4 = 0.5$. In turn, Ω can be expressed as, $\Omega = 4P_1P_2(1+K)(1+S_h) = 4P_1P_2\tilde{K}\tilde{S}_h$, where $\tilde{K} = 1+K$ and $\tilde{S}_h = 1+S_h$.

If the received instantaneous signal power is modulated by Z^2, the instantaneous CSNR per symbol can be defined as, $\gamma = Z^2E_s/N_0$. The average CSNR per symbol can be defined as $\overline{\gamma} = \Omega E_s/N_0$. Hence, the PDF of the instantaneous CSNR per symbol can be written as [38],

$$f_\gamma(\gamma) = f_Z\left(\sqrt{\frac{\Omega\gamma}{\overline{\gamma}}}\right) \Bigg/ \left(2\sqrt{\frac{\overline{\gamma}\gamma}{\Omega}}\right) \tag{4.4}$$

Using the change of variables from (4.4) in (4.2) and putting $\Omega = 4P_1P_2\tilde{K}\tilde{S}_h$, the expression for the PDF of the instantaneous received CSNR per symbol can be expressed as,

$$f_\gamma(\gamma) \;=\; \sum_{j=1}^{4} \sum_{h=1}^{20} \frac{b_j \; \mathcal{R} \; \tilde{K}\tilde{S}_h}{\overline{\gamma}} \; e^{-K-S_h-\frac{2P_1\gamma\tilde{K}\tilde{S}_h}{r_h^2\overline{\gamma}}} \; D\Bigg(4\sqrt{KS_h\tilde{K}\tilde{S}_h\gamma/\overline{\gamma}}; S_h, \Delta\mathsf{M}_j\Bigg) \tag{4.5}$$

In the next section, (4.5) will be used for deriving the ABER expressions for uncoded coherent M-PSK and M-QAM over the JFTS faded/shadowed wireless communication channel using the MGF-based approach.

The JFTS distribution is a general composite fading/shadowing distribution that can reduce to other distributions such as Rayleigh ($K = 0$, $S_h = \infty$), Rician (K as a fading parameter by setting $S_h = \infty$) and Nakagami-m ($K = \frac{\sqrt{m^2-m}}{m-\sqrt{m^2-m}}$ and setting $S_h = \infty$) distributions as special cases. This generalization property of the JFTS distribution can be used many researchers to model a wide variety of wireless propagation conditions. However, the complicated PDF expression does actually limit the consequent evaluation of performance measures over a JFTS faded/shadowed channel model.

4.2.2 CDF of Instantaneous CSNR

If the average CSNR per symbol is given by, $\overline{\gamma} \;=\; \mathrm{E}\{\gamma\} \;=\; \mathrm{E}\{Z^2\}E_s/N_0$, the instantaneous CSNR can be expressed as, $\gamma \;=\; z^2\frac{\overline{\gamma}}{\mathrm{E}\{Z^2\}}$. Using this transformation in terms of the instantaneous and average CSNR per symbol, the CDF of the received instantaneous CSNR can be simply expressed as, $F_\gamma(\gamma) \;=\; F_Z\Bigg(\sqrt{\frac{\gamma\mathrm{E}\{Z^2\}}{\overline{\gamma}}}\Bigg)$. Using (4.3) and $\mathrm{E}\{Z^2\} \;=\; 4P_1P_2\tilde{K}\tilde{S}_h$, the expression for CDF of γ

can be obtained as,

$$F_\gamma(\gamma) \;=\; \sum_{j=1}^{4}\;\sum_{h=1}^{20}\;\frac{b_j\;\mathcal{R}\;r_h}{2P_1\sqrt{P_2}}\;e^{-K-S_h}\;\Big[e^{S_h\Delta\mathsf{M}_j}\;Q_1\Big(\sqrt{KS_h(1-\Delta\mathsf{M}_j r_h)/P_1},\sqrt{4P_1P_2\tilde{K}\tilde{S}_h\gamma/\overline{\gamma}}\Big)$$
$$+\;e^{-S_h\Delta\mathsf{M}_j}\;Q_1\Big(\sqrt{KS_h(1+\Delta\mathsf{M}_j r_h)/P_1},\sqrt{4P_1P_2\tilde{K}\tilde{S}_h\gamma/\overline{\gamma}}\Big)\Big] \tag{4.6}$$

Expansion the Q-function in terms of the infinite series summation, we can arrive at the more generalized form of the CDF of the instantaneous received CSNR, as below,

$$F_\gamma(\gamma) \;=\; \sum_{j=1}^{4}\;\sum_{h=1}^{20}\frac{b_j\mathcal{R}}{2}\;e^{-K-S_h-\frac{2P_1\tilde{K}\tilde{S_h}\gamma}{r_h^2\overline{\gamma}}}\sum_{\mathsf{k}=0}^{\infty}\frac{K^{\mathsf{k}}S_h^{\mathsf{k}}}{(\mathsf{k}!)^2P_1^{\mathsf{k}}P_2^{\mathsf{k}}}\;\sum_{v=0}^{\mathsf{k}}\frac{1}{v!}\left(\frac{2P_1\tilde{K}\tilde{S}_h\gamma}{r_h^2\overline{\gamma}}\right)^v$$
$$\left[(1-\Delta\mathsf{M}_j)^{\mathsf{k}}\;e^{S_h\Delta\mathsf{M}_j}\;+\;(1+\Delta\mathsf{M}_j)^{\mathsf{k}}\;e^{-S_h\Delta\mathsf{M}_j}\right] \tag{4.7}$$

The expression in (4.7) can be expressed in a more shorter form by simple mathematical manipulation as,

$$F_\gamma(\gamma) \;=\; \sum_{j=1}^{4}\;\sum_{h=1}^{20}\frac{b_j\mathcal{R}}{2}\;e^{-K-S_h-\frac{2P_1\tilde{K}\tilde{S_h}\gamma}{r_h^2\overline{\gamma}}}\sum_{\mathsf{k}=0}^{\infty}\;\sum_{v=0}^{\mathsf{k}}\frac{2^{\mathsf{k}}}{v!}\left(\frac{2P_1\tilde{K}\tilde{S}_h\gamma}{r_h^2\overline{\gamma}}\right)^v$$
$$\left[e^{S_h\Delta\mathsf{M}_j}\;I_0\left(\sqrt{KS_h(1-\Delta\mathsf{M}_j)/P_1P_2}\right)\;+\;e^{-S_h\Delta\mathsf{M}_j}\;I_0\left(\sqrt{KS_h(1+\Delta\mathsf{M}_j)/P_1P_2}\right)\right] \tag{4.8}$$

We will be using (4.8) in Section 4.3 for deriving expressions of error probability using the CDF based approach for the easiness in solving integrals using the infinite series summation formats instead of special functions.

Application to Outage Probability :

The CDF of γ is of particular importance as it can be directly applied to analyze the outage probability performance of communication systems. The outage probability is a performance metric that is defined as the probability that the error rate exceeds a pre-defined value or equivalently, the received CSNR drops below a pre-defined threshold, γ_0 [38]. Hence the outage probability, P_{out}, can be given as $P_{\text{out}} = \int_0^{\gamma_0} f_\gamma(\gamma)\mathrm{d}\gamma$, and for the JFTS distribution can be evaluated as,

$$\begin{aligned} P_{\text{out}} &= \int_0^{\gamma_0} f_\gamma(\gamma)\mathrm{d}\gamma \;=\; F_Z\left(\sqrt{\frac{\gamma_0 \mathrm{E}\{Z^2\}}{\overline{\gamma}}}\right) \\ &= \sum_{j=1}^{4} \sum_{h=1}^{20} \frac{b_j\ \mathcal{R}\ r_h}{2P_1\sqrt{P_2}}\ e^{-K-S_h}\ \Big[e^{S_h \Delta \mathsf{M}_j}\ Q_1\Big(\sqrt{KS_h(1-\Delta\mathsf{M}_j r_h)/P_1}, \sqrt{4P_1P_2\tilde{K}\tilde{S}_h\gamma_0/\overline{\gamma}}\Big) \\ &\qquad\qquad + \ e^{-S_h \Delta \mathsf{M}_j}\ Q_1\Big(\sqrt{KS_h(1+\Delta\mathsf{M}_j r_h)/P_1}, \sqrt{4P_1P_2\tilde{K}\tilde{S}_h\gamma_0/\overline{\gamma}}\Big)\Big] \end{aligned} \tag{4.9}$$

where Q_1 is the Marcum Q-function, $\tilde{K} = 1 + K$ and $\tilde{S}_h = 1 + S_h$. Using (4.9), some numerical results for the outage probability over a JFTS faded/shadowed channel are presented in Section 4.5.

4.2.3 MGF of Instantaneous CSNR

One of the most important characteristics of any distribution function is the MGF especially when the considered distribution represents the small scale fading of the multipath channel model. The MGF helps in the performance evaluation of wireless communication systems. For instance, the BER calculation is one of the most important applications that in some cases can be easily evaluated if the exact knowledge of the MGF function is available. For the JFTS distribution, the

MGF can be evaluated as follows,

$$
\begin{aligned}
\mathcal{M}_{\gamma}(s) &= \mathrm{E}\{e^{-s\gamma}\} \\
&= \int_{0}^{\infty} \sum_{j=1}^{4} \sum_{h=1}^{20} \frac{b_j \; \mathcal{R} \; \tilde{K}\tilde{S}_h}{\overline{\gamma}} \; e^{-s\gamma - K - S_h - \frac{2P_1\gamma\tilde{K}\tilde{S}_h}{r_h^2\overline{\gamma}}} \; D\left(4\sqrt{KS_h\tilde{K}\tilde{S}_h\gamma/\overline{\gamma}}; S_h, \Delta\mathsf{M}_j\right)\mathrm{d}\gamma \\
&= \sum_{j=1}^{4}\sum_{h=1}^{20} \frac{b_j \mathcal{R}\tilde{K}\tilde{S}_h r_h^2 \; e^{-K-S_h}}{2P_1\tilde{K}\tilde{S}_h + s r_h^2 \overline{\gamma}} \left[e^{S_h\Delta\mathsf{M}_j + \frac{16KS_h\tilde{K}\tilde{S}_h(1-\Delta\mathsf{M}_j)r_h^2}{2P_1\tilde{K}\tilde{S}_h + sr_h^2\overline{\gamma}}} + e^{-S_h\Delta\mathsf{M}_j + \frac{16KS_h\tilde{K}\tilde{S}_h(1+\Delta\mathsf{M}_j)r_h^2}{2P_1\tilde{K}\tilde{S}_h + sr_h^2\overline{\gamma}}} \right]
\end{aligned}
\tag{4.10}
$$

The evaluation of (4.10) involves calculation using the Whittaker-M function, the details on which is presented in Appendix B. This MGF result is a general result that can reduce easily into other MGF expressions for different channel models such as, Rayleigh, Rician and Nakagami-m as special cases.

4.3 Error Performance Analysis

The primary contribution of this section is to derive expressions for evaluating error probability performances of different fixed modulation techniques with or without near-capacity achieving iterative channel coding techniques over a JFTS faded/shadowed communication channel. The organization of this section is as follows. Closed-form expressions for error rates of a variety of fixed modulation techniques are derived using the MGF-based approach in Subsection 4.3.1. The same analysis is done using the CDF-based approach in Subsection 4.3.2. Error probability expressions for coded modulation techniques are deduced in Subsection 4.3.3, where PEP-based approach is used for performance evaluation of Turbo codes and GA-based approach is used for regular and irregular LDPC codes.

4.3.1 MGF-based Approach

In order to obtain the error probability performance of a large variety of modulation techniques, the MGF-based approach will be used in this subsection. The receivers are considered to be operating over independent and identically distributed (iid) JFTS composite fading/shadowing conditions in absence of any channel interleavers and de-interleavers.

Average Symbol Error Rate (ASER) :

An expression for Average Symbol Error Rate (ASER) can be obtained by averaging the conditional symbol error rate (SER) for AWGN channels over the PDF of the received instantaneous CSNR. Mathematically, ASER, $P_s(e)$ for any modulation technique can be computed as,

$$P_s(e) \;=\; \int_0^\infty P_s(e|\gamma) f_\gamma(\gamma) \mathrm{d}\gamma \tag{4.11}$$

where $P_s(e|\gamma)$ is the conditional SER of the modulation scheme in AWGN channels and $f_\gamma(\gamma)$ is the PDF of the instantaneous received CSNR given by (4.5). The conditional SER performance of M-ary RQAM in AWGN channels is given as [53],

$$P_s(e|\gamma) \;=\; 2\mathsf{p}\; Q(\mathsf{a}\sqrt{\gamma}) \;+\; 2\mathsf{q}\; Q(\mathsf{b}\sqrt{\gamma}) \;-\; 4\mathsf{pq}\; Q(\mathsf{a}\sqrt{\gamma})Q(\mathsf{b}\sqrt{\gamma}) \tag{4.12}$$

where $M = M_{\mathrm{In}} \times M_{\mathrm{Quad}}$, $\mathsf{p} = 1 - 1/M_{\mathrm{In}}$, $\mathsf{q} = 1 - 1/M_{\mathrm{Quad}}$, $\mathsf{a} = \sqrt{6/((M_{\mathrm{In}}^2 - 1) + (M_{\mathrm{Quad}}^2 - 1)\beta^2)}$, $\mathsf{b} = \beta\mathsf{a}$ and $\beta = \mathsf{d}_{\mathrm{In}}/\mathsf{d}_{\mathrm{Quad}}$ is the quadrature-to-in-phase decision distance ration with d_{In} and $\mathsf{d}_{\mathrm{Quad}}$ being the in-phase and quadrature-phase decision distances respectively. The function $Q(\bar{\mathsf{x}})$ is the Gaussian Q-function given by, $Q(\bar{\mathsf{x}}) \;=\; \frac{1}{\sqrt{2\pi}} \int_{\bar{\mathsf{x}}}^\infty \; e^{-\frac{\mathsf{t}^2}{2}} \mathrm{d}\mathsf{t}$. For convenience of analysis, (4.12) can be expressed using an alternate representation of 1-D (1-Dimensional) and 2-D (2-Dimensional) Gaussian Q-functions, $Q_{\tilde{d}}(\bar{\mathsf{x}}, \phi)$ is defined as [38],

$$Q_{\tilde{d}}(\bar{\mathsf{x}}, \phi) \;=\; \frac{1}{\pi} \int_0^\phi \; e^{-\frac{\bar{\mathsf{x}}^2}{2\sin^2\theta}} \mathrm{d}\theta \qquad \bar{\mathsf{x}} > 0 \tag{4.13}$$

From (4.13), it can be shown that $Q(\bar{\mathsf{x}}) = Q_{\tilde{d}}(\bar{\mathsf{x}}, \pi/2)$ [38] and $Q(\bar{\mathsf{x}})Q(\bar{\mathsf{y}}) = \frac{1}{2}[Q_{\tilde{d}}(\bar{\mathsf{x}}, \pi/2 - \arctan(\bar{\mathsf{y}}/\bar{\mathsf{x}})) + Q_{\tilde{d}}(\bar{\mathsf{y}}, \arctan(\bar{\mathsf{y}}/\bar{\mathsf{x}}))]$ for $\bar{\mathsf{x}} > 0$, $\bar{\mathsf{y}} > 0$. Thus using (4.13), (4.12) can be rewritten as,

$$\begin{aligned} P_s(e|\gamma) &= 2\mathsf{p}\; Q_{\tilde{d}}(\mathsf{a}\sqrt{\gamma}, \pi/2) \;+\; 2\mathsf{q}\; Q_{\tilde{d}}(\mathsf{b}\sqrt{\gamma}, \pi/2) \\ &\quad -\; 2\mathsf{pq}\; [Q_{\tilde{d}}(\mathsf{a}\sqrt{\gamma}, \pi/2 - \arctan(\mathsf{b}/\mathsf{a})) \;+\; Q_{\tilde{d}}(\mathsf{b}\sqrt{\gamma}, \arctan(\mathsf{b}/\mathsf{a}))] \end{aligned} \tag{4.14}$$

Substituting (4.14) into (4.11) and by algebraic manipulations, ASER for RQAM scheme denoted by $P_s^{\mathrm{RQAM}}(e)$ can be expressed as,

$$P_s^{\mathrm{RQAM}}(e) \;=\; 2\mathsf{p}\; \mathcal{I}(\mathsf{a}, \pi/2) \;+\; 2\mathsf{q}\; \mathcal{I}(\mathsf{b}, \pi/2) \;-\; 2\mathsf{pq}\; [\mathcal{I}(\mathsf{a}, \pi/2 - \arctan(\mathsf{b}/\mathsf{a})) \;+\; \mathcal{I}(\mathsf{b}, \arctan(\mathsf{b}/\mathsf{a}))] \tag{4.15}$$

where the function $\mathcal{I}(\cdot, \cdot)$ is defined as,

$$\begin{aligned} \mathcal{I}(\mathsf{a}, \phi) &= \int_0^\infty Q_{\tilde{d}}(\mathsf{a}\sqrt{\gamma}, \phi) f_\gamma(\gamma) \mathrm{d}\gamma \\ &= \frac{1}{\pi} \int_0^\phi \int_0^\infty e^{-\frac{\mathsf{a}^2 \gamma}{2\sin^2\theta}} f_\gamma(\gamma) \mathrm{d}\gamma \mathrm{d}\theta \\ &= \frac{1}{\pi} \int_0^\phi \mathcal{M}_\gamma\left(\frac{\mathsf{a}^2}{2\sin^2\theta}\right) \mathrm{d}\theta \end{aligned} \tag{4.16}$$

where $\mathcal{M}_\gamma(\cdot)$ is the MGF of γ. Thus to get an expression for (4.16), the MGF of γ is needed whose PDF is shown in (4.5). An expression for this MGF is given by (4.10). Substituting (4.16) in (4.10), closed-form expressions for $\mathcal{I}(\bar{\mathsf{x}}, \pi/2)$, $\mathcal{I}(\bar{\mathsf{x}}, \pi/2 - \arctan(\bar{\mathsf{y}}/\bar{\mathsf{x}}))$ and $\mathcal{I}(\bar{\mathsf{y}}, \arctan(\bar{\mathsf{y}}/\bar{\mathsf{x}}))$, which will be used to evaluate (4.15) are derived in Appendix C. Thus substituting the expressions from Appendix C and simplifying the resultant expression, a closed-form ASER expression for $P_s^{\mathrm{RQAM}}(e)$

can be given by,

$$
\begin{aligned}
P_s^{\mathrm{RQAM}}(e) \;=\; & \sum_{j=1}^{4}\sum_{h=1}^{20} \frac{\mathsf{pa} b_j \mathcal{R}\tilde{K}\tilde{S}_h r_h^3 \sqrt{\overline{\gamma}}\ e^{-K-S_h}}{(4P_1\tilde{K}\tilde{S}_h + \mathsf{a}^2 r_h^2 \overline{\gamma})^{3/2}} \Bigg[e^{S_h \Delta \mathsf{M}_j - 8KS_h(1-\Delta\mathsf{M}_j) r_h^2/P_1}\ \Phi_1\Bigg(\frac{3}{2}, 1; 2; \frac{4P_1\tilde{K}\tilde{S}_h}{4P_1\tilde{K}\tilde{S}_h + \mathsf{a}^2 r_h^2\overline{\gamma}}, \\
& \frac{32KS_h\tilde{K}\tilde{S}_h(1-\Delta\mathsf{M}_j) r_h^2}{4P_1\tilde{K}\tilde{S}_h + \mathsf{a}^2 r_h^2\overline{\gamma}}\Bigg) \;+\; e^{-S_h \Delta \mathsf{M}_j - 8KS_h(1+\Delta\mathsf{M}_j) r_h^2/P_1}\ \Phi_1\Bigg(\frac{3}{2}, 1; 2; \frac{4P_1\tilde{K}\tilde{S}_h}{4P_1\tilde{K}\tilde{S}_h + \mathsf{a}^2 r_h^2\overline{\gamma}}, \\
& \frac{32KS_h\tilde{K}\tilde{S}_h(1+\Delta\mathsf{M}_j) r_h^2}{4P_1\tilde{K}\tilde{S}_h + \mathsf{a}^2 r_h^2\overline{\gamma}}\Bigg)\Bigg] + \sum_{j=1}^{4}\sum_{h=1}^{20} \frac{\mathsf{qb} b_j \mathcal{R}\tilde{K}\tilde{S}_h r_h^3 \sqrt{\overline{\gamma}}\ e^{-K-S_h}}{(4P_1\tilde{K}\tilde{S}_h + \mathsf{b}^2 r_h^2 \overline{\gamma})^{3/2}} \Bigg[e^{S_h \Delta \mathsf{M}_j - 8KS_h(1-\Delta\mathsf{M}_j) r_h^2/P_1} \\
& \Phi_1\Bigg(\frac{3}{2}, 1; 2; \frac{4P_1\tilde{K}\tilde{S}_h}{4P_1\tilde{K}\tilde{S}_h + \mathsf{b}^2 r_h^2\overline{\gamma}}, \frac{32KS_h\tilde{K}\tilde{S}_h(1-\Delta\mathsf{M}_j) r_h^2}{4P_1\tilde{K}\tilde{S}_h + \mathsf{b}^2 r_h^2\overline{\gamma}}\Bigg) \;+\; e^{-S_h \Delta \mathsf{M}_j - 8KS_h(1+\Delta\mathsf{M}_j) r_h^2/P_1} \\
& \Phi_1\Bigg(\frac{3}{2}, 1; 2; \frac{4P_1\tilde{K}\tilde{S}_h}{4P_1\tilde{K}\tilde{S}_h + \mathsf{b}^2 r_h^2\overline{\gamma}}, \frac{32KS_h\tilde{K}\tilde{S}_h(1+\Delta\mathsf{M}_j) r_h^2}{4P_1\tilde{K}\tilde{S}_h + \mathsf{b}^2 r_h^2\overline{\gamma}}\Bigg)\Bigg] \\
& - \;\sum_{j=1}^{4}\sum_{h=1}^{20} \frac{4\mathsf{pq} b_j \mathcal{R}\tilde{K}\tilde{S}_h r_h^3 \sqrt{\overline{\gamma}}\ e^{-K-S_h}}{3\pi(4P_1\tilde{K}\tilde{S}_h + (\mathsf{a}^2+\mathsf{b}^2) r_h^2 \overline{\gamma})^{3/2}} \Bigg[\mathsf{a}\ e^{S_h \Delta \mathsf{M}_j - 8KS_h(1-\Delta\mathsf{M}_j) r_h^2/P_1}\ \Phi_1^{(3)}\Bigg(\frac{3}{2}, 1, \frac{1}{2}; \frac{5}{2}; \\
& \frac{4P_1\tilde{K}\tilde{S}_h}{4P_1\tilde{K}\tilde{S}_h + (\mathsf{a}^2+\mathsf{b}^2) r_h^2\overline{\gamma}}, \frac{4P_1\tilde{K}\tilde{S}_h + \mathsf{a}^2 r_h^2\overline{\gamma}}{4P_1\tilde{K}\tilde{S}_h + (\mathsf{a}^2+\mathsf{b}^2) r_h^2\overline{\gamma}}, \frac{32KS_h\tilde{K}\tilde{S}_h(1-\Delta\mathsf{M}_j) r_h^2}{4P_1\tilde{K}\tilde{S}_h + (\mathsf{a}^2+\mathsf{b}^2) r_h^2\overline{\gamma}}\Bigg) \\
& + \;\mathsf{a}\ e^{-S_h \Delta \mathsf{M}_j - 8KS_h(1+\Delta\mathsf{M}_j) r_h^2/P_1}\ \Phi_1^{(3)}\Bigg(\frac{3}{2}, 1, \frac{1}{2}; \frac{5}{2}; \frac{4P_1\tilde{K}\tilde{S}_h}{4P_1\tilde{K}\tilde{S}_h + (\mathsf{a}^2+\mathsf{b}^2) r_h^2\overline{\gamma}}, \\
& \frac{4P_1\tilde{K}\tilde{S}_h + \mathsf{a}^2 r_h^2\overline{\gamma}}{4P_1\tilde{K}\tilde{S}_h + (\mathsf{a}^2+\mathsf{b}^2) r_h^2\overline{\gamma}}, \frac{32KS_h\tilde{K}\tilde{S}_h(1+\Delta\mathsf{M}_j) r_h^2}{4P_1\tilde{K}\tilde{S}_h + (\mathsf{a}^2+\mathsf{b}^2) r_h^2\overline{\gamma}}\Bigg) + \mathsf{b}\ e^{S_h \Delta \mathsf{M}_j - 8KS_h(1-\Delta\mathsf{M}_j) r_h^2/P_1} \\
& \Phi_1^{(3)}\Bigg(\frac{3}{2}, 1, \frac{1}{2}; \frac{5}{2}; \frac{4P_1\tilde{K}\tilde{S}_h}{4P_1\tilde{K}\tilde{S}_h + (\mathsf{a}^2+\mathsf{b}^2) r_h^2\overline{\gamma}}, \frac{4P_1\tilde{K}\tilde{S}_h + \mathsf{b}^2 r_h^2\overline{\gamma}}{4P_1\tilde{K}\tilde{S}_h + (\mathsf{a}^2+\mathsf{b}^2) r_h^2\overline{\gamma}}, \\
& \frac{32KS_h\tilde{K}\tilde{S}_h(1-\Delta\mathsf{M}_j) r_h^2}{4P_1\tilde{K}\tilde{S}_h + (\mathsf{a}^2+\mathsf{b}^2) r_h^2\overline{\gamma}}\Bigg) \;+\; \mathsf{b}\ e^{-S_h \Delta \mathsf{M}_j - 8KS_h(1+\Delta\mathsf{M}_j) r_h^2/P_1}\ \Phi_1^{(3)}\Bigg(\frac{3}{2}, 1, \frac{1}{2}; \frac{5}{2}; \\
& \frac{4P_1\tilde{K}\tilde{S}_h}{4P_1\tilde{K}\tilde{S}_h + (\mathsf{a}^2+\mathsf{b}^2) r_h^2\overline{\gamma}}, \frac{4P_1\tilde{K}\tilde{S}_h + \mathsf{b}^2 r_h^2\overline{\gamma}}{4P_1\tilde{K}\tilde{S}_h + (\mathsf{a}^2+\mathsf{b}^2) r_h^2\overline{\gamma}}, \frac{32KS_h\tilde{K}\tilde{S}_h(1+\Delta\mathsf{M}_j) r_h^2}{4P_1\tilde{K}\tilde{S}_h + (\mathsf{a}^2+\mathsf{b}^2) r_h^2\overline{\gamma}}\Bigg)\Bigg]
\end{aligned}
\tag{4.17}
$$

where $\Phi_1(\cdot)$ is a confluent hypergeometric function of two variables. It can be expressed either in the series form or in integral form [80] and [81],

$$\Phi_1(\bar{\mathsf{a}},\bar{\mathsf{b}};\bar{\mathsf{c}};\bar{\mathsf{x}}_1,\bar{\mathsf{x}}_2)=\sum_{\bar{\mathsf{k}},\bar{\mathsf{l}}=0}^{\infty}\frac{(\bar{\mathsf{a}})_{\bar{\mathsf{k}}+\bar{\mathsf{l}}}\ (\bar{\mathsf{b}})_{\bar{\mathsf{k}}}\ \bar{\mathsf{x}}_1^{\bar{\mathsf{k}}}\ \bar{\mathsf{x}}_2^{\bar{\mathsf{l}}}}{(\bar{\mathsf{c}})_{\bar{\mathsf{k}}+\bar{\mathsf{l}}}\ \Gamma(\bar{\mathsf{k}}+1)\ \Gamma(\bar{\mathsf{l}}+1)}=\frac{\Gamma(\bar{\mathsf{c}})}{\Gamma(\bar{\mathsf{a}})\ \Gamma(\bar{\mathsf{c}}-\bar{\mathsf{a}})}\int_0^1\frac{\bar{\mathsf{u}}^{\bar{\mathsf{a}}-1}\ (1-\bar{\mathsf{u}})^{\bar{\mathsf{c}}-\bar{\mathsf{a}}-1}\ e^{\bar{\mathsf{u}}\bar{\mathsf{x}}_2}}{(1-\bar{\mathsf{u}}\bar{\mathsf{x}}_1)^{\bar{\mathsf{b}}}}d\bar{\mathsf{u}} \tag{4.18}$$

where $(\bar{\mathsf{a}})_{\bar{\mathsf{n}}}=\Gamma(\bar{\mathsf{a}}+\bar{\mathsf{n}})/\Gamma(\bar{\mathsf{a}})$ is the Pochammer symbol for $|\bar{\mathsf{x}}_1|<1,\bar{\mathsf{n}}\geq 0$. It can be easily and accurately evaluated by using its finite integral representation and its infinite series representation. For the special case of M-ary SQAM, that is when $M_{\text{In}}=M_{\text{Quad}}=\sqrt{M}$ and $\beta=1$, it can be shown that (4.17) reduces to (4.19), where $\mathsf{p}=1-1/\sqrt{M}$ and $\mathsf{a}=\sqrt{3/(M-1)}$.

$$\begin{aligned}
P_s^{\text{SQAM}}(e) \;=\; & \sum_{j=1}^{4}\sum_{h=1}^{20}\frac{2\mathsf{pa}b_j\mathcal{R}\tilde{K}\tilde{S}_h r_h^3\sqrt{\overline{\gamma}}\ e^{-K-S_h}}{(4P_1\tilde{K}\tilde{S}_h+\mathsf{a}^2r_h^2\overline{\gamma})^{3/2}}\Bigg[e^{S_h\Delta\mathsf{M}_j-8KS_h(1-\Delta\mathsf{M}_j)r_h^2/P_1}\ \Phi_1\Bigg(\frac{3}{2},1;2;\frac{4P_1\tilde{K}\tilde{S}_h}{4P_1\tilde{K}\tilde{S}_h+\mathsf{a}^2r_h^2\overline{\gamma}},\\
& \frac{32KS_h\tilde{K}\tilde{S}_h(1-\Delta\mathsf{M}_j)r_h^2}{4P_1\tilde{K}\tilde{S}_h+\mathsf{a}^2r_h^2\overline{\gamma}}\Bigg)\;+\;e^{-S_h\Delta\mathsf{M}_j-8KS_h(1+\Delta\mathsf{M}_j)r_h^2/P_1}\ \Phi_1\Bigg(\frac{3}{2},1;2;\frac{4P_1\tilde{K}\tilde{S}_h}{4P_1\tilde{K}\tilde{S}_h+\mathsf{a}^2r_h^2\overline{\gamma}},\\
& \frac{32KS_h\tilde{K}\tilde{S}_h(1+\Delta\mathsf{M}_j)r_h^2}{4P_1\tilde{K}\tilde{S}_h+\mathsf{a}^2r_h^2\overline{\gamma}}\Bigg)\Bigg]\;-\;\sum_{j=1}^{4}\sum_{h=1}^{20}\frac{8\mathsf{ap}^2b_j\mathcal{R}\tilde{K}\tilde{S}_h r_h^3\sqrt{\overline{\gamma}}\ e^{-K-S_h}}{3\pi(4P_1\tilde{K}\tilde{S}_h+2\mathsf{a}^2r_h^2\overline{\gamma})^{3/2}}\\
& \Bigg[e^{S_h\Delta\mathsf{M}_j-8KS_h(1-\Delta\mathsf{M}_j)r_h^2/P_1}\ \Phi_1^{(3)}\Bigg(\frac{3}{2},1,\frac{1}{2};\frac{5}{2};\frac{4P_1\tilde{K}\tilde{S}_h}{4P_1\tilde{K}\tilde{S}_h+2\mathsf{a}^2r_h^2\overline{\gamma}},\frac{4P_1\tilde{K}\tilde{S}_h+\mathsf{a}^2r_h^2\overline{\gamma}}{4P_1\tilde{K}\tilde{S}_h+2\mathsf{a}^2r_h^2\overline{\gamma}},\\
& \frac{32KS_h\tilde{K}\tilde{S}_h(1-\Delta\mathsf{M}_j)r_h^2}{4P_1\tilde{K}\tilde{S}_h+2\mathsf{a}^2r_h^2\overline{\gamma}}\Bigg)\;+\;e^{-S_h\Delta\mathsf{M}_j-8KS_h(1+\Delta\mathsf{M}_j)r_h^2/P_1}\\
& \Phi_1^{(3)}\Bigg(\frac{3}{2},1,\frac{1}{2};\frac{5}{2};\frac{4P_1\tilde{K}\tilde{S}_h}{4P_1\tilde{K}\tilde{S}_h+2\mathsf{a}^2r_h^2\overline{\gamma}},\frac{4P_1\tilde{K}\tilde{S}_h+\mathsf{a}^2r_h^2\overline{\gamma}}{4P_1\tilde{K}\tilde{S}_h+2\mathsf{a}^2r_h^2\overline{\gamma}},\frac{32KS_h\tilde{K}\tilde{S}_h(1+\Delta\mathsf{M}_j)r_h^2}{4P_1\tilde{K}\tilde{S}_h+2\mathsf{a}^2r_h^2\overline{\gamma}}\Bigg)\Bigg]
\end{aligned} \tag{4.19}$$

where $\Phi_1(\cdot)^{(3)}$ is a confluent Lauricella's hypergeometric function of three variables. It can be expressed either in the series form or in integral form [80] and [81],

$$\Phi_1^{(3)}(\bar{a}, \bar{b}_1, \bar{b}_2; \bar{c}; \bar{x}_1, \bar{x}_2, \bar{x}_3) = \sum_{\bar{k},\bar{l},\bar{m}=0}^{\infty} \frac{(\bar{a})_{\bar{k}+\bar{l}+\bar{m}} \ (\bar{b}_1)_{\bar{k}} \ (\bar{b}_2)_{\bar{l}} \ \bar{x}_1^{\bar{k}} \ \bar{x}_2^{\bar{l}} \ \bar{x}_3^{\bar{m}}}{(\bar{c})_{\bar{k}+\bar{l}+\bar{m}} \ \Gamma(\bar{k}+1) \ \Gamma(\bar{l}+1) \ \Gamma(\bar{m}+1)} \quad |\bar{x}_1| < 1, |\bar{x}_2| < 1$$

$$= \frac{\Gamma(\bar{c})}{\Gamma(\bar{a}) \ \Gamma(\bar{c}-\bar{a})} \int_0^1 \bar{u}^{\bar{a}-1} \ (1-\bar{u})^{\bar{c}-\bar{a}-1} \ e^{\bar{u}\bar{x}_3} \prod_{i=1}^{2} (1-\bar{u}\bar{x}_i)^{-\bar{b}_i} d\bar{u} \tag{4.20}$$

It can also be easily and accurately evaluated by using its finite integral representation or its infinite series representation.

Average Bit Error Rate (ABER) :

The bit error rate (BER) of most coherent modulation techniques can be found using the MGF approach as [84],

$$\begin{aligned} P_b(\psi) &= \int_0^{\infty} Q(\sqrt{2\psi\gamma}) f_\gamma(\gamma) d\gamma = \frac{1}{\pi} \int_0^{\pi/2} \mathcal{M}_\gamma\left(\frac{\psi}{\sin^2\theta}\right) d\theta \\ &= \sum_{j=1}^{4} \sum_{h=1}^{20} \frac{1}{\pi} \int_0^{\pi/2} \frac{b_j \mathcal{R} \tilde{K} \tilde{S}_h r_h^2 \ e^{-K-S_h} \sin^2\theta}{2P_1 \tilde{K} \tilde{S}_h \sin^2\theta + \psi r_h^2 \bar{\gamma}} \\ &\quad \cdot \left[e^{S_h \Delta \mathsf{M}_j + \frac{16 K S_h \tilde{K} \tilde{S}_h (1-\Delta \mathsf{M}_j) r_h^2 \sin^2\theta}{2P_1 \tilde{K} \tilde{S}_h \sin^2\theta + \psi r_h^2 \bar{\gamma}}} + e^{-S_h \Delta \mathsf{M}_j + \frac{16 K S_h \tilde{K} \tilde{S}_h (1+\Delta \mathsf{M}_j) r_h^2 \sin^2\theta}{2P_1 \tilde{K} \tilde{S}_h \sin^2\theta + \psi r_h^2 \bar{\gamma}}} \right] d\theta \end{aligned} \tag{4.21}$$

where ψ is a constant associated with the modulation technique used, for example, for BPSK $\psi = 1$, for coherent detection of binary frequency shift keying (BFSK) $\psi = 0.5$, for coherent detection of minimum shift keying (MSK) $\psi = 0.715$ and for coherent detection of M-PSK, $\psi = \sin^2(2i-1)\pi/M$. The integration in (4.21) can be evaluated using the similar tactics as for (4.17) and (4.19) in order to obtain,

$$
\begin{aligned}
P_b(\psi) \;=\; & \sum_{j=1}^{4}\sum_{h=1}^{20} \frac{\sqrt{2\psi} b_j \mathcal{R}\tilde{K}\tilde{S}_h r_h^3 \sqrt{\overline{\gamma}}\; e^{-K-S_h}}{2(4P_1\tilde{K}\tilde{S}_h + 2\psi r_h^2\overline{\gamma})^{3/2}} \Bigg[e^{S_h \Delta\mathsf{M}_j - 8KS_h(1-\Delta\mathsf{M}_j) r_h^2/P_1}\; \Phi_1\Bigg(\frac{3}{2}, 1; 2; \frac{4P_1\tilde{K}\tilde{S}_h}{4P_1\tilde{K}\tilde{S}_h + 2\psi r_h^2\overline{\gamma}}, \\
& \frac{32KS_h\tilde{K}\tilde{S}_h(1-\Delta\mathsf{M}_j) r_h^2}{4P_1\tilde{K}\tilde{S}_h + 2\psi r_h^2\overline{\gamma}}\Bigg) \;+\; e^{-S_h \Delta\mathsf{M}_j - 8KS_h(1+\Delta\mathsf{M}_j) r_h^2/P_1}\; \Phi_1\Bigg(\frac{3}{2}, 1; 2; \frac{4P_1\tilde{K}\tilde{S}_h}{4P_1\tilde{K}\tilde{S}_h + 2\psi r_h^2\overline{\gamma}}, \\
& \frac{32KS_h\tilde{K}\tilde{S}_h(1+\Delta\mathsf{M}_j) r_h^2}{4P_1\tilde{K}\tilde{S}_h + 2\psi r_h^2\overline{\gamma}}\Bigg)\Bigg]
\end{aligned}
\tag{4.22}
$$

Using (4.22), we can arrive at the final expression for ABER of coherent M-PSK as below,

$$
\begin{aligned}
P_b^{\mathrm{MPSK}}(e) \;=\; & \frac{2}{\max(\log_2 M, 2)} \sum_{i=1}^{\max(M/4,1)} \sum_{j=1}^{4}\sum_{h=1}^{20} \frac{\sqrt{\sin(2i-1)\pi/M}\, b_j \mathcal{R}\tilde{K}\tilde{S}_h r_h^3 \sqrt{\overline{\gamma}}\; e^{-K-S_h}}{\sqrt{2}(4P_1\tilde{K}\tilde{S}_h + 2\psi r_h^2\overline{\gamma})^{3/2}} \\
& \Bigg[e^{S_h \Delta\mathsf{M}_j - 8KS_h(1-\Delta\mathsf{M}_j) r_h^2/P_1}\; \Phi_1\Bigg(\frac{3}{2}, 1; 2; \frac{2P_1\tilde{K}\tilde{S}_h}{2P_1\tilde{K}\tilde{S}_h + \sin^2(2i-1)\pi/M r_h^2\overline{\gamma}}, \\
& \frac{16KS_h\tilde{K}\tilde{S}_h(1-\Delta\mathsf{M}_j) r_h^2}{2P_1\tilde{K}\tilde{S}_h + \sin^2(2i-1)\pi/M r_h^2\overline{\gamma}}\Bigg) \;+\; e^{-S_h \Delta\mathsf{M}_j - 8KS_h(1+\Delta\mathsf{M}_j) r_h^2/P_1} \\
& \Phi_1\Bigg(\frac{3}{2}, 1; 2; \frac{2P_1\tilde{K}\tilde{S}_h}{2P_1\tilde{K}\tilde{S}_h + \sin^2(2i-1)\pi/M r_h^2\overline{\gamma}}, \frac{16KS_h\tilde{K}\tilde{S}_h(1+\Delta\mathsf{M}_j) r_h^2}{2P_1\tilde{K}\tilde{S}_h + \sin^2(2i-1)\pi/M r_h^2\overline{\gamma}}\Bigg)\Bigg]
\end{aligned}
\tag{4.23}
$$

Following the same procedure as in [82], BER expressions for each bit in M-PSK over the JFTS fading/shadowing communication link can also be derived.

4.3.2 CDF-based Approach

In order to obtain the ABER of a large variety of modulation techniques, the CDF-based approach of [57] will be used in this section. In this case also, the receivers are assumed to be operating over iid JFTS composite fading/shadowing conditions.

Binary Modulation :

For any binary coherent and non-coherent modulation technique, the ABER over a composite flat faded and slow shadowed wireless communication channel suffering from AWGN can be expressed in terms of the instantaneous CSNR as [83],

$$P_b^{\text{Binary}}(e) \;=\; \frac{\bar{\alpha}^{\bar{\beta}}}{2\Gamma(\bar{\beta})}\int_0^{\infty} \gamma^{\bar{\beta}-1}\; e^{-\bar{\alpha}\gamma} F_{\gamma}(\gamma)\mathrm{d}\gamma \tag{4.24}$$

where $\bar{\alpha}=1$ for BPSK and $\bar{\alpha}=1/2$ for BPSK. If the modulation is differential or non-coherent, $\bar{\beta}=1$, while for coherent modulation, $\bar{\beta}=1/2$. The function $\Gamma(\bar{\xi},\bar{\eta}) = \int_{\bar{\eta}}^{\infty} \bar{\mathsf{t}}^{\bar{\xi}-1}\; e^{-\bar{\mathsf{t}}}\mathrm{d}\bar{\mathsf{t}}$ is a complimentary incomplete Gamma function. By substituting (4.8) in (4.24) and using the integral solution from [48], the ABER expression for any coherent or non-coherent binary modulation technique over a JFTS channel can be obtained as,

$$\begin{aligned} P_b^{\text{Binary}}(e) \;=\; & \frac{\bar{\alpha}^{\bar{\beta}}}{2\Gamma(\bar{\beta})}\sum_{j=1}^{4}\sum_{h=1}^{20}\frac{b_j\mathcal{R}}{2}\; e^{-K-S_h}\,\Bigg[e^{S_h\Delta\mathsf{M}_j} I_0\bigg(\sqrt{KS_h(1-\Delta\mathsf{M}_j)/P_1P_2}\bigg) \\ & +\; e^{-S_h\Delta\mathsf{M}_j} I_0\bigg(\sqrt{KS_h(1+\Delta\mathsf{M}_j)/P_1P_2}\bigg)\Bigg] \\ & \sum_{\mathsf{k}=0}^{\infty}\sum_{v=0}^{\mathsf{k}}\frac{(-1)^v 2^{\mathsf{k}}}{v!}(v+\bar{\beta}-1)!\left(\frac{2P_1\tilde{K}\tilde{S}_h}{r_h^2\overline{\gamma}}\right)^{v}\left(\frac{r_h^2\overline{\gamma}}{\bar{\alpha}r_h^2\overline{\gamma}+2P_1\tilde{K}\tilde{S}_h}\right)^{v+\bar{\beta}} \end{aligned} \tag{4.25}$$

Using the finite series summation formulas for $v=0$ to k, (4.25) can be expressed as,

$$\begin{aligned} P_b^{\text{Binary}}(e) \;=\; & \frac{\bar{\alpha}^{\bar{\beta}}}{2\Gamma(\bar{\beta})}\sum_{j=1}^{4}\sum_{h=1}^{20}\frac{b_j\mathcal{R}}{2}\; e^{-K-S_h}\,\Bigg[e^{S_h\Delta\mathsf{M}_j} I_0\bigg(\sqrt{KS_h(1-\Delta\mathsf{M}_j)/P_1P_2}\bigg) +\; e^{-S_h\Delta\mathsf{M}_j} \\ & I_0\bigg(\sqrt{KS_h(1+\Delta\mathsf{M}_j)/P_1P_2}\bigg)\Bigg]\Bigg[\sum_{\mathsf{k}=0}^{\infty}\frac{(-2)^{\mathsf{k}}(\bar{\beta}+\mathsf{k})!}{(\mathsf{k}+1)!}\left(\frac{2P_1\tilde{K}\tilde{S}_h}{\bar{\alpha}r_h^2\overline{\gamma}+2P_1\tilde{K}\tilde{S}_h}\right)^{\mathsf{k}+1} \\ & \left(\frac{r_h^2\overline{\gamma}}{\bar{\alpha}r_h^2\overline{\gamma}+2P_1\tilde{K}\tilde{S}_h}\right)^{\bar{\beta}}\;{}_2F_1\left(1,\bar{\beta}+\mathsf{k}+1;\mathsf{k}+2;\frac{2P_1\tilde{K}\tilde{S}_h}{\bar{\alpha}r_h^2\overline{\gamma}+2P_1\tilde{K}\tilde{S}_h}\right) - \frac{(\bar{\beta}-1)!}{\bar{\alpha}^{\bar{\beta}}}\Bigg] \end{aligned} \tag{4.26}$$

The details on the solution to the integral and finite series summation is provided in Appendix C.

Coherent M-ary Modulation :

In order to evaluate the error performance of M-ary coherent modulation techniques over a composite fading/shadowing channel, the following integral is needed to be solved,

$$P_b^{M\text{-ary}}(e,g) \;=\; \frac{1}{\sqrt{2\pi}}\int_0^{\infty} F_\gamma\left(\frac{\bar{\mathsf{t}}^2}{g}\; e^{-\frac{\bar{\mathsf{t}}^2}{2}}\right)\mathrm{d}\bar{\mathsf{t}} \tag{4.27}$$

where g depends on the modulation type [84]. For a JFTS channel, substituting (4.8) in (4.27), using the change of variables, $\tilde{\mathsf{u}} = \bar{\mathsf{t}}^2$ and then using the integral solution from [48], $P_b^{M\text{-ary}}(e,g)$ can be expressed as,

$$\begin{aligned} P_b^{M\text{-ary}}(e,g) \;=\; & \sum_{j=1}^{4}\sum_{h=1}^{20}\frac{b_j\mathcal{R}}{2}\; e^{-K-S_h}\;\Bigg[e^{S_h\Delta\mathsf{M}_j} I_0\left(\sqrt{KS_h(1-\Delta\mathsf{M}_j)/P_1P_2}\right) + \; e^{-S_h\Delta\mathsf{M}_j} \\ & I_0\left(\sqrt{KS_h(1+\Delta\mathsf{M}_j)/P_1P_2}\right)\Bigg]\Bigg[\sum_{\mathsf{k}=0}^{\infty}\frac{(-2)^{\mathsf{k}}(1/2+\mathsf{k})!}{(\mathsf{k}+1)!}\left(\frac{4P_1\tilde{K}\tilde{S}_h}{gr_h^2\overline{\gamma}+4P_1\tilde{K}\tilde{S}_h}\right)^{\mathsf{k}+1} \\ & \left(\frac{2gr_h^2\overline{\gamma}}{gr_h^2\overline{\gamma}+4P_1\tilde{K}\tilde{S}_h}\right)^{1/2}\;{}_2F_1\left(1,\mathsf{k}+3/2;\mathsf{k}+2;\frac{4P_1\tilde{K}\tilde{S}_h}{gr_h^2\overline{\gamma}+4P_1\tilde{K}\tilde{S}_h}\right)+\frac{1}{\sqrt{2}}\Bigg] \end{aligned} \tag{4.28}$$

This generalized ABER expression (4.28) for M-ary coherent modulation techniques can be used to derive a closed-form ABER expression for any coherent modulation techniques only by changing the value of g. Using this procedure, closed-form ABER expressions for Gray-coded RQAM and coherently detected M-PSK over a JFTS faded/shadowed channel are deduced.

Using unified approximation, as is done in [84], the ABER expression of general order M-QAM modulation over a fading, shadowing, or composite fading/shadowing channel is given by,

$$P_b^{M\text{-QAM}}(e) \;=\; \frac{4}{\log_2 M}(1-1/\sqrt{M})\sum_{i=1}^{\sqrt{M}/2} P_b^{M\text{-ary}}(e, g_{i,M\text{-QAM}}) \tag{4.29}$$

where $g_{i,M\text{-QAM}} = 3(2i-1)^2\log_2 M/(M-1)$. Substituting (4.29) in (4.28), the ABER expression for general order MQAM modulation technique over a JFTS channel can be obtained in closed form as,

$$
\begin{aligned}
P_b^{M\text{-QAM}}(e) \;=\; & \frac{4\ e^{-K-S_h}}{\log_2 M}\left(1-\frac{1}{\sqrt{M}}\right)\sum_{i=1}^{\sqrt{M}/2}\sum_{j=1}^{4}\sum_{h=1}^{20}\frac{b_j\mathcal{R}}{2}\left[e^{S_h\Delta\mathsf{M}_j} I_0\left(\sqrt{KS_h(1-\Delta\mathsf{M}_j)/P_1P_2}\right)+e^{-S_h\Delta\mathsf{M}_j}\right. \\
& \left. I_0\left(\sqrt{KS_h(1+\Delta\mathsf{M}_j)/P_1P_2}\right)\right]\left[\sum_{\mathsf{k}=0}^{\infty}\frac{(-2)^{\mathsf{k}}(1/2+\mathsf{k})!}{(\mathsf{k}+1)!}\left(\frac{4P_1\tilde{K}\tilde{S}_h}{g_{i,M\text{-QAM}}r_h^2\overline{\gamma}+4P_1\tilde{K}\tilde{S}_h}\right)^{\mathsf{k}+1}\right. \\
& \left.\left(\frac{2g_{i,M\text{-QAM}}r_h^2\overline{\gamma}}{g_{i,M\text{-QAM}}r_h^2\overline{\gamma}+4P_1\tilde{K}\tilde{S}_h}\right)^{1/2} {}_2F_1\left(1,\mathsf{k}+3/2;\mathsf{k}+2;\frac{4P_1\tilde{K}\tilde{S}_h}{g_{i,M\text{-QAM}}r_h^2\overline{\gamma}+4P_1\tilde{K}\tilde{S}_h}\right)+\frac{1}{\sqrt{2}}\right]
\end{aligned}
\tag{4.30}
$$

Using the same approach as followed for MQAM, the ABER expression of Gray-coded coherent MPSK modulation over a fading and/or shadowing channel is given by,

$$
P_b^{M\text{-PSK}}(e) \;=\; \frac{2}{\max(\log_2 M, 2)}\sum_{i=1}^{\max(M/4-1)} P_b^{M\text{-ary}}(e, g_{i,M\text{-PSK}}) \tag{4.31}
$$

where $g_{i,M\text{-PSK}} = 2\log_2 M\sin^2((2i-1)\pi/M)$. Substituting (4.31) in (4.28), the ABER expression for coherent MPSK modulation technique over a JFTS channel can be obtained in closed form as,

$$
\begin{aligned}
P_b^{M\text{-PSK}}(e) \;=\; & \frac{2\ e^{-K-S_h}}{\max(\log_2 M, 2)}\sum_{i=1}^{\max(M/4-1)}\sum_{j=1}^{4}\sum_{h=1}^{20}\frac{b_j\mathcal{R}}{2}\left[e^{S_h\Delta\mathsf{M}_j} I_0\left(\sqrt{KS_h(1-\Delta\mathsf{M}_j)/P_1P_2}\right)+e^{-S_h\Delta\mathsf{M}_j}\right. \\
& \left. I_0\left(\sqrt{KS_h(1+\Delta\mathsf{M}_j)/P_1P_2}\right)\right]\left[\sum_{\mathsf{k}=0}^{\infty}\frac{(-2)^{\mathsf{k}}(1/2+\mathsf{k})!}{(\mathsf{k}+1)!}\left(\frac{4P_1\tilde{K}\tilde{S}_h}{g_{i,M\text{-PSK}}r_h^2\overline{\gamma}+4P_1\tilde{K}\tilde{S}_h}\right)^{\mathsf{k}+1}\right. \\
& \left.\left(\frac{2g_{i,M\text{-PSK}}r_h^2\overline{\gamma}}{g_{i,M\text{-PSK}}r_h^2\overline{\gamma}+4P_1\tilde{K}\tilde{S}_h}\right)^{1/2} {}_2F_1\left(1,\mathsf{k}+3/2;\mathsf{k}+2;\frac{4P_1\tilde{K}\tilde{S}_h}{g_{i,M\text{-PSK}}r_h^2\overline{\gamma}+4P_1\tilde{K}\tilde{S}_h}\right)+\frac{1}{\sqrt{2}}\right]
\end{aligned}
\tag{4.32}
$$

It is evident from the error probability performance expressions derived using both the MGF and CDF based approaches over a JFTS channel depends on the channel model parameters. The slope of the ABER/ASER curve is proportional to the product of the square of the fading parameter K and the shadowing parameter S_h. Hence, either as K or S_h or both increases, ABER performance improves. It can also be concluded from the expressions that error performance depends on the Δ-parameter of the JFTS channel model. However, exactly how much error rate is affected by a change in Δ is difficult to predict strictly by inspecting the error rate expressions. The sensitivity to changes in Δ is best evaluated using the plots presented in the Section 4.5.

It is also evident from the error rate expressions derived using the MGF-approach, that they become independent of the parameter P_2. The expressions derived using the CDF-approach are though not independent of P_2 is very negligibly affected by it. These observations can be generalized to infer that error probability performance of any modulation technique over a JFTS faded/shadowed channel will be independent of P_2 which is the variation of the shadowing distribution only. Intuitively, P_2 represents the spread of the shadowing distribution, the shape of which is also determined by Δ making P_2 a redundant parameters. Although, the P_1 parameter appears in the error rate expression, its effect can be considered negligible as it appears both in the numerator and the denominator with almost equal powers.

4.3.3 Coded BER

The primary contribution of this subsection is to analyze the ABER performance of BPSK in combination with iterative coding techniques like Turbo coding and LDPC coding over fully interleaved JFTS block fading/shadowing channels. In order to do that, $s_{\bar{m}} \in \{\pm E_s\}$ is used to represent a BPSK symbol amplitude that is transmitted over a composite slow shadowed and flat faded wireless communication channel with JFTS statistics, where $\bar{m}$ is an integer symbol index. With appropriate sampling and perfect coherent demodulation, the discrete representation of the demodulator output can be expressed as,

$$\bar{y}_{\bar{m}} = z_{\bar{m}} s_{\bar{m}} + n_{\bar{m}} \tag{4.33}$$

where $n_{\bar{m}}$ is the iid complex AWGN component with zero mean, variance of σ_n^2 and power spectral density of $N_0/2$. The amplitude, $z_{\bar{m}}$ denotes the JFTS distributed composite fading/shadowing envelope. Since, the communication channel is assumed to be fully interleaved, the $z_{\bar{m}}$'s are independent. For this analysis, an R_c-rate Turbo code or regular LDPC code is used with an input size of L bits and an output encoded stream of N bits.

As $z_1, z_2, \ldots, z_\tau$ are modeled as independent JFTS random variables, each of the z_τ^2 terms will have a PDF of,

$$f_{\mathcal{Z}}(\zeta_\tau) = \sum_{j=1}^{4}\sum_{h=1}^{20} \frac{b_j \mathcal{R}}{P_1 P_2}\, e^{-K-S_h-\frac{\zeta_\tau}{2P_2 r_h^2}}\, D\left(\sqrt{\frac{2K\zeta_\tau}{P_1P_2}}; S_h, \Delta\mathsf{M}_j\right) \tag{4.34}$$

where $\zeta_\tau = z_\tau^2$. The expression of the PDF in (4.34) can be derived using the procedures for deducing bivariate and joint distributions followed in [43]. Using the infinite series expansion of the modified Bessel function, (4.34) can be expressed as,

$$\begin{aligned} f_{\mathcal{Z}}(\zeta_\tau) = & \sum_{j=1}^{4}\sum_{h=1}^{20} \frac{b_j \mathcal{R}}{P_1 P_2}\, e^{-K-S_h-\frac{\zeta_\tau}{2P_2 r_h^2}} \left[e^{S_h \Delta\mathsf{M}_j}\, I_0\left(2\sqrt{KS_h(1-\Delta\mathsf{M}_j)/P_1P_2}\right)\right. \\ & \left. + \; e^{-S_h\Delta\mathsf{M}_j}\, I_0\left(2\sqrt{KS_h(1+\Delta\mathsf{M}_j)/P_1P_2}\right)\right] \sum_{\mathsf{k}=0}^{\infty} \zeta_\tau^{\mathsf{k}} \end{aligned} \tag{4.35}$$

In the rest of this section, (4.35) will be used to derive the PEP expression for Turbo coded BPSK and BER expression for LDPC coded BPSK over a fully interleaved JFTS faded/shadowed communication link.

PEP-based Approach :

Assuming the all-zero codeword and ML decoding at the receiver, the upper bound on the word error probability of Turbo coding can be expressed as, [85]

$$P_{\text{word}} \;\leq\; \sum_{\delta_1=1}^{\mathsf{N}} \mathcal{C}(\delta_1)\; \mathcal{P}_2(\delta_1) \tag{4.36}$$

where $\mathcal{C}(\delta_1)$ is the number of codewords and $\mathcal{P}_2(\delta_1)$ is the probability of incorrectly decoding a codeword with weight δ_1. In order to eliminate a computationally exhaustive search, an average bound can be constructed using the average weight distribution over all possible interleavers. In this case, the average weight distribution can be written as,

$$\overline{\mathcal{C}(\delta_1)} \;=\; \sum_{\mathsf{l}=1}^{\mathsf{L}} \binom{\mathsf{L}}{\mathsf{l}}\, p(\delta_1|\mathsf{l}) \tag{4.37}$$

where $\binom{\mathsf{L}}{\mathsf{l}}$ is the number of input words with Hamming weight l and $p(\delta_1|\mathsf{l})$ is the probability that an input word with Hamming weight l can be encoded to a codeword with Hamming weight δ_1.

The average upper bound for word error rate over any fading, shadowing or composite fading / shadowing communication channel can be given by,

$$\begin{aligned}
\overline{P}_{\text{word}} \;&\leq\; \sum_{\delta_1=\delta_{1\min}}^{\mathsf{N}} \overline{\mathcal{C}(\delta_1)}\; \mathcal{P}_2(\delta_1) \\
&\leq\; \sum_{\delta_1=\delta_{1\min}}^{\mathsf{N}} \sum_{\mathsf{l}=1}^{\mathsf{L}} \binom{\mathsf{L}}{\mathsf{l}}\, p(\delta_1|\mathsf{l})\; \mathcal{P}_2(\delta_1) \\
&\leq\; \sum_{\mathsf{l}=1}^{\mathsf{L}} \binom{\mathsf{L}}{\mathsf{l}}\, \mathrm{E}_{\delta_1|\mathsf{l}}\big[\mathcal{P}_2(\delta_1)\big]
\end{aligned} \tag{4.38}$$

where $\delta_{1\min}$ is the minimum Hamming weight of the generated codewords and $\mathrm{E}_{\delta_1|\mathsf{l}}\big[\,\cdot\,\big]$ is the expectation with respect to $p(\delta_1|\mathsf{l})$. Consequently, the average upper bound for bit error rate can be expressed as,

$$\overline{P}_{\text{bit}} \;\leq\; \sum_{\mathsf{l}=1}^{\mathsf{L}} \frac{\mathsf{l}}{\mathsf{L}} \binom{\mathsf{L}}{\mathsf{l}} \, \mathrm{E}_{\delta_1|\mathsf{l}}\big[\mathcal{P}_2(\delta_1)\big]. \tag{4.39}$$

This average bound can be used for computing $p(\delta_1|\mathsf{l})$ by utilizing the state transition matrix of the recursive systematic convolutional (RSC) encoders proposed in [86]. Subsequently, using $p(\delta_1|\mathsf{l})$, the PEP $\mathcal{P}_2(\delta_1)$ of Turbo coded BPSK over a JFTS fading / shadowing channel will be formulated using the PEP-based approach of [76].

Assuming perfect CSI at the receiver, the conditional PEP of decoding a codeword c_0 into a codeword c_{j} over a fading/shadowing channel can be given by,

$$P(\mathbf{c_0}, \mathbf{c}_{\mathrm{j}}|\mathcal{Z}) \;=\; Q\left[\sqrt{\frac{E_s}{N_0}\sum_{\tau=1}^{\delta_1}\zeta_\tau}\right] \tag{4.40}$$

where c_{j} differs from c_0 in δ_1 bit positions with a known composite fading/shadowing vector $\mathcal{Z}$ indexed by $1, 2, \ldots, \delta_{1\min}$ and $Q(\cdot)$ is the Gaussian Q-function. As mentioned before, the PEP can be deduced by taking the expectation over (4.40) as,

$$\mathcal{P}_2(\delta_1) \;=\; \mathrm{E}\left\{Q\left[\sqrt{\frac{E_s}{N_0}\sum_{\tau=1}^{\delta_1}\zeta_\tau}\right]\right\} \tag{4.41}$$

By putting (4.35) in (4.41), the expression of PEP can be obtained as,

$$\begin{aligned}\mathcal{P}_2(\delta_1) \;=\; & \sum_{j=1}^{4}\sum_{h=1}^{20}\frac{b_j\mathcal{R}}{2P_1P_2}\, e^{-K-S_h}\, \Bigg[e^{S_h\Delta\mathsf{M}_j}\, I_0\bigg(2\sqrt{KS_h(1-\Delta\mathsf{M}_j)/P_1P_2}\bigg) + e^{-S_h\Delta\mathsf{M}_j} \\ & I_0\bigg(2\sqrt{KS_h(1+\Delta\mathsf{M}_j)/P_1P_2}\bigg)\Bigg] \int_0^\infty \left(\int_{\sqrt{\frac{E_s}{N_0}\zeta_\tau}}^{\infty} e^{\nu^2/2}\mathrm{d}\nu\right) \sum_{\mathsf{k}=0}^{\infty} \zeta_\tau^{\mathsf{k}\delta_1}\, e^{-\frac{\zeta_\tau}{2P_2r_h^2}}\mathrm{d}\zeta_\tau \end{aligned} \tag{4.42}$$

Changing the order of integration and solving them using solutions from [51], the final expression for PEP of Turbo coded BPSK over a JFTS faded/shadowed communication channel can be obtained as,

$$
\begin{aligned}
\mathcal{P}_2(\delta_1) \; = & \sum_{j=1}^{4}\sum_{h=1}^{20}\frac{b_j\mathcal{R}}{2P_1P_2}\; e^{-K-S_h}\;\Bigg[e^{S_h\Delta\mathsf{M}_j}\; I_0\bigg(2\sqrt{KS_h(1-\Delta\mathsf{M}_j)/P_1P_2}\bigg)+e^{-S_h\Delta\mathsf{M}_j} \\
& I_0\bigg(2\sqrt{KS_h(1+\Delta\mathsf{M}_j)/P_1P_2}\bigg)\Bigg]\Bigg[\sum_{\mathsf{k}=0}^{\infty}(\mathsf{k}\delta_1)!\sqrt{\frac{\pi}{2}}\bigg(\frac{1}{2P_2r_h^2}\bigg)^{\mathsf{k}\delta_1+1}-\sum_{v=0}^{\mathsf{k}\delta_1}\frac{(\mathsf{k}\delta_1)!}{2v!(E_s/N_0)^v} \\
& \frac{\Gamma(v+1/2)}{(1/2P_2r_h^2)^{\mathsf{k}\delta_1-v+1}(1/2+N_0/2E_sP_2r_h^2)^{v+1/2}}\Bigg] \qquad (4.43)
\end{aligned}
$$

the detailed calculation of which is provided in Appendix C.

Finally (4.43) will be used to evaluate ABER performance of Turbo coded BPSK over JFTS fading/shadowing wireless channels in Section 4.5. with the simulated ABER performance. It is to be noted that for simulation, an iterative suboptimal soft-decision decoder will be used where each constituent RSC is decoded separately. The constituent decoders exchange bit-likelihood information iteratively using a log-MAP decoding algorithm.

GA-based Approach :

In this subsection, the performance of LDPC coded BPSK is analyzed over an iid JFTS fading/shadowing channels. The exact expressions for LDPC codes are mathematically intractable due to the iterative evolution of the message PDFs. Furthermore, performance analysis methods like Density Evolution (DE) and simulations are time consuming tasks to perform. Hence the Gaussian Approximation (GA) approach will be used in this chapter to compute approximate BER expressions for LDPC coded BPSK. In order to this, it is assumed that the composite fading/shadowing on each bit is independent. It is mentioned in [87], that for LDPC codes, the PDF of the bit node message is close to the Gaussian distribution, while the PDF of the check node message will also tend to the Gaussian distribution as the number of iterations increases. Hence, for a GA approach, both the PDFs of the bit and check node messages are assumed to be Gaussian distributed. Only the mean value needs to be updated iteratively, as compared to numerically tracking and updating the PDFs in DE, resulting in a significant reduction in computational time. It is also assumed that perfect CSI is available and the block length of the code is infinite resulting in a cycle free graph.

Let the edge degree distribution of the LDPC graph is given by, $\overline{\lambda}(\bar{z}) = \sum_{\mathsf{k}_1=2}^{\delta_{\bar{v}}} \overline{\lambda}_{\mathsf{k}_1} \bar{z}^{\mathsf{k}_1-1}$ and $\overline{\rho}(\bar{z}) = \sum_{\mathsf{l}_1=2}^{\delta_{\bar{c}}} \overline{\rho}_{\mathsf{l}_1} \bar{z}^{\mathsf{l}_1-1}$, where $\overline{\lambda}_{\mathsf{k}_1}$ is the fraction of edges connected to a bit node of degree k_1, $\overline{\rho}_{\mathsf{l}_1}$ is the fraction of edges connected to a check node of degree l_1, $\delta_{\bar{v}}$ is the maximum bit node degree, and $\delta_{\bar{c}}$ is the maximum check node degree. The message passed from the bit node to the check node is the summation of channel log-likelihood ratio (LLR) and incoming LLRs from the neighbors of the bit node except the check node that gets the message. As the LLRs are random variables, the summation process is equivalent to the convolution of their PDFs. Since GA-based approach is used here, the PDFs of the bit and check node messages are approximated by Gaussian distribution and are given by, [88]

$$p_v(c) \;=\; \frac{1}{\sqrt{4\pi\mu_v}}\, e^{-\frac{(c-\mu_v)^2}{4\mu_v}} \tag{4.44}$$

where μ_v is the mean value. The BER is derived by integrating the convolution of the PDF of channel LLR and (4.44) from $-\infty$ to 0 due to the all-zero codeword assumption, and averaging this expression over all the bit node degrees during the δ_2th iteration. The BER is in turn used to obtain the new mean value of the check node message. The computation is carried out iteratively until the BER converges to zero or a constant value.

The conditional PDF of the channel LLR can be given by [89],

$$p_o(\mathbf{c}|\zeta_\tau, s_{\bar{m}} = +1) \; = \; \frac{\sigma_n}{2\zeta_\tau\sqrt{2\pi}} \; e^{-\frac{(c-2\zeta_\tau^2/\sigma_n^2)^2}{8\zeta_\tau^2/\sigma_n^2}} \tag{4.45}$$

with mean $2\zeta_\tau^2/\sigma_n^2$ and variance $4\zeta_\tau^2/\sigma_n^2$. The unconditional PDF of the channel LLR is obtained by averaging (4.45) over the PDF of ζ_τ with the integral solution in [48] which can be evaluated as,

$$\begin{aligned} p_o(c) \; &= \int_0^\infty p_o(\mathbf{c}|\zeta_\tau, s_{\bar{m}} = +1) f_{\mathcal{Z}}(\zeta_\tau)\mathrm{d}\zeta_\tau \\ &= \sum_{j=1}^{4}\sum_{h=1}^{20} \frac{b_j \mathcal{R}\sigma_n}{2\sqrt{2\pi}P_1P_2} \; e^{-K-S_h+c/2} \left[e^{S_h\Delta\mathsf{M}_j} \; I_0\left(2\sqrt{KS_h(1-\Delta\mathsf{M}_j)/P_1P_2}\right) + e^{-S_h\Delta\mathsf{M}_j}\right. \\ &\left. I_0\left(2\sqrt{KS_h(1+\Delta\mathsf{M}_j)/P_1P_2}\right)\right] \sum_{\mathsf{k}=0}^{\infty} \left(\frac{c\sigma_n^2 r_h}{2}\sqrt{\frac{P_2}{\sigma_n^2+P_2r_h^2}}\right)^{\mathsf{k}+1/2} \mathcal{K}_{\mathsf{k}+1/2}\left(\frac{c}{2r_h}\sqrt{\frac{\sigma_n^2+P_2r_h^2}{P_2}}\right) \end{aligned} \tag{4.46}$$

where $\mathcal{K}_{\overline{\nu}}(\cdot)$ is the modified Bessel function of the second kind. The PDF of the bit node message is obtained by convolving (4.46) with (4.44) [75], which can be expressed as,

$$\begin{aligned} p_{\mathcal{D}}(c) \; &= p_o(c) \; * \; p_v(c) \\ &= \sum_{j=1}^{4}\sum_{h=1}^{20} \frac{b_j\mathcal{R}}{2\sqrt{32\pi}P_1P_2} \; e^{-K-S_h-\frac{c^2}{4\mu_v}+\frac{c}{2}-\frac{\mu_v}{4}+\frac{\mu_v(\sigma_n^2+P_2r_h^2)}{8r_h^2P_2}} \left[e^{S_h\Delta\mathsf{M}_j} \; I_0\left(2\sqrt{KS_h(1-\Delta\mathsf{M}_j)/P_1P_2}\right)\right. \\ &\left. + \; e^{-S_h\Delta\mathsf{M}_j} \; I_0\left(2\sqrt{KS_h(1+\Delta\mathsf{M}_j)/P_1P_2}\right)\right] \sum_{\mathsf{k}=0}^{\infty} \Gamma(\mathsf{k}+1)(\mu_v)^{\mathsf{k}/2-1/4} \left(\frac{r_h^2\sigma_n^2P_2}{\sigma_n^2+P_2r_h^2}\right)^{\mathsf{k}+1} \\ &\mathcal{W}_{-\mathsf{k}/2+1/4,\mathsf{k}/2+1/4}\left(\frac{\mu_v(\sigma_n^2+P_2r_h^2)}{8r_h^2P_2}\right) \end{aligned} \tag{4.47}$$

where $\mathcal{W}_{\overline{\mu},\overline{\kappa}}(\cdot)$ is the Whittaker function of the second kind and can be defined in terms of Kummer's confluent hypergeometric function, as in [48].

The final expression for BER is obtained by integrating (4.47) from $-\infty$ to 0 based on all-zero codeword assumption and averaging it over all the bit node degrees for the (δ_2+1)th iteration, which is evaluated as,

$$\begin{aligned}
P_b^{\delta_2+1}(e) &= \int_{-\infty}^{0} p_{\mathcal{D}}(c)\mathrm{d}c \\
&= 1-\int_{0}^{\infty} p_{\mathcal{D}}(c)\mathrm{d}c \\
&= 1-\sum_{j=1}^{4}\sum_{h=1}^{20}\frac{b_j\mathcal{R}}{2\sqrt{32}P_1P_2}\; e^{-K-S_h+\frac{\mu_v^{\delta_2+1}(\sigma_n^2+P_2r_h^2)}{8r_h^2P_2}}\;\Bigg[e^{S_h\Delta\mathsf{M}_j}\; I_0\Big(2\sqrt{KS_h(1-\Delta\mathsf{M}_j)/P_1P_2}\Big) \\
&\quad+\; e^{-S_h\Delta\mathsf{M}_j} I_0\Big(2\sqrt{KS_h(1+\Delta\mathsf{M}_j)/P_1P_2}\Big)\Bigg]\sum_{\mathsf{k}=0}^{\infty}\Gamma(\mathsf{k}+1)\left(\frac{r_h^2\sigma_n^2P_2\sqrt{\mu_v^{\delta_2+1}}}{\sigma_n^2+P_2r_h^2}\right)^{\mathsf{k}+1} \\
&\quad\mathcal{W}_{-\mathsf{k}/2+1/4,\mathsf{k}/2+1/4}\left(\frac{\mu_v^{\delta_2+1}(\sigma_n^2+P_2r_h^2)}{8r_h^2P_2}\right)
\end{aligned} \tag{4.48}$$

The detailed calculations behind (4.46), (4.47) and (4.48) are provided in Appendix C. Finally (4.48) will be used to evaluate ABER performance of LDPC coded BPSK over JFTS fading/shadowing wireless channels in Section 4.5 with the simulated ABER performance. For simulation, the block size of the LDPC code will be set to 10^4 and maximum number of iterations for decoding will be set to 100. Performance of both regular and irregular LDPC codes will be evaluated.

The main difference between the error probability expressions of the fixed modulation techniques and fixed coded modulation techniques is their dependence on the parameter P_2. Error rates for coded modulation over the JFTS channel is no longer independent of P_2, as observed in case of fixed modulations only. In this case, the slope of the BER curves both in case of Turbo coded and LDPC coded modulations is found to be proportional to P_2. Hence as P_2 increases, performance improves, since a higher P_2 represents higher variance of the shadowing distribution and hence lower severity in shadowing.

4.4 Capacity Analysis

The principal contribution of this section is to determine the achievable channel capacity over a JFTS faded/shadowed channel. Therefore, this section quantifies the maximum achievable information transmission rate over a bandlimited composite flat faded and slow shadowed JFTS channel, while maintaining an arbitrarily low probability of error, in the quest for more error-resilient, power-efficient and bandwidth-efficient channel coding schemes. In order to achieve that, expressions for channel capacity, $\mathtt{C}$, channel cut-off rate, $\mathtt{R}_0$, and bandwidth efficiency, η, are derived for the JFTS faded/shadowed channel in Subsections 4.4.1, 4.4.2 and 4.4.3 respectively. For all these derivations in this section, it has been assumed that perfect CSI is available at the transmitter and the receiver.

4.4.1 Channel Capacity

The Shannon bound of AWGN channel is obtained by finding the capacity of a continuous input continuous output AWGN channel, where the modulated signal itself, $s(t)$, may be modeled by bandlimited Gaussian noise at the channel input. The channel input is assumed to be contaminated by the AWGN channel noise $n(t)$. After bandlimiting, the samples of both noise sources are taken at the Nyquist rate. The sample are iid Gaussian random variables with zero mean and variance σ_s^2 for $s(t)$ and $N_0/2$ for $n(t)$. The resultant sampled waveforms can be described by vectors of $\tilde{N}$ discrete-time but continuous-valued samples, where $\tilde{N} = 2BT$ is the signal dimensionality such that the input waveform is constrained to an ideal lowpass or bandpass bandwidth, B, and the waveform is limited to the time interval, $0 \leq t \leq T$. Upon exploiting that the PDFs of the input and output waveforms are Gaussian, the Shannon bound can be expressed as [60],

$$\mathtt{C}_{\mathrm{CCMC}}^{\mathrm{AWGN}} = BT \log_2(1+\gamma) \quad \text{[bits/symbol]} \tag{4.49}$$

where CCMC stands for Continuous Input Continuous Output Memoryless Channel. In this case, the channel capacity is only restricted either by the signaling energy, γ, or by the bandwidth, B. Therefore CCMC capacity can also be referred to as the unrestricted bound.

In $\tilde{N}$ dimensional M-ary signals are transmitted over a Discrete Input Continuous Output Memoryless Channel (DCMC), the achievable capacity can be given by,

$$p(s_i) = \frac{1}{M}, \qquad i = 1, \ldots, M \tag{4.50}$$

assuming equiprobable M-ary input symbols conveying $\log_2 M$ bits/symbol information. The conditional probability of receiving $\bar{y}$ given that s was transmitted when communicating over an AWGN channel is determined by the PDF of the noise yielding,

$$p(\bar{y}|s_i) = \prod_{\tilde{n}=1}^{\tilde{N}} \frac{1}{\sqrt{\pi N_0}} \, e^{-\frac{(\bar{y}_{\tilde{n}} - s_{i\tilde{n}})^2}{N_0}} \tag{4.51}$$

where N_0 is the channel's noise variance. It is to be noted here that $p(\bar{y}|s_i)$ is also referred to as the channel's transition probability. By using (4.50) and (4.51), the capacity expression of the DCMC can be simplified to [90],

$$\mathsf{C}_{\mathrm{DCMC}}^{\mathrm{AWGN}} = \log_2(M) - \frac{1}{M(\sqrt{\pi})^{\tilde{N}}} \sum_{i=1}^{M} \int_{-\infty}^{\infty} \cdots \int_{-\infty}^{\infty} e^{-|\mathbf{t}|^2} \log_2\left[\sum_{l=1}^{M} e^{-2\mathbf{t}\cdot\mathbf{d}_{il} - |\mathbf{d}_{il}|^2}\right] \mathrm{d}\mathbf{t} \quad \text{[bits/symbol]} \tag{4.52}$$

where $\mathbf{d}_{il} = (\mathbf{s}_i - \mathbf{s}_l)/\sqrt{N_0}$ and $\mathbf{t} = (t[1], \ldots, t[\tilde{N}])$ is an integration variable.

The capacity of continuous-input continuous-output (memoryless) JFTS fading/shadowing channels can be evaluated based on the capacity formula of the Gaussian channel given in (4.49) by simply weighting the CSNR γ of the Gaussian channel by the probability of encountering the specific CSNR determined by the JFTS fading/shadowing magnitude z i.e. $z\gamma$. Then the resultant capacity value must be averaged, either by integration or summation over the legitimate range of the CSNR given by $z\gamma$, yielding [91],

$$\mathsf{C}_{\mathrm{CCMC}}^{\mathrm{JFTS}} = \mathrm{E}\big[BT\ \log_2(1+z\gamma)\big] \quad \text{[bits/symbol]} \tag{4.53}$$

where the expectation is taken over z. Hence, by substituting (4.5) in (4.53), an integral of the form,

$$\begin{aligned}\mathsf{C}_{\mathrm{CCMC}}^{\mathrm{JFTS}} &= \int_0^{\infty} BT\ \log_2(1+\gamma) f_{\gamma}(\gamma)\mathrm{d}\gamma \quad \text{[bits/symbol]} \\ &= BT\sum_{j=1}^{4}\sum_{h=1}^{20}\frac{b_j\mathcal{R}\tilde{K}\tilde{S}_h}{\overline{\gamma}\ \ln 2}\ e^{-K-S_h}\ \int_0^{\infty}\ln(1+\gamma)\ e^{-\frac{2P_1\tilde{K}\tilde{S}_h\gamma}{r_h^2\overline{\gamma}}}\ D\Big(4\sqrt{KS_h\tilde{K}\tilde{S}_h\gamma/\overline{\gamma}}; S_h, \Delta\mathsf{M}_j\Big)\mathrm{d}\gamma\end{aligned} \tag{4.54}$$

is obtained. By expressing $\ln(1+\gamma) = \sum_{n=1}^{\infty}\frac{1}{n}\big(\frac{\gamma}{1+\gamma}\big)^n$ for $\gamma \geq 0$, and using the infinite series expansion of modified Bessel function, the integral in (4.54) can be solved by using the integral solution from [48] in order to obtain,

$$\begin{aligned}\mathsf{C}_{\mathrm{CCMC}}^{\mathrm{JFTS}} = &\frac{BT}{2\ln 2}\sum_{j=1}^{4}\sum_{h=1}^{20}\frac{b_j\mathcal{R}r_h^2}{2P_1}\ e^{\frac{2P_1\tilde{K}\tilde{S}_h}{r_h^2\overline{\gamma}}-K-S_h}\sum_{\mathsf{k}=0}^{\infty}\frac{1}{\mathsf{k}!}\sum_{v=0}^{\mathsf{k}}\left(\frac{2P_1\tilde{K}\tilde{S}_h}{r_h^2\overline{\gamma}}\right)^{v}\ \Gamma\Big(-v, \frac{2P_1\tilde{K}\tilde{S}_h}{r_h^2\overline{\gamma}}\Big) \\ &\Big[(KS_h(1-\Delta\mathsf{M}_j))^{\mathsf{k}}\ e^{S_h\Delta\mathsf{M}_j} + (KS_h(1+\Delta\mathsf{M}_j))^{\mathsf{k}}\ e^{-S_h\Delta\mathsf{M}_j}\Big]\end{aligned} \tag{4.55}$$

where $\Gamma(\cdot,\cdot)$ is the incomplete Gamma function [48]. The achievable capacity bound derived in (4.55) for a JFTS faded/shadowed channel will be used for analysis of achievable channel capacity using M-ary modulators like coherent M-PSK in Section 4.5. The detailed derivation used for obtaining (4.55) is provided in Appendix C.

4.4.2 Channel Cut-off Rate

The channel cut-off rate $\mathtt{R}_0$ of the communication link is defined as a channel capacity related quantity such that for any $\mathtt{R}_{\mathtt{c}} < \mathtt{R}_0$, it is possible to construct a channel code having a block length $\tilde{n}$ and coding rate of at least $\mathtt{R_c}$ capable of maintaining an average error probability that obeys $P_e(b) \leq 2^{-\tilde{n}(\mathtt{R_0}-\mathtt{R_c})}$. The channel cut-off rate is also used as an analytical bound limiting the bit error ratio performance of various classes of random codes designed for specific channels [64]. Furthermore, $\mathtt{R_0}$ constitutes a lower bound of the channel capacity and it is more straightforward to compute compared to the channel capacity. In general, the cut-off rate associated with M-ary signaling over a fading/shadowing channel in presence of perfect channel magnitude and phase estimates is given by, [92], [93],

$$\mathtt{R_0} \;=\; 2\log_2(M) - \log_2\Bigg(\sum_{i=1}^{M}\sum_{l=1}^{M} C(\mathbf{s}_i, \mathbf{s}_l)\Bigg) \quad \text{[bits/symbol]} \tag{4.56}$$

where $C(\mathbf{s}_i, \mathbf{s}_l)$ is the Chernoff bound on the pairwise error probability expressed as [93],

$$\begin{aligned} C(\mathbf{s}_i, \mathbf{s}_l) \; &= \mathrm{E}_z\bigg[\; e^{-z^2\frac{|\mathbf{d}_{il}|^2}{4}} \bigg] \quad \text{[bits/symbol]} \\ &= \int_0^\infty f_Z(z)\; e^{-z^2\frac{|\mathbf{d}_{il}|^2}{4}} \mathrm{d}z \quad \text{[bits/symbol]} \end{aligned} \tag{4.57}$$

where $f_Z(z)$ is the channel envelope PDF and $|\mathbf{d}_{il}|^2 = |\mathbf{s}_i - \mathbf{s}_l|^2/N_0$. For a JFTS channel, the Chernoff bound can be calculated using the integral solution form [48] and can be obtained as,

$$\begin{aligned} C(\mathbf{s}_i, \mathbf{s}_l) \; &= \sum_{j=1}^{4}\sum_{h=1}^{20} \frac{b_j \mathcal{R}}{2P_1P_2}\; e^{-K-S_h} \int_0^\infty z\; e^{-\frac{z^2}{2P_2 r_h^2} - z^2\frac{|\mathbf{d}_{il}|^2}{4}} \\ &\quad \Big[e^{S_h \Delta \mathsf{M}_j}\; I_0\big(4z\sqrt{KS_h(1-\Delta\mathsf{M}_j)/P_1P_2}\big) + e^{-S_h\Delta\mathsf{M}_j}\; I_0\big(4z\sqrt{KS_h(1+\Delta\mathsf{M}_j)/P_1P_2}\big) \Big] \mathrm{d}z \\ &= \sum_{j=1}^{4}\sum_{h=1}^{20} \frac{b_j \mathcal{R} r_h^2\; e^{-K-S_h}}{P_1(2+|\mathbf{d}_{il}|^2P_2r_h^2)} \left[e^{S_h\Delta\mathsf{M}_j + \frac{8KS_h(1-\Delta\mathsf{M}_j)r_h^2}{P_1(4+|\mathbf{d}_{il}|^2P_2r_h^2)}} \;+\; e^{-S_h\Delta\mathsf{M}_j + \frac{8KS_h(1+\Delta\mathsf{M}_j)r_h^2}{P_1(4+|\mathbf{d}_{il}|^2P_2r_h^2)}} \right] \text{[bits/symbol]}. \end{aligned} \tag{4.58}$$

Note that (4.58) will be applied in Section 4.5 for computation of the cut-off rate for a range of M-ary digital signaling sets, when communicating over a JFTS faded/shadowed channel.

4.4.3 **Bandwidth Efficiency**

The capacity analysis of the CCMC provided in Subsection 4.4.3 determines the maximum number of information bits conveyed per transmission symbol, as a function of the received CSNR. The system's bandwidth efficiency may be expressed as the capacity $\mathtt{C}$ normalized by the product of the bandwidth B occupied and the symbol period T, given by,

$$\eta \;=\; \frac{\mathtt{C}}{BT} \quad \text{[bits/s/Hz]} \tag{4.59}$$

where the associated unit is bits/s/Hz. The bandwidth efficiency of the CCMC can be expressed as,

$$\eta_{\text{CCMC}} \;=\; \frac{\mathtt{C}_{\text{CCMC}}}{BT} \quad \text{[bits/s/Hz]} \tag{4.60}$$

and therefore for a JFTS faded/shadowed channel can be obtained from (4.55) as,

$$\begin{aligned}\eta_{\text{CCMC}}^{\text{JFTS}} \;=\; \eta_{\text{JFTS}} \;=\; & \frac{1}{2\ln 2}\sum_{j=1}^{4}\sum_{h=1}^{20}\frac{b_j\mathcal{R}r_h^2}{2P_1}\; e^{\frac{2P_1\tilde{K}\tilde{S}_h\gamma}{r_h^2\overline{\gamma}}-K-S_h}\sum_{\mathsf{k}=0}^{\infty}\frac{1}{\mathsf{k}!}\sum_{v=0}^{\mathsf{k}}\left(\frac{2P_1\tilde{K}\tilde{S}_h\gamma}{r_h^2\overline{\gamma}}\right)^{v}\Gamma\left(-v,\frac{2P_1\tilde{K}\tilde{S}_h\gamma}{r_h^2\overline{\gamma}}\right)\\ & \left[(KS_h(1-\Delta\mathsf{M}_j))^{\mathsf{k}}\; e^{S_h\Delta\mathsf{M}_j}+(KS_h(1+\Delta\mathsf{M}_j))^{\mathsf{k}}\; e^{-S_h\Delta\mathsf{M}_j}\right] \quad \text{[bits/s/Hz]}\end{aligned} \tag{4.61}$$

The bandwidth efficiency of CCMC can be referred to as the normalized unrestricted bound. However the computation of the capacity according to (4.61) requires the evaluation of an infinite series. To efficiently evaluate the series, the series in (4.61) will be truncated and the lower and upper bounds for η_{JFTS} and for the truncation error will be derived.

The bandwidth efficiency in (4.61) can be written as $\eta_{\text{JFTS}} = \eta_{\varpi\text{JFTS}} + \eta_{\epsilon\text{JFTS}}$, where $\eta_{\varpi\text{JFTS}}$ is the expression in (4.61) with the infinite series truncated at $\mathsf{k} = \varpi$ and can be expressed as,

$$\eta_{\varpi\text{JFTS}} = \frac{1}{2\ln 2} \sum_{j=1}^{4} \sum_{h=1}^{20} \frac{b_j \mathcal{R} r_h^2}{2P_1} \, e^{\frac{2P_1 \tilde{K}\tilde{S}_h \gamma}{r_h^2 \overline{\gamma}} - K - S_h} \sum_{\mathsf{k}=0}^{\varpi} \frac{1}{\mathsf{k}!} \sum_{v=0}^{\mathsf{k}} \left(\frac{2P_1 \tilde{K}\tilde{S}_h \gamma}{r_h^2 \overline{\gamma}} \right)^v \Gamma\left(-v, \frac{2P_1 \tilde{K}\tilde{S}_h \gamma}{r_h^2 \overline{\gamma}} \right)$$
$$\left[(KS_h(1-\Delta\mathsf{M}_j))^{\mathsf{k}} \, e^{S_h \Delta\mathsf{M}_j} + (KS_h(1+\Delta\mathsf{M}_j))^{\mathsf{k}} \, e^{-S_h \Delta\mathsf{M}_j} \right] \quad \text{[bits/s/Hz]} \qquad (4.62)$$

and $\eta_{\epsilon\text{JFTS}}$ is the associated truncation error resulting from truncating the infinite series in (4.61).

Lower Bound :

The lower bound for η_{JFTS} can be derived by using the relationship between the expression for η_{JFTS} in (4.61) and the area under the PDF of the received CSNR, γ, $f_\gamma(\gamma)$ given by (4.5). The first observation that can be made from (4.5) is that,

$$\tilde{P}_{\text{JFTS}} = e^{-K-S_h} \sum_{\mathsf{k}=0}^{\infty} \frac{1}{2\mathsf{k}!} \left[(KS_h(1-\Delta\mathsf{M}_j))^{\mathsf{k}} \, e^{S_h \Delta\mathsf{M}_j} + (KS_h(1+\Delta\mathsf{M}_j))^{\mathsf{k}} \, e^{-S_h \Delta\mathsf{M}_j} \right] = 1 \qquad (4.63)$$

where $\tilde{P}_{\text{JFTS}}$ is the area under the PDF in (4.5). Let,

$$\tilde{P}_{(\varpi-1)\text{JFTS}} = e^{-K-S_h} \sum_{\mathsf{k}=0}^{\varpi-1} \frac{1}{2\mathsf{k}!} \left[(KS_h(1-\Delta\mathsf{M}_j))^{\mathsf{k}} \, e^{S_h \Delta\mathsf{M}_j} + (KS_h(1+\Delta\mathsf{M}_j))^{\mathsf{k}} \, e^{-S_h \Delta\mathsf{M}_j} \right] \qquad (4.64)$$

be the sum of the series in (4.63) from $\mathsf{k} = 0$ to $\mathsf{k} = \varpi - 1$ and let,

$$\partial\tilde{P}_{(\varpi-1)\text{JFTS}} = e^{-K-S_h} \frac{1}{2\varpi!} \left[(KS_h(1-\Delta\mathsf{M}_j))^{\varpi} \, e^{S_h \Delta\mathsf{M}_j} + (KS_h(1+\Delta\mathsf{M}_j))^{\varpi} \, e^{-S_h \Delta\mathsf{M}_j} \right] \qquad (4.65)$$

be the contribution from the next term corresponding to $\mathsf{k} = \varpi$, then $\tilde{P}_{\varpi\text{JFTS}} = \tilde{P}_{(\varpi-1)\text{JFTS}} + \partial\tilde{P}_{(\varpi-1)\text{JFTS}}$. Similarly, from (4.61), let,

$$\eta_{(\varpi-1)\text{JFTS}} = \frac{1}{2\ln 2} \sum_{j=1}^{4} \sum_{h=1}^{20} \frac{b_j \mathcal{R} r_h^2}{2P_1} \, e^{\frac{2P_1 \tilde{K}\tilde{S}_h}{r_h^2 \overline{\gamma}} - K - S_h} \sum_{\mathsf{k}=0}^{\varpi-1} \frac{1}{\mathsf{k}!} \sum_{v=0}^{\mathsf{k}} \left(\frac{2P_1 \tilde{K}\tilde{S}_h}{r_h^2 \overline{\gamma}} \right)^v \Gamma\left(-v, \frac{2P_1 \tilde{K}\tilde{S}_h}{r_h^2 \overline{\gamma}} \right)$$
$$\left[(KS_h(1-\Delta\mathsf{M}_j))^{\mathsf{k}} \, e^{S_h \Delta\mathsf{M}_j} + (KS_h(1+\Delta\mathsf{M}_j))^{\mathsf{k}} \, e^{-S_h \Delta\mathsf{M}_j} \right] \quad \text{[bits/s/Hz]} \qquad (4.66)$$

and,

$$\partial\eta_{(\varpi-1)\text{JFTS}} = \frac{1}{2\varpi!\ln 2}\sum_{j=1}^{4}\sum_{h=1}^{20}\frac{b_j\mathcal{R}r_h^2}{2P_1}\; e^{\frac{2P_1\tilde{K}\tilde{S}_h}{r_h^2\overline{\gamma}}-K-S_h}\sum_{v=0}^{\mathsf{k}}\left(\frac{2P_1\tilde{K}\tilde{S}_h}{r_h^2\overline{\gamma}}\right)^v\Gamma\left(-v,\frac{2P_1\tilde{K}\tilde{S}_h}{r_h^2\overline{\gamma}}\right)$$
$$\left[(KS_h(1-\Delta\mathsf{M}_j))^{\varpi}\; e^{S_h\Delta\mathsf{M}_j}+(KS_h(1+\Delta\mathsf{M}_j))^{\varpi}\; e^{-S_h\Delta\mathsf{M}_j}\right] \quad \text{[bits/s/Hz]} \quad (4.67)$$

be the corresponding values with respect to η_{JFTS}, such that $\eta_{\varpi\text{JFTS}} = \eta_{(\varpi-1)\text{JFTS}} + \partial\eta_{(\varpi-1)\text{JFTS}}$. Dividing (4.67) by (4.65) yields,

$$\frac{\partial\eta_{(\varpi-1)\text{JFTS}}}{\partial\tilde{P}_{(\varpi-1)\text{JFTS}}} = \frac{1}{\ln 2}\sum_{j=1}^{4}\sum_{h=1}^{20}\frac{b_j\mathcal{R}r_h^2}{2P_1}\; e^{\frac{2P_1\tilde{K}\tilde{S}_h}{r_h^2\overline{\gamma}}}\sum_{v=0}^{\mathsf{k}}\left(\frac{2P_1\tilde{K}\tilde{S}_h}{r_h^2\overline{\gamma}}\right)^v\Gamma\left(-v,\frac{2P_1\tilde{K}\tilde{S}_h}{r_h^2\overline{\gamma}}\right) \quad \text{[bits/s/Hz]} \quad (4.68)$$

Observing that $\frac{\partial\eta_{(\varpi-1)\text{JFTS}}}{\partial\tilde{P}_{(\varpi-1)\text{JFTS}}}$ monotonically increases with increasing ϖ, that is,

$$\frac{\partial\eta_{\mathsf{r}\text{JFTS}}}{\partial\tilde{P}_{\mathsf{r}\text{JFTS}}} > \frac{\partial\eta_{(\varpi-1)\text{JFTS}}}{\partial\tilde{P}_{(\varpi-1)\text{JFTS}}} \qquad \text{for} \;\; \mathsf{r}\geq\varpi \quad (4.69)$$

then,

$$\sum_{\mathsf{r}=\varpi}^{\infty}\partial\eta_{\mathsf{r}\text{JFTS}} > \frac{\partial\eta_{(\varpi-1)\text{JFTS}}}{\partial\tilde{P}_{(\varpi-1)\text{JFTS}}}\sum_{\mathsf{r}=\varpi}^{\infty}\partial\tilde{P}_{\mathsf{r}\text{JFTS}} = \frac{\partial\eta_{(\varpi-1)\text{JFTS}}}{\partial\tilde{P}_{(\varpi-1)\text{JFTS}}}\left(1-\tilde{P}_{\varpi\text{JFTS}}\right) \quad (4.70)$$

Thus η_{JFTS} can be lower bounded by using (4.61) and (4.70) as $\eta_{\text{JFTS}} > \eta_{\varpi\text{JFTS}} + \eta_{\epsilon-\text{LowJFTS}}$, where $\eta_{\epsilon-\text{LowJFTS}}$ is the lower bound for $\eta_{\epsilon\text{JFTS}}$ and can be expressed as,

$$\eta_{\epsilon-\text{LowJFTS}} = \frac{\partial\eta_{(\varpi-1)\text{JFTS}}}{\partial\tilde{P}_{(\varpi-1)\text{JFTS}}}\times\Bigg(1-\; e^{-K-S_h}\sum_{\mathsf{k}=0}^{\varpi}\frac{1}{2\mathsf{k}!}$$
$$\left[(KS_h(1-\Delta\mathsf{M}_j))^{\mathsf{k}}\; e^{S_h\Delta\mathsf{M}_j}+(KS_h(1+\Delta\mathsf{M}_j))^{\mathsf{k}}\; e^{-S_h\Delta\mathsf{M}_j}\right]\Bigg) \quad \text{[bits/s/Hz]} \quad (4.71)$$

Upper Bound :

For deriving the upper bound for the bandwidth efficiency achievable over a JFTS faded/shadowed communication link, let (4.61) be expressed as,

$$\begin{aligned}
\eta_{\mathrm{JFTS}} &= \frac{1}{2\ln 2}\sum_{j=1}^{4}\sum_{h=1}^{20}\frac{b_j\mathcal{R}\tilde{K}\tilde{S}_h}{\overline{\gamma}}\ e^{-K-S_h}\int_0^\infty \ln(1+\gamma)\ e^{-\frac{2P_1\tilde{K}\tilde{S}_h\gamma}{r_h^2\overline{\gamma}}} \\
&\times\left(\sum_{\mathsf{k}=0}^{\varpi}\frac{1}{(\mathsf{k}!)^2}\left[e^{S_h\Delta\mathsf{M}_j}\ \left(\frac{2P_1KS_h\tilde{K}\tilde{S}_h(1-\Delta\mathsf{M}_j)\gamma}{r_h^2\overline{\gamma}}\right)^{\mathsf{k}}+e^{-S_h\Delta\mathsf{M}_j}\ \left(\frac{2P_1KS_h\tilde{K}\tilde{S}_h(1+\Delta\mathsf{M}_j)\gamma}{r_h^2\overline{\gamma}}\right)^{\mathsf{k}}\right]\right. \\
&+\left.\sum_{\mathsf{k}=\varpi+1}^{\infty}\frac{1}{(\mathsf{k}!)^2}\left[e^{S_h\Delta\mathsf{M}_j}\ \left(\frac{2P_1KS_h\tilde{K}\tilde{S}_h(1-\Delta\mathsf{M}_j)\gamma}{r_h^2\overline{\gamma}}\right)^{\mathsf{k}}+e^{-S_h\Delta\mathsf{M}_j}\ \left(\frac{2P_1KS_h\tilde{K}\tilde{S}_h(1+\Delta\mathsf{M}_j)\gamma}{r_h^2\overline{\gamma}}\right)^{\mathsf{k}}\right]\right)\mathrm{d}\gamma \\
&\qquad [\text{bits/s/Hz}] \qquad (4.72)
\end{aligned}$$

Let us denote,

$$\mathsf{C}_{\varpi} = \sum_{\mathsf{k}=0}^{\varpi}\frac{1}{(\mathsf{k}!)^2}\left[e^{S_h\Delta\mathsf{M}_j}\ \left(\frac{2P_1KS_h\tilde{K}\tilde{S}_h(1-\Delta\mathsf{M}_j)}{r_h^2\overline{\gamma}}\right)^{\mathsf{k}}+e^{-S_h\Delta\mathsf{M}_j}\ \left(\frac{2P_1KS_h\tilde{K}\tilde{S}_h(1+\Delta\mathsf{M}_j)}{r_h^2\overline{\gamma}}\right)^{\mathsf{k}}\right] \qquad (4.73)$$

and

$$\mathsf{C}_{\mathsf{R}} = \sum_{\mathsf{k}=\varpi+1}^{\infty}\frac{1}{(\mathsf{k}!)^2}\left[e^{S_h\Delta\mathsf{M}_j}\ \left(\frac{2P_1KS_h\tilde{K}\tilde{S}_h(1-\Delta\mathsf{M}_j)}{r_h^2\overline{\gamma}}\right)^{\mathsf{k}}+e^{-S_h\Delta\mathsf{M}_j}\ \left(\frac{2P_1KS_h\tilde{K}\tilde{S}_h(1+\Delta\mathsf{M}_j)}{r_h^2\overline{\gamma}}\right)^{\mathsf{k}}\right] \qquad (4.74)$$

Therefore, $\eta_{\epsilon\mathrm{JFTS}}$ can be expressed as,

$$\eta_{\epsilon\mathrm{JFTS}} = \frac{1}{2\ln 2}\sum_{j=1}^{4}\sum_{h=1}^{20}\frac{b_j\mathcal{R}\tilde{K}\tilde{S}_h}{\overline{\gamma}}\ e^{-K-S_h}\int_0^\infty \ln(1+\gamma)\ e^{-\frac{2P_1\tilde{K}\tilde{S}_h\gamma}{r_h^2\overline{\gamma}}}\ \mathsf{C}_{\mathsf{R}}\mathrm{d}\gamma \quad [\text{bits/s/Hz}] \qquad (4.75)$$

where C_{R} is presented in (4.74). Noting that $\mathsf{k}!$ in C_{R} can be written as [39],

$$\mathsf{k}! = \sqrt{2\pi\mathsf{k}}\ \mathsf{k}^{\mathsf{k}}\ e^{-\mathsf{k}+\tilde{\theta}/12\mathsf{k}} \quad \text{for} \quad \mathsf{k}>0, 0<\tilde{\theta}<1 \qquad (4.76)$$

and substituting (4.76) into (4.72) and after some manipulations, $\mathsf{C_R}$ can be upper bounded by,

$$\mathsf{C_R} \; < \; \sum_{\mathsf{k}=\varpi+1}^{\infty} \frac{(\varpi+1)^{-\mathsf{k}} \; e^{\mathsf{k}}}{\mathsf{k}!\sqrt{2\pi(\varpi+1)}}\Bigg[e^{S_h \Delta \mathsf{M}_j} \; \left(\frac{2P_1 K S_h \tilde{K}\tilde{S}_h(1-\Delta \mathsf{M}_j)}{r_h^2\overline{\gamma}}\right)^{\mathsf{k}} + \; e^{-S_h \Delta \mathsf{M}_j} \; \left(\frac{2P_1 K S_h \tilde{K}\tilde{S}_h(1+\Delta \mathsf{M}_j)}{r_h^2\overline{\gamma}}\right)^{\mathsf{k}}\Bigg] \tag{4.77}$$

and hence can be calculated as,

$$\mathsf{C_R} \; = \frac{1}{\sqrt{2\pi(\varpi+1)}}\Bigg(e^{S_h\Delta\mathsf{M}_j + \frac{2P_1 e K S_h \tilde{K}\tilde{S}_h(1-\Delta\mathsf{M}_j)}{(\varpi+1)r_h^2\overline{\gamma}}} + e^{-S_h\Delta\mathsf{M}_j + \frac{2P_1 e K S_h \tilde{K}\tilde{S}_h(1+\Delta\mathsf{M}_j)}{(\varpi+1)r_h^2\overline{\gamma}}} - \sum_{\mathsf{k}=0}^{\varpi}\frac{1}{\mathsf{k}!} \Bigg[e^{S_h \Delta \mathsf{M}_j} \; \left(\frac{2P_1 e K S_h \tilde{K}\tilde{S}_h(1-\Delta \mathsf{M}_j)}{(\varpi+1)r_h^2\overline{\gamma}}\right)^{\mathsf{k}} + e^{-S_h \Delta \mathsf{M}_j} \; \left(\frac{2P_1 e K S_h \tilde{K}\tilde{S}_h(1+\Delta \mathsf{M}_j)}{(\varpi+1)r_h^2\overline{\gamma}}\right)^{\mathsf{k}}\Bigg]\Bigg) \tag{4.78}$$

After substituting (4.78) into (4.75) and evaluating the integrals by using partial integration followed by some mathematical manipulations, the upper bound for η_{JFTS} can be obtained as,

$$\eta_{\epsilon-\mathrm{UpJFTS}} \; = \; \sum_{j=1}^{4}\sum_{h=1}^{20}\frac{b_j \mathcal{R} \; e^{(1-K)(1-S_h)-1}}{2\ln 2(\varpi+1)}\sqrt{\frac{\varpi+1}{2\pi}}\Bigg[\frac{\varpi+1}{\varpi+1-KS_h e}\Bigg(e^{S_h\Delta\mathsf{M}_j + \frac{2P_1\tilde{K}\tilde{S}_h(\varpi+1-KS_h e(1-\Delta\mathsf{M}_j))}{(\varpi+1)r_h^2\overline{\gamma}}} + \; e^{-S_h\Delta\mathsf{M}_j + \frac{2P_1\tilde{K}\tilde{S}_h(\varpi+1-KS_h e(1+\Delta\mathsf{M}_j))}{(\varpi+1)r_h^2\overline{\gamma}}}\Bigg) \; - \; e^{\frac{2P_1\tilde{K}\tilde{S}_h}{r_h^2\overline{\gamma}}}\sum_{\mathsf{k}=0}^{\varpi}\sum_{v=0}^{\mathsf{k}}\left(\frac{2P_1\tilde{K}\tilde{S}_h}{r_h^2\overline{\gamma}}\right)^{v}\Gamma\Bigg(-v, \frac{2P_1\tilde{K}\tilde{S}_h}{r_h^2\overline{\gamma}}\Bigg) \Bigg(e^{S_h\Delta\mathsf{M}_j}\left(\frac{KS_h e(1-\Delta\mathsf{M}_j)}{\varpi+1}\right)^{\mathsf{k}} + \; e^{-S_h\Delta\mathsf{M}_j}\left(\frac{KS_h e(1+\Delta\mathsf{M}_j)}{\varpi+1}\right)^{\mathsf{k}}\Bigg)\Bigg] \tag{4.79}$$

Thus, ϖ can be chosen such that $KS_h e(1-\Delta\mathsf{M}_j)-1$ and $KS_h e(1+\Delta\mathsf{M}_j)-1$ satisfy any desired accuracy level. Combining (4.62) and (4.79) yields the upper bound for the expression in (4.61) as $\eta_{\mathrm{JFTS}} < \eta_{\varpi\mathrm{JFTS}} + \eta_{\epsilon-\mathrm{UpJFTS}}$. Finally from (4.71) and (4.79), $\eta_{\epsilon\mathrm{JFTS}}$ can be bounded by,

$$\eta_{\epsilon-\mathrm{UpJFTS}} > \eta_{\epsilon\mathrm{JFTS}} > \eta_{\epsilon-\mathrm{LowJFTS}} \tag{4.80}$$

Using (4.71) and (4.80), $\eta_{\varpi\mathrm{JFTS}}$ can be evaluated at different truncation levels for different JFTS parameters. The truncation error bounds for each set of JFTS parameters can also be calculated.

4.5 Numerical Results and Discussion

In this section, The derived analytical expressions for error probability performance and channel capacity of coherent/non-coherent binary modulation techniques like BPSK and BFSK, general order M-QAM snd coherently detected M-PSK are numerically evaluated and plotted as functions of the parameters of the communication channel model with and without iterative and non-iterative FEC coding techniques. The analytical results are compared with the simulation results in order to verify the validity of the derived expressions. The parameters of the JFTS channel model are also varied in order to demonstrate how the channel model influences system performance. For the simulation results, Monte Carlo simulation has been used in MATLAB to generate the modulated symbols, codewords, AWGN and JFTS random variables using the JFTS PDF of (2.20)).

The wireless communication channel between the transmitter and the receiver is assumed to be suffering from AWGN and the composite fading/shadowing envelope is JFTS distributed, where all the channel samples are statistically independent. All the analytical and simulation results are evaluated using a single input single output (SISO) system and are averaged over 100 independent random channel realizations. All the error probability performances and capacity analyses are plotted as functions of the average received CSNR per bit, E_b/N_0 in dBs.

The rest of this section is organized as follows. Subsection 4.5.1 and 4.5.2 illustrate the effects of the modulation parameters like constellation size and the coding parameters like code length and rate on the performance of different fixed modulation and coding techniques over a JFTS faded/shadowed link respectively. Subsection 4.5.3 demonstrates the effect of the JFTS parameters on the error rates, channel capacities and bandwidth efficiencies. Finally Subsection 4.5.4 exhibits

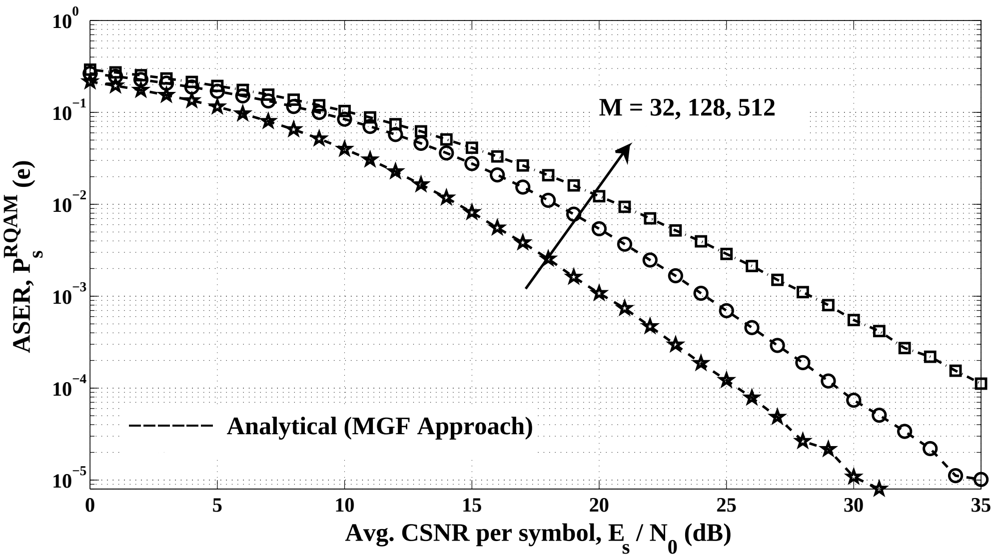

Figure 4.1: Comparative average symbol error rate performances of RQAM, where the curves are generated by varying the size of QAM constellation ($M = 32, 128, 512$) over JFTS faded/shadowed communication link with fixed set of parameters, $K = 5$ dB, $S_h = -6$ dB and $\Delta = 0.5$.

how JFTS channel performance compares to more conventional channel models.

4.5.1 Effect of Modulation Techniques and Parameters

The first set of curves in Fig. 4.1 are generated for evaluating the ASER performance of general order M-QAM over a JFTS fading/shadowing communication channel, where the plots are generated by varying the constellation size M. Both analytical and simulation results are plotted for each M, where the analytical results are computed using the MGF approach. The JFTS parameters, K, S_h and Δ are fixed at 5 dB, - 6 dB and 0.5 respectively. This set of parameters are encountered when the mobile WLAN user and the access point are separated by 2 - 3 sets of partitions are tabulated in Chapter 3. It is evident that the derived analytical results from (4.17) offer a good agreement with that of the simulation results. For this set of curves, three values of M are considered, $M = 32, 128, 512$. It is evident that error performance degrades with the increase in M. How-

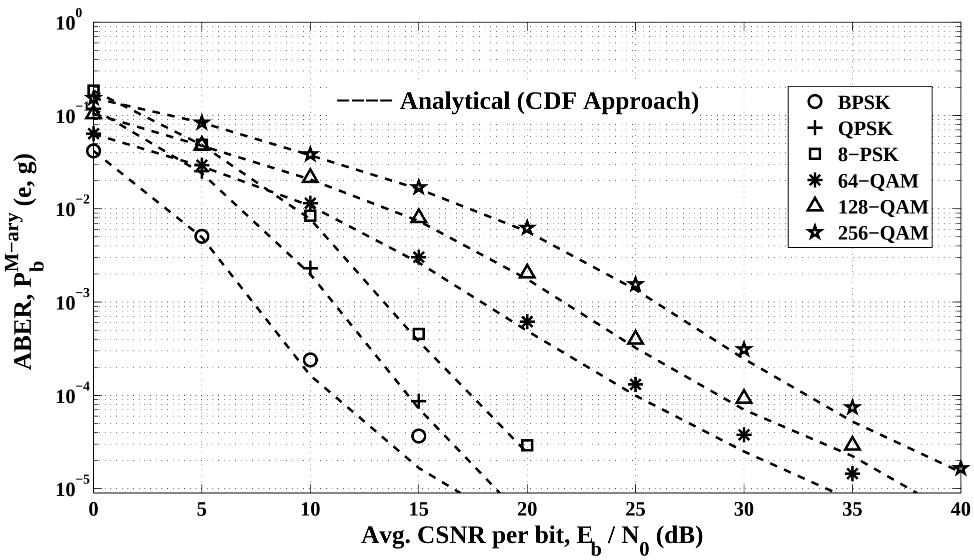

Figure 4.2: Comparative simulation and analytical average bit error rate performances of coherent M-PSK and M-QAM over a JFTS faded / shadowed communication link, where the curves are generated for a fixed set of JFTS parameters, with $K = 6.5$ dB, $S_h = 3$ dB and $\Delta = 0.8$.

ever, this degradation gradually reduces with the increase in M, for a fixed set of JFTS parameters.

The next set of curves in Fig. 4.2 are generated for comparing analytical results with simulation results for different modulation techniques, where the analytical results are computed using the CDF-based approach. For this ste of curves, JFTS parameters are kept fixed at $K = 6.5$ dB, $S_h = 3$ dB and $\Delta = 0.8$. This set of parameters are encountered when the user and the access point are separated by 1 set of dry-wall or partition. It is evident from Fig. 4.2 that the derived analytical results from (4.26) and (4.28) offer a good agreement with that of the simulation results and they fall within 1 - 2 dB of the simulation results.

It is to be noted here that like in case of the MGF approach, the analytical results using the CDF

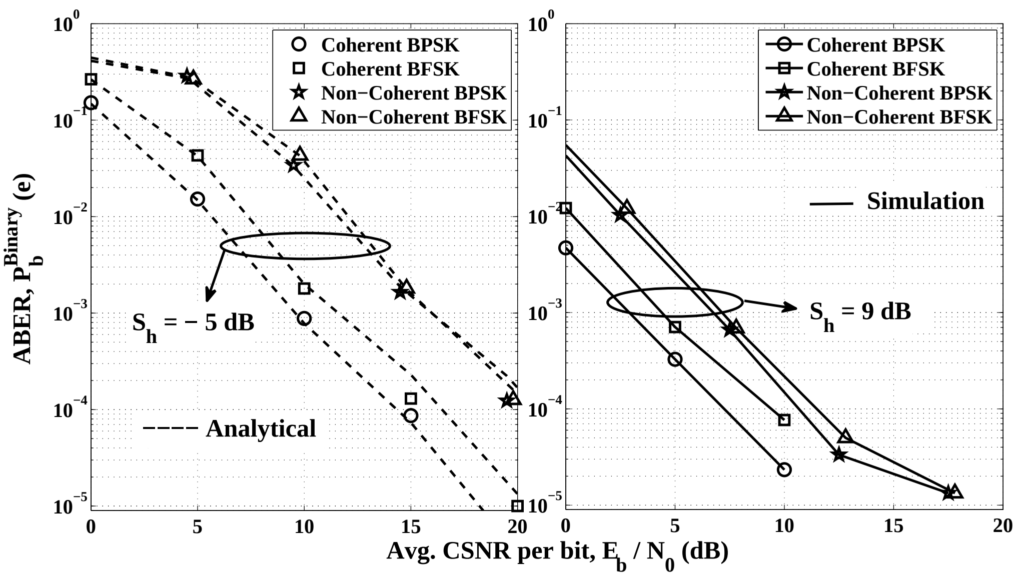

Figure 4.3: Comparative simulation and analytical average bit error rate performances of coherent BPSK and BFSK with that of non-coherent BPSK and BFSK over JFTS faded/shadowed communication link with fixed $K = 5$ dB and $\Delta = 0.7$ but two different S_h of 9 dB and - 5 dB.

approach do not exactly match the simulation results as the analytical expressions contain the approximation index m. For this analysis, $\mathsf{m} = 20$ is used. Increasing m further will provide a better approximation of the error probability performances. However, only a nominal improvement in approximation can be achieved for a large increase of m for $\mathsf{m} > 20$ thereby making the expressions computationally complex.

Comparison of ABER performances between binary modulation techniques like coherent and non-coherent BPSK and BFSK is presented in Fig. 4.3. Two sets of JFTS parameters are selected. For the first set of curves, K, S_h and Δ are kept fixed at 5 dB, 9 dB and 0.7 respectively. These set of parameters typically represent a scenario where both the user and the access point are in the same room.

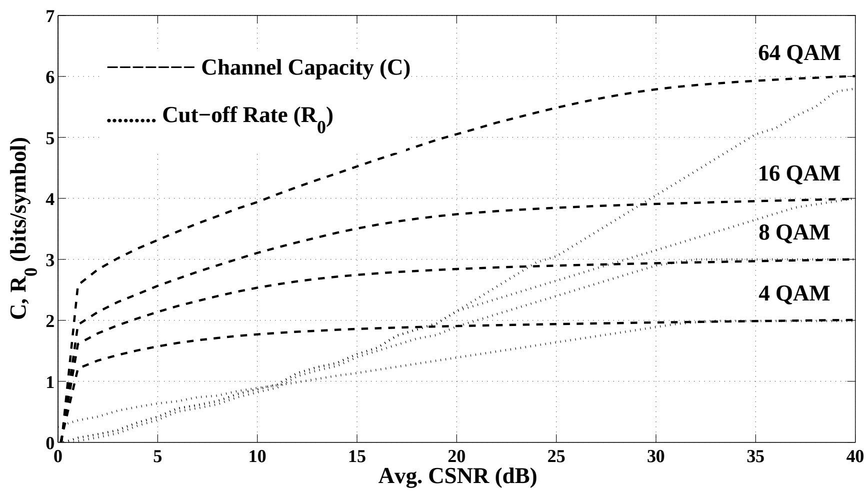

Figure 4.4: Achievable channel capacity and cut-off rate of M-QAM when communicating over a JFTS faded/shadowed communication link with $K = 8$ dB, $S_h = 8.5$ dB and $\Delta = 0.45$, where the curves are generated by varying the constellation size M.

When $S_h = 9$ dB, the performance difference between non-coherent BPSK and BFSK degrades between 2 dB and 3 dB relative to the corresponding coherent schemes. This is roughly consistent with the results seen over standard Rayleigh or Nakagami-m channels. However, this changes when S_h drops to - 9 dB. When this occurs, non-coherent binary modulation techniques suffer an extra penalty of 2 - 3 dB from the coherent ones resulting in total non-coherent performance degradation of 7 - 8 dB, as is evident from the second set of curves. A value of $S_= -9$ dB represents a scenario when the user and the access point are separated by more than 3 partitions. A low S_h-factor combined with a low K value resulted in severe fading and shadowing statistics yielding a larger degradation in performance for non-coherent techniques in comparison to traditional small scale fading channels.

Fig. 4.4 and Fig. 4.5 show the achievable capacity, cut-off rate and bandwidth efficiency of the family of M-QAM signals when communicating over JFTS fading/shadowing channel with $K = 8$ dB, $S_h = 8.5$ dB and $\Delta = 0.45$. It is evident from Fig. 4.4 and Fig. 4.5 that in order to achieve a capacity of b bits/symbol, it is better to employ 2^{b+1}-ary QAM, rather than the QAM scheme having $M = 2^b$ or $M > 2^{b+1}$. Explicitly, by doubling M from 2^b to 2^{b+1}, most of the achievable capacity gain may be obtained when aiming for a capacity of $\mathtt{C} = b$ bits/symbol. For example, as evidenced in Fig. 4.4, the CSNR required for 4-QAM, 8-QAM, 16-QAM and 64-QAM is about 25 dB, 5 dB, 2dB and 2 dB respectively when communicating over JFTS channels at a capacity of $b = 2$ bits/symbol.

4.5.2 Effect of Coding Techniques and Parameters

The first three figures in this section are only simulation based, where ABER of coherently detected BPSK is plotted in presence of non-iterative FEC coding techniques like Convolutional and Hamming codes. Fig. 4.6 shows that performance improves at higher CSNR if Hamming codes (HC) and Convolutional codes (CC) are employed at the transmit side. For the sake of comparison, hard-decision decoding (HDD) is used at the receiver side for both the coding techniques. Viterbi Decoding (VD) with no trace back memory is employed for CC and Hamming Decoding (HD) is applied for the HC technique. Using the same generator polynomial, 1/2-rate CC [7, 5] with VD is seem to offer an improvement in performance of around 5 dB and 3 dB in case of HC [7, 4] with HD, for K-factors of 5 dB and 8 dB in the JFTS channels respectively. However, for Rayleigh fading channels, using the same set of conditions, CC offers only a minor improvement of around 0.5 dB over HC.

Improvement in performance at higher CSNR can be achieved by employing HC and CC at the

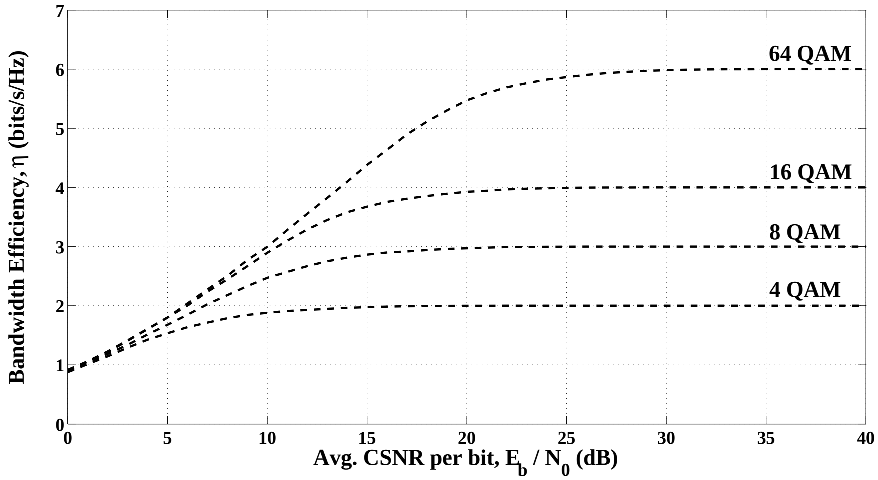

Figure 4.5: Achievable bandwidth efficiency of M-QAM when communicating over a JFTS faded/shadowed communication link with $K = 8$ dB, $S_h = 8.5$ dB and $\Delta = 0.45$, where the curves are generated by varying the constellation size M.

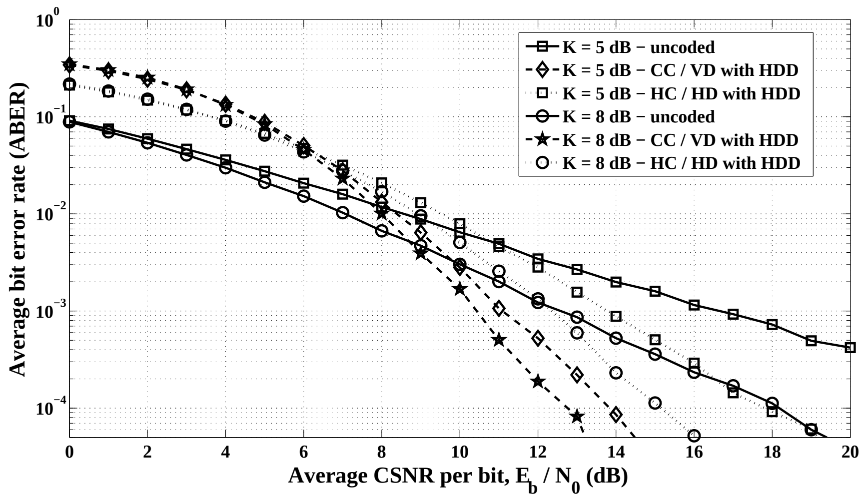

Figure 4.6: Comparative simulated average bit error rate (ABER) performances of BPSK with non-iterative coding technique like Convolutional Coding (1/2-rate, [7, 5] octal) with Hard-Decision Viterbi Decoding and Hamming Coding ([7, 4]) with Hard-Decision Hamming Decoding over JFTS faded / shadowed communication link, where the curves are generated by varying the K-parameter of the JFTS distribution, with fixed $S_h = 2$ dB and fixed $\Delta = 0.3$.

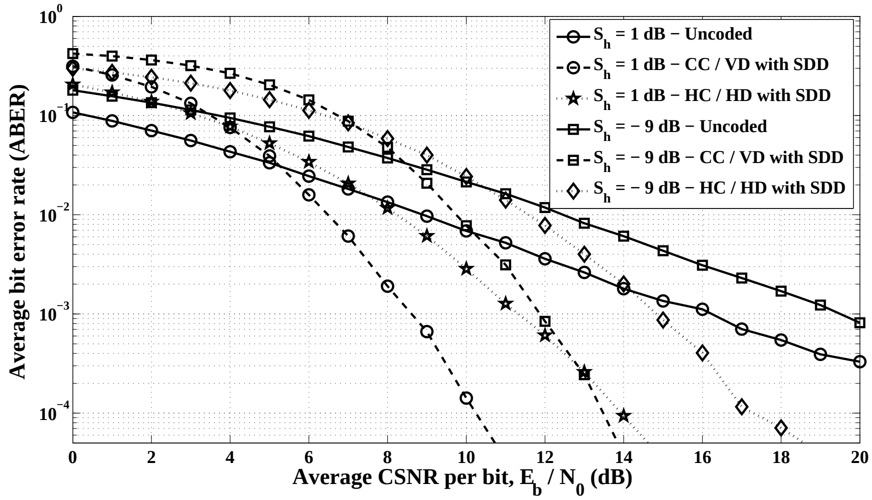

Figure 4.7: Comparative simulated average bit error rate (ABER) performances of BPSK with non-iterative coding technique like Convolutional Coding (1/2-rate, [7, 5] octal) with Soft-Decision Viterbi Decoding and Hamming Coding ([7, 4]) with Soft-Decision Hamming Decoding over JFTS faded / shadowed communication link, where the curves are generated by varying the S_h-parameter of the JFTS distribution, with fixed $K = 6$ dB and fixed $\Delta = 0.8$.

transmit side with soft-decision decoding (SDD) at the receiver side as is evident in Fig. 4.7. Similar to the results in Fig. 4.6, CC with VD is seen to offer around 3 dB improvement in BER performance over HC with HD. This surprising behavior, for both HDD and SDD can be attributed to the statistical characteristics of a JFTS channel, which are quite different from traditional fading channels like Rayleigh, Rician, or Nakagami-m fading channels. Summing up both the results from Fig. 4.6 and Fig. 4.7, it can also be concluded that, for the same set of JFTS parameters, CC offers a considerable enhancement in performance over linear block coding techniques like HC. Fig. 4.8 is used to compare performances of non-iterative coding techniques with HDD and SDD. As expected, each coding technique with SDD offers a 3 dB improvement in performance over HDD for a fixed set of JFTS parameters.

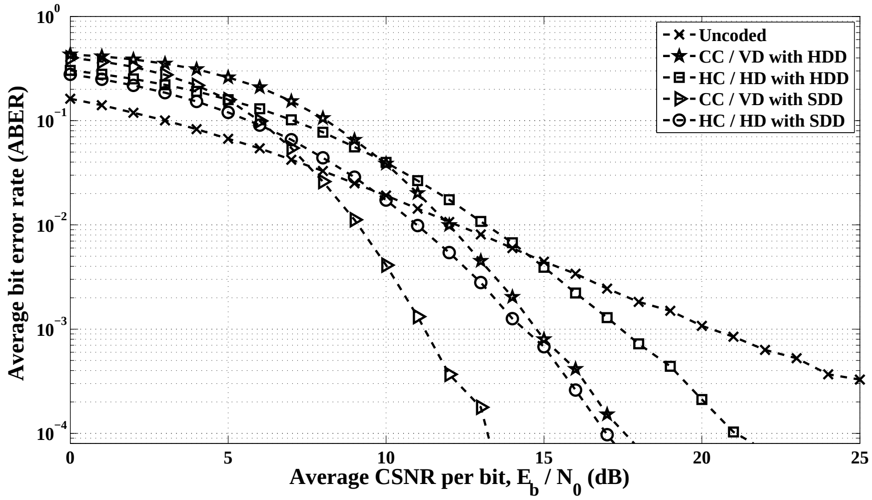

Figure 4.8: Comparative simulated average bit error rate (ABER) performances of BPSK with non-iterative coding technique like Convolutional Coding (1/2-rate, [7, 5] octal) with Hard-Decision and Soft-Decision Viterbi Decoding and Hamming Coding ([7, 4]) with Hard-Decision and Soft-Decision Hamming Decoding over JFTS faded / shadowed communication link, where the curves are generated for fixed JFTS parameters $K = 5$ dB, $S_h = -5$ dB and $\Delta = 0.3$.

The results in Fig. 4.9 are generated by varying the JFTS parameters, K, S_h and Δ. The values for each set of parameters are chosen from the range of their numerical values proposed in Chapter 3, depending on the relative position of the mobile WLAN user and the access point. Fig. 4.9 compares the simulated ABER with the analytical average upper bound for BER, where the exact PEP is calculated using (4.43). For this set of results, the 1/2-rate Turbo coding with a memory of 4 is used with generators (23, 35) and a frame size of $\mathsf{N} = 2 \times 512$ coded bits. It is evident from Fig. 4.9 that the analytical average upper bound for BER tightly approximates the simulated ABER for a broad range of JFTS channel parameter values. However, a minor difference exists between the simulated and the predicted results for lower ABERs. The reason behind this can be attributed to the fact that the analytical bound is truncated after codewords with distances $\delta_1 > 8$.

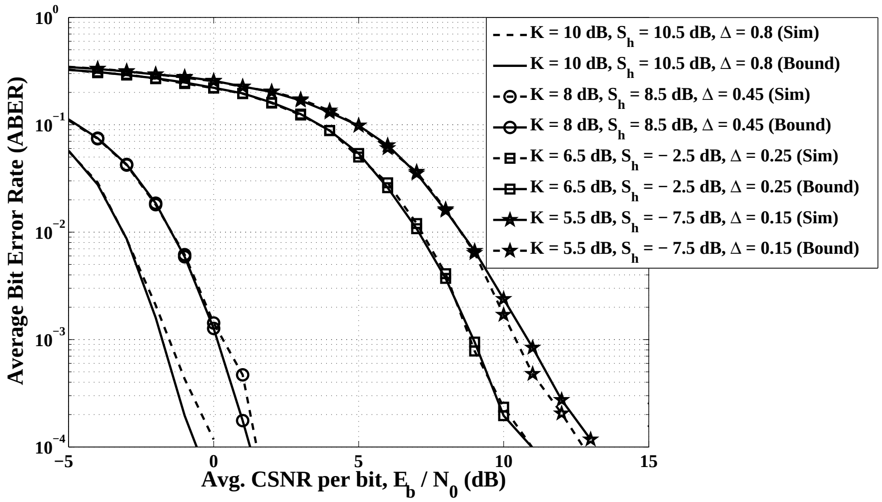

Figure 4.9: Analytical and simulated average bit error rates (ABER) of 1/2-rate TC coded BPSK with code length, $\mathsf{N} = 1024$ over fully interleaved JFTS faded / shadowed communication link, where the curves are generated by varying all the JFTS parameters, K, S_h and Δ simultaneously.

The firsts set of curves in Fig. 4.9 are generated for $K = 10$ dB, $S_h = 10.5$ dB and $\Delta = 0.8$, representing a condition where both the user and the access point are located in the same room. As the user moves to a different room separated by one set of partition or wall form that of the access point, system performance degrades, as exhibited by the second set of curves in Fig. 4.9. In order to achieve an ABER of 10^{-4}, the average CSNR per bit requirement increases by around 1.5 dB. The average CSNR requirement increases even further by around 10 dB if the user and the access point are separated by 2 or 3 sets of partitions. This happens due to the lack of strong specular components and the presence of at least two scattering clusters between the transmitter and the receiver, which jointly deteriorates the overall system performance.

Fig. 4.10 compares the simulated ABER of regular and irregular LDPC coded BPSK with the analytical average BER calculated using GA approach (4.48). For this set of plots, the block

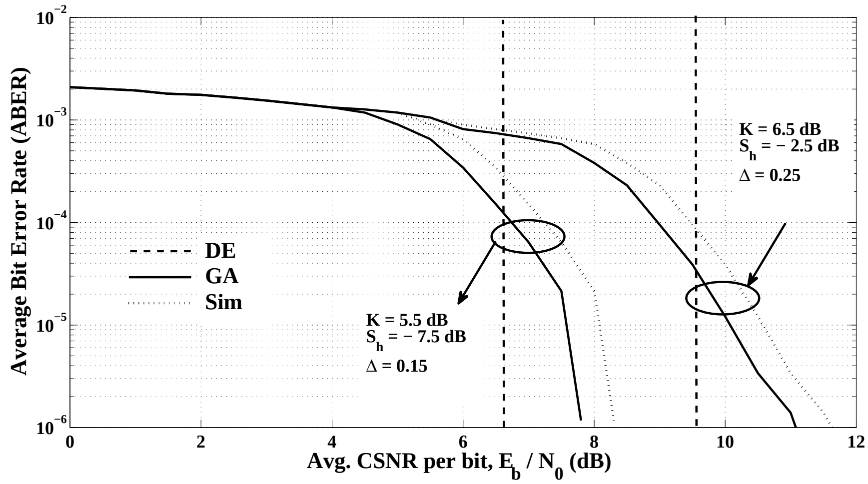

Figure 4.10: Analytical and simulated average bit error rates (ABER) of 1/2-rate LDPC coded BPSK with code length, $\mathsf{N} = 10^4$ over fully interleaved JFTS faded / shadowed communication link, where the curves are generated by varying all the JFTS parameters, K, S_h and Δ simultaneously.

size of the LDPC code is set to 10^4 and the maximum number of iterations for decoding is set to 100. The rate 1/2 (3, 6) regular LDPC code and irregular LDPC code with degree distribution $\overline{\lambda}(\bar{z}) = 0.3321\bar{z} + 0.3307\bar{z}^2 + 0.3372\bar{z}^5$ and $\overline{\rho}(\bar{z}) = 0.982\bar{z}^5 + 0.018\bar{z}^6$ are investigated. For the irregular LDPC code, the degree-two nodes of parity check matrix $\overline{\mathsf{H}}$, corresponding to the non-systematic bits, are constructed to be free of cycles. Furthermore, $\overline{\mathsf{H}}$ is designed to be free of 4-cycles. The CSNR threshold is obtained using DE and it is presented in Fig. 4.10. Here, the CSNR threshold is defined as the smallest CSNR required for the system to obtain a BER of less than 10^{-6}.

It is evident from Fig. 4.10, that the GA results provide a good estimate for the simulated results. The difference between the GA and simulated CSNR to achieve a BER of 10^{-4} is approximately 0.5 - 1 dB. Next it can be observed that the difference between the CSNR threshold of DE and GA is

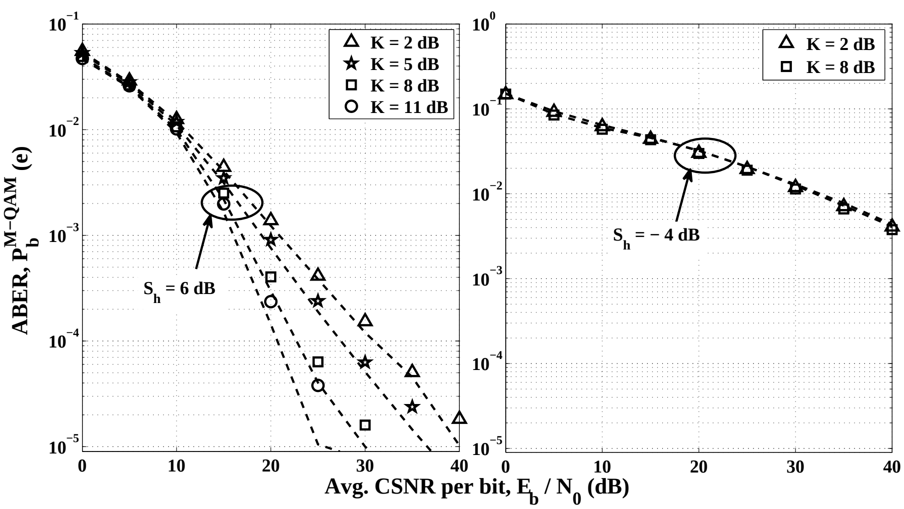

Figure 4.11: Average bit error rate performances of 16-QAM over JFTS faded / shadowed communication link, where the curves are generated by varying the K-parameter of the JFTS distribution, with two sets of fixed S_h, 6 dB and -4 dB and fixed Δ, 0.3 and 0.9 respectively.

around 0.5 - 0.8 dB. The simulation results will approach the DE results when the simulated code length approaches infinity. However, it is not feasible to use an infinite code length in practice. The results obtained using the GA analysis provides a good and fast estimate for the performance of LDPC codes with a practical length. The reason for the mismatch between DE and GA is mainly due to approximating the message densities as Gaussian distributed. The computational complexity of DE is high as it involves tracking the PDFs passing between bit and check nodes, where density updates, transformation of random variables and fast Fourier transformation need to be performed iteratively.

4.5.3 **Effect of JFTS Parameters**

The curves in the first subplot of Fig. 4.11 are generated by varying the K-parameter of the JFTS distribution. The other parameters of the distribution like S_h and Δ are kept constant at 6 dB and 0.3 respectively, representing a condition where the user and the access point are separated by

1 dry-wall or partition. Simulation and analytical ABER performances are plotted for 16-QAM. The performance of 16-QAM deteriorates as the value of K decreases with fixed S_h and Δ. This is due to the fact that as K decreases, the power contributed by the strong specular components decreases in comparison to that contributed by the diffused and scattered components, resulting in degradation of overall system performance.

The improvement in performance due to the increase in K-factor from 2 dB to 5 dB or 5 dB to 8 dB is not proportional to the improvement for increasing K from 8 dB to 11 dB. This is due to the fact that for a JFTS channel, the S_h and Δ parameters also influence the channel behavior. A high S_h factor corresponds to a low severity in shadowing. A low Δ represents a scenario where only one scattering cluster dominates instead of two thereby also resulting in low shadowing severity. Hence, with a high S_h and low Δ coupled with high K-factors, the communication channel approaches the "no fading" scenario. As a result, changing the K-factor from 8 dB to 11 dB does not cause any further improvement in performance.

To emphasize the effect of S_h and Δ, the ABER performance of 16-QAM is plotted for only $K = 2$ dB and 8 dB in the second subplot of Fig. 4.11. In this case, a low S_h-factor of - 4 dB and a high Δ factor of 0.9 is used. This represents a condition where the user and the access point are separated by 2 - 3 partitions. The difference in performance due to increase in K-factor is completely obliterated for this set of shadowing parameters. A low S_h and a high Δ corresponds to a very high severity in shadowing and further degrading fading by a reduction in K does not further degrade performance in any significant way.

Fig. 4.12, is generated by varying the S_h parameter of the JFTS distribution with fixed K and

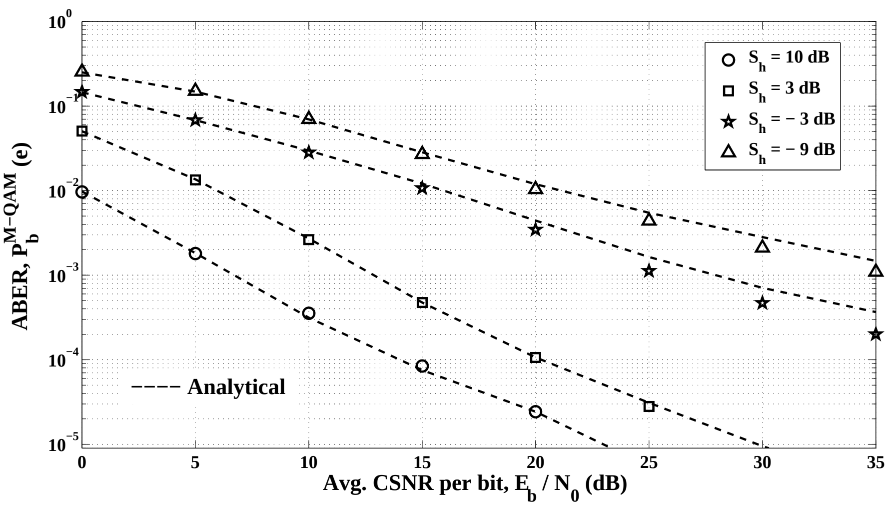

Figure 4.12: Average bit error rate performances of 16-QAM over JFTS faded / shadowed communication link, where the curves are generated by varying the S_h-parameter of the JFTS distribution, with fixed $K = 6.5$ dB and fixed $\Delta = 0.8$.

Δ at 6.5 dB and 0.8 respectively. This set of K and Δ parameters represent a scenario where the user and the access point are separated by 2 - 3 dry-walls or partitions. It is evident from Fig. 4.12 that lowering the S_h-parameter value results in deteriorated system performance. A larger S_h factor represents large variations in the main wave amplitudes contributed by each scattering neighborhood resulting in approximately equable number of high and low, thereby reducing the overall severity of shadowing. On the other hand, a low S_h factor depicts a scenario where each scattering cluster contributes a very small range of discrete shadowing values, higher in magnitude and encountered repeatedly. This condition results in an increased severity in shadowing, thereby degrading overall system performance.

The curves in Fig. 4.13 are generated by varying only the Δ-parameter of the JFTS distribution but keeping a fixed K and S_h at 6 dB and -4 dB respectively. This set of K and S_h is encountered

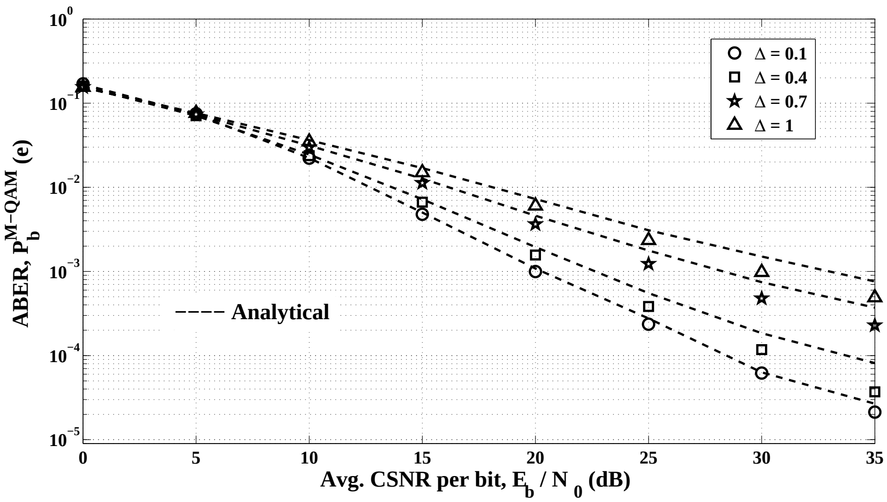

Figure 4.13: Average bit error rate performances of 16-QAM over JFTS faded / shadowed communication link, where the curves are generated by varying the Δ-parameter of the JFTS distribution, with fixed $K = 6$ dB and fixed $S_h = -4$.

when the mobile WLAN user and the access point are separated by 2 - 3 dry-walls or partitions. Variations in the value of the Δ-parameter affects the system performance in a way opposite to that of the K or S_h parameter. Performance of 16-QAM degrades as Δ increases from 0.1 to 0.7. This is due to the fact that as Δ increases, the relative magnitudes of the shadowing values contributed by two successive scattering clusters visited by the user increases. This results in an increase in the shadowing severity.

The results in Fig. 4.14 are generated by varying the JFTS parameters, K, S_h and Δ. The values for each set of parameters are chosen from the ranges of their numerical values proposed in Chapter 3, depending on the relative position of the mobile LAN user and the access point. The first curve is generated for $K = 10$ dB, $S_h = 10.5$ dB and $\Delta = 0.75$, representing a condition where both the user and the access point are located in the same room. As the user moves to a different

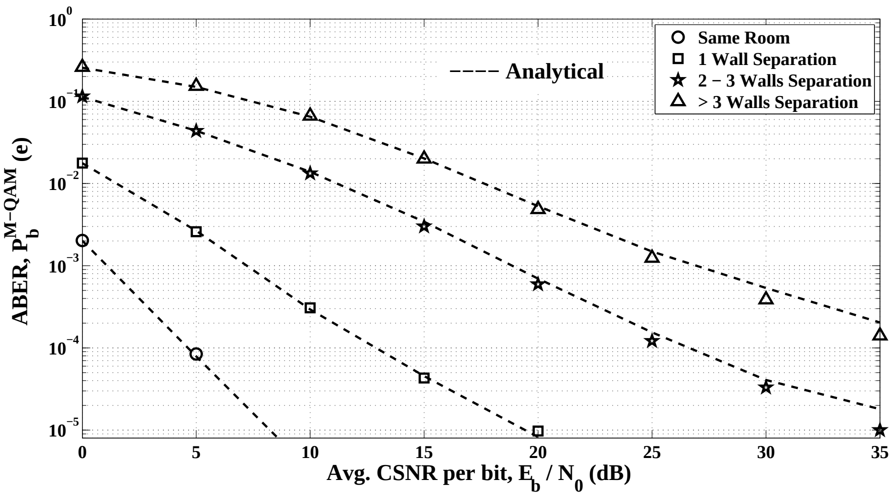

Figure 4.14: Average bit error rate performances of 16-QAM over JFTS faded / shadowed communication link, where the curves are generated by varying all the JFTS parameters, K, S_h and Δ simultaneously.

room separated by one set of wall or partition from that of the access point ($K = 8$ dB, $S_h = 6.5$ dB and $\Delta = 0.45$), system performance degrades, as exhibited by the second curve in Fig. 4.14. In order to achieve an ABER of 10^{-3}, the average CSNR per symbol requirement increases by around 5 dB for the second set of parameters with respect to the first set of JFTS parameters. It should be emphasized that Fig. 4.14 assumes a common path loss for all four scenarios. This means that for a given CSNR, all four scenarios experience the same average path loss and the difference in BER shown on the plot is a result of the different small scale fading and shadowing statistics imposed by the JFTS model.

The average CSNR per symbol requirement increases even further by around 10 dB, if the user and the access point is separated by 2 - 3 sets of partitions ($K = 6.5$ dB, $S_h = -1.5$ dB and $\Delta = 0.25$). This happens due to the lack of strong specular components and the presence of at least two

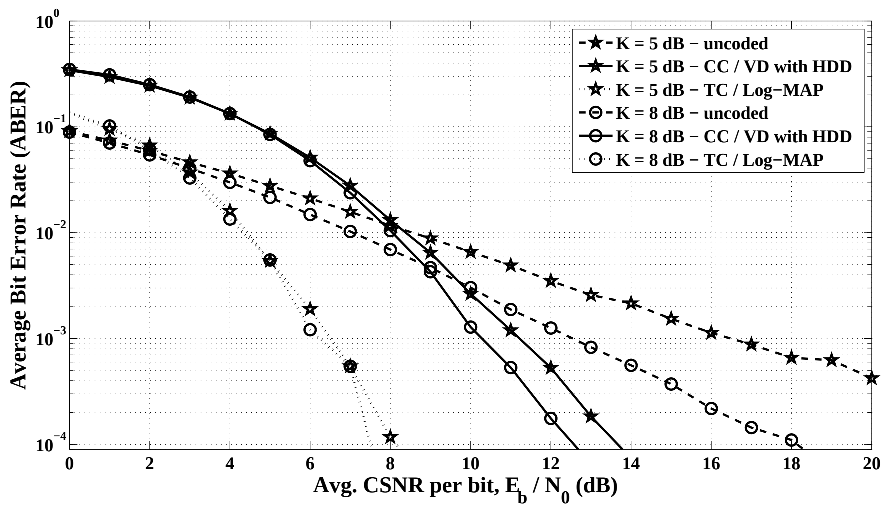

Figure 4.15: Comparative simulated average bit error rates (ABER) of BPSK with iterative coding technique like Turbo Coding (1/2-rate, $\mathsf{N} = 1024$), non-iterative coding technique like Convolutional Coding (1/2-rate, [7, 5] octal) with Hard-Decision Decoding and uncoded BPSK over JFTS block fading / shadowing communication link, where the curves are generated by varying the K-parameter of the JFTS distribution, with fixed $S_h = 2$ dB and fixed $\Delta = 0.3$.

scattering clusters between the transmitter and the receiver, which jointly deteriorates the overall system performance. However, for propagation conditions that correspond to an increase in the number of separations by more than 3 (i. e. $K = 5.5$ dB, $S_h = -7.5$ dB, $\Delta = 0.15$), the average CSNR per symbol requirement only increases by a maximum of 5 dB, in order to achieve the same ABER performance. The reason for this can be imparted to the low Δ-factor, where the effect of one scattering cluster is much stronger than the other one. As a result system performance is effectively affected by only one scattering cluster, even in the presence of at least two scattering clusters.

Fig. 4.15 shows that the performance improves at higher CSNR if non-iterative FEC coding like CC is employed at the transmit side. HDD using VD with no trace back memory is applied at the receiver side. Both in the case of uncoded and CC coded BPSK, performance deteriorates with the

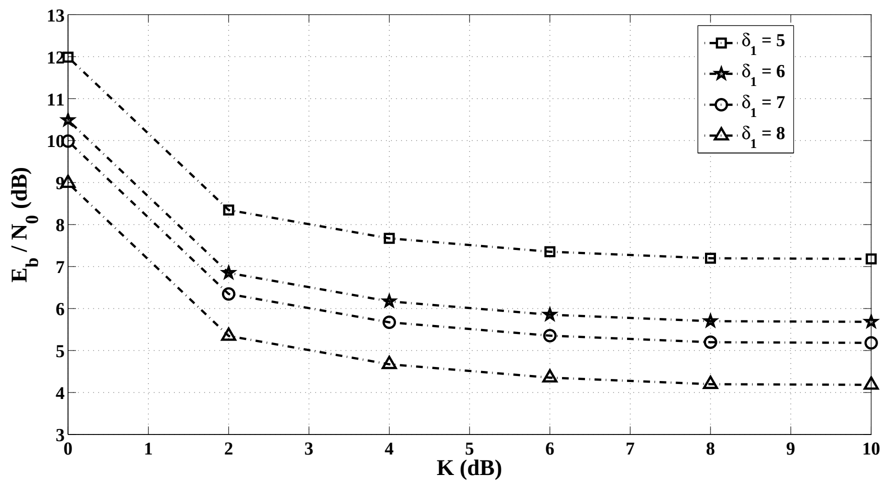

Figure 4.16: CSNR requirement for a (23, 35) Turbo coded BPSK to achieve an ABER of $\overline{P}_{\text{bit}} = 10^{-4}$ for varying K-factors of the JFTS distribution with fixed $S_h = 2$ dB and fixed $\Delta = 0.3$, where the curves are generated for different codeword distances, δ_1.

decrease in K-factor. As K decreases, the power contributed by the strong specular component decreases in comparison to that contributed by the diffused and the scattered components resulting in the degradation of the overall system performance. This difference in performance is obliterated over the application of 1/2-rate Turbo coding with a memory of 4 and a frame size of $\mathsf{N} = 2 \times 512$ coded bits ($\delta_1 = 5$). At the receiver Log-MAP is used for decoding with at most 25 iterations.

The fact that Turbo coding is able to eliminate the performance reduction experienced by a 3 dB drop in K-factor is quite surprising if compared with the results for simple Rician fading channels. The JFTS fading distribution combines Rician fading with that TWDP shadowing model. This means that, in addition to K-factor, the shadowing factor S_h, and the shape parameter, Δ, also affect the channel behavior. For this set of analyses, $S_h = 2$ dB and fixed $\Delta = 0.3$. A high S_h factor corresponds to a low severity in shadowing. A low Δ represents a scenario where only one

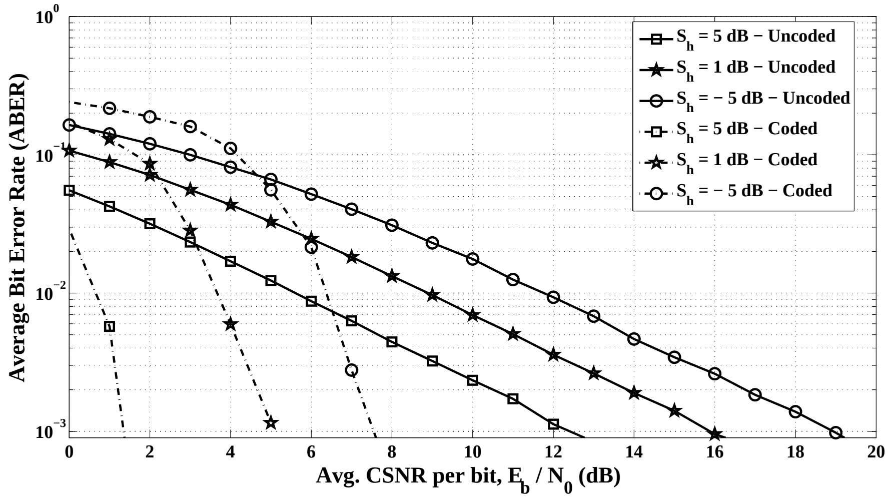

Figure 4.17: Comparative simulated average word error rates (ABER) of BPSK with Turbo Coding (1/3-rate, $\mathsf{N} = 3006$) and uncoded BPSK over JFTS block fading / shadowing communication link, where the curves are generated by varying the S_h-parameter of the JFTS distribution, with fixed $K = 6$ dB and fixed $\Delta = 0.8$.

scattering cluster dominates instead of two thereby also resulting in low shadowing severity. Hence, with a high S_h and low Δ coupled with high K-factors, the communication channel approaches the "no fading" scenario. This means that changing the K-factor from 5 dB to 8 dB does not increase fading enough to cause a meaningful performance degradation when Turbo codes are used.

To expand on this point, it is possible to further improve performance over a range of K-factors by increasing the codeword distance, δ_1. Fig. 4.16 exhibits the CSNR requirement to achieve an ABER of $\overline{P}_{\text{bit}} = 10^{-4}$ for different K-factors but same S_h and Δ as in Fig. 4.15. Since we are assuming the channel to be fully interleaved, all the fading amplitudes are independent of each other. In that case, the codeword distance δ_1 corresponds to the diversity order of the system. As a result with the increase in diversity order, the overall performance improves for a high K-factor even in presence of a high S_h and low Δ.

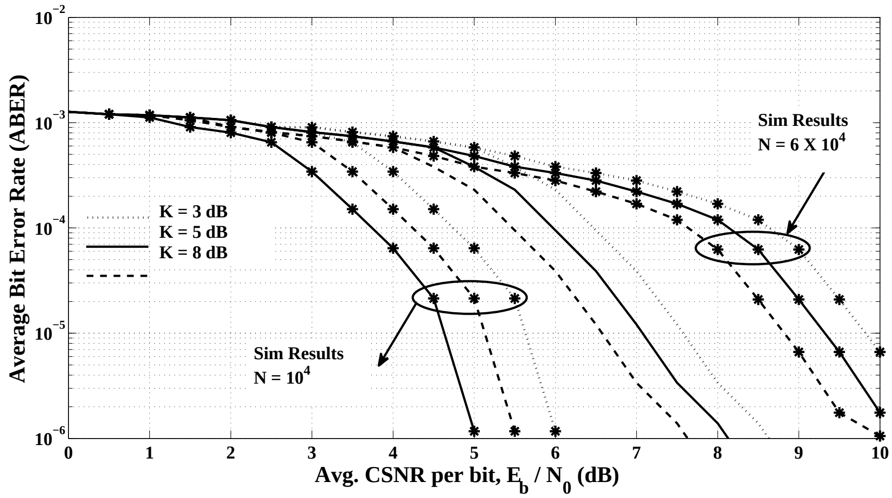

Figure 4.18: Comparative simulated average word error rates (ABER) of BPSK with LDPC Coding (1/3-rate) over JFTS block fading / shadowing communication link, where the curves are generated by varying the K-parameter of the JFTS distribution, with fixed $S_h = 6$ dB and fixed $\Delta = 0.8$ for two different sets of code length.

The effect of the variation in S_h-parameter on the performance of uncoded BPSK is preserved even when TC is employed, as can be seen in Fig. 4.17. A rate 1/3 turbo code with a memory of 2, code structure of (1, 7/5, 7/5), an input block size of L bits and an output encoded stream of $\mathsf{N} = 3(\mathsf{L} + 2)$ bits is used. With both encoders terminating in the zero state, ABER performance is analyzed for two selected codes with message block length of $\mathsf{L} = 1000$ bits. The performance of both coded and uncoded BPSK degrades with the decrease in S_h-parameter while the employment of Turbo codes offers an average coding gain of 11 dB at an ABER of $\overline{P}_{\text{bit}} = 10^{-3}$. A large S_h-factor represents large variations in the main wave amplitudes contributed by each scattering neighborhood resulting in approximately equable number of high and low discrete shadowing values contributing to a lower severity in shadowing. While a low S_h factor represents a high severity in shadowing as a very small range of discrete shadowing values are encountered repeatedly.

If LDPC coding is applied, it can be observed that the CSNR thresholds found using GA analysis are better for the more severe fading conditions (smaller K-factor) over the JFTS channel. It can be noticed from Fig. 4.15 that the uncoded BER performance for a JFTS channel is better when K is smaller for the lower values of average CSNR. When the CSNR increases, the performance improves for larger values of K-factors. With the introduction of LDPC codes to JFTS channels, and by using GA analysis, the CSNR threshold is reached at the lower values of CSNR before increasing the CSNR. This explains why the system reaches the CSNR threshold earlier for more severe fading conditions. For the simulation results in Fig. 4.18, it can be observed that for the code length of 10^4, the performance is better for $K = 5$ dB followed by $K = 8$ dB and $K = 3$ dB. However, for a larger code length of 6×10^4, the performance is better for the smaller values of K-factor, which is consistent with the GA results, where the assumption made is an infinite code length in the analyses.

The last set of curves of this subsection shown in Fig. 4.19 are generated by plotting the transmission outage probability as a function of BERs over the JFTS channel with different K-factors but fixed S_h and Δ. The curves are plotted at a fixed $\overline{\gamma}$ of 10 dB. As the BER increases, the probability of no transmission decreases. As the fading parameter K decreases, the power contributed by the diffused and scattered components. exceeds the power contributed by the specular components. As a result, the transmission outage probability increases for the same BER.

4.5.4 Comparison with Common Channel Models

To illustrate how JFTS channel performance compares to more conventional channel models, Fig. 4.20 is used to compare performances of 16-QAM over JFTS and Nakagami-log-normal (NL)

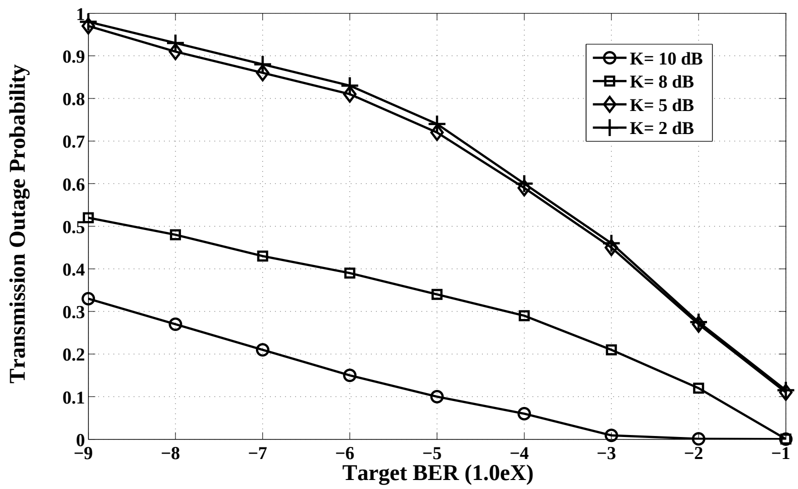

Figure 4.19: Transmission outage probability (P_{out}) of 16-QAM at different bit error rates over JFTS faded / shadowed channel at a fixed average received carrier-to-noise ratio ($\overline{\gamma}$) of 10 dB, where the curves are generated by varying the K-parameter of the JFTS distribution, with fixed $S_h = 2$ dB and fixed $\Delta = 0.3$.

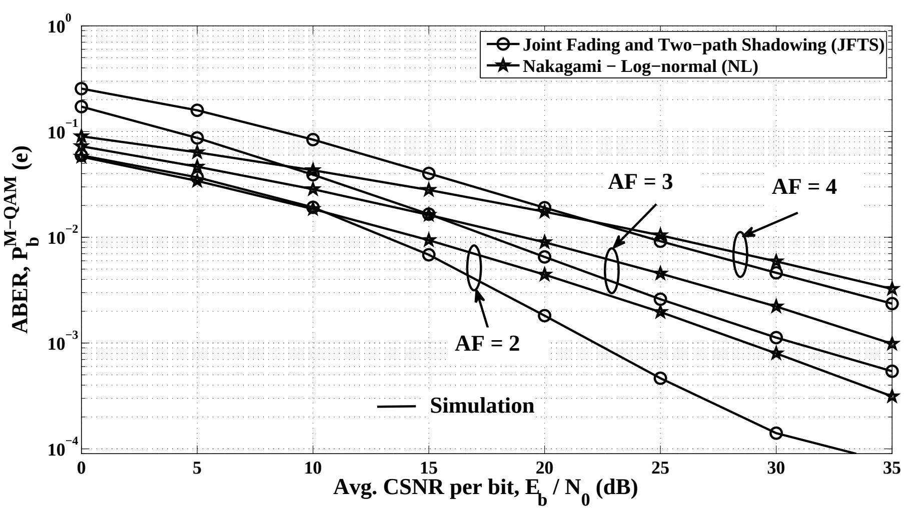

Figure 4.20: Average bit error rate of 16-QAM over a JFTS faded / shadowed communication link with three different sets of JFTS parameters in comparison with that over composite Nakagami - log-normal (NL) faded / shadowed link with three sets of NL parameters that contribute the same Amount of Fading (AF) as the JFTS parameters.

faded/shadowed communication channels. The channel parameters are chosen so that the JFTS and NL channels contribute the same amount of fading (AF). As shown in Chapter 3, a JFTS distribution with $K = 7$ dB, $S_h = 6$ dB and $\Delta = 0.7$, contributes an AF of 2 which is same as that contributed by NL distribution with $m = 1$ and $\sigma = 2.8$ (4.4 dB). For these sets of parameters, performance over a JFTS channel is worse than that over a NL channel for CSNRs less than 10 dB ($\overline{\gamma} \leq 10$ dB). For higher CSNRs per bit of around 10 dB and more, JFTS offers a performance gain over NL. While only the simulation results are shown for brevity, this same pattern in performance repeats itself even for the sets of JFTS ($K = 5, 2$ dB, $S_h = -5, -10$ dB and $\Delta = 0.3, 0.5$) and NL ($m = 1, 1, \mu = 1, 1, \sigma = 3.6, 4.2$) parameters that contribute AFs of 3 and 4 respectively. This improvement in performance for the JFTS distribution at higher CSNRs occurs due to the fact that for the JFTS distribution, there still exists a very small group of specular components as long as $K \neq 0$. While $m = 1$ for NL distribution represents a small scale fading condition, which is equivalent to Rayleigh fading with the absence of any specular component.

It can be observed from Fig. 4.4 that it is harder to approach the capacity of the JFTS channel compared to Rayleigh channel in the context of QAM, as a consequence of having wider CSNR gap between the capacity and cut-off rate. For example, at a capacity of 3 bits/symbol, the CSNR gap between the capacity curve and cut-off rate curve of 16-QAM when communicating over a JFTS and a Rayleigh channel is about 18 dB and 5 dB respectively. An important conclusion that can be made from this observation is that it is dangerous to use traditional fading models like Rayleigh or Nakagami-m distributions to characterize composite wifi fading/shadowing scenarios due to this very large error. This establishes the necessity of analyzing performance of different communication techniques over a JFTS faded/shadowed communication link.

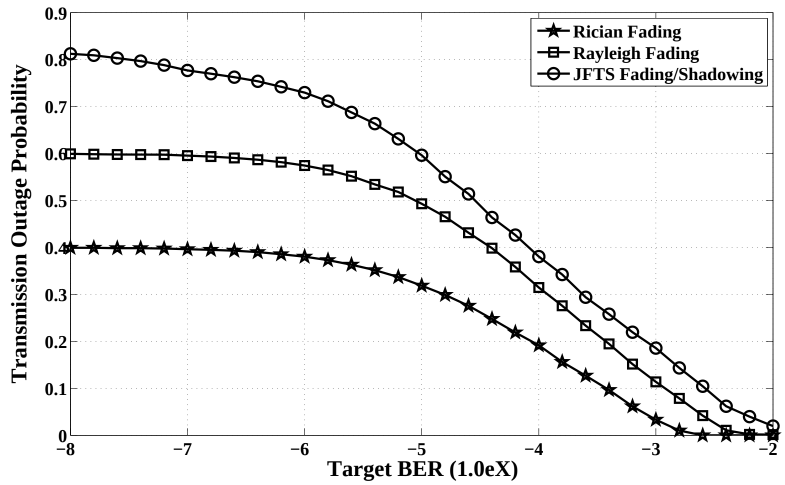

Figure 4.21: Comparative transmission outage probability (P_{out}) of 16-QAM at different bit error rates with a fixed average received carrier-to-noise ratio ($\overline{\gamma}$) of 15 dB, where the curves are generated over Rayleigh faded, Rician faded and JFTS faded/shadowed channels.

The last set of curves of this subsection plotted in Fig. 4.21 are generated by plotting the outage probability as a function of BER over Rayleigh, Rician ($K = 5$ dB) and JFTS ($K = 6.5$ dB, $S_h = -2.5$ dB, $\Delta = 0.15$) channels. The curves are plotted at a fixed $\overline{\gamma}$ of 15 dB. The outage probability over the JFTS channel is higher than over both Rayleigh or Rician fading channels. The poorer performance over the JFTS channel can be attributed to low S_h factor, which represents a scenario where each scattering cluster contributes a very small range of discrete shadowing values, that are encountered repeatedly resulting in an increased severity in shadowing.

4.6 Summary

The primary contribution of this chapter is to derive closed-form analytical expressions for the error probability performance, channel capacity and outage probability of a wireless communication system using M-QAM and coherent M-PSK modulation techniques over JFTS fading/shadowing channels. In order to do so, expressions for the PDF and the CDF of the received instantaneous composite CSNR are utilized. The derived analytical expressions are numerically evaluated and plotted as functions of the parameters of the communication channel model and the modulation techniques. Performance degrades as K and S_h decreases and enhances as Δ decreases. The analytical results are found to be in agreement with the simulation results verifying the validity of the derived expressions. It can also be concluded that for higher CSNRs, performance over a JFTS channel model is better than the NL channel model for the same AF.

For the case of ABER performance with FEC coding techniques, it is evident that CC with VD offers a 3 dB improvement in performance over HC with HD, and SDD offers another 3 dB improvement in performance over HDD for a fixed set of JFTS parameters. The ABER performances of Turbo coded and LDPC coded BPSK are simulated assuming coherent detection and perfect CSI at the receiver side. Simulated performances fall within 0.1 - 0.5 dB of CSNR difference with that of the analytical upper bound of ABER over JFTS communication channels.

Chapter 5

Adaptive Coded Modulation

5.1 Background

Shannon capacity is the most common measure of the maximum achievable information rate over a communication channel. In the case of a fading/shadowing channel, ergodic capacity is determined by averaging the achievable information rate over the composite fading/shadowing distribution. The ergodic channel capacity depends on the knowledge of the CSI available at the receiver and/or the transmitter. This channel capacity can be achieved by optimizing the transmission techniques through adaptive variation of the transmit power level, symbol transmission rate, modulation constellation size, coding rate/scheme or any combination of these parameters, [110], [111].

The primary contribution of this chapter is to derive analytically tractable expressions for JFTS capacity under different adaptive transmission schemes with or without iterative channel coding techniques. Subsection 5.1.1 introduces different adaptive transmission techniques, while a brief summary of different adaptive coded modulation schemes is provided in Subsection 5.1.2.

5.1.1 Adaptive Transmission Techniques

If perfect CSI is available both at the transmitter and the receiver (TR-CSI), the Shannon capacity can be achieved by adapting the transmission power and rate simultaneously relative to the channel quality [99]. This technique is called Optimal Power and Rate Adaptation (OPRA). Shannon capacity can also be reached by using fixed power variable rate transmission if only receiver CSI

(R-CSI) is available [112]. This technique is coined Optimal Rate Adaptation (ORA).

Variable rate transmission strategies can impose variable delays making them unfavorable for some real-time applications. For these applications, maximum constant information rate can be maintained only through optimal power control with perfect transmit and receive CSI [99], [112]. The techniques introduced in [99], [112] use fading inversion to maintain a constant carrier signal-to-noise ratio (CSNR). Any technique that maintains a constant received CSNR by adapting transmit power is known as Channel Inversion with Fixed Rate (CIFR). The main difference between CIFR and OPRA is that OPRA adapts both the transmission power and rate while CIFR adapts only the transmission power while keeping the transmission rate fixed. However, in case of Rayleigh faded communication channel, the CIFR capacity is found to be zero.

In order to mitigate this problem, an adaptive transmission technique was introduced in [107] referred to as Truncated Channel Inversion with Fixed Rate (TIFR). In case of TIFR, the channel fading is compensated only when the received CSNR is above a certain cut-off fade depth. The constant information rate that can be achieved using TIFR with an outage probability under a certain threshold is referred to as the outage capacity [108].

Hence the first contribution of this chapter is to present the analytical expressions for the achievable ergodic and outage channel capacities of a JFTS fading/shadowing communication channel with different adaptation techniques like OPRA, ORA, TIFR and CIFR. The relationship between the optimal cut-off CSNR and the average received CSNR is also explored for JFTS faded/shadowed links when adaptive techniques like OPRA, ORA, CIFR or TIFR is applied. These results will demonstrate the effect of JFTS parameters on the achievable channel capacity assuming perfect

CSI to be available at the transmitter and/or the receiver.

5.1.2 Adaptive Coded Modulation

Adaptive coded modulation is an established technique to increase the data rate that can be reliably transmitted over fading, shadowing or composite fading/shadowing channels. For this reason, some form of adaptive coded modulation (or without coding) is being proposed or implemented n many next generation wireless systems. The basic premise of adaptive coded modulation is a real-time balancing of the link budget in flat fading and/or slow shadowing through adaptive variation of the transmitted power level, symbol transmission rate, constellation size, BER, coding rate/scheme, or any combination of these parameters, [94] - [100], [102], [106], [109]. Thus, without wasting power or sacrificing BER, these schemes provide a higher average link spectral efficiency (bps/Hz) by taking advantage of fading and/or shadowing through adaptation. Good performance of adaptive coded modulation requires accurate channel estimation at the receiver and a reliable feedback path between the receiver and the transmitter. The impact of estimation error and delay on adaptive modulation schemes has been studied in [100] - [102].

Adaptive coded modulation provides many parameters that can be adjusted relative to the channel fading, including data rate, transmit power, instantaneous BER, symbol rate and channel code rate or scheme. The question therefore arises as to which of these parameters should be adapted to obtain the best performance. Results from [99] indicate that the Shannon capacity of a flat-fading channel is achieved by varying both transmission rate and power and this capacity can also be achieved by varying the transmit power alone [107]. Moreover, [99] also indicate that varying both power and rate leads to a negligibly higher capacity over varying just the rate alone. However, Shannon capacity assumes that the BER is arbitrarily small, coding schemes are random and of unbounded length and complexity, and there is no delay constraint. Therefore, capacity results do not necessarily yield insight into the best adaptive schemes to use under more practical constraints. There is much recent work on adaptive coded modulation that varies one or two modulation parameters. In particular, [94] - [96], [99] and [100] investigate adapting power and/or rate, [97] and [102] investigate adapting rate and coding, and [98] investigates adapting power, rate and instantaneous BER. A unified study on the trade-offs in adapting all combinations of different modulation parameters is presented in [111].

Hence, the second contribution of this chapter is to provide a systematic study on the increase in spectral efficiency obtained by optimally varying combinations of the transmission rate, power and instantaneous BER over a JFTS faded/shadowed communication link. It will be assumed here that the resulting adaptive modulation schemes are subject to an average power and BER constraint. Symbol rate adaptation is not taken into account since it is difficult to implement in real systems. Analysis is done for both an average and an instantaneous BER constraint with or without channel coding, where only a discrete finite set of constellations is available. Hence the goal of this chapter is to determine the impact on spectral efficiency of a JFTS channel achievable by adapting various modulation parameters under different constellation restrictions and BER constraints, for a large class of modulation techniques over the JFTS fading/shadowing distribution.

The remainder of this chapter is organized as follows. Section 5.2 derives the analytical expressions for the channel capacity under different adaptive transmission policies. Section 5.3 studies the performance of constant power optimal rate adaptive (ORA) multi-level quadrature amplitude modulation (M-QAM) over the JFTS channel. Section 5.4 derives the optimal power and rate adaptation under different constraints for adaptive discrete rate M-QAM over a JFTS channel while the optimal rate adaptation under a BER constraint using Trellis coded adaptive M-QAM are derived in Section 5.4. Numerical results are presented in Section 5.5 followed by some concluding remarks in Section 5.6.

5.2 Analysis of Channel Capacity

The principal contribution of this section is to derive analytically tractable expressions for JFTS ergodic capacity under different adaptive transmission schemes. These expressions will provide new insight into the behavior of ergodic capacity for indoor WLAN systems due to the nature of the JFTS model. Subsection 5.2.1 presents the PDF of the received instantaneous CSNR over a JFTS communication channel. Subsection 5.2.2 and Subsection 5.2.3 derives expressions for the ergodic and outage channel capacity under different adaptive transmission policies.

5.2.1 Instantaneous CSNR

The mean-squared value of the joint faded and two-path shadowed envelope, Z, can then be calculated using (4.2) and the integral solution from [48] as,

$$\Omega = \mathrm{E}\{Z^2\} = \sum_{i=1}^{4}\sum_{h=1}^{20} \frac{b_i P_2 \mathcal{R} r_h^4}{P_1^2}\; e^{-K-S_h}\Bigg[e^{S_h \Delta\mathsf{M}_i - K S_h (1-\Delta\mathsf{M}_i)\frac{r_h^2}{2P_1}}\big(P_1 + K S_h r_h^2(1-\Delta\mathsf{M}_i)\big) \\ +\; \big(P_1 + K S_h r_h^2 (1+\Delta\mathsf{M}_i)\big)\; e^{-S_h \Delta\mathsf{M}_i - K S_h (1+\Delta\mathsf{M}_i)\frac{r_h^2}{2P_1}}\Bigg]. \tag{5.1}$$

Putting (5.1) back in that expression for the PDF of γ, the final expression can be obtained in terms of $\overline{\gamma}$ and Ω as,

$$f_\gamma(\gamma) = \sum_{h=1}^{20} \frac{\Omega}{2\gamma P_2 r_h^2}\left[1 \;-\; e^{-\frac{\Omega\gamma}{2\overline{\gamma} P_2 r_h^2}}\right]. \tag{5.2}$$

Given an average transmit power constraint, the optimal cut-off CSNR level (γ_0) for any adaptive transmission technique must satisfy the relationship [111], $\int_{\gamma_0}^{+\infty}\left(\frac{1}{\gamma_0} - \frac{1}{\gamma}\right) f_\gamma(\gamma)\mathrm{d}\gamma \;=\; 1$. If the received instantaneous CSNR level γ falls below γ_0, data transmission will be suspended. In order to find the relationship between γ and γ_0 for adaptive transmission over a JFTS faded / shadowed channel, we need to solve two integrals, [48]

$$I_1 = \int_{\gamma_0}^{+\infty} f_\gamma(\gamma)\,\mathrm{d}\gamma = \int_{\gamma_0}^{+\infty} \frac{\mathcal{B}}{\gamma}\,\mathrm{d}\gamma - \int_{\gamma_0}^{+\infty} \frac{\mathcal{B}}{\gamma}\,e^{-\frac{\mathcal{B}\gamma}{\overline{\gamma}}}\,\mathrm{d}\gamma = \mathcal{B}\,\mathrm{Ei}\bigg(-\frac{\mathcal{B}\gamma_0}{\overline{\gamma}}\bigg) - \mathcal{B}\log(\gamma_0) \tag{5.3}$$

and

$$I_2 = \int_{\gamma_0}^{+\infty} \frac{1}{\gamma} f_\gamma(\gamma)\mathrm{d}\gamma = \int_{\gamma_0}^{+\infty} \frac{\mathcal{B}}{\gamma^2}\mathrm{d}\gamma - \int_{\gamma_0}^{+\infty} \frac{\mathcal{B}}{\gamma^2} e^{-\frac{\mathcal{B}\gamma}{\overline{\gamma}}}\mathrm{d}\gamma = -\frac{\mathcal{B}}{\gamma_0} e^{-\frac{\mathcal{B}\gamma_0}{\overline{\gamma}}} - \frac{\mathcal{B}^2}{\overline{\gamma}}\,\mathrm{Ei}\bigg(-\frac{\mathcal{B}\gamma_0}{\overline{\gamma}}\bigg) - \frac{\mathcal{B}}{\gamma_0} \tag{5.4}$$

where $\mathrm{Ei}(\cdot)$ is the exponential integral given by [39] and $\mathcal{B} = \sum_{h=1}^{20} \frac{\Omega}{2P_2 r_h^2}$. Now, putting the integral solutions obtained in (5.3) and (5.4), back in the above mentioned relationship, we can find the equation which the optimal cut-off CSNR should satisfy for adaptive transmission. Therefore, in case of a JFTS faded/shadowed channel, γ_0 should satisfy the following relationship,

$$\bigg(\frac{\mathcal{B}}{\gamma_0} + \frac{\mathcal{B}^2}{\overline{\gamma}}\bigg)\mathrm{Ei}\bigg(-\frac{\mathcal{B}\gamma_0}{\overline{\gamma}}\bigg) + \frac{\mathcal{B}}{\gamma_0}\bigg(1 - \log(\gamma_0) + e^{-\frac{\mathcal{B}\gamma_0}{\overline{\gamma}}}\bigg) = 1. \tag{5.5}$$

5.2.2 Ergodic Capacity

Optimal Power and Rate Adaptation (OPRA):

Assuming perfect CSI at the transmitter and the receiver, the ergodic channel capacity $\langle \mathtt{C} \rangle_{\mathrm{OPRA}}$ in bits/sec under an average transmit power constraint is given by, $\langle \mathtt{C} \rangle_{\mathrm{OPRA}} = B \int_{\gamma_0}^{+\infty} \log_2\Big(\frac{\gamma}{\gamma_0}\Big) f_\gamma(\gamma)\mathrm{d}\gamma$, where B (Hz) is the channel bandwidth and γ_0 is the optimal cut-off CSNR. A water-filling algorithm is used for optimal power adaptation given by $\mathtt{S}(\gamma) = \frac{1}{\gamma_0} - \frac{1}{\gamma}$ for all $\gamma \geq \gamma_0$. The optimal rate adaptation sends a rate of $\log_2(\gamma/\gamma_0)$ bits/sec for a fade level of γ. In order to find the final expression for channel capacity per unit bandwidth over a JFTS faded / shadowed channel

($\langle \mathtt{C}/B\rangle^{\text{JFTS}}_{\text{OPRA}}$ [bits/sec/Hz]), we need to solve four sets of integrals in,

$$\left\langle \frac{\mathtt{C}}{B} \right\rangle^{\text{JFTS}}_{\text{OPRA}} = \frac{1}{\log(2)}\Bigg[\underbrace{\int_{\gamma_0}^{+\infty} \log(\gamma)\frac{\mathcal{B}}{\gamma}\mathrm{d}\gamma}_{I_3} - \underbrace{\int_{\gamma_0}^{+\infty} \log(\gamma_0)\frac{\mathcal{B}}{\gamma}\mathrm{d}\gamma}_{I_4} - \underbrace{\int_{\gamma_0}^{+\infty} \log(\gamma)\frac{\mathcal{B}}{\gamma}e^{-\frac{\mathcal{B}\gamma}{\overline{\gamma}}}\mathrm{d}\gamma}_{I_5}$$
$$+ \underbrace{\int_{\gamma_0}^{+\infty} \log(\gamma_0)\frac{\mathcal{B}}{\gamma}e^{-\frac{\mathcal{B}\gamma}{\overline{\gamma}}}\mathrm{d}\gamma}_{I_6}\Bigg]. \tag{5.6}$$

The expression in (5.6) can be obtained in a tractable form through the following steps of integral solutions and mathematical manipulations. Firstly we can express,

$$I_3 - I_4 = \frac{\mathcal{B}}{2}\log^2(\gamma_0). \tag{5.7}$$

Using the identities, $\mathrm{Ei}(-x) = -\Gamma(0,x) - \log(x) + \frac{1}{2}(\log(-x) - \log(-\frac{1}{x}))$ and $\log(-x) = \log(x) + \imath\pi$, valid for $x > 0$ [39] and [48], and assuming that, $(\mathcal{B}\gamma_0/\overline{\gamma}) > 0$ and $(\overline{\gamma}/\mathcal{B}\gamma_0) > 0$ and after some algebraic manipulations, we can express,

$$I_6 - I_5 = \mathcal{B}\log(\gamma_0)\log\left(\frac{\mathcal{B}\gamma_0}{\overline{\gamma}}\right) + \mathcal{B}\mathcal{E}\log(\gamma_0) - \frac{\mathcal{B}}{2}\log^2(\gamma_0) - \frac{\mathcal{B}^2\gamma_0}{\overline{\gamma}}\,{}_3F_3\left(1,1,1;2,2,2;-\frac{\mathcal{B}\gamma_0}{\overline{\gamma}}\right). \tag{5.8}$$

where $\mathcal{E}$ is the Euler-Mascheroni constant with a numerical value of $\mathcal{E} \approx 0.577216$. Finally, using (5.7) and (5.8), the expression in (5.6) can be obtained as,

$$\left\langle \frac{\mathtt{C}}{B} \right\rangle^{\text{JFTS}}_{\text{OPRA}} = \frac{\mathcal{B}\log(\gamma_0)}{\log(2)}\left[\log\left(\frac{\mathcal{B}\gamma_0}{\overline{\gamma}}\right) + \mathcal{E}\right] - \frac{\mathcal{B}^2\gamma_0}{\overline{\gamma}\log(2)}\,{}_3F_3\left(1,1,1;2,2,2;-\frac{\mathcal{B}\gamma_0}{\overline{\gamma}}\right) \tag{5.9}$$

where ${}_pF_q(\cdot)$ is the generalized confluent hyper-geometric function [39] and p, q are integers.

Optimal Rate Adaptation (ORA):

Assuming perfect CSI at the receiver only, the ergodic channel capacity $\langle \mathtt{C}\rangle_{\text{ORA}}$ in bits/sec with constant power over any composite fading and shadowing channel is given by, $\langle \mathtt{C}\rangle_{\text{ORA}} = B\int_0^{+\infty}\log_2(1+$

$\gamma)f_\gamma(\gamma)\mathrm{d}\gamma$. It is shown in [113] that $\langle \mathtt{C}\rangle_{\mathrm{OPRA}}$ becomes equal to $\langle \mathtt{C}\rangle_{\mathrm{ORA}}$ when the transmit power is kept constant for OPRA. Using the identity $\log(1+y) = \log(y) - \sum_{n=1}^{+\infty}\frac{(-1)^n}{ny^n}$ for $|y|>1$, we can solve the integral in the above definition [48]. Using (5.3), the final expression for channel capacity per unit bandwidth with ORA transmission ($\langle \mathtt{C}/B\rangle_{\mathrm{ORA}}^{\mathrm{JFTS}}$) over a JFTS faded / shadowed communication link can be written as,

$$\left\langle \frac{\mathtt{C}}{B}\right\rangle_{\mathrm{ORA}}^{\mathrm{JFTS}} = \frac{1}{\log(2)}\left[\int_0^\infty \sum_{n=1}^{+\infty}\frac{(-1)^n}{n}\frac{\mathcal{B}}{\gamma^{n+1}}e^{-\frac{\mathcal{B}\gamma}{\overline{\gamma}}}\mathrm{d}\gamma\right] = \sum_{n=1}^{+\infty}\frac{\mathcal{B}\Gamma(-n)}{n\,\log(2)}\left(-\frac{\mathcal{B}}{\overline{\gamma}}\right)^n. \tag{5.10}$$

It is evident from (5.9) and (5.10), that ergodic capacity over a JFTS distributed link depends on the mean-squared value of the joint faded and two-path shadowed envelope, Ω. Now from (5.1), we observe that Ω decreases exponentially with the increase either in K or S_h or both. In (5.9), the capacity term is directly proportional to $\left[\log\left(\frac{\mathcal{B}\gamma_0}{\overline{\gamma}}\right)+\mathcal{E}\right]$. Hence, as Ω decreases, $\left|\log\left(\frac{\mathcal{B}\gamma_0}{\overline{\gamma}}\right)\right|$ increases, since $\Omega<1$. As a result, the term $\left[\log\left(\frac{\mathcal{B}\gamma_0}{\overline{\gamma}}\right)+\mathcal{E}\right]$ increases with the increase in the fading and/or the shadowing parameters resulting in the overall increase in the ergodic capacity. Similar intuitive conclusions can also be made from (5.10), where capacity increases with the decrease in Ω, since $\left\langle\frac{\mathtt{C}}{B}\right\rangle \propto \left(-\frac{\mathcal{B}}{\overline{\gamma}}\right)^n$ for $n>0$.

Channel Inversion with Fixed Rate (CIFR):

Assuming perfect CSI at the transmitter and the receiver, the channel capacity of this technique for any fading/shadowing communication link is given by,

$$\mathtt{C}_{\mathrm{CIFR}} = B\log_2\left(1 + \frac{1}{\int_0^\infty \frac{1}{\gamma}f_\gamma(\gamma)\,\mathrm{d}\gamma}\right) \tag{5.11}$$

Using the integral solution from (5.4) and putting it back in (5.11), it can be shown that CIFR channel capacity is equal to zero for the JFTS channel. This result can be referred to as the zero outage capacity or delay-limited capacity. The zero outage capacity can be defined as the maximum constant information rate that can be maintained over any fading and/or shadowing conditions through the optimal control of transmission power. Since for a JFTS channel, the CIFR channel capacity becomes equal to zero, a large amount of transmitted power will be required to compensate for the deep channel fades if this technique is used for adaptive transmission. A better approach will be to use truncated channel inversion with fixed rate, the channel capacity for which has been derived in the next subsection.

5.2.3 **Outage Capacity**

Truncated Channel Inversion with Fixed Rate (TIFR):

In case of TIFR, channel fading is inverted only if the received instantaneous CSNR level is above the cut-off fade depth (γ_0). The channel capacity with TIFR over any fading channel is obtained by maximizing the outage capacity ($\mathtt{C}_{\text{out}}$) over all possible γ_0 and can be expressed as, $\mathtt{C}_{\text{TIFR}} = \max_{\gamma_0} \mathtt{C}_{\text{out}}$, where $\mathtt{C}_{\text{out}}$ is the outage capacity. The outage channel capacity for a fading/shadowing channel can be calculated as, $\langle \mathtt{C}_{\text{out}} \rangle_{\text{TIFR}} = B \ \log_2\Big(1 + \frac{1}{\int_{\gamma_0}^{+\infty} \frac{1}{\gamma} f_\gamma(\gamma) \text{d}\gamma}\Big)(1 - P_{\text{out}})$, where P_{out} is the outage probability. For a JFTS fading/shadowing channel, P_{out} can be calculated as,

$$P_{\text{out}} = \int_0^{\gamma_0} f_\gamma(\gamma) \ \text{d}\gamma = \mathcal{B} \ \log(\gamma_0) - \mathcal{B} \ \text{Ei}\bigg(- \frac{\mathcal{B}\gamma_0}{\overline{\gamma}} \bigg) \tag{5.12}$$

using the integral solution provided in (5.3). Using (5.4), we can evaluate the channel capacity with TIFR in a JFTS faded / shadowed communication link which can be expressed as,

$$\left\langle \frac{\mathtt{C}_{\text{out}}}{B} \right\rangle_{\text{TIFR}}^{\text{JFTS}} = \bigg(1 + \mathcal{B} \ \text{Ei}\bigg(- \frac{\mathcal{B}\gamma_0}{\overline{\gamma}} \bigg) - \mathcal{B} \ \log(\gamma_0)\bigg) \log_2\Bigg(1 - \frac{\gamma_0 \overline{\gamma}}{\mathcal{B}\overline{\gamma} \ e^{-\frac{\mathcal{B}\gamma_0}{\overline{\gamma}}} + \mathcal{B}^2 \gamma_0 \ \text{Ei}\big(- \frac{\mathcal{B}\gamma_0}{\overline{\gamma}} \big) + \mathcal{B}\overline{\gamma}}\Bigg). \tag{5.13}$$

5.3 Adaptive Modulation

This section provides a performance analysis of constant power ORA M-QAM schemes for spectrally efficient transmission over slowly varying flat fading and slow shadowing JFTS channels. Rate adaptation is achieved through the variation of the constellation size based on its advantage of easy hardware implementation. Assuming perfect CSI is available at the receiver side and negligible time delay, the analysis is done both for continuous modulation rate and discrete constellations sets based on average BER constraint. However, rate adaptation based on instantaneous BER constraint is not considered in this section, however will be studied in Section 5.4.

The remainder of this section is organized as follows. Subsection 5.3.1 describes the adaptive M-QAM techniques considered in this thesis. The performance of constant power ORA M-QAM schemes over JFTS channels assuming perfect channel estimation and negligible time delay is analyzed in Subsection 5.3.2 and Subsection 5.3.3.

5.3.1 Adaptive M-QAM Modulation

For this analysis, a family of M-QAM signal constellation is considered where M denotes the number of signal constellation points. It is assumed that the transmission is done with a fixed symbol rate τ_s and ideal Nyquist data pulses are used for each constellation. Since each of the M-QAM constellations use Nyquist data pulses ($B = 1/\tau_s$), the average E_s/N_0 equals the average CSNR, $\overline{E}_s/N_0 = \overline{\gamma}$, where B in Hz, is the channel bandwidth. The BER of any M-QAM technique over a wireless communication channel suffering from AWGN can be approximated by,

$$\mathrm{BER}(M,\gamma) \;\approx\; 0.2\mathrm{exp}\left(-\frac{1.6\gamma}{M-1}\right) \tag{5.14}$$

where Gray-coded bit mapping is used on the transmitter side and perfect clock and carrier recovery is applied on the receive side. The inverse of the approximation in (5.14) will be used to derive closed-form expressions for link spectral efficiency of M-QAM as a function of the CSNR and the BER. Performance analysis over JFTS fading/shadowing channels will be done for two kinds of adaptive M-QAM techniques, Adaptive Continuous Rate (ACR) M-QAM and Adaptive Discrete Rate (ADR) M-QAM.

Adaptive Continuous Rate (ACR) M-QAM

Adaptive Continuous Rate (ACR) refers to adaptive modulation technique in which the number of bits per symbol is not restricted to integer values. The spectral efficiency for any fixed M is given by the data rate per unit bandwidth ($\mathtt{R}/B$) and therefore can be expressed in bits per symbol per Hz (bps/Hz). Assuming ideal Nyquist pulses and for a fixed CSNR (γ) and BER (B_0), the spectral efficiency of the constant power ORA ACR M-QAM is given by,

$$\left\langle \frac{\mathtt{R}}{B} \right\rangle_{\mathrm{ACR}} = \int_0^{\infty} \log_2\left(1 - \frac{1.6\gamma}{\ln(5B_0)}\right) f_\gamma(\gamma)\mathrm{d}\gamma \tag{5.15}$$

where $\mathtt{R}$ is the data rate given by $\mathtt{R} = \log_2(M/\tau_s)$.

Adaptive Discrete Rate (ADR) M-QAM

If the constellation size $M_{\mathtt{n}}$ is restricted to $2^{\mathtt{n}}$ for any positive integer $\mathtt{n}$, the adaptive modulation technique is called Adaptive Discrete Rate (ADR) M-QAM. In this technique, the entire CSNR range is divided into $\mathtt{N}+1$ fading regions and the constellation size $M_{\mathtt{n}}$ is assigned to the $\mathtt{n}$th fading region ($\mathtt{n} = 0, 1, \ldots, \mathtt{N}$). hence, if the received CSNR falls in the $\mathtt{n}$th region, M-QAM with constellation size $M_{\mathtt{n}}$ is used for transmission. The average link spectral efficiency for ORA and constant power ADR M-QAM given by,

$$\left\langle \frac{\mathtt{R}}{B} \right\rangle_{\mathrm{ADR}} = \sum_{\mathtt{n}=1}^{\mathtt{N}} \mathtt{n} \int_{\gamma_{\mathtt{n}}}^{\gamma_{\mathtt{n}+1}} f_\gamma(\gamma)\mathrm{d}\gamma \tag{5.16}$$

5.3.2 Average Spectral Efficiency

Using (5.15), the average link spectral efficiency of ACR M-QAM with constant power ORA over JFTS faded/shadowed channel can be obtained using the identity for the logarithmic function,

$$\ln(1+\kappa\bar{y}) \;=\; \sum_{\mathtt{m}=1}^{\infty}\frac{(-1)^{\mathtt{m}+1}}{\mathtt{m}}\,(\kappa\bar{y})^{\mathtt{m}} \qquad |\kappa\bar{y}|<1 \tag{5.17}$$

In this case, this identity can only be used as the logarithmic function is only defined for positive arguments and hence the argument in the integral in (5.15) is only valid for logarithmic operation if and only if $1-\frac{1.6\gamma}{\ln(5B_0)}>0$ or $1>\frac{1.6\gamma}{\ln(5B_0)}$ or equivalently $1>\kappa\bar{y}$. Hence the final expression for the spectral efficiency of ACR M-QAM with ORA over a JFTS channel can be obtained by putting (5.17) and (5.2) in (5.15) as below,

$$\left\langle\frac{\mathtt{R}}{B}\right\rangle_{\mathrm{ACR}}^{\mathrm{JFTS}} \;=\; \sum_{\mathtt{m}=1}^{\infty}\sum_{\mathtt{k}=0}^{\infty}\frac{(-1)^{\mathtt{m}+1}}{\mathtt{m}\ln 2}\left(\frac{1.6}{\ln(5B_0)}\right)^{\mathtt{m}}\frac{\overline{\gamma}}{(\mathtt{k}+1)!(\mathtt{k}+\mathtt{m})!}\left(\frac{2\overline{\gamma}P_2r_h^2}{\Omega}\right)^{\mathtt{m}-1} \tag{5.18}$$

The average spectral efficiency of constant power ORA ADR M-QAM over the JFTS fading/shadowing channel is then determined by putting (5.2) back in (5.16) and then solving the integral to obtain,

$$\left\langle\frac{\mathtt{R}}{B}\right\rangle_{\mathrm{ADR}}^{\mathrm{JFTS}} \;=\; \sum_{\mathtt{n}=1}^{\mathtt{N}}\frac{\mathtt{n}\Omega}{2P_2r_h^2}\left[\log\left(\frac{\gamma_{\mathtt{n}+1}}{\gamma_{\mathtt{n}}}\right)-\mathrm{Ei}\left(-\frac{\Omega\gamma_{\mathtt{n}+1}}{2\overline{\gamma}P_2r_h^2}\right)+\mathrm{Ei}\left(-\frac{\Omega\gamma_{\mathtt{n}}}{2\overline{\gamma}P_2r_h^2}\right)\right] \tag{5.19}$$

Illustrative examples demonstrating achievable spectral efficiencies by ORA with ACR M-QAM and ADR M-QAM techniques over JFTS faded/shadowed wireless communication link are presented in Section 5.6.

5.3.3 Average Bit Error Rate

The expression for BER of ADR M-QAM with constant power ORA transmission over JFTS faded/shadowed communication channel can be computed as the ratio of the number of bits in error to the total average number of transmitted bits,

$$\left\langle\mathrm{BER}\right\rangle_{\mathrm{ADR}}^{\mathrm{JFTS}} \;=\; \frac{\sum_{\mathtt{n}=1}^{\mathtt{N}}\mathtt{n}\overline{\mathrm{BER}}_{\mathtt{n}}}{\langle\mathtt{R}/B\rangle_{\mathrm{ADR}}^{\mathrm{JFTS}}} \tag{5.20}$$

where $\langle \mathtt{R}/B\rangle_{\text{ADR}}^{\text{JFTS}}$ is given by (5.19) while,

$$\overline{\text{BER}}_{\mathtt{n}} = \int_{\gamma_{\mathtt{n}}}^{\gamma_{\mathtt{n}+1}} \text{BER}(M_{\mathtt{n}},\gamma)\ f_{\gamma}(\gamma)\text{d}\gamma \tag{5.21}$$

Using the closed-form solution to the integral from [48], the final expression of $\overline{\text{BER}}_{\mathtt{n}}$ can be obtained in terms of the JFTS parameters as,

$$\begin{aligned}\overline{\text{BER}}_{\mathtt{n}} =& \frac{0.2\Omega}{2P_2 r_h^2}\Bigg[\text{Ei}\bigg(-\frac{1.6\gamma_{\mathtt{n}+1}}{M_{\mathtt{n}}-1}\bigg) + \text{Ei}\bigg(\gamma_{\mathtt{n}}\bigg(\frac{\Omega}{2\overline{\gamma}P_2 r_h^2} + \frac{1.6}{M_{\mathtt{n}}-1}\bigg)\bigg)\\ &-\ \text{Ei}\bigg(-\frac{1.6\gamma_{\mathtt{n}}}{M_{\mathtt{n}}-1}\bigg) - \text{Ei}\bigg(\gamma_{\mathtt{n}+1}\bigg(\frac{\Omega}{2\overline{\gamma}P_2 r_h^2} + \frac{1.6}{M_{\mathtt{n}}-1}\bigg)\bigg)\Bigg]\end{aligned} \tag{5.22}$$

Simulation results for the ABER over JFTS faded/shadowed channel for the different number of fading regions $\mathtt{N}$ are presented in Section 5.6.

5.4 Degrees of Freedom in Adaptive Modulation

The instantaneous CSNR and its PDF only reflect the influence of the channel on the CSNR and not the influence of a varying transmit power. In general, in an adaptive modulation scheme, the transmit power will vary depending on $\gamma(\mathsf{i})$ and will thus be denoted by $\mathtt{S}[\gamma(\mathsf{i})]$, where $\gamma(\mathsf{i})$ is the instantaneous received CSNR over the ith symbol. Hence, the instantaneously received CSNR can then be given by $\gamma(\mathsf{i})\mathtt{S}[\gamma(\mathsf{i})]/\overline{\mathtt{S}}$. It should be noted that the PDF of the received CSNR is different from the PDF in (5.2) when the modulation uses a varying transmit power. To make the notation simpler, the time index i will be omitted and γ and $\mathtt{S}(\gamma)$ will be used instead.

The rest of this section is organized as below. Subsection 5.4.1 derives the instantaneous BER (I-BER) of adaptive power and/or rate M-QAM over a JFTS faded/shadowed channel. The optimum rate region and power region boundaries are derived in Subsections 5.4.2, 5.4.3, 5.4.4 and 5.4.5 under different constraints of rate, power and BER.

5.4.1 Adaptive Rate and Power M-QAM

The transmitter adjusts the constellation size, and possibly also the transmit power, based on the instantaneous CSNR, γ. Evaluation of the optimal power and constellation size (or rate) adjustments, which maximize the spectral efficiency and satisfy the BER requirements, requires an invertible expression for the BER as a function of γ. Assuming a square M-QAM with Gray-coded bits, constellation size, $M_{\mathtt{n}}$ and transmit power, $\mathtt{S}(\gamma)$, the instantaneous BER (I-BER) as a function of γ on an AWGN channel is approximated by,

$$\mathrm{BER}(\gamma) \;\approx\; 0.2\mathrm{exp}\left(-\frac{1.6\gamma\mathtt{S}(\gamma)}{(M_{\mathtt{n}}-1)\overline{\mathtt{S}}}\right) \tag{5.23}$$

which is tight within 1 dB for $M_{\mathtt{n}} \geq 4$ and BER $\leq 10^{-3}$. Moreover the I-BER as a function of the instantaneous CSNR γ over a JFTS faded/shadowed channel can be obtained as,

$$\begin{aligned}
\mathrm{BER}_{\mathtt{n}}(\gamma_{\mathtt{n}}\mathtt{S}/\overline{\mathtt{S}}) &= \int_{\gamma_{\mathtt{n}}}^{\infty} \mathrm{BER}(\gamma) f_{\gamma}(\gamma)\mathrm{d}\gamma \\
&= \int_{\gamma_{\mathtt{n}}}^{\infty} \frac{0.2\Omega}{2\gamma P_2 r_h^2}\, e^{-\frac{1.6\mathtt{S}\gamma}{\overline{\mathtt{S}}(M_{\mathtt{n}}-1)}}\,\mathrm{d}\gamma - \int_{\gamma_{\mathtt{n}}}^{\infty} \frac{0.2\Omega}{2\gamma P_2 r_h^2}\, e^{-\frac{1.6\mathtt{S}\gamma}{\overline{\mathtt{S}}(M_{\mathtt{n}}-1)} - \frac{\Omega\gamma}{2\overline{\gamma}P_2 r_h^2}}\,\mathrm{d}\gamma \\
&= \frac{0.2\;\Omega}{2P_2 r_h^2}\left[\mathrm{Ei}\left(\frac{1.6\mathtt{S}\gamma_{\mathtt{n}}}{\overline{\mathtt{S}}(1-M_{\mathtt{n}})} - \frac{\Omega\gamma_{\mathtt{n}}}{2\overline{\gamma}P_2 r_h^2}\right) - \mathrm{Ei}\left(\frac{1.6\mathtt{S}\gamma_{\mathtt{n}}}{\overline{\mathtt{S}}(1-M_{\mathtt{n}})}\right)\right]
\end{aligned} \tag{5.24}$$

where $\mathrm{Ei}(\cdot)$ is the exponential integral.

5.4.2 Adaptive Rate, Maximum BER and Constant Power

One simple form of adaptive modulation is when only the transmission rate $\mathtt{R} = \mathtt{R}[\gamma(\mathtt{i})]$ is changed when the channel power gain changes. The BER can be kept below a certain maximum value, although the number of bits per symbol $b = b[\gamma(\mathtt{i})]$ is increased with increasing channel power gain. In this case, however, no transmission should be done below a certain value of the channel power gain or the BER will be higher than the maximum allowed value. Assuming that $\mathtt{N}$ different modulation constellations are used, each with $b_{\mathtt{n}}$ bits per symbol, we can use the $\mathtt{n}$th constellation when $\gamma_{\mathtt{n}} \leq \gamma < \gamma_{\mathtt{n}+1}$, where $0 \leq \mathtt{n} \leq \mathtt{N}-1$ and $\gamma_{\mathtt{N}} = \infty$. These intervals are referred to as rate regions. The transmit power becomes,

$$\mathtt{S}(\gamma) = \begin{cases} \mathtt{S} & \gamma \geq \gamma_0 \\ 0 & \gamma < \gamma_0 \end{cases}$$

such that the average transmitted power is the same as when $\mathtt{S}(\gamma) = \overline{\gamma}$ for all γ. The transmitted power can be increased when transmission occurs, resulting in a somewhat higher received CSNR for a given channel power gain as compared with the case when the transmit power is constant. Thus the channel can be used at somewhat lower channel power gains without violating the BER requirement, which will increase the spectral efficiency of the link.

A communication link should normally operate at or below a certain maximum BER. This design goal parameter will be denoted by TBER. Thus $\mathrm{BER}(\gamma\mathtt{S}/\overline{\mathtt{S}}) \leq \mathrm{TBER}$ for all $\gamma \geq \gamma_0$, where $\mathrm{BER}(\cdot)$ is a function relating the BER to the instantaneous SNR for the modulation scheme considered. For this particular scheme, this will be fulfilled if, $\mathrm{BER}_{\mathtt{n}}(\gamma_{\mathtt{n}}\mathtt{S}/\overline{\mathtt{S}}) \leq \mathrm{TBER}$ for $0 \leq n \leq \mathtt{N}-1$, where $\mathrm{BER}_{\mathtt{n}}(\gamma_{\mathtt{n}}\mathtt{S}/\overline{\mathtt{S}})$ refers to the BER for modulation $\mathtt{n}$ at the received CSNR, $\gamma_{\mathtt{n}}\mathtt{S}/\overline{\mathtt{S}}$, which corresponds to the lowest CSNR for this modulation . Now it remains to find the $\mathtt{N}$ rate region boundaries $\gamma_{\mathtt{n}}$ fulfilling the TBER constraint with equality. Hence,

$$\mathrm{BER}_{\mathtt{n}}(\gamma_{\mathtt{n}}\mathtt{S}/\overline{\mathtt{S}}) = \mathrm{TBER} \tag{5.25}$$

Using infinite series expansion of the exponential function used in (5.24) and putting it back in

(5.25), the final expression for the rate region boundaries can be obtained as,

$$\gamma_{\mathtt{n}} = \sum_{\mathsf{k}=0}^{\infty}\sum_{v=0}^{\mathsf{k}}\left(\frac{\overline{\gamma}\overline{\mathtt{S}}(1-M_{\mathtt{n}})v}{1.6\mathtt{S}\overline{\gamma}+\mathcal{B}\overline{\mathtt{S}}(M_{\mathtt{n}}-1)}\right)\mathsf{W}\left[\left(\frac{1.6\mathtt{S}\overline{\gamma}+\mathcal{B}\overline{\mathtt{S}}(M_{\mathtt{n}}-1)}{\overline{\gamma}\overline{\mathtt{S}}(1-M_{\mathtt{n}})v}\right)\right.$$
$$\left.\cdot\left(\frac{\mathrm{TBER}(\mathsf{k}+1)\overline{\gamma}^{\mathsf{k}+1}}{0.2(v!)\mathcal{B}^{\mathsf{k}+2}}\right)^{1/v}\left(\frac{1.6\mathtt{S}\overline{\gamma}-\mathcal{B}\overline{\mathtt{S}}(M_{\mathtt{n}}-1)}{\overline{\gamma}\overline{\mathtt{S}}(1-M_{\mathtt{n}})}\right)^{\frac{\mathsf{k}+1-v}{v}}\right] \tag{5.26}$$

where $\mathcal{B} = \frac{\Omega}{2P_2 r_h^2}$ and $\mathsf{W}(\cdot)$ is the Product Log function defined as the Lambert-W function.

The two most important performance measures of this adaptive modulation scheme is the spectral efficiency and the average BER for a given value of $\mathtt{N}$ for a given value of $\overline{\mathtt{S}}$ and $\overline{\gamma}$. Assuming Nyquist data pulses at the lowest possible bandwidth $1/\tau_s$, where τ_s is the symbol period of the modulation. The spectral efficiency becomes,

$$\begin{aligned}\eta &= \sum_{\mathtt{n}=0}^{\mathtt{N}-1} b_{\mathtt{n}}\int_{\gamma_{\mathtt{n}-1}}^{\gamma_{\mathtt{n}}} f_{\gamma}(\gamma)\mathrm{d}\gamma \\ &= \sum_{\mathtt{n}=0}^{\mathtt{N}-1} b_{\mathtt{n}}\mathcal{B}\left[\log\left(\frac{\gamma_{\mathtt{n}}}{\gamma_{\mathtt{n}-1}}\right)-\mathrm{Ei}\left(-\frac{\mathcal{B}\gamma_{\mathtt{n}}}{\overline{\gamma}}\right)+\mathrm{Ei}\left(-\frac{\mathcal{B}\gamma_{\mathtt{n}-1}}{\overline{\gamma}}\right)\right]\end{aligned} \tag{5.27}$$

where $\mathrm{Ei}(\cdot)$ is the exponential integral.

5.4.3 Adaptive Rate, Average BER and Constant Power

One drawback with design procedure described above is that the instantaneous BER is lower than the target BER, TBER at all instantaneous SNRs except the rate region boundary points, $\gamma_{\mathtt{n}}$ for $0 \leq \mathtt{n} \leq \mathtt{N}-1$. Therefore, the average BER will also be lower than TBER for all channels. Another design rule avoiding this drawback is to require the average BER to become equal to the target BER. It is hard to find the rate region boundaries for this case. A suboptimal solution to this optimization problem is to assume that all the rate region boundaries for the average BER constraint optimization problem are equal to a constant (< 1) times the corresponding rate boundaries for the maximum BER design above. Then the constant needs to be found such that the average BER constraint is fulfilled. This constant will depend on the average SNR. In order to investigate this technique first of all the constant transmit power (average transmit power) constraint is needed to be calculated as below,

$$\frac{\mathtt{S}}{\overline{\mathtt{S}}} = \frac{1}{\int_{\gamma_0}^{\infty} f_\gamma(\gamma)\mathrm{d}\gamma} \tag{5.28}$$

where γ_0 is the lower threshold for instantaneous CSNR and hence,

$$\mathtt{S} = \frac{\overline{\mathtt{S}}}{\mathcal{B}}\left[\mathrm{Ei}\left(-\frac{\mathcal{B}\gamma_0}{\overline{\gamma}}\right) - \log(\gamma_0)\right]^{-1} \tag{5.29}$$

From the optimization criterion, the Lagrangian function can be used to form the following equality constraint,

$$J(\gamma_0, \gamma_1, \ldots, \gamma_{\mathtt{N}-1}) = \sum_{\mathtt{n}=0}^{\mathtt{N}-1} b_{\mathtt{n}} \int_{\gamma_{\mathtt{n}-1}}^{\gamma_{\mathtt{n}}} f_\gamma(\gamma)\mathrm{d}\gamma + \lambda\Big(\sum_{\mathtt{n}=0}^{\mathtt{N}-1} b_{\mathtt{n}} \int_{\gamma_{\mathtt{n}-1}}^{\gamma_{\mathtt{n}}} (\mathrm{BER}_{\mathtt{n}}(\gamma_{\mathtt{n}}) - \mathrm{TBER}) f_\gamma(\gamma)\mathrm{d}\gamma\Big) \tag{5.30}$$

Using the above mentioned optimization technique, the optimum rate region boundaries can be found through solving,

$$\frac{\partial J}{\partial \gamma_{\mathtt{n}}} = 0 \qquad\qquad 0 \le \mathtt{n} \le \mathtt{N} - 1 \tag{5.31}$$

resulting in,

$$\mathrm{BER}_{\mathtt{n}}(\gamma_{\mathtt{n}}) = \mathrm{TBER} - \frac{1}{\lambda} \tag{5.32}$$

Using infinite series expansion of the exponential function used in (5.24) and putting it back in (5.32), the final expression for the rate region boundaries can be obtained as,

$$\begin{aligned}\gamma_{\mathtt{n}} \; &= \sum_{\mathsf{k}=0}^{\infty}\sum_{v=0}^{\mathsf{k}} \left(\frac{\overline{\gamma}\overline{\mathtt{S}}(1-M_{\mathtt{n}})v}{1.6\mathtt{S}\overline{\gamma} + \mathcal{B}\overline{\mathtt{S}}(M_{\mathtt{n}}-1)}\right) \mathsf{W}\Bigg[\left(\frac{1.6\mathtt{S}\overline{\gamma} + \mathcal{B}\overline{\mathtt{S}}(M_{\mathtt{n}}-1)}{\overline{\gamma}\overline{\mathtt{S}}(1-M_{\mathtt{n}})v}\right) \\ &\cdot \left(\frac{(\mathrm{TBER} - 1/\lambda)(\mathsf{k}+1)\overline{\gamma}^{\mathsf{k}+1}}{0.2(v!)\mathcal{B}^{\mathsf{k}+2}}\right)^{1/v} \left(\frac{1.6\mathtt{S}\overline{\gamma} - \mathcal{B}\overline{\mathtt{S}}(M_{\mathtt{n}}-1)}{\overline{\gamma}\overline{\mathtt{S}}(1-M_{\mathtt{n}})}\right)^{\frac{\mathsf{k}+1-v}{v}}\Bigg]\end{aligned} \tag{5.33}$$

where $\mathsf{W}(\cdot)$ is the Product Log function defined as the Lambert-W function.

5.4.4 Constant Rate and Adaptive Power

In the section above, the channel power gain defined the rate used in the transmitter, while the power was kept constant. It is also possible to keep the bit rate constant but adapt the power such that the target BER constraint is fulfilled. This means that a fixed modulation with b bits per symbol is used when $\gamma \geq \gamma_0$. If the transmit power $\mathtt{S}(\gamma)$ is chosen such that BER becomes equal to the TBER for all $\gamma \geq \gamma_0$, an instantaneous BER constraint is fulfilled. Hence,

$$\sum_{\mathsf{k}=0}^{\infty}\sum_{v=0}^{\mathsf{k}} \frac{0.2v!}{(\mathsf{k}+1)} \frac{\mathcal{B}^{\mathsf{k}+2}}{\overline{\gamma}^{\mathsf{k}+1}} \left(\frac{\overline{\mathtt{S}}\overline{\gamma}}{1.6\mathtt{S}\overline{\gamma} - \mathcal{B}\overline{\mathtt{S}}}\right)^{\mathsf{k}+1-v} \gamma^{v}\ e^{-\left(\frac{1.6\mathtt{S}}{\overline{\mathtt{S}}}+\frac{\mathcal{B}}{\overline{\gamma}}\right)\gamma} = \text{TBER} \tag{5.34}$$

The final expression for the transmit power $\mathtt{S}(\gamma)$ can be obtained as,

$$\mathtt{S} = \sum_{\mathsf{k}=0}^{\infty}\sum_{v=0}^{\mathsf{k}} \frac{\mathsf{k}+1-v}{\mathtt{D}_3}\ \mathsf{W}\left[\frac{\mathtt{D}_3}{\mathtt{D}_1(\mathsf{k}+1-v)}\left(\mathtt{D}_4\ e^{-\frac{\mathtt{D}_2\mathtt{D}_3}{\mathtt{D}_1}}\right)^{\frac{1}{\mathsf{k}+1-v}}\right] + \mathtt{D}_2 \qquad \gamma \geq \gamma_0 \tag{5.35}$$

where

$$\mathtt{D}_1 = 1.6\overline{\gamma}, \mathtt{D}_2 = \mathcal{B}\overline{\mathtt{S}}, \mathtt{D}_3 = \frac{1.6\gamma}{\overline{\mathtt{S}}}, \mathtt{D}_4 = (\overline{\mathtt{S}}\overline{\gamma})^{\mathsf{k}+1-v}\ e^{-\mathcal{B}\gamma/\overline{\gamma}}\left(\frac{\gamma^{v}\ 0.2\ v!\ \mathcal{B}^{\mathsf{k}+2}}{\text{TBER}\ (\mathsf{k}+1)\ \overline{\gamma}^{\mathsf{k}+1}}\right) \tag{5.36}$$

Here γ_0 must be chosen such that the average power $\overline{\mathtt{S}}$ becomes,

$$\int_{\gamma_0}^{\infty} \mathtt{S}(\gamma) f_\gamma(\gamma)\mathrm{d}\gamma = \overline{\mathtt{S}} \tag{5.37}$$

After evaluating the transmit power function $S_{\mathtt{n}}(\gamma)$ and the corresponding lower CSNR threshold $\gamma_{0,\mathtt{n}}$ for all considered modulations $0 \leq \mathtt{n} \leq \mathtt{N}-1$ using the formulas above, the spectral efficiency becomes,

$$\begin{aligned} \eta &= \max_{b_{\mathtt{n}};0\leq\mathtt{n}\leq\mathtt{N}-1}\left\{b_{\mathtt{n}} \int_{\gamma_{0,\mathtt{n}}}^{\infty} f_\gamma(\gamma)\mathrm{d}\gamma\right\} \\ &= \max_{b_{\mathtt{n}};0\leq\mathtt{n}\leq\mathtt{N}-1} \sum_{\mathsf{k}=0}^{\infty} \frac{b_{\mathtt{n}}\mathcal{B}}{(\mathsf{k}+1)!}\ \Gamma\left(\mathsf{k}+1, \frac{\mathcal{B}\gamma_{0,\mathtt{n}}}{\overline{\gamma}}\right) \end{aligned} \tag{5.38}$$

It can also be verified that the average BER becomes equal to the target BER which the scheme was designed for.

5.4.5 Adaptive Rate and Power

Let us now turn to the most general case of adaptive QAM modulation, where both the rate and the power are chosen based on channel power gain information. We assume $\mathtt{N}$ modulations, with the $\mathtt{n}$th used when $\gamma_{\mathtt{n}-1} \leq \gamma < \gamma_{\mathtt{n}}$ and carrying $b_{\mathtt{n}}$ bits per symbol. When the instantaneous BER is required to be equal to the target BER for all CSNRs, the transmit power can be obtained using the constraint in (5.25) as,

$$\mathtt{S}_{\mathtt{n}} = \sum_{\mathsf{k}=0}^{\infty}\sum_{v=0}^{\mathsf{k}} \frac{(\mathsf{k}+1-v)\overline{\mathtt{S}}(M_{\mathtt{n}}-1)}{1.6\gamma_{\mathtt{n}}} \mathsf{W}\left[\frac{\gamma_{\mathtt{n}}}{\overline{\gamma}(v-\mathsf{k}-1)}\left(\frac{\gamma_{\mathtt{n}}^{v}0.2v!\mathcal{B}^{\mathsf{k}+2}}{\overline{\gamma}^{v}(\mathsf{k}+1)\mathrm{TBER}}\right)^{\frac{1}{\mathsf{k}+1-v}}\right] + \frac{\mathcal{B}\overline{\mathtt{S}}(1-M_{\mathtt{n}})}{1.6\overline{\gamma}} \tag{5.39}$$

The optimization problem can be simplified to a search for the optimal rate region boundaries. For this purpose, the Lagrangian function can be formed from the spectral efficiency criterion and the power constraint, which here will be treated as an equality constraint. It is given by,

$$J(\gamma_0,\gamma_1,\ldots,\gamma_{\mathtt{N}-1}) = \sum_{\mathtt{n}=0}^{\mathtt{N}-1} b_{\mathtt{n}} \int_{\gamma_{\mathtt{n}-1}}^{\gamma_{\mathtt{n}}} f_{\gamma}(\gamma)\mathrm{d}\gamma + \lambda\Big(\sum_{\mathtt{n}=0}^{\mathtt{N}-1} b_{\mathtt{n}} \int_{\gamma_{\mathtt{n}-1}}^{\gamma_{\mathtt{n}}} \mathtt{S}_{\mathtt{n}}(\gamma) f_{\gamma}(\gamma)\mathrm{d}\gamma - \overline{\mathtt{S}}\Big) \tag{5.40}$$

where $\lambda \neq 0$ is the Lagrange multiplier. Solving,

$$\frac{\partial J}{\partial \gamma_{\mathtt{n}}} = 0 \qquad\qquad 0 \leq \mathtt{n} \leq \mathtt{N}-1 \tag{5.41}$$

results in,

$$\mathtt{S}_{\mathtt{n}-1}(\gamma_{\mathtt{n}}) - \mathtt{S}_{\mathtt{n}}(\gamma_{\mathtt{n}}) = \frac{b_{\mathtt{n}} - b_{\mathtt{n}-1}}{\lambda} \tag{5.42}$$

where $b_{-1} = 0$ and $\mathtt{S}_{-1}(\gamma) = 0$. From (5.25) and (5.38), the following expression can be arrived at,

$$\sum_{\mathsf{k}=0}^{\infty}\sum_{v=0}^{\mathsf{k}} \frac{(\mathsf{k}+1-v)\overline{\mathtt{S}}}{1.6\gamma_{\mathtt{n}}} \mathsf{W}\left[\frac{\gamma_{\mathtt{n}}}{\overline{\gamma}(v-\mathsf{k}-1)}\left(\frac{\gamma_{\mathtt{n}}^{v}0.2v!\mathcal{B}^{\mathsf{k}+2}}{\overline{\gamma}^{v}(\mathsf{k}+1)\mathrm{TBER}}\right)^{\frac{1}{\mathsf{k}+1-v}}\right]\Big(M_{\mathtt{n}-1} - M_{\mathtt{n}}\Big) + \frac{\mathcal{B}\overline{\mathtt{S}}}{1.6\overline{\gamma}}\Big(M_{\mathtt{n}-1} - M_{\mathtt{n}}\Big)$$
$$= \frac{b_{\mathtt{n}} - b_{\mathtt{n}-1}}{\lambda} \tag{5.43}$$

or,

$$\sum_{\mathsf{k}=0}^{\infty}\sum_{v=0}^{\mathsf{k}}\frac{1}{\gamma_{\mathtt{n}}}\,\mathsf{W}\left[\left(\frac{\gamma_{\mathtt{n}}}{\overline{\gamma}}\right)^{\frac{\mathsf{k}+1}{\mathsf{k}+1-v}}\frac{1}{(v-\mathsf{k}-1)}\left(\frac{0.2v!\mathcal{B}^{\mathsf{k}+2}}{(\mathsf{k}+1)\mathrm{TBER}}\right)^{\frac{1}{\mathsf{k}+1-v}}\right]$$
$$= \sum_{\mathsf{k}=0}^{\infty}\sum_{v=0}^{\mathsf{k}}\frac{1.6\overline{\mathsf{S}}}{\mathsf{k}+1-v}\left(\frac{b_{\mathtt{n}}-b_{\mathtt{n}-1}}{\lambda(M_{\mathtt{n}-1}-M_{\mathtt{n}})}+\frac{\mathcal{B}\overline{\mathsf{S}}}{1.6\overline{\gamma}}\right) \tag{5.44}$$

Solving the above equation the expression for the optimum rate region boundaries $\gamma_{\mathtt{n}}$ can be obtained.

Also in a general case, an average BER constraint can be used instead of an instantaneous BER constraint. Then the power does not have to be chosen such that BER is equal to the target BER for all CSNRs, but it is enough that BER on average is equal to the constraint. This problem can also be solved using a Lagrangian method but now the Lagrangian equation has to include a third term that corresponds to the average BER constraint in addition to the two terms used already above in (5.41).

5.5 Adaptive Coded Modulation

The purpose of this section is to obtain closed-form expressions for average spectral efficiency (ASE), ABER and outage probability of the adaptive Trellis coded modulation (TCM) M-QAM over a JFTS faded/shadowed communication channel, assuming perfect CSI to be available at the receiver. The expressions for ASE and outage probability are exact, the derivations of which are provided in Subsection 5.5.1 and Subsection 5.5.4. The ABER expression is derived in Subsection 5.5.3 and is an approximation which relies on the exponential type curve fitting for the conditional BER (CBER).

The proposed adaptive TCM scheme utilizes a set of $\mathtt{L}$ two-dimensional (2$\mathtt{L}$-D) trellis codes with different constellation sizes, similar to [114], where $\mathtt{L}$ is a positive integer. Let $\mathtt{N}$ denote the number of constellations available at the transmitter, each of size $M_{\mathtt{n}}$ with $b_{\mathtt{n}} = \log_2 M_{\mathtt{n}}$ bits per symbol for $\mathtt{n} = 1, \ldots, \mathtt{N}$. A 2$\mathtt{L}$-D signal constellation is obtained by $\mathtt{L}$-fold Cartesian products of 2-D signal constellations. At every $\mathtt{L}$th transmission time instant, $\mathtt{B} = \mathtt{L} \times b_{\mathtt{n}}$ coded bits are mapped onto $\mathtt{L}$ symbols, each from a 2-D constellation of size $M_{\mathtt{n}}$ for $\mathtt{n} = 1, \ldots, \mathtt{N}$. These symbols are sent during $\mathtt{L}$ consecutive symbol intervals. At the receiver, soft decoding based on the Viterbi algorithm is performed where the squared Euclidean distance is used as metric in the decoder.

Let $\{\gamma_{\mathtt{n}}\}_{\mathtt{n}=0}^{\mathtt{N}}$ represent the set of CSNR thresholds used to switch between $\mathtt{N}+1$ different transmission modes, including no transmission when $0 \leq \gamma \leq \gamma_0$. For convenience, let $\gamma_{-1} \approx 0$ and $\gamma_{\mathtt{N}} \approx \infty$. When $\gamma_{\mathtt{n}-1} \leq \gamma \leq \gamma_{\mathtt{n}}$, the $\mathtt{n}$th transmission mode is set at the transmitter employing a coding scheme with rate $\mathtt{R}_{\mathtt{n}}$ and CBER in this case will be denoted by $\mathrm{CBER}_{\mathtt{n}}(\gamma)$.

5.5.1 Average Spectral Efficiency

If the variable rate ACM over JFTS channels uses a set of $\mathtt{N}$ different codes with different spectral efficiencies, the ASE can be expressed as the weighted sum of the information rates, $\mathtt{R}_{\mathtt{n}}$, for the individual codes, $\mathtt{n}$. Hence, the final expression for ASE can be given by,

$$\mathrm{ASE}(\gamma) = \sum_{\mathtt{n}=1}^{\mathtt{N}} \mathtt{R}_{\mathtt{n}} \int_{\gamma_{\mathtt{n}-1}}^{\gamma_{\mathtt{n}}} f_\gamma(\gamma) \mathrm{d}\gamma \tag{5.45}$$

Using the integral solution from [48], the expression from (5.45) can be written as,

$$\mathrm{ASE}(\gamma) = \sum_{\mathtt{n}=1}^{\mathtt{N}} \mathtt{R}_{\mathtt{n}} \mathcal{B} \left[\log\left(\frac{\gamma_{\mathtt{n}}}{\gamma_{\mathtt{n}-1}}\right) - \mathrm{Ei}\left(-\frac{\mathcal{B}\gamma_{\mathtt{n}}}{\overline{\gamma}}\right) + \mathrm{Ei}\left(-\frac{\mathcal{B}\gamma_{\mathtt{n}-1}}{\overline{\gamma}}\right)\right] \tag{5.46}$$

Subsection 5.5.2 will be concentrated on finding the optimum rate region boundaries such that the ASE is maximized subject to two constraints. The first constraint considered in this study is the

TBER constraint given by, $\mathrm{BER}_{\mathtt{n}}(\gamma) \leq \mathrm{TBER}$, where $\mathrm{BER}_{\mathtt{n}}(\gamma)$ is the instantaneous BER of the modulation with constellation size of $M_{\mathtt{n}}$ in terms of the instantaneous CSNR and TBER denotes the target BER. This constraint guarantees that the average BER does not exceed the TBER. The second constraint is the use of constant average transmit power. However, in this analysis for adaptive coded modulation (ACM), power adaptation is not included since the gain achieved in spectral efficiency by rate adaptation is higher than by using power adaptation and it increases the complexity.

To find the optimal rate region boundaries, an expression for $\mathrm{BER}_{\mathtt{n}}(\gamma)$ is needed. The expression is obtained by averaging $\mathrm{BER}_{\mathtt{n}}(\gamma)$, the instantaneous BER as a function of the instantaneous CSNR, on an AWGN channel over all values of γ, $\mathrm{BER}_{\mathtt{n}}(\gamma) = \int_0^\infty \mathrm{BER}_{\mathtt{n}}(\gamma) f_\gamma(\gamma)\mathrm{d}\gamma$ for $\mathtt{n} = 1, \ldots, \mathtt{N}$, where $f_\gamma(\gamma)$ is given by (5.2).

5.5.2 Adaptive Trellis-coded Modulation (TCM)

Tight approximations for the TCM BER performance on AWGN channels at high CSNR, based on analytical or numerical methods can be expressed as,

$$\mathrm{BER}_{\mathtt{n}}(\gamma) \approx \sum_{\mathtt{l}=1}^{\mathtt{L}} \mathtt{a}_{\mathtt{n}}(\mathtt{l})\exp\left(-\frac{\mathtt{b}_{\mathtt{n}}(\mathtt{l})\gamma}{(M_{\mathtt{n}}-1)}\right) \tag{5.47}$$

Here the parameters $\{\mathtt{a}_{\mathtt{n}}(\mathtt{l})\}_{\mathtt{l}=1}^{\mathtt{L}}$ and $\{\mathtt{b}_{\mathtt{n}}(\mathtt{l})\}_{\mathtt{l}=1}^{\mathtt{L}}$ are real numbers where the later set takes only non-negative values. Consequently, using (5.47) leads to,

$$\mathrm{BER}_{\mathtt{n}}(\gamma) \approx \sum_{\mathtt{l}=1}^{\mathtt{L}} \mathtt{a}_{\mathtt{n}}(\mathtt{l})\mathcal{B}\left[\mathrm{Ei}\left(\frac{\mathtt{b}_{\mathtt{n}}(\mathtt{l})\gamma_{\mathtt{n}}}{1-M_{\mathtt{n}}} - \frac{\mathcal{B}\gamma_{\mathtt{n}}}{\overline{\gamma}}\right) - \mathrm{Ei}\left(\frac{\mathtt{b}_{\mathtt{n}}(\mathtt{l})\gamma_{\mathtt{n}}}{1-M_{\mathtt{n}}}\right)\right] \tag{5.48}$$

The optimal rate region boundaries can then be found by using the TBER constraint as below,

$$\gamma_{\mathtt{n}} = \sum_{\mathtt{k}=0}^{\infty}\sum_{v=0}^{\mathtt{k}}\sum_{\mathtt{l}=1}^{\mathtt{L}}\left(\frac{\overline{\gamma}(1-M_{\mathtt{n}})v}{\mathtt{b}_{\mathtt{n}}(\mathtt{l})\overline{\gamma}+\mathcal{B}(M_{\mathtt{n}}-1)}\right)\mathsf{W}\Bigg[\left(\frac{\mathtt{b}_{\mathtt{n}}(\mathtt{l})\overline{\gamma}+\mathcal{B}(M_{\mathtt{n}}-1)}{\overline{\gamma}(1-M_{\mathtt{n}})v}\right)$$
$$\cdot\left(\frac{\mathrm{TBER}(\mathsf{k}+1)\overline{\gamma}^{\mathsf{k}+1}}{\mathtt{a}_{\mathtt{n}}(\mathtt{l})(v!)\mathcal{B}^{\mathsf{k}+2}}\right)^{1/v}\left(\frac{\mathtt{b}_{\mathtt{n}}(\mathtt{l})\overline{\gamma}-\mathcal{B}(M_{\mathtt{n}}-1)}{\overline{\gamma}(1-M_{\mathtt{n}})}\right)^{\frac{\mathtt{k}+1-v}{v}}\Bigg] \tag{5.49}$$

5.5.3 ABER Performance

The ABER for a general ACM technique is given by,

$$\mathrm{ABER} \approx \frac{1}{\mathrm{ASE}}\sum_{\mathtt{n}=1}^{\mathtt{N}}\mathtt{R}_{\mathtt{n}}\int_{\gamma_{\mathtt{n}-1}}^{\gamma_{\mathtt{n}}}\mathrm{CBER}_{\mathtt{n}}(\bar{\mathsf{x}})f_{\gamma}(\bar{\mathsf{x}})\mathrm{d}\bar{\mathsf{x}} \tag{5.50}$$

where $f_{\gamma}(\cdot)$ represents the PDF of the instantaneous CSNR. This ABER analysis is based on the following well-known assumption for the CBER of the Trellis coded ACM scheme,

$$\langle\mathrm{CBER}_{\mathtt{n}}(\gamma)\rangle_{\mathrm{TCM}} \approx \sum_{\mathtt{l}=1}^{\mathtt{L}}\mathtt{a}_{\mathtt{n}}(\mathtt{l})\exp\left(-\frac{\mathtt{b}_{\mathtt{n}}(\mathtt{l})\gamma}{M_{\mathtt{n}}-1}\right) \qquad (1\leq\mathtt{n}\leq\mathtt{N}) \tag{5.51}$$

where $\{\mathtt{a}_{\mathtt{n}}(\mathtt{l}),\mathtt{b}_{\mathtt{n}}(\mathtt{l})\}_{\mathtt{l}=1,\dots,\mathtt{L},\mathtt{n}=1,\dots,\mathtt{N}}$ is the set of exponential fitting coefficients and $\mathtt{L}$ is the number of exponential approximants. Thus using the approximation (5.45) in the ABER definition given in (5.46) yields,

$$\begin{aligned}\langle\mathrm{ABER}\rangle_{\mathrm{TCM}} &\approx \frac{1}{\mathrm{ASE}}\sum_{\mathtt{n}=1}^{\mathtt{N}}\sum_{\mathtt{l}=1}^{\mathtt{L}}\mathtt{R}_{\mathtt{n}}\mathtt{a}_{\mathtt{n}}(\mathtt{l})\\ &\quad\cdot\left[\int_{0}^{\gamma_{\mathtt{n}}}\exp\left(-\frac{\mathtt{b}_{\mathtt{n}}(\mathtt{l})\gamma}{M_{\mathtt{n}}-1}\right)f_{\gamma}(\bar{\mathsf{x}})\mathrm{d}\bar{\mathsf{x}}-\int_{0}^{\gamma_{\mathtt{n}-1}}\exp\left(-\frac{\mathtt{b}_{\mathtt{n}}(\mathtt{l})\gamma}{M_{\mathtt{n}}-1}\right)f_{\gamma}(\bar{\mathsf{x}})\mathrm{d}\bar{\mathsf{x}}\right]\\ &\approx \frac{1}{\mathrm{ASE}(\gamma)}\sum_{\mathtt{n}=1}^{\mathtt{N}}\sum_{\mathtt{l}=1}^{\mathtt{L}}\mathtt{R}_{\mathtt{n}}\mathtt{a}_{\mathtt{n}}(\mathtt{l})\left[\tilde{\mathcal{G}}_{\gamma}\left(-\frac{\mathtt{b}_{\mathtt{n}}(\mathtt{l})}{M_{\mathtt{n}}-1};\gamma_{\mathtt{n}}\right)-\tilde{\mathcal{G}}_{\gamma}\left(-\frac{\mathtt{b}_{\mathtt{n}}(\mathtt{l})}{M_{\mathtt{n}}-1};\gamma_{\mathtt{n}-1}\right)\right]\end{aligned} \tag{5.52}$$

where $\tilde{\mathcal{G}}_{\gamma}(s;\xi)\triangleq\int_{0}^{\xi}e^{\bar{\mathsf{x}}s}f_{\gamma}(\bar{\mathsf{x}})\mathrm{d}\bar{\mathsf{x}}$ is defined as the complementary moment generating function (complimentary MGF). Hence, first of all, we need to calculate the complimentary MGF for JFTS fading/shadowing, which can be done using the integral solution from [48],

$$\tilde{\mathcal{G}}_{\gamma}(s;\xi) = \mathcal{B}\int_{0}^{\xi}\frac{e^{\bar{\mathsf{x}}s}}{\bar{\mathsf{x}}}\left[1-e^{-\frac{\mathcal{B}\bar{\mathsf{x}}}{2\overline{\gamma}}}\right]\mathrm{d}\bar{\mathsf{x}} = \mathcal{B}\left[\mathrm{Ei}(s\xi)-\mathrm{Ei}\left(\xi\left(\frac{\mathcal{B}}{\overline{\gamma}}-s\right)\right)\right]\ [\xi\geq0]. \tag{5.53}$$

Putting (5.53) back in (5.52), the expression for ABER of the Trellis coded ACM over the JFTS faded/shadowed channel can be obtained as,

$$\begin{aligned}\langle \text{ABER}(\gamma)\rangle_{\text{TCM}} \approx \frac{1}{\text{ASE}(\gamma)} \sum_{\mathtt{n}=1}^{\mathtt{N}} \sum_{\mathtt{l}=1}^{\mathtt{L}} \mathtt{R_n a_n(l)}\, \mathcal{B} \Bigg[&\text{Ei}\Bigg(-\frac{\mathtt{b_n(l)}}{M_{\mathtt{n}}-1}\gamma_{\mathtt{n}} \Bigg) + \text{Ei}\Bigg(\gamma_{\mathtt{n}-1}\Bigg(\frac{\mathcal{B}}{\overline{\gamma}} + \frac{\mathtt{b_n(l)}}{M_{\mathtt{n}}-1} \Bigg)\Bigg) \\ - \ &\text{Ei}\Bigg(\gamma_{\mathtt{n}}\Bigg(\frac{\mathcal{B}}{\overline{\gamma}} + \frac{\mathtt{b_n(l)}}{M_{\mathtt{n}}-1} \Bigg)\Bigg) - \text{Ei}\Bigg(-\frac{\mathtt{b_n(l)}}{M_{\mathtt{n}}-1}\gamma_{\mathtt{n}-1} \Bigg)\Bigg] \end{aligned} \tag{5.54}$$

where $\text{Ei}(\cdot)$ is the exponential integral [39] and therefore can be expressed in terms of elementary functions and infinite series summation.

5.5.4 Outage Probability

For a generic ACM, the outage probability (P_{out}) over a JFTS faded/shadowed channel can then be expressed as,

$$P_{\text{out}}(\gamma) = 1 - \int_{\gamma_0}^{\infty} f_\gamma(\gamma) \mathrm{d}\gamma \;=\; 1 - \left[\sum_{\mathsf{k}=0}^{\infty} \frac{\mathcal{B}}{(\mathsf{k}+1)!} \Gamma\left(\mathsf{k}+1, \frac{\mathcal{B}\gamma_0}{\overline{\gamma}} \right) \right] \tag{5.55}$$

where γ_0 is the threshold instantaneous CSNR below which data transmission over a JFTS channel will be suspended.

5.6 Numerical Results and Discussion

In this section, the derived analytical expressions for achievable channel capacity, spectral efficiencies and average BER of coded and uncoded adaptive M-QAM are numerically evaluated and plotted as functions of the adaptive modulation parameters, JFTS parameters and the adaptive transmission techniques. The analytical results for spectral efficiency and ABER are compared with the simulation results in order to verify the validity of the derived expression. All the results are evaluated using a single input single output (SISO) system and are averaged over 100 inde-

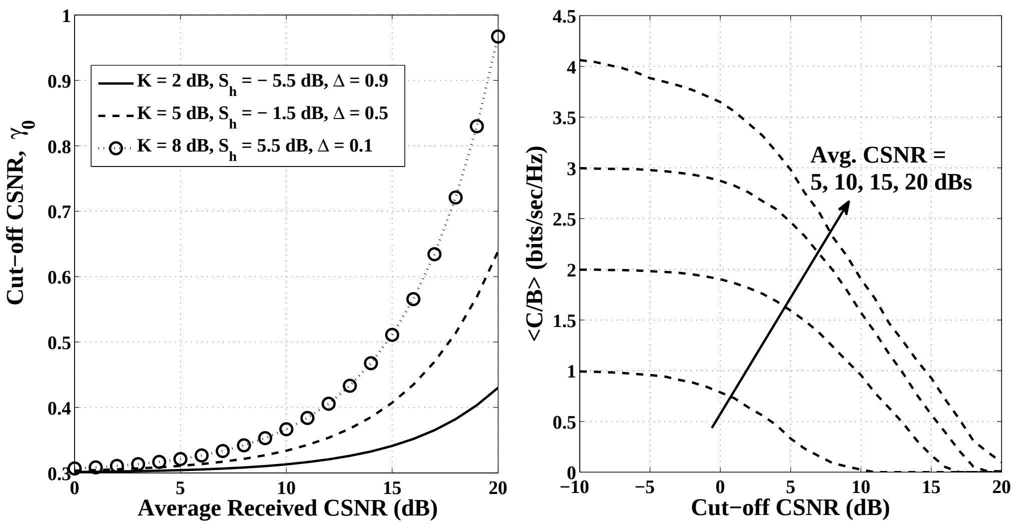

Figure 5.1: (a) Calculated optimal cut-off CSNR (γ_0) for different values of average received CSNR ($\overline{\gamma}$), (b) Channel capacity per unit bandwidth with TIFR over a JFTS channel with $K = 6.5$ dB, $S_h = -2.5$ dB and $\Delta = 0.25$.

pendent random channel realizations.

The rest of this section is organized as follows. Subsection 5.6.1 illustrates the effects of the JFTS parameters on achievable channel capacity of different adaptive transmission techniques over a JFTS faded/shadowed link. Subsection 5.6.2 and Subsection 5.6.3 simulates the performances of adaptive M-QAM and adaptive coded M-QAM over a JFTS faded/shadowed communication link respectively.

5.6.1 Channel Capacity

It has been claimed in [12] that for any fading channel, the optimal cut-off CSNR or optimal threshold satisfies $0 \leq \gamma_0 \leq 1$, if both the transmit power and the modulation rate are varied for optimal adaptation. Results from [113], [115] also indicate that for Rayleigh and Nakagami-m

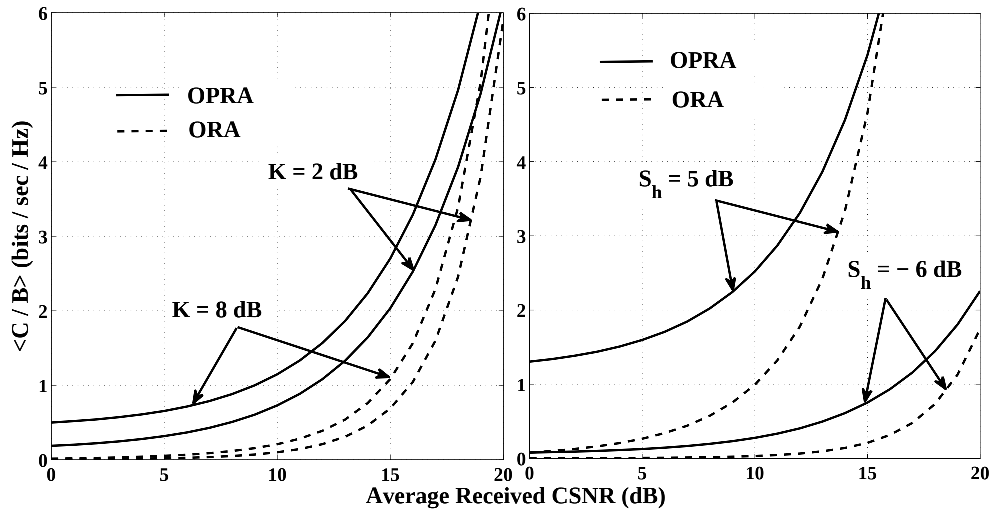

Figure 5.2: Ergodic capacity per unit bandwidth of JFTS communication link with OPRA and ORA, where the curves are generated by (a) varying the K-factor ($S_h = -2$ dB and $\Delta = 0.4$) and (b) varying the S_h-factor ($K = 5$ dB and $\Delta = 0.9$).

fading channels, γ_0 converges to 1 as $\overline{\gamma}$ increases. For a JFTS fading/shadowing channel, the relationship between γ_0 and $\overline{\gamma}$ is demonstrated in Fig. 5.1(a). For a communication link with high K and S_h (low fading and shadowing severity), γ_0 converges to 1 with the increase in $\overline{\gamma}$, as is observed in [12]. However, as the channel condition deteriorates with lower K and S_h, γ_0 remains significantly lower than 1 even at high $\overline{\gamma}$. In such a scenario, perfect knowledge of both the transmit side and the receive side CSI should provide an edge over the perfect knowledge of only the receive side CSI, as claimed in [12]. As a result, regulating both the transmit power and the modulation rate (OPRA) will result in a considerable increase in ergodic capacity over adapting only the modulation rate (ORA). This will be verified by the next plot (Fig. 5.2).

However, for a JFTS faded/shadowed link, the value of γ_0 does not obey the rule that it should be less than 1 or 0 dB in case of sub-optimal adaptation techniques like TIFR. To illustrate this point,

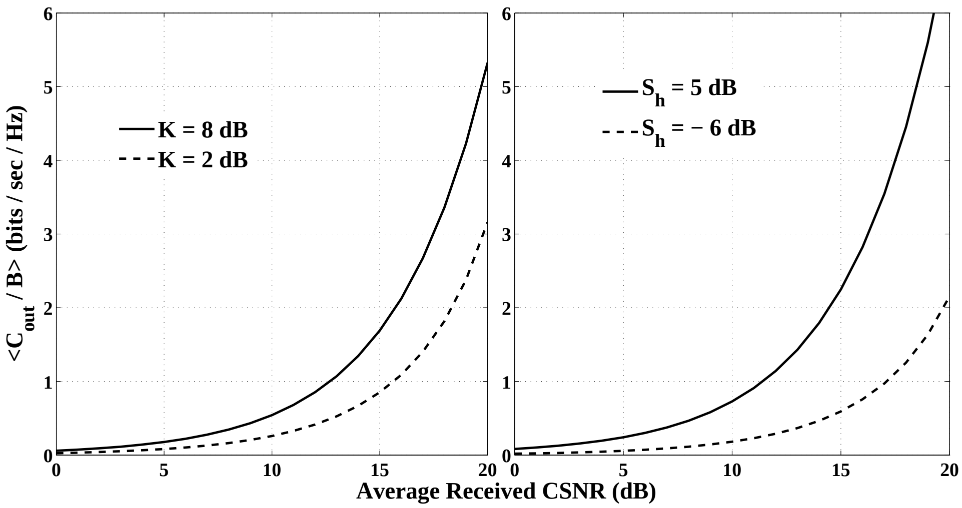

Figure 5.3: Outage capacity per unit bandwidth of JFTS communication link with TIFR, where the curves are generated by (a) varying the K-factor ($S_h = -2$ dB and $\Delta = 0.4$) and (b) varying the S_h-factor ($K = 5$ dB and $\Delta = 0.9$).

the dependence of outage capacity on the cut-off CSNR is plotted in Fig. 5.1(b). The curves are generated for four sets of fixed $\overline{\gamma}$, where the capacity is maximized at the optimal γ_0. For $\overline{\gamma} \geq 5$ dB, γ_0 is bigger than 0 dB. Similar results have also been exhibited in [12] for TIFR in a Rayleigh fading channel, where $\gamma_0 > 0$ dB only for $\overline{\gamma} > 5$ dB. While for JFTS channels, γ_0 has values more than 0 dB even for $\overline{\gamma} = 5$ dB. The reason can be attributed to the high severity in shadowing with a low S_h. As a consequence, at a fixed $\overline{\gamma}$, TIFR has a lower channel capacity and higher outage probability than either OPRA or ORA.

It is claimed in [12] that the difference in channel capacity between OPRA and ORA is bounded by $\mathtt{C}_{\mathrm{OPRA}} - \mathtt{C}_{\mathrm{ORA}} \geq B \log_2\!\left(1 + \int_0^{\gamma_0} (\gamma - \gamma_0) f_\gamma(\gamma) \mathrm{d}\gamma\right)$. As a result, the channel capacity obtained using ORA starts approaching that achievable using OPRA with the increase in $\overline{\gamma}$ for JFTS channels, as is evident in Fig. 5.2(a) and Fig. 5.2(b). Hence it can be concluded by summarizing the results from Fig. 5.2(a) and Fig. 5.2(b) that OPRA offers improvement in ergodic capacity over ORA only when γ_0 remains significantly lower than 1. These observations are similar to that made in [12] and [115] for Rayleigh and Nakagami-m fading channels. The gap between $\mathtt{C}_{\mathrm{OPRA}}$ and $\mathtt{C}_{\mathrm{ORA}}$ increases at lower $\overline{\gamma}$ with the increase in severity of fading (decrease in K) and shadowing (decrease in S_h) both of which degrade the channel quality. These results are in accordance with the general behavior of a wireless communication system over a JFTS faded/shadowed channel. As noted in Chapter 4, performance of any communication system over a JFTS channel deteriorates with the decrease in K and S_h-factors.

The degradation in ergodic capacity due to the decrease in K-factor from 8 dB to 2 dB (refer to Fig. 5.2(a)) is much less compared to the decrease in achievable channel capacity due to the lowering of S_h-factor from 5 dB to -6 dB (refer to Fig. 5.2(b)). These results do not agree with the observations made in Chapter 4, where bit error rate performance of BPSK is found degrade equally either due to the decrease in the K-factor or the S_h-factor. The reason for this can be attributed to the Δ-value chosen for each plot. For Fig. 5.2(a) a low Δ of 0.4 is chosen. In this case shadowing severity is reduced by the fact that only one scattering cluster dominates instead of two clusters. For Fig. 5.2(b) a high Δ of 0.9 is chosen, where the magnitudes of the shadowing values contributed by each scattering cluster are almost equal. As a result, even for a high $\overline{\gamma}$ of 12 dB a penalty of 3 bits/sec/Hz of achievable channel capacity is observed only for decreasing the S_h factor.

On the other hand, the outage capacity with TIFR degrades equally with the lowering of either the small scale fading (K) factor or the shadowing (S_h) factor, as is evident in Fig. 5.3. Hence it can be concluded that the outage capacity of a JFTS communication channel is more sensitive than ergodic capacity to the changes in small scale fading and shadowing. This observation agrees

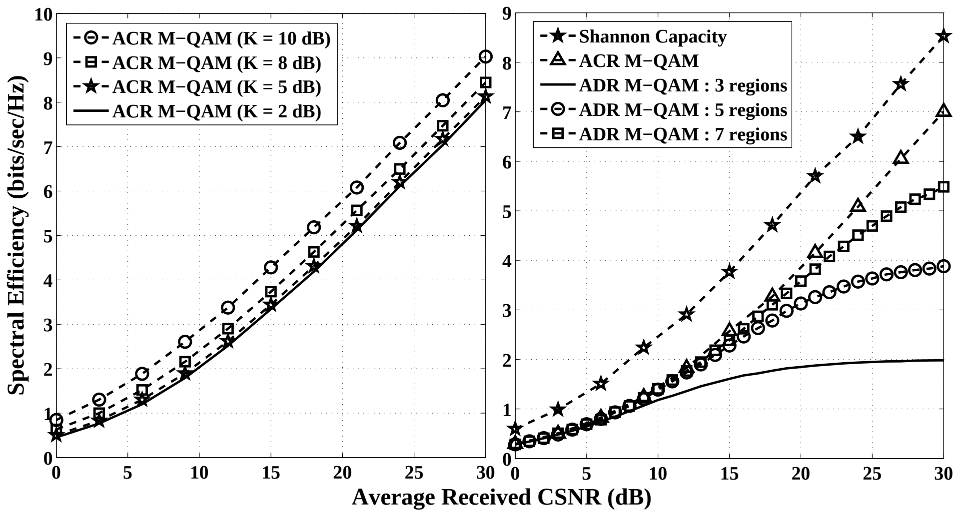

Figure 5.4: Spectral Efficiency of JFTS faded/shadowed link for (a) ACR M-QAM, where curves are generated by varying K, with fixed $S_h = 2$ dB and $\Delta = 0.3$ and (b) ADR M-QAM, where curves are generated by varying $\mathtt{N}$, with $K = 5.5$ dB, $S_h = -7.5$ dB and $\Delta = 0.15$.

with that made in case of Rician channel in presence of shadow fading in [116]. It has also been observed in [116], increase in the severity of shadow fading improves ergodic capacity and degrades outage capacity of a shadowed Rician channel. However, for a JFTS faded/shadowed channel both ergodic and outage capacities are degraded significantly due to the increase in shadowing severity, as is evident from Fig. 5.2 and Fig. 5.3.

5.6.2 Adaptive Modulation

The effect of K-parameter of the JFTS distribution on the spectral efficiency achieved by ACR M-QAM with over JFTS faded/shadowed communication channel are demonstrated in Fig. 5.4(a). As K decreases, the power contributed by the strong specular components reduces in comparison to that contributed by the diffused and scattered components. This yields to a decrease in achievable spectral efficiency using ACR M-QAM with the decrease in K as is evident in Fig. 5.4(a).

However, the improvement in spectral efficiency due to the increase in K-factor from 2 dB to 5 dB is not proportional to the improvement achieved with the increase in K-factor from 8 dB to 10 dB. The reason can be attributed to the fact that both at $K = 2$ dB and $K = 5$ dB, the channel condition is poor and the adaptive transmission is dominated by lower order modulation $(M = 2, 4)$. Data transmission using modulation with higher constellation sizes is only allowed as the channel state improves with the increase in K from 5 dB to 8 dB and then to 10 dB.

Fig. 5.4(b) exhibits the average link spectral efficiency of ACR M-QAM and ADR M-QAM over the JFTS fading/shadowing communication link with parameters, $K = 5.5$ dB, $S_h = -7.5$ dB and $\Delta = 0.15$ at a target BER of 10^{-3}. The Shannon capacity for ORA is also plotted for comparison. The achievable spectral efficiency of ACR M-QAM falls within 4 dB of the Shannon capacity limit. A marginal additional penalty of 1 dB is inflicted by ADR M-QAM with 7 fading regions. These results are similar to that obtained over Rayleigh fading channels in [12], except for lower average CSNRs, $\overline{\gamma} \leq 5$ dB. For Rayleigh fading channels, achievable spectral efficiency with ADR M-QAM is close to zero for $\overline{\gamma} \leq 3$ dB. For JFTS channels, achievable spectral efficiencies using ACR M-QAM and ADR M-QAM are same for $\overline{\gamma} \leq 7$ dB. This enhanced performance at low $\overline{\gamma}$ can have resulted from the high K-factor of 5.5 dB for this set of JFTS parameters. For Rayleigh fading, K-factor is generally considered to be equal to 0 dB. It should be noted that this set of JFTS parameters, the Δ-factor is very low, where the effect of one scattering cluster dominates the other one. As a result, the system performance is effectively affected by only one scattering cluster, even in presence of two. It can also be concluded that higher the number of fading regions taken into account, the better will be the achievable link spectral efficiency using ADR M-QAM.

As an illustrative example, Fig. 5.5(a) exhibits the average BER for ADR M-QAM in JFTS fad-

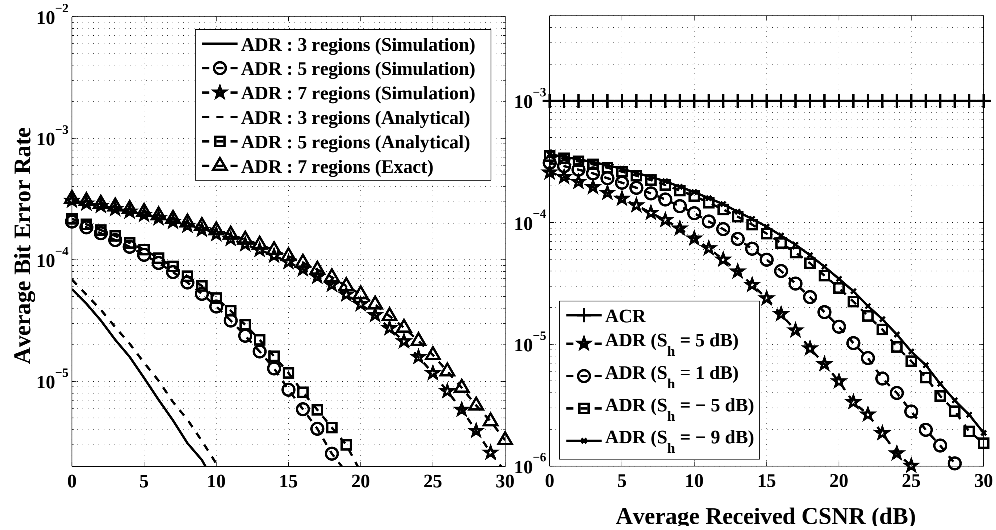

Figure 5.5: ABER of ADR M-QAM over a JFTS faded/shadowed link (a) with $K = 8$ dB, $S_h = 8.5$ dB and $\Delta = 0.45$, where curves are generated by varying $\mathtt{N}$ and (b) with $K = 6$ dB and $\Delta = 0.8$, where curves are generated by varying the S_h-factor.

ing/shadowing for a TBER of 10^{-3}. The curves are generated by plotting the analytical and simulated ABER for a variable number of fading regions. It can be noted that both the simulated and analytical results are always below the TBER of 10^{-3}, while in each case of the analytically predicted BER is slightly higher than the simulated one. This slight difference in performance can be attributed to the approximation considered in the analytical expression using the roots of the Hermite polynomial. It can also be observed that ABER at higher CSNRs for the case of ADR M-QAM with a larger number of fading regions is more than that with a lower number of fading regions. This happens due to the fact that a higher number of fading regions allow a larger constellation size and ADR M-QAM uses the highest available constellation size at high CSNRs. In this case, as the average CSNR increases, the ABER performance becomes dominated by the BER performance of the highest available constellation size. These results are also similar to the observations made in [12] for Rayleigh fading channels except for $\overline{\gamma} \leq 10$ dB, where the analytical

BER is lower than the exact BER. The reason for this observation in [103] is contributed to the fact that ADR M-QAM often uses the 2-QAM constellation at low $\overline{\gamma}$ and the resultant BER is dominated by the BER of 2-QAM. In our case, the JFTS parameters chosen for this set of simulation is $K = 8$ dB, $S_h = 8.5$ dB and $\Delta = 0.45$. With high K and S_h-factors, the adaptive transmission is not dominated by only 2-QAM constellation and hence, the predicted BER is not lower than that of the simulated BER for $\overline{\gamma} \leq 10$ dB.

The final set of curves in this subsection in Fig. 5.5(b) are generated by plotting the average BER of ADR M-QAM with 5 fading regions in comparison with that of ACR M-QAM over a JFTS faded / shadowed communication channel with varying S_h-factor but fixed K and Δ. A larger S_h factor represents larger variations in the main wave amplitudes contributed by each scattering neighborhood. As a result, some discrete shadowing values are higher in magnitude while others are lower, thereby reducing the overall severity of shadowing. On the other hand, a low S_h factor depicts a scenario where each scattering cluster contributes a very small range of discrete shadowing values, higher in magnitude and encountered repeatedly. As the link condition degrades with the decrease in the S_h parameter, average BER performance of ADR M-QAM deteriorates. Average BER of continuous rate adaptation remains fixed at the target BER of 10^{-3} while that of discrete rate adaptation always remains below the target BER.

5.6.3 Adaptive Coded Modulation

For analyzing performance of ACM over a JFTS faded/shadowed channel, a 4-D TCM ($\mathtt{L} = 2$) with 16 states, are utilized with a rate 2/3 convolutional encoder and a bit mapper similar to those used in the International Telecommunication Union's ITU-T V.34 modem standard. Nyquist data pulsing that is $B = 1/\tau_s$ and $\mathtt{N} = 7$ 2-D signaling constellations of sizes $M_{\mathtt{n}} \in \{4, 8, 16, 32, 64, 128, 256\}$,

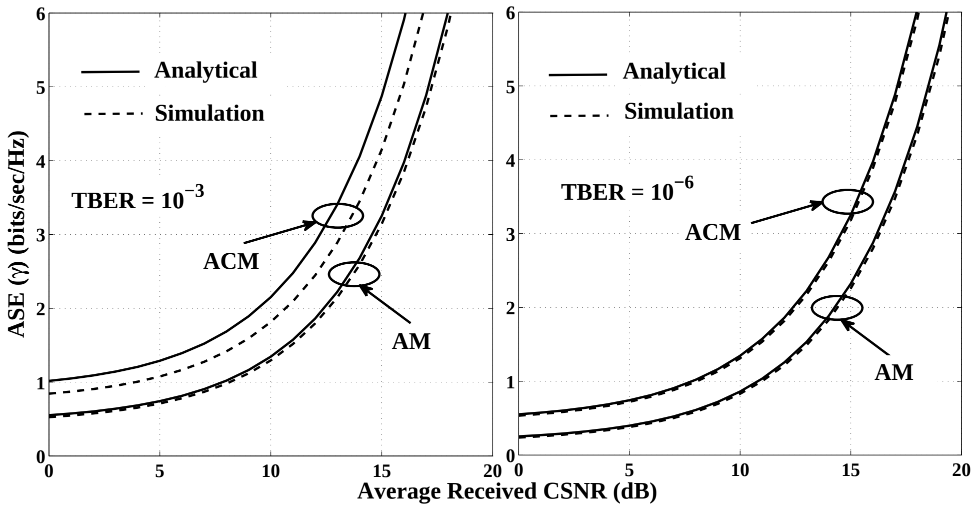

Figure 5.6: Coding gain over the JFTS faded/shadowed channel, with $K = 5$ dB, $S_h = 5.5$ dB and $\Delta = 0.1$ at a TBER of (a) 10^{-3} and (b) 10^{-6}.

corresponding to 4-QAM, 8-STAR, 16-QAM, 32-CROSS, 64-QAM, 128-CROSS and 256-QAM respectively are presumed. At each even time instant, $2 \times b_{\mathtt{n}} - 1$ information bits are encoded to $2 \times b_{\mathtt{n}}$ coded bits whicha re mapped onto two symbols, each from a 2-D constellation of size $M_{\mathtt{n}}$. These symbols are transmitted during the next two time instants and result in an instantaneous data rate given by $\mathtt{R}_{\mathtt{n}} = (b_{\mathtt{n}} - 1/2)B$.

Fig. 5.6(a) shows the simulation results for spectral efficiency of the 7-state 2-D TCM coded M-QAM at a TBER of 10^{-3} in JFTS fading with $K = 5$ dB, $S_h = 5.5$ dB and $\Delta = 0.1$. For comparison, the analytical results for spectral efficiency with and without coding are plotted. The analytical results of the coded case do not exhibit the 3 dB gain predicted by analytical results for Rayleigh fading in [109] relative to the uncoded scheme. The reason for this can be contributed to the presence of shadowing in a JFTS channel model along with fading. A high S_h and a high K is assumed for this set of plot, that means low severity in fading and shadowing. The coding

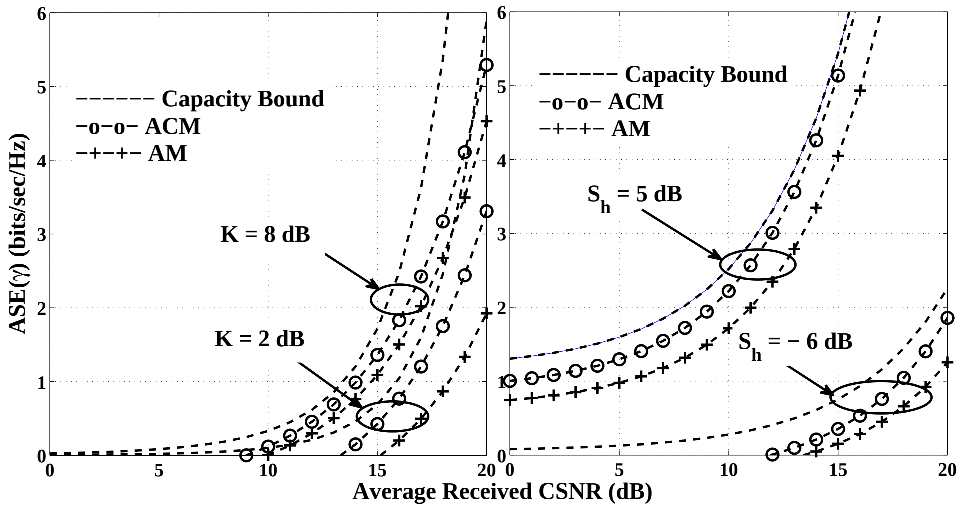

Figure 5.7: Coding gain of JFTS communication link with adaptive modulation (with and without coding), where the curves are generated by (a) varying the K-factor ($S_h = -2$ dB and $\Delta = 0.4$) and (b) varying the S_h-factor ($K = 5$ dB and $\Delta = 0.9$).

gain will get reduced even more if deep fading and shadowing are considered, which are confirmed in Fig. 5.7(a) and Fig. 5.7(b).

The simulation results exhibit even smaller gain in comparison to the uncoded results lessened by another 0.7 - 0.8 dB relative to the analytical results. This results from the fact that the coding gain offered by TCM is achieved asymptotically at large CSNRs where the probability of error is dominated by the probability of mistaking a given codeword for one of its neighbors. The CSNR which achieves a BER of 10^{-3} is moderate so the effect of codewords other than the nearest neighbor codewords decreases the effective coding gain.

The difference between analytical and simulation results is also higher for the coded technique in comparison to the uncoded one. The reason can be attributed to the amount of approximation used in obtaining the rate region boundaries, $\gamma_{\mathtt{n}}$, in either case. For the TCM case, an extra set of exponential fitting co-efficients $\{\mathtt{a}_{\mathtt{n}}(\mathtt{l}), \mathtt{b}_{\mathtt{n}}(\mathtt{l})\}$ are involved which are though real numbers are exponential approximants. The level of accuracy of approximation in that case depends on the number of exponential approximants, $\mathtt{L}$, considered. For this analysis, $\mathtt{L} = 2$. Increasing $\mathtt{L}$ further may result in better accuracy of the analytical results but will impose a higher computational complexity. Moreover the analytical bound with $\mathtt{L} = 2$ lies within 0.5 dB of the simulation results and hence can be considered as a believable upper bound for performance analysis of a JFTS channel.

The difference in analytical bound and simulation results gets reduced for a lower TBER $< 10^{-3}$ i.e. 10^{-6} as is exhibited in Fig. 5.6(b). This is due to the fact that for a TBER of 10^{-3}, smallest gain is exhibited by the largest signal constellation, where the total number of codewords contributing to the error probability is the largest as confirmed in case of AWGN channels in [109]. Hence lowering the TBER than 10^{-3} for the TCM will ensure higher asymptotic gain, thereby making the simulation results closer to the analytical bound, though sacrificing a little bit of average spectral efficiency.

Adaptive TCM coded M-QAM offer higher improvement in performance in comparison to Adaptive M-QAM in presence of deep fading only (refer to Fig. 5.7(a)) than to in presence of deep shadowing only (refer to Fig. 5.7(b)). For Fig. 5.7(a), only the K-factor is decreased from 8 dB to 2 dB, in presence of a moderately high S_h-factor of - 2 dB and moderately low Δ factor of 0.4. Hence in this case TCM is able to offer enhancement in performance approaching closer to the upper achievable capacity bound at high CSNRs, as this set of JFTS parameters represents relatively low severity in shadowing.

But in presence of high severity in shadowing (refer to Fig. 5.7(b)), TCM fails to offer considerable enhancement in performance. The reason can be attributed to the design of TCM which were first proposed as bandwidth codes for Rician channels in [93]. The JFTS distribution combines Rician fading with TWDP shadowing model. This means, that in addition to K-factor, the shadowing factor S_h and the shape parameter, Δ, also affect the channel behavior. This leaves ample opportunity to explore other iterative coding techniques like adaptive Turbo coded M-QAM and adaptive LDPC coded M-QAM, in order to find the right set of coset codes that can improve spectral efficiency in presence of both deep fading and deep shadowing.

5.7 Summary

The first aim of this chapter is to derive the analytical expressions for achievable ergodic and outage channel capacities of different adaptive transmission techniques over JFTS fading/shadowing distribution assuming perfect CSI at the receiver and/or the transmitter. As a consequence, the effect of the JFTS parameters on the achievable channel capacities is also determined. Both ergodic and outage capacity decreases with a decrease in JFTS parameters K, S_h and an increase in Δ while outage capacity is more sensitive than ergodic capacity to the changes in the JFTS parameters. Adaptation techniques like OPRA and ORA offer a considerable improvement in performance in comparison to CIFR and TIFR.

The second contribution of this chapter is to derive the analytical expressions for performance evaluation of constant power ORA ACR and ADR M-QAM techniques over JFTS faded/shadowing distribution assuming perfect CSI and negligible delay at the receiver. As a consequence, the effect of the JFTS parameters on the spectral efficiency and system performance achieved by these adaptive modulation techniques under different average BER constraints is also determined ABER increases with the decrease in JFTS parameters K and S_h. On the other hand, spectral efficiency decreases with the decrease in JFTS parameters K and S_h. It can also be concluded that optimal rate adaptive techniques with continuous rate policies outperforms discrete rate ones.

The final contribution of this chapter is to provide a systematic study on the increase in spectral efficiency obtained by the application of adaptive Trellis coded M-QAM over a JFTS faded/shadowed link. The analytical results exhibit an asymptotic coding gain of only 2 dB, much less than the 3 dB gain over the uncoded technique as promised in case of that traditional fading channel models like Rayleigh or Rician. The simulation results offer even smaller coding gain reduced by a margin of 0.7 - 0.8 dB in comparison to the analytical results. The difference between analytical and simulation results is also higher for the coded technique in comparison to the uncoded one. Finally adaptive TCM coded M-QAM offers improvement in performance over uncoded adaptive M-QAM in presence of deep fading only (lower K), however fails to offer any significant enhancement in performance if deep fading is present in combination with deep shadowing (low K and low S_h).

Chapter 6

Impact of Channel Estimation

6.1 Background

A typical scenario for indoor wireless radio communication assumes a channel changing so slowly that an entire frame can be transmitted without any appreciable variation in the channel characteristics [38]. If this assumption (also known as quasi-static fading/shadowing channel) is valid, the system performance can be enhances if the receiver is made aware of the so-called channel state information (CSI) i.e. the realization of the random channel gains affecting the transmission paths between the transmitter and the receiver. The quality of the CSI available at the receiver depends on the quality of the estimate of the instantaneous carrier signal-to-noise ratio (CSNR) obtained at the receiver. The instantaneous CSNR is an indicator of the quality of the communication link and is utilized for system functions like channel access, hand-off and power control. The efficiency of these functions depends on how accurately the system estimates the received instantaneous CSNR. To this purpose, a portion of the transmitted frame may consist of pilot symbols, whose composition is known to the receiver an dis used by the later to estimate the instantaneous CSNR. Due to noise and the finite number of pilot symbols in a frame, the CSNR estimate is not perfect. The main purpose of this chapter is to investigate the effects of this imperfect estimation on the system performance over a JFTS distributed channel.

The PDF, the CDF and the moments of the estimated instantaneous CSNR and the respective estimation error obtained using pilot symbols have been derived in [117] and [17] for Rayleigh and Nakagami-m fading channels respectively. In these cases, the true instantaneous CSNR is assumed to be Gamma distributed with a shape factor of 1. Analyses of Rayleigh fading channels are presented as a special case of Nakagami-m fading channels, where $m = 0$. In these scenarios, the estimated signal envelope is a sum of two zero-mean complex Gaussian random variables, the transmitted signal envelope and the AWGN. As a result, the estimated signal envelope is itself complex Gaussian distributed with zero mean. Hence, the estimated instantaneous CSNR will be Gamma distributed with a shape factor of 1, same as the true instantaneous CSNR.

For a JFTS faded/shadowed channel, the transmitted signal envelope will be JFTS distributed while the AWGN corrupting the envelope will be complex Gaussian distributed under the assumption of perfectly coherent reception. In this case, the estimated envelope and the corresponding estimated CSNR will no longer be JFTS distributed. Hence, in order to analyze the impact of channel estimation on the performance of different communication techniques over a JFTS faded/shadowed channel, we need to analyze the statistical properties of the CSNR estimation error and the estimated instantaneous CSNR, where the true and the estimated CSNR do not follow the same distribution. This analysis will enable us to predict the range of acceptable amount of error in CSNR over which a system can operate in JFTS channel conditions. this analysis will also provide insight into how fading compensation techniques like ACM performs in JFTS channels when compared to traditional fading channel models like Rayleigh, Nakagami-m, where the true and the estimated CSNRs follow the same distributions.

The first contribution of this chapter is to analyze the statistical properties of the estimated instantaneous CSNR and the corresponding estimation error when pilot symbol assisted modulation (PSAM) is applied to a JFTS faded/shadowed communication link. In order to do that, the PDF of the estimated JFTS faded/shadowed envelope is derived which in turn is used to obtain the PDF of the estimated CSNR. The joint PF of the true and the estimated CSNRs is used to obtain the PDF and moments of the estimation error. Numerical results demonstrate that the range of acceptable amount of error in CSNR over which the system can operate correctly in a JFTS channel increases with the decrease in the mean-squared voltages of the shadowed components.

The second contribution of this chapter is to derive analytically tractable expressions for ABER of coherent and non-coherent modulation techniques like, BPSK, BFSK, coherent M-PSK and M-QAM over a JFTS channel, where PSAM is used at the receiver in order to estimate the present CSI. The most common techniques prevalent in literature for doing this is to exploit the MGF [38] and the CDF [57] of the estimated received CSNR. Hence, both the MGF and the CDF expressions for the estimated CSNR will be derived, but will be focused on the CDF based approach for deriving the error probability expressions.

The third focus of this chapter is to provide expressions that are numerically efficient and simpler to handle. In order to achieve that, we will be deriving all the expressions in terms of the mean power of the estimated received signal envelope. However, even in terms of mean estimated power, the PDF of the estimated CSNR has to be represented in terms of infinite series summation. So in order to obtain computationally simple expressions for error probability performances, we provide analysis in two conditions, the low CSNR case and the high CSNR case. In such a scenario, the low CSNR case is of most importance, as the estimates will more probably be affected by noise and other channel impairments. However, considering both the scenarios, high and low CSNRs, will provide us the flexibility of analyzing performances over a wide variety of practical indoor WLAN environments. In all of these cases, the low CSNR evaluation will provide the lower bound and the high CSNR evaluation will provide the upper bound of the analytical error probability performances.

The rest of this chapter is organized as below. Section 6.2 derives the statistics like the PDF, CDF and moments of the estimated instantaneous CSNR and the corresponding estimation error. The CDF of the estimated CSNR in turn is used to evaluate error performance of different fixed modulation techniques in Section 6.3. Numerical results and discussions are provided in Section 6.4 and the concluding remarks are summarized in Section 6.5.

6.2 Pilot Symbol Assisted Channel Estimation

PSAM estimation of the composite fading/shadowing envelope estimates the received instantaneous CSNR using a linear combination of preceding and subsequent known pilot symbols as is done in [17]. Let $\mathcal{L}$ be the number of pilot symbols that are used to estimate the received instantaneous CSNR. The fading envelope can be estimated by dividing with the known symbols s, as

$$\hat{Z} \;=\; Z + N/s \tag{6.1}$$

where N is the independent and identically distributed zero mean complex AWGN component. Using the PDF of Z from Chapter 2 and that of N, the statistics of the estimated received envelope, estimated CSNR and CSNR estimation error in Subsection 6.2.1, 6.2.2 and 6.2.3 respectively.

6.2.1 Statistics of Estimated Envelope

Since, we are assuming coherent detection at the receiver, the phase of the information signal is detected and rectified at the receiver. However, since the distribution of N is symmetric, dividing by s (equal to $+/-1$) will not have any effect on the statistical properties of the estimated instantaneous CSNR. Hence, the PDF of the estimated fading/shadowing envelope at the time instant of receiving the pilot symbols can be obtained as,

$$f_{\hat{Z}}(\hat{z}) \;=\; f_{\hat{Z}}(\hat{z}+n) \;=\; \int_0^\infty f_{Z,N}(\hat{z}-z,n)\mathrm{d}z \tag{6.2}$$

where $f_Z(z)$ is the JFTS distributed envelope given by (4.2) and $f_N(n)$ is assumed to be Gaussian distributed and can be expressed as,

$$f_N(n) \;=\; \frac{1}{\sqrt{2\pi\sigma_n^2/\mathcal{L}}}\; e^{-\frac{n^2\mathcal{L}}{2\sigma_n^2}}. \tag{6.3}$$

where σ_n^2 is the noise variance. Solving the integral in (6.2), the expression for the PDF of the estimated fading/shadowing envelope ($\hat{Z}$) can be obtained. However, to obtain mathematically efficient expression for $f_{\hat{Z}}(\hat{z})$, two different scenarios are considered.

Case I : Magnitude/Power of the received envelope is low

If the magnitude/power of the received composite envelope is low i.e. $z \to 0$, the PDF of Z becomes,

$$f_Z(z)_{\text{low}} \;=\; \sum_{j=1}^{4}\sum_{h=1}^{20} \frac{z\; b_j\; \mathcal{R}}{P_1P_2}\; e^{-K-S_h-\frac{z^2}{2P_2r_h^2}}\; \left[e^{S_h\Delta\mathsf{M}_j} + e^{-S_h\Delta\mathsf{M}_j}\right] \tag{6.4}$$

where, since $z \to 0$, $2z\sqrt{KS_h(1-\Delta\mathsf{M}_j)/P_1P_2} \to 0$ and $2z\sqrt{KS_h(1+\Delta\mathsf{M}_j)/P_1P_2} \to 0$. Hence, $I_0(2z\sqrt{KS_h(1-\Delta\mathsf{M}_j)/P_1P_2}) \to 1$ and $I_0(2z\sqrt{KS_h(1+\Delta\mathsf{M}_j)/P_1P_2}) \to 1$ [39]. In this case, assuming that Z and N are independent random variables, the PDF of the estimated received envelope can be obtained as,

$$
\begin{aligned}
f_{\hat{Z}}(\hat{z})_{\text{low}} &= \sum_{j=1}^{4} \sum_{h=1}^{20} \frac{b_j\ \mathcal{R}}{P_1 P_2} \frac{e^{-K-S_h}}{\sqrt{2\sigma_n^2/\mathcal{L}}} \left[e^{S_h \Delta \mathsf{M}_j} + e^{-S_h \Delta \mathsf{M}_j} \right] \int_0^\infty z\ e^{\frac{z\hat{z}\mathcal{L}}{2\sigma_n^2} - \frac{z^2}{2P_2 r_h^2} - \frac{\hat{z}^2\mathcal{L}}{2\sigma_n^2}} \mathrm{d}z \\
&= \sum_{j=1}^{4} \sum_{h=1}^{20} \frac{b_j\ \mathcal{R}}{P_1 P_2} \frac{e^{-K-S_h}}{\sqrt{2\sigma_n^2/\mathcal{L}}} \frac{e^{-\frac{\hat{z}^2\mathcal{L}}{2\sigma_n^2}} \left[e^{S_h \Delta \mathsf{M}_j} + e^{-S_h \Delta \mathsf{M}_j} \right]}{(1/2P_2 r_h^2 + \mathcal{L}/2\sigma_n^2)^{1/4}} \mathsf{H}_{-\frac{1}{2}} \left(-\frac{\hat{z}\mathcal{L}/\sigma_n^2}{\sqrt{1/2P_2 r_h^2 + \mathcal{L}/2\sigma_n^2}} \right)
\end{aligned}
\tag{6.5}
$$

where $\mathsf{H}_{-\frac{1}{2}}(\cdot)$ is the Hermite polynomial of order $-\frac{1}{2}$. In this case, the mean power of the estimated envelope, $\hat{Z}$ can be obtained as,

$$
\begin{aligned}
\hat{\Omega}_{\text{low}} &= \mathrm{E}\{\hat{Z}_{\text{low}}^2\} \\
&= \sum_{j=1}^{4} \sum_{h=1}^{20} \frac{b_j\ \mathcal{R}\sqrt{\pi} e^{-K-S_h}}{32 P_1 P_2} \frac{\left[e^{S_h \Delta \mathsf{M}_j} + e^{-S_h \Delta \mathsf{M}_j} \right]}{(1/2P_2 r_h^2 + \mathcal{L}/2\sigma_n^2)^{3/2}} F\left(\frac{1}{4}, \frac{3}{2}; \frac{1}{2}; \frac{\mathcal{L}/4\sigma_n^2}{1/2P_2 r_h^2 + \mathcal{L}/2\sigma_n^2} \right)
\end{aligned}
\tag{6.6}
$$

where ${}_pF_q(\cdot)$ is the generalized hyper-geometric function and p, q are integers.

Case II **: Magnitude/Power of the received envelope is high**

If the magnitude/power of the received composite envelope is high i.e. $z \to \infty$, the PDF of Z becomes,

$$
\begin{aligned}
f_Z(z)_{\text{high}} &= \sum_{j=1}^{4} \sum_{h=1}^{20} \frac{\sqrt{z}\ b_j\ \mathcal{R}}{4\sqrt{\pi} P_1 P_2} e^{-K-S_h-\frac{z^2}{2P_2 r_h^2}} \left(\frac{P_1 P_2}{K S_h} \right)^{1/4} \\
&\cdot \left[\frac{e^{S_h \Delta \mathsf{M}_j}}{(1-\Delta \mathsf{M}_j)^{1/4}} e^{2z\sqrt{K S_h (1-\Delta \mathsf{M}_j)/P_1 P_2}} + \frac{e^{-S_h \Delta \mathsf{M}_j}}{(1+\Delta \mathsf{M}_j)^{1/4}} e^{2z\sqrt{K S_h (1+\Delta \mathsf{M}_j)/P_1 P_2}} \right]
\end{aligned}
\tag{6.7}
$$

where, since $z \to \infty$, $2z\sqrt{K S_h (1-\Delta \mathsf{M}_j)/P_1 P_2} \to \infty$ and $2z\sqrt{K S_h (1+\Delta \mathsf{M}_j)/P_1 P_2} \to \infty$. Hence, $I_0(2z\sqrt{K S_h (1-\Delta \mathsf{M}_j)/P_1 P_2}) \to \frac{1}{2\sqrt{\pi z}} \left(\frac{P_1 P_2}{K S_h (1-\Delta \mathsf{M}_j)} \right)^{1/4} e^{2z\sqrt{K S_h (1-\Delta \mathsf{M}_j)/P_1 P_2}}$ and $I_0(2z\sqrt{K S_h (1+\Delta \mathsf{M}_j)/P_1 P_2}) \to \frac{1}{2\sqrt{\pi z}} \left(\frac{P_1 P_2}{K S_h (1+\Delta \mathsf{M}_j)} \right)^{1/4} e^{2z\sqrt{K S_h (1+\Delta \mathsf{M}_j)/P_1 P_2}}$ [39]. In this case, the

PDF of the estimated received envelope can be obtained as,

$$
\begin{aligned}
f_{\hat{Z}}(\hat{z})_{\text{high}} &= \sum_{j=1}^{4} \sum_{h=1}^{20} \frac{b_j \ \mathcal{R}}{4\sqrt{\pi}P_1P_2} \frac{e^{-K-S_h}}{\sqrt{2\sigma_n^2/\mathcal{L}}} \frac{e^{-\frac{\hat{z}^2\mathcal{L}}{2\sigma_n^2}}\left(\frac{P_1P_2}{KS_h}\right)^{1/4}}{(1/2P_2r_h^2+\mathcal{L}/2\sigma_n^2)^{1/4}} \Bigg[\frac{e^{S_h\Delta\mathsf{M}_j}}{(1-\Delta\mathsf{M}_j)^{1/4}} \\
&\quad \cdot \ \mathsf{H}_{-\frac{1}{2}}\left(- \frac{\sqrt{KS_h(1-\Delta\mathsf{M}_j)/P_1P_2} + \hat{z}\mathcal{L}/\sigma_n^2}{\sqrt{1/2P_2r_h^2+\mathcal{L}/2\sigma_n^2}} \right) + \frac{e^{-S_h\Delta\mathsf{M}_j}}{(1+\Delta\mathsf{M}_j)^{1/4}} \\
&\quad \cdot \ \mathsf{H}_{-\frac{1}{2}}\left(- \frac{\sqrt{KS_h(1+\Delta\mathsf{M}_j)/P_1P_2} + \hat{z}\mathcal{L}/\sigma_n^2}{\sqrt{1/2P_2r_h^2+\mathcal{L}/2\sigma_n^2}} \right) \Bigg].
\end{aligned} \tag{6.8}
$$

In this case, the mean power of the estimated envelope, $\hat{Z}$ can be expressed as,

$$
\begin{aligned}
\hat{\Omega}_{\text{high}} &= \mathrm{E}\{\hat{Z}^2_{\text{high}}\} \\
&= \sum_{j=1}^{4} \sum_{h=1}^{20} \frac{b_j \ \mathcal{R}e^{-K-S_h}\mathcal{L}}{32\sqrt{\pi}P_1P_2\sigma_n^2} \left(\frac{P_1P_2/KS_h}{1/2P_2r_h^2+\mathcal{L}/2\sigma_n^2} \right)^{1/4} \left[\frac{e^{S_h\Delta\mathsf{M}_j}}{(1-\Delta\mathsf{M}_j)^{1/4}} + \frac{e^{-S_h\Delta\mathsf{M}_j}}{(1+\Delta\mathsf{M}_j)^{1/4}} \right] \\
&\quad \cdot \ \mathsf{H}_{-\frac{1}{2}}\left(- \frac{\mathcal{L}/\sigma_n^2}{\sqrt{1/2P_2r_h^2+\mathcal{L}/2\sigma_n^2}} \right).
\end{aligned} \tag{6.9}
$$

6.2.2 Statistics of Estimated CSNR

Let $\hat{\gamma}$ be the estimated instantaneous CSNR with mean $\mathrm{E}\{\hat{\gamma}\} = \overline{\hat{\gamma}}$. When the magnitude of the estimated envelope $\hat{Z}$ is high, the estimated CSNR will also be high, while a low magnitude estimated envelope will render a low estimated CSNR. This can only be said under the assumption that only the composite fading/shadowing envelope will contribute to the received CSNR. Hence, the PDF of the estimated CSNR, $\hat{\gamma}$, can be calculated in terms of the $\overline{\hat{\gamma}}$ and $\hat{\Omega}$,

$$
\begin{aligned}
f_{\hat{\gamma}}(\hat{\gamma}) &= f_{\hat{Z}}\left(\sqrt{\frac{\hat{\Omega}\hat{\gamma}}{\overline{\hat{\gamma}}}} \right) \Bigg/ \left(2\sqrt{\frac{\overline{\hat{\gamma}}\hat{\gamma}}{\hat{\Omega}}} \right) \\
&= \frac{\hat{\Omega}}{2\hat{\gamma}(P_2r_h^2+\sigma_n^2/\mathcal{L})} \left[\sum_{k=0}^{\infty} \frac{1}{(k+1)!} \Gamma\left(k+2, \frac{\hat{\Omega}\hat{\gamma}}{2\overline{\hat{\gamma}}(P_2r_h^2+\sigma_n^2/\mathcal{L})} \right) - e^{-\frac{\hat{\Omega}\hat{\gamma}}{2\overline{\hat{\gamma}}(P_2r_h^2+\sigma_n^2/\mathcal{L})}} \right]
\end{aligned} \tag{6.10}
$$

where the definition for instantaneous CSNR is used as before. Now the expression in (6.10) involves infinite series summation which is not that computationally attractive. Hence, it will be better to resort to the two limiting conditions and there by arrive at the lower and upper bounds of the estimated instantaneous CSNR. Similar to the case of the estimated envelope, two scenarios will be considered, the low CSNR and the high CSNR scenarios. However, the high CSNR case will be more useful for system performance evaluation since most communication systems are designed to have a fairly high CSNR for their pilot symbols.

Case I **: Low CSNR** ($\hat{\gamma} \to 0$)

In this case, as $\hat{\gamma} \to 0$, $\Gamma(\cdot)$ in (6.10) approaches 1. Hence the PDF in (6.10) reduces to,

$$f_{\hat{\gamma}}(\hat{\gamma})_{\text{low}} \;=\; \frac{\mathcal{F}}{\hat{\gamma}}\left[1 - e^{-\frac{\mathcal{F}\hat{\gamma}}{\bar{\hat{\gamma}}}}\right] \tag{6.11}$$

where $\mathcal{F} = \hat{\Omega}/2(P_2 r_h^2 + \sigma_n^2/\mathcal{L})$. In this expression of (6.11), $\hat{\Omega}$ can be calculated in terms of the JFTS distribution parameter using (6.6). The CDF of the corresponding estimated instantaneous CSNR, $\hat{\gamma}$ can be obtained using integral solution from [48] as,

$$F_{\hat{\gamma}}(\hat{\gamma})_{\text{low}} \;=\; \mathcal{F}\,\log(\hat{\gamma}) - \mathcal{F}\,\text{Ei}\left(-\frac{\mathcal{F}\hat{\gamma}}{\bar{\hat{\gamma}}}\right) \tag{6.12}$$

where $\text{Ei}(\cdot)$ is the exponential integral. It is evident from (6.11) and (6.12) that the PDF and CDF of $\hat{\gamma}$ is not valid for $\hat{\gamma} = 0$. In practicality, $\hat{\gamma} = 0$ denotes a condition, where the signal power is 0 or equivalently the absence of any transmitted signal. Hence, the lower bound for $\hat{\gamma}$ will be assumed to be equal to 1 (0 dB), while evaluating moments and other statistical properties of $\hat{\gamma}$. By substituting (6.11) in the definition for MGF, the expression for MGF can be given by,

$$\mathcal{M}_{\hat{\gamma}}(s)_{\text{low}} \;=\; \mathcal{F}\left[\text{Ei}\left(-s - \frac{\mathcal{F}}{\bar{\hat{\gamma}}}\right) - \text{Ei}(-s)\right] \tag{6.13}$$

Using (6.11) in the nth order moment expression, $\mu_{\hat{\gamma}}(n) = \text{E}\{\hat{\gamma}^n\}$, the moments of the estimated

CSNR can be obtained as,

$$\mu_{\hat{\gamma}}(n)_{\text{low}} \;=\; -\left[\frac{\mathcal{F}}{n} + \left(\frac{\bar{\hat{\gamma}}}{\mathcal{F}}\right)^n \Gamma\left(n, \frac{\mathcal{F}}{\bar{\bar{\hat{\gamma}}}}\right)\right] \tag{6.14}$$

which is calculated using the integral solution from [48].

Case II : High CSNR ($\hat{\gamma} \to \infty$)

In this scenario, as $\hat{\gamma} \to \infty$, $\Gamma(\cdot)$ in (6.10) approaches 0. Hence the PDF in (6.10) reduces to,

$$f_{\hat{\gamma}}(\hat{\gamma})_{\text{high}} \;=\; -\frac{\mathcal{F}}{\hat{\gamma}} e^{-\frac{\mathcal{F}\hat{\gamma}}{\bar{\bar{\hat{\gamma}}}}}. \tag{6.15}$$

In this expression of (6.15), $\hat{\Omega}$ can be calculated in terms of the JFTS distribution parameter using (6.9). The CDF of the corresponding estimated instantaneous CSNR, $\hat{\gamma}$ can be expressed as,

$$F_{\hat{\gamma}}(\hat{\gamma})_{\text{high}} \;=\; -\mathcal{F}\ \mathrm{Ei}\left(-\frac{\mathcal{F}\hat{\gamma}}{\bar{\bar{\hat{\gamma}}}}\right) \tag{6.16}$$

Using (6.15), the expression for MGF can be calculated as,

$$\mathcal{M}_{\hat{\gamma}}(s)_{\text{high}} \;=\; \mathcal{F}\mathrm{Ei}\left(-s - \frac{\mathcal{F}}{\bar{\bar{\hat{\gamma}}}}\right) \tag{6.17}$$

and the nth order moment can be obtained as,

$$\mu_{\hat{\gamma}}(n)_{\text{high}} \;=\; -\left(\frac{\bar{\hat{\gamma}}}{\mathcal{F}}\right)^n \Gamma\left(n, \frac{\mathcal{F}}{\bar{\bar{\hat{\gamma}}}}\right) \tag{6.18}$$

where $\Gamma(\cdot)$ is the upper incomplete function given in [39].

6.2.3 Statistics of Estimation Error

Let γ and $\hat{\gamma}$ are considered to be correlated with a power correlation coefficient of ρ. Using the derivation of $\bar{\hat{\gamma}}$ and ρ from [17], as $\mathrm{E}\{\hat{\gamma}\} = \bar{\gamma} + 1$ and $\rho = \frac{\bar{\gamma}}{1+\bar{\gamma}}$, the joint PDF of γ and $\hat{\gamma}$ can be derived in terms of ρ, $\overline{\gamma}$ and $(\overline{\gamma}+1)$. Hence, the final expression of the joint PDF can be obtained as,

$$
\begin{aligned}
f_{\gamma\hat{\gamma}}(\gamma,\hat{\gamma}) &= \frac{\mathcal{BF}}{\hat{\gamma}(\gamma-\rho\hat{\gamma})}\big[1 - \ e^{-\frac{\mathcal{B}(\gamma-\rho\hat{\gamma})}{\overline{\gamma}}} - \ e^{-\frac{\mathcal{F}\hat{\gamma}}{1+\overline{\gamma}}} + \ e^{-\frac{\mathcal{B}\gamma}{\overline{\gamma}}+\frac{\mathcal{B}\rho\hat{\gamma}}{\overline{\gamma}}-\frac{\mathcal{F}\hat{\gamma}}{1+\overline{\gamma}}}\big] \qquad \hat{\gamma}\to 0 \\
&= \frac{\mathcal{BF}}{\hat{\gamma}(\gamma-\rho\hat{\gamma})}\big[e^{-\frac{\mathcal{B}\gamma}{\overline{\gamma}}+\frac{\mathcal{B}\rho\hat{\gamma}}{\overline{\gamma}}-\frac{\mathcal{F}\hat{\gamma}}{1+\overline{\gamma}}} - \ e^{-\frac{\mathcal{F}\hat{\gamma}}{1+\overline{\gamma}}}\big] \qquad \hat{\gamma}\to\infty
\end{aligned}
\tag{6.19}
$$

where $\mathcal{B} = \frac{\Omega}{2P_2r_h^2}$ and Ω is the mean-squared value of the JFTS distributed composite fading/shadowing envelope. The CSNR estimation error in this case can be given by $\Phi = \hat{\gamma}-\gamma$. Using this equation, the statistical properties of the estimation error, Φ can be derived.

The PDF of Φ, $f_\Phi(\phi)$ can be determined by directly differentiating the distribution function $F_\Phi(\phi)$. Hence, $f_\Phi(\phi) = \int_0^\infty f_{\gamma\hat{\gamma}}(\gamma,\phi+\gamma)\mathrm{d}\gamma$, $\Phi \geq 0$. The first step to solve this integration is to express (6.19) in terms of γ and $\Phi+\gamma$. Putting the integrand back, the integration can be solved using the integral solutions from [48]. Hence for the low CSNR case, the PDF of the estimation error can be expressed as,

$$
f_\Phi(\phi)_{\text{low}} = \mathsf{I}_1 - \mathsf{I}_2 - \mathsf{I}_3 + \mathsf{I}_4 \tag{6.20}
$$

where,

$$
\mathsf{I}_1 = \frac{\mathcal{BF}}{\phi}\log\left(\frac{\rho-1}{\rho}\right) \tag{6.21}
$$

$$
\mathsf{I}_2 = \frac{\mathcal{BF}}{\phi}\ e^{\frac{\mathcal{B}\rho\phi}{\overline{\gamma}}}\left[e^{\frac{\mathcal{B}\phi(1-\rho)}{\overline{\gamma}}}\ \mathrm{Ei}\left(\frac{\mathcal{B}\phi(1-\rho)}{\overline{\gamma}}\right) - \ e^{-\frac{\mathcal{B}\rho}{\overline{\gamma}}}\ \mathrm{Ei}\left(\frac{\mathcal{B}\rho}{\overline{\gamma}}\right)\right] \tag{6.22}
$$

$$
\mathsf{I}_3 = \frac{\mathcal{BF}}{\phi}\ e^{-\frac{\mathcal{F}\phi}{\overline{\gamma}+1}}\left[e^{\frac{\mathcal{F}\phi}{\overline{\gamma}+1}}\ \mathrm{Ei}\left(-\frac{\mathcal{F}\phi}{\overline{\gamma}+1}\right) - \ e^{\frac{\mathcal{F}\rho}{(\overline{\gamma}+1)(\rho-1)}}\ \mathrm{Ei}\left(\frac{\mathcal{F}\rho}{(\overline{\gamma}+1)(1-\rho)}\right)\right] \tag{6.23}
$$

$$\begin{aligned}\mathsf{I}_4 \;=\; & \frac{\mathcal{BF}}{\phi}\; e^{\left(\frac{\mathcal{B}\rho}{\overline{\gamma}}-\frac{\mathcal{F}}{1+\overline{\gamma}}\right)\phi}\Bigg[e^{-\frac{\mathcal{B}\rho\phi}{\overline{\gamma}}+\frac{\mathcal{F}\phi}{1+\overline{\gamma}}+\frac{\mathcal{B}\phi}{\overline{\gamma}}}\;\mathrm{Ei}\left(\frac{\mathcal{B}\rho\phi}{\overline{\gamma}}-\frac{\mathcal{F}\phi}{1+\overline{\gamma}}-\frac{\mathcal{B}\phi}{\overline{\gamma}}\right)\\ & -\; e^{\frac{\rho}{\rho-1}\left(-\frac{\mathcal{B}\rho}{\overline{\gamma}}+\frac{\mathcal{F}}{\overline{\gamma}+1}+\frac{\mathcal{B}}{\overline{\gamma}}\right)}\;\mathrm{Ei}\left(\frac{\rho}{\rho-1}\left(-\frac{\mathcal{B}\rho}{\overline{\gamma}}+\frac{\mathcal{F}}{\overline{\gamma}+1}+\frac{\mathcal{B}}{\overline{\gamma}}\right)\right)\Bigg] \qquad (6.24)\end{aligned}$$

For the high CSNR case, the PDF of the estimation error simply reduces to,

$$f_{\Phi}(\phi)_{\mathrm{high}} \;=\; \mathsf{I}_4 - \mathsf{I}_3 \qquad (6.25)$$

where I_3 and I_4 are given by (6.23) and (6.24) respectively. Hence for the numerical analysis, only the low CSNR case will be used for plotting the PDF of the CSNR estimation error. A brief discussion on the statistical properties of the estimation error in presence of low CSNR is provided in Section 6.4, where pilot symbols are used over a JFTS faded/shadowed communication channel.

6.3 Error Performance Analysis

In order to obtain the ABER of a large variety of modulation techniques, the CDF based approach of [5] will be used in this section. The receivers are considered to be operating over independent and identical distributed (iid) fading conditions. The error probability performances in each case will be determined in terms of the lower bound for low CSNR and the upper bound for high CSNR. The organization of this section is as follows. Closed-form expressions for error rates of a variety of fixed binary modulation techniques are derived using the CDF-based approach in Subsection 6.3.1. The same analysis is done for error probability performance of fixed M-ary modulation techniques in Subsection 6.3.2.

6.3.1 Binary Modulation Schemes

For any binary coherent and non-coherent modulation technique, the ABER over a composite flat faded and slow shadowed wireless communication channel suffering from AWGN can be expressed in terms of the CDF of the instantaneous SNR as [57],

$$P_b^{\text{Binary}}(e) = \frac{\alpha^\beta}{2\Gamma(\beta)} \int_0^\infty \hat{\gamma}^{\beta-1}\ e^{-\alpha\hat{\gamma}}\ F_{\hat{\gamma}}(\hat{\gamma})\mathrm{d}\hat{\gamma} \tag{6.26}$$

where $\alpha = 1$ for Binary Phase Shift Keying (BPSK) and $\alpha = 1/2$ for Binary Frequency Shift Keying (BFSK). If the modulation is differential or non-coherent, $\beta = 1$, while for coherent modulation, $\beta = 1/2$. By substituting (6.12) and (6.16) in (6.26) and using the integral solution from [48], the ABER expression for any coherent or non-coherent binary modulation technique over a JFTS channel with estimated CSI can be obtained as,

$$\begin{aligned} P_b^{\text{Binary}}(e)_{\text{low}} &= \frac{\mathcal{F}}{2}\left[\psi(\beta)\ -\ \log(\beta)\ +\ \frac{1}{\beta}\left(\frac{\alpha\bar{\hat{\gamma}}}{\alpha\bar{\hat{\gamma}}+\mathcal{F}}\right)^\beta {}_2F_1\left(1,\beta;\beta+1;\frac{\alpha\bar{\hat{\gamma}}}{\alpha\bar{\hat{\gamma}}+\mathcal{F}}\right)\right] \\ P_b^{\text{Binary}}(e)_{\text{high}} &= \frac{\mathcal{F}}{2\beta}\left(\frac{\alpha\bar{\hat{\gamma}}}{\alpha\bar{\hat{\gamma}}+\mathcal{F}}\right)^\beta {}_2F_1\left(1,\beta;\beta+1;\frac{\alpha\bar{\hat{\gamma}}}{\alpha\bar{\hat{\gamma}}+\mathcal{F}}\right) \end{aligned} \tag{6.27}$$

where $\psi(\cdot)$ is the Euler-Psi function given by $\psi(\cdot) = \frac{\mathrm{d}}{\mathrm{d}(\cdot)}\log(\Gamma(\cdot))$.

6.3.2 M-ary Coherent Modulation Schemes

In order to evaluate the error performance of M-ary coherent modulation techniques over a composite fading/shadowing channel, we need to calculate an integral of the form,

$$P_b^{M-\text{ary}}(e,g) = \frac{1}{\sqrt{2\pi}} \int_0^\infty F_{\hat{\gamma}}\left(\frac{v^2}{g}\right) e^{-v^2/2}\mathrm{d}v \tag{6.28}$$

where g depends on the modulation type [84]. For a JFTS channel, substituting (6.12) and (6.16) in (6.28), using the change of variables $u = v^2$ and then using the integral solution from [48], $P_b^{M-\text{ary}}(e,g)$ can be expressed as,

$$\begin{aligned} P_b^{M-\text{ary}}(e,g)_{\text{low}} &= \mathcal{F}\left[2\sqrt{\frac{g\bar{\hat{\gamma}}}{g\bar{\hat{\gamma}}+2\mathcal{F}}}\ {}_2F_1\left(1,\frac{1}{2};\frac{3}{2};\frac{g\bar{\hat{\gamma}}}{g\bar{\hat{\gamma}}+2\mathcal{F}}\right) - \frac{\mathcal{E}}{2} - \frac{\log(2g)}{2}\right] \\ P_b^{M-\text{ary}}(e,g)_{\text{high}} &= 2\mathcal{F}\sqrt{\frac{g\bar{\hat{\gamma}}}{g\bar{\hat{\gamma}}+2\mathcal{F}}}\ {}_2F_1\left(1,\frac{1}{2};\frac{3}{2};\frac{g\bar{\hat{\gamma}}}{g\bar{\hat{\gamma}}+2\mathcal{F}}\right) \end{aligned} \tag{6.29}$$

where $\mathcal{E}$ is the Euler-Mascheroni constant with a numerical value of $\mathcal{E} \approx 0.577216$ [39]. This generalized ABER expression (6.29) for M-ary coherent modulation techniques can be used to derive ABER expressions for any coherent modulation technique only by changing the value of g.

M-ary Quadrature Amplitude Modulation (M-QAM)

Using unified approximation, as is done in [84], the ABER expression of general order M-QAM modulation over a composite fading / shadowing channel is given by,

$$P_b^{M\mathrm{QAM}}(e) \cong \frac{4}{\log_2 M}\left(1-\frac{1}{\sqrt{M}}\right)\sum_{n=1}^{\sqrt{M}/2} P_b^{M-\mathrm{ary}}(e, g_{n-Q}) \tag{6.30}$$

where $g_{n-Q} = 3(2n-1)^2 \log_2 M/(M-1)$. Substituting (6.29) in (6.30), the ABER expression for general order M-QAM modulation technique over a JFTS channel can be expressed as,

$$\begin{aligned} P_b^{M\mathrm{QAM}}(e)_{\mathrm{low}} \cong {} & \frac{4\mathcal{F}}{\log_2 M}\left(1-\frac{1}{\sqrt{M}}\right)\sum_{n=1}^{\sqrt{M}/2}\left[2\sqrt{\frac{g_{n-Q}\bar{\hat{\gamma}}}{g_{n-Q}\bar{\hat{\gamma}}+2\mathcal{F}}}\;{}_2F_1\left(1,\frac{1}{2};\frac{3}{2};\frac{g_{n-Q}\bar{\hat{\gamma}}}{g_{n-Q}\bar{\hat{\gamma}}+2\mathcal{F}}\right)\right. \\ & \left. -\frac{\mathcal{E}}{2}-\frac{\log(2g_{n-Q})}{2}\right] \\ P_b^{M\mathrm{QAM}}(e)_{\mathrm{high}} \cong {} & \frac{8\mathcal{F}}{\log_2 M}\left(1-\frac{1}{\sqrt{M}}\right)\sum_{n=1}^{\sqrt{M}/2}\sqrt{\frac{g_{n-Q}\bar{\hat{\gamma}}}{g_{n-Q}\bar{\hat{\gamma}}+2\mathcal{F}}}\;{}_2F_1\left(1,\frac{1}{2};\frac{3}{2};\frac{g_{n-Q}\bar{\hat{\gamma}}}{g_{n-Q}\bar{\hat{\gamma}}+2\mathcal{F}}\right). \quad (6.31) \end{aligned} \tag{6.32}$$

M-ary Phase Shift Keying (M-PSK)

Using unified approximation, as is done in [84], the ABER expression of Gray coded coherent M-PSK modulation over a composite fading / shadowing channel is given by,

$$P_b^{M\mathrm{PSK}}(e) \cong \frac{2}{\max(\log_2 M, 2)}\sum_{n=1}^{\max(M/4,1)} P_b^{M-\mathrm{ary}}(e, g_{n-P}) \tag{6.33}$$

where $g_{n-P} = 2(\log_2 M)\sin^2((2n-1)\pi/M)$. Substituting (6.29) in (6.33), the ABER expression for coherent M-PSK modulation technique over a JFTS channel can be obtained as,

$$P_b^{M\text{PSK}}(e)_{\text{low}} \cong \frac{2\mathcal{F}}{\max(\log_2 M, 2)} \sum_{n=1}^{\max(M/4,1)} \Bigg[2\sqrt{\frac{g_{n-P}\bar{\hat{\gamma}}}{g_{n-P}\bar{\hat{\gamma}}+2\mathcal{F}}}\; {}_2F_1\left(1,\frac{1}{2};\frac{3}{2};\frac{g_{n-P}\bar{\hat{\gamma}}}{g_{n-P}\bar{\hat{\gamma}}+2\mathcal{F}}\right) - \frac{\mathcal{E}}{2} - \frac{\log(2g_{n-P})}{2}\Bigg]$$

$$P_b^{M\text{PSK}}(e)_{\text{high}} \cong \frac{4\mathcal{F}}{\max(\log_2 M, 2)} \sum_{n=1}^{\max(M/4,1)} \sqrt{\frac{g_{n-P}\bar{\hat{\gamma}}}{g_{n-P}\bar{\hat{\gamma}}+2\mathcal{F}}}\; {}_2F_1\left(1,\frac{1}{2};\frac{3}{2};\frac{g_{n-P}\bar{\hat{\gamma}}}{g_{n-P}\bar{\hat{\gamma}}+2\mathcal{F}}\right). \quad (6.34)$$

It is evident from (6.27), (6.31) and (6.34) that bit error probability performance of any modulation technique over a JFTS communication channel is directly proportional to the mean power of the joint faded and two-path shadowed envelope, $\hat{\Omega}$. Now from (6.6) and (6.9), we observe that $\hat{\Omega}$ decreases exponentially with the increase either in K or S_h or both. As a result, the mean power of the received envelope decreases with the increase in the fading and/or the shadowing parameters resulting in the overall decrease in the error probability.

6.4 Numerical Analysis and Discussion

In this section, the derived expressions for the PDF of the CSNR estimation error and error rate performances of a variety of modulation techniques are numerically evaluated and plotted as functions of JFTS parameters, AWGN parameters and average received CSNR. The ABER results are compared with the simulation results in order to verify the validity of the derived expressions. All the results are evaluated using a single input single output (SISO) system and are averaged over 100 independent random channel realizations.

The rest of this section is organized as below. Subsection 6.4.1 illustrates the effects of different channel and estimation parameters on the statistics of the CSNR estimation error. Subsection 6.4.2

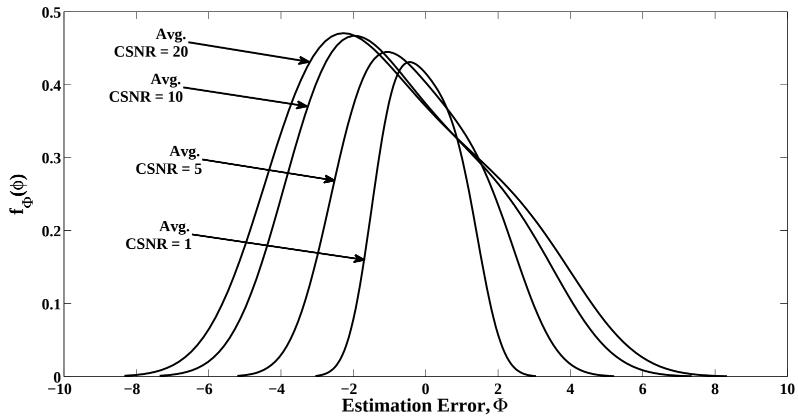

Figure 6.1: Plots of the PDF of the CSNR estimation error, Φ over a JFTS faded/shadowed communication channel with $K = 4$ dB, $S_h = -1$ dB, $\Delta = 0.5$, $P_1 = 0.45$, $P_2 = 0.4$ and a noise variance of $\sigma_n^2 = 1$, where the curves are generated by varying $\overline{\gamma}$.

simulates and analyzes the performance of a variety of modulation techniques over the JFTS link in presence of estimated CSI.

6.4.1 Statistics of Estimated CSNR

An example set of PDFs of the CSNR estimation error are plotted in Fig. 6.1, where the estimation is done using pilot symbols. For this set of curves, the access point and the mobile WLAN user are assumed to be separated by two sets of dry-walls ($K = 7$ dB, $S_h = -1$ dB, $\Delta = 0.5$). The other JFTS parameters like P_1 and P_2 are kept constant at 0.45 and 0.4 respectively. The noise variance of the AWGN is considered to be constant at 1 for the PDF plots, where the estimation error is measured either in natural units or in Logarithm units. Similar to the observations made in case of Rayleigh fading channels in [57], the variance of both γ and $\hat{\gamma}$ increase with the square of the average received CSNR, $\overline{\gamma}$. It is reasonable that the variance of the CSNR estimation error also increases.

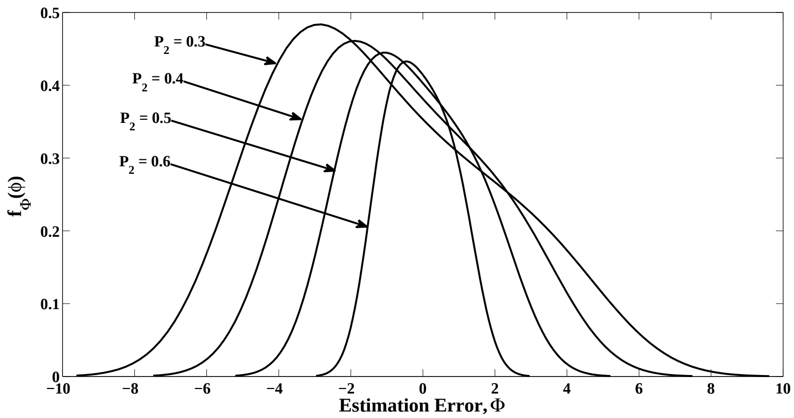

Figure 6.2: Plots of the PDF of the CSNR estimation error, Φ over a JFTS faded/shadowed communication channel with $K = 4$ dB, $S_h = -1$ dB, $\Delta = 0.5$, $P_1 = 0.45$, a noise variance of $\sigma_n^2 = 1$ and $\overline{\gamma} = 10$, where the curves are generated by varying P_2.

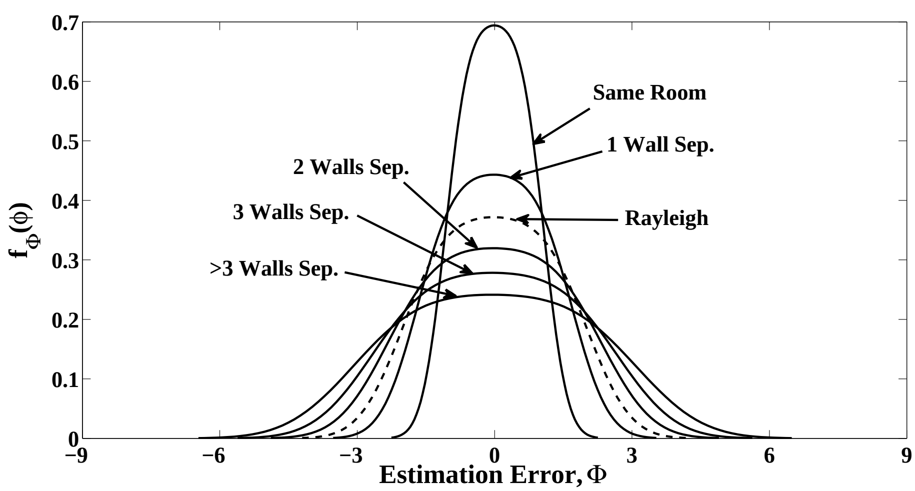

Figure 6.3: Plots of the PDF of the CSNR estimation error, Φ over a JFTS faded/shadowed communication channel with $P_1 = 0.45$, $P_2 = 0.4$, a noise variance of $\sigma_n^2 = 1$ and $\overline{\gamma} = 10$, where the curves are generated by varying the JFTS parameters K, S_h and Δ.

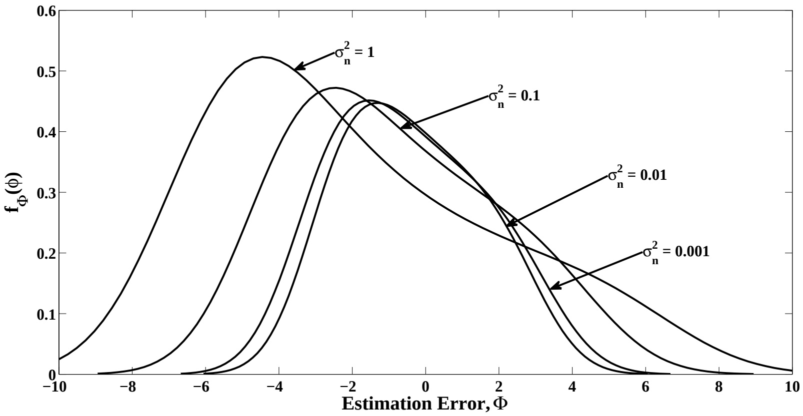

Figure 6.4: Plots of the PDF of the CSNR estimation error, Φ over a JFTS faded/shadowed communication channel with $K = 4$ dB, $S_h = -1$ dB, $\Delta = 0.5$, $P_1 = 0.45$, $P_2 = 0.4$ and $\overline{\gamma} = 10$, where the curves are generated by varying the noise variance σ_n^2.

The second figure, Fig. 6.2 shows that the estimation error variance over a JFTS communication link increases with the decrease in the shape parameter, P_2. The parameter P_2 defines the mean-squared voltage of the scattered components in a composite JFTS faded / shadowed channel and intuitively represents the variance of the shadowing distribution. As a result, with the increase in P_2, a large range of shadowing values contributed by each scattering cluster will be encountered. This will result in equal number of high and low main wave amplitudes thereby lowering the overall shadowing severity. In such a condition, the higher the value of P_2, lower will be the range of values of CSNR estimation error, thereby decreasing the variance of the difference $\hat{\gamma} - \gamma$.

Fig. 6.3 is used to compare the effect of different parameters on the estimation error variance over JFTS faded/shadowed and Rayleigh faded channels. Four different indoor WLAN communication scenarios are considered, where the user and the access point are in the same room ($K = 13$ dB, $S_h = 12$ dB, $\Delta = 0.9$), separated by one ($K = 10$ dB, $S_h = 6$ dB, $\Delta = 0.7$), two ($K = 7$ dB, $S_h = -1$ dB, $\Delta = 0.5$), three ($K = 4$ dB, $S_h = -6$ dB, $\Delta = 0.3$) or more than three partitions

($K = 1$ dB, $S_h = -12$ dB, $\Delta = 0.1$) and Rayleigh fading no shadowing case ($K = 0$ dB, $S_h = 0$ dB, $\Delta = 0$). The average received CSNR $\overline{\gamma}$ are kept constant at 10 dB respectively in case of both the channel models. The corrupting AWGN is assumed to have zero mean and unit variance. In case of JFTS fading, error variance decreases with the increase in the JFTS parameters, K and S_h. Estimation error variance gets higher than the Rayleigh fading case as soon as K decreases to 7 dB and S_h to -1 dB (2-walls separation scenario). The reason for this behavior is that smaller the K and S_h, higher is the range of differences between the true and the estimated CSNR resulting in the increase of the error variance.

It can also be concluded that in case of the communication scenario where both the user and the access point (high K and S_h factors) are in the same room, the range of acceptable amount of error in CSNR over which the system can operate correctly is higher than when the user and the access point are separated by two sets of dry-walls (low K and S_h factors). This will be verified by Fig. 6.5 in Subsection 6.4.2, where the estimated error rate performance starts approaching the performance with perfect CSI at a much lower CSNR, in case of the propagation scenario where the user and the AP are separated by one set of dry-wall than the case where the user and the AP are separated by more than three sets of dry-walls.

The last figure, Fig. 6.4 demonstrates the effect of noise variance of the corrupting AWGN on the CSNR estimation error over a JFTS channel. These plots inspect the WLAN scenario where the user and the access point are separated by two sets of dry-walls ($K = 7$ dB, $S_h = -1$ dB, $\Delta = 0.5$). The overall average CSNR, $\overline{\gamma}$ is kept constant at 10 dB. In the case of the Rayleigh and Nakagami fading channels, the estimated signal envelope is complex Gaussian distributed with zero mean. However, for the JFTS distributed envelope, the variance of the estimation error decreases with

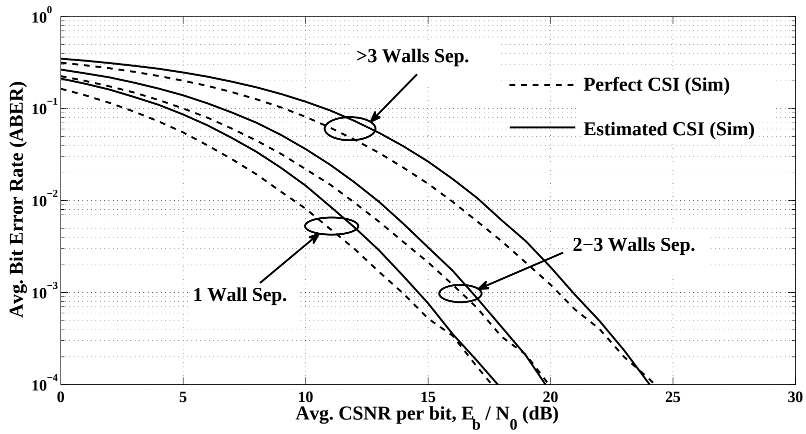

Figure 6.5: Simulated ABER performance of BPSK over a JFTS link with varying sets of parameters K, S_h and Δ, where performances with perfect CSI are plotted as benchmarks in each propagation scenario.

the decrease in noise variance. The reason can be attributed to the fact that the PDF of the estimated CSNR ($\hat{\gamma}$) is a function of the individual noise variance terms whereas for the Rayleigh and Nakagami fading channels, the PDF of $\hat{\gamma}$ is a function of CSNR only. For a JFTS channel, $f_{\hat{\gamma}}(\hat{\gamma})$ is inversely proportional to the noise variance. Hence as the noise variance decreases, the variance of $\hat{\gamma}$ decreases thereby decreasing the variance of the difference $\hat{\gamma} - \gamma$.

6.4.2 Error Performance Analysis

The ABER performance of BPSK over a JFTS faded/shadowed link with perfect CSI is depicted in Fig. 6.5 as the benchmark of the achievable performance. Three sets of indoor WLAN communication scenarios are considered, where the user and the AP are separated by one ($K = 10$ dB, $S_h = 6$ dB, $\Delta = 0.7$), two-three ($K = 7$ dB, $S_h = -1$ dB, $\Delta = 0.5$) and more than three partitions ($K = 1$ dB, $S_h = -12$ dB, $\Delta = 0.1$). The corrupting AWGN is assumed to have zero mean and unit variance. A fixed pilot length of $\mathcal{L} = 100$ is considered for simulation only set of results with estimated CSI. As mentioned in Subsection 6.4.1 the estimated error rate performance starts

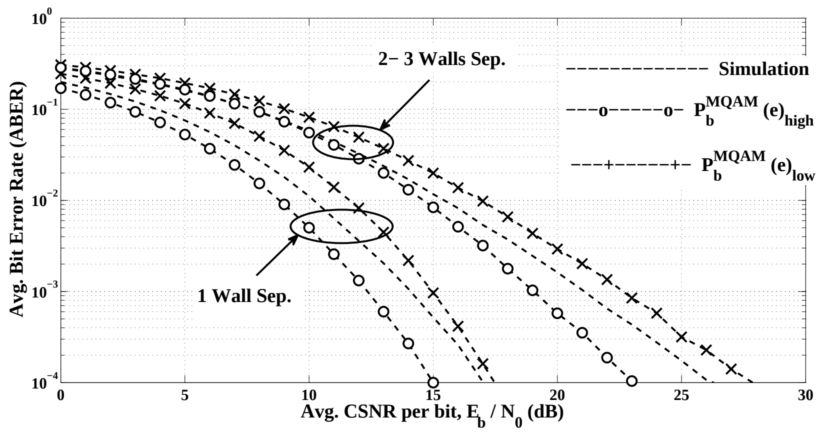

Figure 6.6: Comparative simulation and analytical ABER performances of 16QAM over JFTS faded / shadowed communication links in presence of estimated CSI, where two sets of indoor WLAN communication scenarios are considered.

approaching the performance with perfect CSI at a low CSNR in case of the propagation scenario where the user and the AP are separated by one set of dry-wall. The reason can be attributed to the fact that higher the K and S_h factors, lower will be the severity in fading and shadowing in the communication link and higher will be the range of acceptable amount of error in CSNR over which the system can operate correctly.

The final set of curves in this section (Fig. 6.6) are plotted to compare the analytical bounds derived in Subsection 6.3.2 with that of the simulation results in presence of estimated CSI using pilot symbols. In this case two sets propagation scenarios are considered, where the user and the AP are separated by one ($K = 10$ dB, $S_h = 6$ dB, $\Delta = 0.7$) and two-three sets of dry-walls($K = 7$ dB, $S_h = -1$ dB, $\Delta = 0.5$). The corrupting AWGN is assumed to have zero mean and unit variance. A fixed pilot length of $\mathcal{L} = 100$ is considered for estimating CSNR both in case of the simulation and the analytical results. Both the analytical bounds, one considering the low CSNR case and other considering the high CSNR case are plotted.

In case of both the propagation scenarios, the analytical bound with high CSNR overestimates and that with low CSNR underestimates the error rate performance. However, in case when the AP and user are separated by 1 partition, low CSNR bound starts approaching the simulation result at higher average CSNR. While when the AP and user are separated by 2-3 partitions, the high CSNR bound accurately predicts performance at low CSNR region but grossly overestimates error rate as the average CSNR increases. The low CSNR bound though underestimates the performance in this case, manages to follow the simulated performance within 1 dB over the entire average CSNR range. Hence it can be concluded that it will be more useful to use the low CSNR bound while evaluating system performance in presence of estimated CSI over a JFTS link.

6.5 Summary

The primary contribution of this chapter is to analyze the estimation error statistics when pilot symbol assisted channel estimation is applied to a JFTS faded / shadowed communication link. The PDF of the estimation error in natural units is derived using the PDF of the instantaneous CSNR. Numerical results demonstrate that the range of acceptable amount of error in CSNR over which the system can operate correctly in a JFTS faded/shadowed channel increases with the decrease in the mean-squared voltages of the shadowed components.The observations also reveal that the estimation error variance increases with the increase in average received CSNR and the increase in small scale fading parameter K and the shadowing parameter S_h. The error variance decreases with the increase in P_2 and decrease in corrupting noise variance Numerical results also show that it will be more useful to use the low CSNR bound while evaluating system performance in presence of estimated CSI over a JFTS link.

Chapter 7

Conclusions

In order to give an outline of the major achievements described in this thesis, the next section will state the main contributions. The chapter will end with some suggestions for further research.

7.1 Major Contributions of the Thesis

- This thesis designed and conducted a measurement campaign consisting of over 30 thousand individual channel measurements in an indoor wireless environment which represent an open concept office or laboratory. The collected measurement data are analyzed to develop the first ever propagation model that combines small scale fading and large scale shadowing for mobility constrained indoor wireless LAN users.

- Statistical properties of the newly developed propagation model are also derived and used them to compare the severity of fading imparted by the JFTS distribution with the fading severity of Rayleigh, Nakagami-m, $\mathcal{K}$-distribution and Nakagami-m - log-normal distribution.

- This thesis developed the first ever expressions for average bit error rate of different fixed modulation techniques over a practical measurement-based indoor composite fading/shadowing propagation model both using MGF and CDF methods. A study on the impact of different JFTS distribution parameters on the performance is also be conducted based on the numerical results.

- These expressions also provide an added advantage that they are able to predict performance for different JFTS parameter values as long as the mean power is the same. Hence, these expressions will provide us the flexibility of analyzing performances over a broad variety of practical indoor WLAN environments with or without the knowledge of the distribution parameters.

- Quantifying the information theoretic limit for an indoor wireless propagation environment is another contribution of this thesis where JFTS channel model is used to characterize the communication scenario. The capacity expressions evaluated over the JFTS channel model provides us with the achievable ergodic capacity measures over a large variety of practical channel conditions, without assuming that the propagation environment is complex Gaussian distributed.

- This thesis also derives the first ever analytically tractable expressions for JFTS ergodic capacity under different adaptive transmission schemes. The relationship between the optimal cut-off CSNR and the average received CSNR is explored for JFTS faded/shadowed links when adaptive transmission techniques are applied.

- Finally this thesis has derived the first ever expressions for distribution of estimation error for non-Gaussian joint faded/shadowed random variables. This provides us a chance to analyze the statistical properties of the CSNR estimation error, where the true and the estimated CSNR do not follow the same distribution.

7.2 Suggestions for Further Research

A natural extension of the work done in this thesis is to propose a complete combination of discrete-rate adaptive coded modulation at the transmit side along with channel estimation, prediction and data detection at the receive side in order to improve overall performance in a large office-type indoor environment. The optimal rate region boundaries for ACM can be chosen based on the analytical expression of the BER derived from the newly developed propagation model. Finally, the newly developed channel statistics can be incorporated as an additional inner code for the joint channel estimator and data detector at the receiver in order to increase reliability of channel prediction and enhance quality of the feedback information.

An investigation can be conducted into the practicality of adaptive signaling due to the variations in the JFTS channel parameters over time, resulting in a different channel at the time of data transmission from that at the time of channel estimation. First of all, the need to consider the channel statistics in the system design of ACM techniques can be demonstrated by calculating the degradation in the error probability due to feedback delay. Then improvement in BER performance of ACM techniques can also be studied using JFTS channel statistics as an inner code for the channel estimator at the receiver, when neither the Doppler frequency nor the exact shape of the auto-correlation function of the channel fading/shadowing process is known. Trellis and LDPC-coded M-QAM techniques can be used as competitive candidates for improvement in bandwidth efficiency.

Power prediction can be used as a means to avoid signaling delays resulting in outdated feedback CSI for ACM techniques over a JFTS faded/shadowed channel. Sub-sampled Auto-regressive

(AR) models can be used to characterize the dynamics of the channel taps and in turn can be used in a particle filter based predictor to predict the instantaneous CSNR at any range that is multiple of the chosen delay spacing. The optimum design of different ACM techniques can be studied, where adaptation of channel parameters is assisted by channel prediction for the at JFTS faded/shadowed channel. The data rate and in some cases, the transmit power can be adapted to maximize the spectral efficiency, subject to average power and BER constraints. Finally the feedback anomaly due to the presence of noise in the feedback channel can be conquered by the inclusion of the JFTS statistics as an inner code at the joint channel estimator and detector of the receiver.

Although, most of the derivations, analyses, implementations and discussions made in this thesis are in the context of indoor WLAN applications, it is possible to apply the propagation model and the performance analysis techniques to a wide range of problems in any field that involves dynamic wave propagation. This is due to the fact that the parameters of the JFTS distribution can be varied to represent a wide variety of channel conditions like direct line-of-sight (LOS) (infinitely high fading parameter), no obstruction or scattering cluster (infinitely high shadowing parameter), Non-LOS (NLOS) (low fading parameter), Obstructed-LOS (OLOS) (low shadowing parameter) between the transmitter and the receiver. Therefore the application of the JFTS model in a wide variety of wireless propagation scenarios is a potential subject for further research.

The choice of higher frequency bands for terrestrial communications is an inevitable consequence of scarcity of microwave spectrum and extensively high wireless traffic demands. So far, these increasing traffic demands have been catered to by increased LTE deployments and small cell off-loading (particularly in Wifi). However, availability of large amounts of new spectrum will be an indispensable requirement for couping up with the projected traffic needs of 2020 and beyond. Millimeter wave (mmW) bands (20 - 300 GHz) is the only place where a significant amount of unused or lightly used spectrum will be available. This has made the mmW bands an attractive front-runner for the next generation wireless heterogeneous cellular networks. Hence, a logical extension of this work will be to find out the appropriateness of using JFTS propagation model to characterize the joint small scale and large scale channel effects on a dual-polarized mmW indoor wireless channel.

Appendix A

Joint Distribution

A.1 Calculation of the Derivatives

Calculation of $\frac{\partial A_i}{\partial K}$ and $\frac{\partial A_i}{\partial P_1}$:

To calculate $\frac{\partial A_i}{\partial K}$ and $\frac{\partial A_i}{\partial P_1}$, we denote, $\frac{x_i}{P_1} = B$, $\exp\left(\frac{-{x_i}^2}{2P_1} - K\right) = C$ and $I_0\left(x_i\sqrt{\frac{2K}{P_1}}\right) = D$. Therefore,

$$\begin{aligned}
\frac{\partial B}{\partial K} &= 0 \\
\frac{\partial C}{\partial K} &= -\exp\left(\frac{-{x_i}^2}{2P_1} - K\right) \\
\frac{\partial D}{\partial K} &= \frac{x_i}{\sqrt{2KP_1}} {I_0}'\left(x_i\sqrt{\frac{2K}{P_1}}\right)
\end{aligned} \tag{A.1}$$

where ${I_0}'(.)$ is the first order derivative of the modified Bessel function of the first kind and zeroth order. Hence,

$$\frac{\partial A_i}{\partial K} = \frac{x_i}{P_1}\exp\left(\frac{-{x_i}^2}{2P_1} - K\right) I_0\left(x_i\sqrt{\frac{2K}{P_1}}\right) - \frac{{x_i}^2}{P_1\sqrt{2KP_1}}\exp\left(\frac{-{x_i}^2}{2P_1} - K\right) {I_0}'\left(x_i\sqrt{\frac{2K}{P_1}}\right) \tag{A.2}$$

Similarly,

$$\begin{aligned}
\frac{\partial B}{\partial P_1} &= \frac{-x_i}{{P_1}^2} \\
\frac{\partial C}{\partial P_1} &= \frac{{x_i}^2}{2{P_1}^2}\exp\left(\frac{-{x_i}^2}{2P_1} - K\right) \\
\frac{\partial D}{\partial P_1} &= -\frac{x_i}{P_1}\sqrt{\frac{K}{2P_1}} {I_0}'\left(x_i\sqrt{\frac{2K}{P_1}}\right)
\end{aligned} \tag{A.3}$$

Hence, it follows,

$$\frac{\partial A_i}{\partial P_1} = \frac{x_i}{{P_1}^2}\exp\left(\frac{-{x_i}^2}{2P_1} - K\right) I_0\left(x_i\sqrt{\frac{2K}{P_1}}\right) - \frac{{x_i}^3}{2{P_1}^3}\exp\left(\frac{-{x_i}^2}{2P_1} - K\right) I_0\left(x_i\sqrt{\frac{2K}{P_1}}\right) + \frac{{x_i}^2}{{P_1}^2}\sqrt{\frac{K}{2P_1}}\exp\left(\frac{-{x_i}^2}{2P_1} - K\right) {I_0}'\left(x_i\sqrt{\frac{2K}{P_1}}\right) \tag{A.4}$$

Putting the results of (A.2) back in (2.6) and that of (A.4) in (2.7), numerical solutions for the values of K and P_1 are obtained.

Calculation of $\frac{\partial G_i}{\partial S_h}$, $\frac{\partial G_i}{\partial \Delta}$ and $\frac{\partial G_i}{\partial P_2}$:

$$\sum_{j=1}^{4} a_j D\left(\frac{y}{\sqrt{P_2}}; S_h, \Delta\cos\frac{\pi(j-1)}{2M-1}\right) = \frac{751}{17280}T_1 + \frac{3577}{17280}T_2 + \frac{49}{640}T_3 + \frac{2989}{17280}T_4 \tag{A.5}$$

where, $a_1 = \frac{751}{8640}$, $a_2 = \frac{3577}{8640}$, $a_3 = \frac{49}{320}$ and $a_4 = \frac{2949}{8640}$ (values directly used from [15]).

$$T_1 = \exp(\Delta S_h) I_0\left(\frac{y}{\sqrt{P_2}}\sqrt{2S_h(1-\Delta)}\right) + \exp(-\Delta S_h) I_0\left(\frac{y}{\sqrt{P_2}}\sqrt{2S_h(1+\Delta)}\right)$$
$$T_2 = \exp(0.9\Delta S_h) I_0\left(\frac{y}{\sqrt{P_2}}\sqrt{2S_h(1-0.9\Delta)}\right) + \exp(-0.9\Delta S_h) I_0\left(\frac{y}{\sqrt{P_2}}\sqrt{2S_h(1+0.9\Delta)}\right)$$
$$T_3 = \exp(0.6\Delta S_h) I_0\left(\frac{y}{\sqrt{P_2}}\sqrt{2S_h(1-0.6\Delta)}\right) + \exp(-0.6\Delta S_h) I_0\left(\frac{y}{\sqrt{P_2}}\sqrt{2S_h(1+0.6\Delta)}\right)$$
$$T_4 = \exp(0.2\Delta S_h) I_0\left(\frac{y}{\sqrt{P_2}}\sqrt{2S_h(1-0.2\Delta)}\right) + \exp(-0.2\Delta S_h) I_0\left(\frac{y}{\sqrt{P_2}}\sqrt{2S_h(1+0.2\Delta)}\right) \tag{A.6}$$

To calculate $\frac{\partial G_i}{\partial S_h}$, $\frac{\partial G_i}{\partial \Delta}$ and $\frac{\partial G_i}{\partial P_2}$, the notations, $H = \frac{y_i}{P_2}$, $I = \exp\left(\frac{-{y_i}^2}{2P_2} - S_h\right)$ and $K' = \frac{751}{17280}T_1 + \frac{3577}{17280}T_2 + \frac{49}{640}T_3 + \frac{2989}{17280}T_4$ are used.

Therefore,

$$\frac{\partial G_i}{\partial S_h} = HI\frac{\partial K'}{\partial S_h} + HK'\frac{\partial I}{\partial S_h} + IK'\frac{\partial H}{\partial S_h}$$
$$\frac{\partial G_i}{\partial \Delta} = HI\frac{\partial K'}{\partial \Delta} + HK'\frac{\partial I}{\partial \Delta} + IK'\frac{\partial H}{\partial \Delta}$$
$$\frac{\partial G_i}{\partial P_2} = HI\frac{\partial K'}{\partial P_2} + HK'\frac{\partial I}{\partial P_2} + IK'\frac{\partial H}{\partial P_2} \tag{A.7}$$

where,

$$\frac{\partial H}{\partial S_h} = 0 \text{ and } \frac{\partial I}{\partial S_h} = -\exp\left(\frac{-{y_i}^2}{2P_2} - S_h\right)$$
$$\frac{\partial H}{\partial \Delta} = 0 \text{ and } \frac{\partial I}{\partial \Delta} = 0$$
$$\frac{\partial H}{\partial P_2} = -\frac{y_i}{{P_2}^2} \text{ and } \frac{\partial I}{\partial P_2} = \frac{{y_i}^2}{2{P_2}^2}\exp\left(\frac{-{y_i}^2}{2P_2} - S_h\right) \tag{A.8}$$

and,

$$\frac{\partial K}{\partial S_h} = \frac{751}{17280}\frac{\partial T_1}{\partial S_h} + \frac{3577}{17280}\frac{\partial T_2}{\partial S_h} + \frac{49}{640}\frac{\partial T_3}{\partial S_h} + \frac{2989}{17280}\frac{\partial T_4}{\partial S_h}$$
$$\frac{\partial K}{\partial \Delta} = \frac{751}{17280}\frac{\partial T_1}{\partial \Delta} + \frac{3577}{17280}\frac{\partial T_2}{\partial \Delta} + \frac{49}{640}\frac{\partial T_3}{\partial \Delta} + \frac{2989}{17280}\frac{\partial T_4}{\partial \Delta}$$
$$\frac{\partial K}{\partial P_2} = \frac{751}{17280}\frac{\partial T_1}{\partial P_2} + \frac{3577}{17280}\frac{\partial T_2}{\partial P_2} + \frac{49}{640}\frac{\partial T_3}{\partial P_2} + \frac{2989}{17280}\frac{\partial T_4}{\partial P_2} \tag{A.9}$$

Here $\frac{\partial T_1}{\partial S_h}$, $\frac{\partial T_1}{\partial \Delta}$ and $\frac{\partial T_1}{\partial P_2}$ can be calculated as below,

$$\begin{aligned}\frac{\partial T_1}{\partial S_h} = {} & \Delta\exp(\Delta S_h) I_0\left(\frac{y}{\sqrt{P_2}}\sqrt{2S_h(1-\Delta)}\right) + \frac{y\sqrt{1-\Delta}}{\sqrt{2P_2S_h}}\exp(\Delta S_h) {I_0}'\left(\frac{y}{\sqrt{P_2}}\sqrt{2S_h(1-\Delta)}\right) \\ & - \Delta\exp(-\Delta S_h) I_0\left(\frac{y}{\sqrt{P_2}}\sqrt{2S_h(1+\Delta)}\right) + \frac{y\sqrt{1+\Delta}}{\sqrt{2P_2S_h}}\exp(-\Delta S_h) {I_0}'\left(\frac{y}{\sqrt{P_2}}\sqrt{2S_h(1+\Delta)}\right)\end{aligned} \tag{A.10}$$

$$\begin{aligned}\frac{\partial T_1}{\partial \Delta} = {} & S_h\exp(\Delta S_h) I_0\left(\frac{y}{\sqrt{P_2}}\sqrt{2S_h(1-\Delta)}\right) - \frac{y\sqrt{S_h}}{\sqrt{2P_2(1-\Delta)}}\exp(\Delta S_h) {I_0}'\left(\frac{y}{\sqrt{P_2}}\sqrt{2S_h(1-\Delta)}\right) \\ & - S_h\exp(-\Delta S_h) I_0\left(\frac{y}{\sqrt{P_2}}\sqrt{2S_h(1+\Delta)}\right) + \frac{y\sqrt{S_h}}{\sqrt{2P_2(1+\Delta)}}\exp(-\Delta S_h) {I_0}'\left(\frac{y}{\sqrt{P_2}}\sqrt{2S_h(1+\Delta)}\right)\end{aligned} \tag{A.11}$$

and,

$$\begin{aligned}\frac{\partial T_1}{\partial P_2} = {} & -\frac{y}{P_2}\sqrt{\frac{S_h(1-\Delta)}{2P_2}}\exp(\Delta S_h) {I_0}'\left(\frac{y}{\sqrt{P_2}}\sqrt{2S_h(1-\Delta)}\right) \\ & - \frac{y}{P_2}\sqrt{\frac{S_h(1+\Delta)}{2P_2}}\exp(-\Delta S_h) {I_0}'\left(\frac{y}{\sqrt{P_2}}\sqrt{2S_h(1+\Delta)}\right)\end{aligned} \tag{A.12}$$

Similarly $\frac{\partial T_2}{\partial S_h}$, $\frac{\partial T_2}{\partial \Delta}$, $\frac{\partial T_2}{\partial P_2}$, $\frac{\partial T_3}{\partial S_h}$, $\frac{\partial T_3}{\partial \Delta}$, $\frac{\partial T_3}{\partial P_2}$, $\frac{\partial T_4}{\partial S_h}$, $\frac{\partial T_4}{\partial \Delta}$ and $\frac{\partial T_4}{\partial P_2}$ are calculated, which in turn are used to numerically solve for the values of S_h, Δ and P_2.

A.2 Calculation of the Joint PDF

The term, $\frac{751}{17280} T_1 I_0\left(x\sqrt{\frac{2K}{P_1}}\right)$ can be calculated using infinite series expansion of Modified Bessel Function as,

$$\frac{751}{17280} T_1 I_0\left(x\sqrt{\frac{2K}{P_1}}\right) = \frac{751}{17280} T_1 \sum_{k=0}^{\infty} \frac{\left(\frac{x^2 2K}{4P_1}\right)^k}{(k!)^2} \tag{A.13}$$

Expanding and rearranging, (A.13) can be written as,

$$\begin{aligned} \frac{751}{17280} T_1 I_0\left(x\sqrt{\frac{2K}{P_1}}\right) = \frac{751}{17280} \Bigg[& \exp\,(\Delta S_h) \sum_{k=0}^{\infty} \frac{\left(\frac{x^2 2K}{4P_1}\right)^k}{(k!)^2} \cdot \sum_{k=0}^{\infty} \frac{\left(\frac{y^2 2S_h(1-\Delta)}{4P_2}\right)^k}{(k!)^2} \\ & + \exp\,(-\Delta S_h) \sum_{k=0}^{\infty} \frac{\left(\frac{x^2 2K}{4P_1}\right)^k}{(k!)^2} \cdot \sum_{k=0}^{\infty} \frac{\left(\frac{y^2 2S_h(1+\Delta)}{4P_2}\right)^k}{(k!)^2} \Bigg] \end{aligned} \tag{A.14}$$

Rearranging again, (A.14) can be written as,

$$\begin{aligned} \frac{751}{17280} T_1 I_0\left(x\sqrt{\frac{2K}{P_1}}\right) = \frac{751}{17280} \Bigg[& \exp\,(\Delta S_h) \sum_{k=0}^{\infty} \frac{\left(\frac{4x^2y^2 K S_h(1-\Delta)}{4P_1P_2}\right)^k}{(k!)^2} \sum_{k=0}^{\infty} \frac{\left(\frac{1}{4}\right)^k}{(k!)^2} \\ & + \exp\,(-\Delta S_h) \sum_{k=0}^{\infty} \frac{\left(\frac{4x^2y^2 K S_h(1+\Delta)}{4P_1P_2}\right)^k}{(k!)^2} \sum_{k=0}^{\infty} \frac{\left(\frac{1}{4}\right)^k}{(k!)^2} \Bigg] \end{aligned} \tag{A.15}$$

If (A.14) is then returned to representing the infinite series as Modified Bessel Function, it can be expressed as,

$$\begin{aligned} \frac{751}{17280} T_1 I_0\left(x\sqrt{\frac{2K}{P_1}}\right) = \frac{751}{17280} \Bigg[& \exp\,(\Delta S_h) I_0\left(2xy\sqrt{\frac{K S_h(1-\Delta)}{P_1P_2}}\right) I_0(1) \\ & + \exp\,(-\Delta S_h) I_0\left(2xy\sqrt{\frac{K S_h(1+\Delta)}{P_1P_2}}\right) I_0(1) \Bigg] \end{aligned} \tag{A.16}$$

which can be written in terms of $D(\alpha; K, \beta)$ as,

$$\frac{751}{17280} T_1 I_0\left(x\sqrt{\frac{2K}{P_1}}\right) = b_1 D\left(xy\sqrt{\frac{2K}{P_1P_2}}; S_h, \Delta\right) \tag{A.17}$$

It can be obtained from (2.14) that,

$$f_{XY}(r, z/r) = \frac{z}{P_1P_2} \exp\left(-\frac{r^2}{2P_1} - \frac{z^2}{2P_2r^2} - K - S_h\right)\sum_{j=1}^{4} b_j D\left(z\sqrt{\frac{2K}{P_1P_2}}; S_h, \Delta\cos\frac{\pi(j-1)}{2M-1}\right) \tag{A.18}$$

Hence, (A.17) can be rewritten as,

$$\begin{aligned} f_Z(z) = \frac{z}{P_1P_2} \exp\left(-K - S_h\right) \sum_{j=1}^{4} b_j D\left(z\sqrt{\frac{2K}{P_1P_2}}; S_h, \Delta\cos\frac{\pi(j-1)}{2M-1}\right) \\ \int_{-\infty}^{\infty} \frac{1}{|r|} \exp\left(-\frac{r^2}{2P_1} - \frac{z^2}{2P_2r^2}\right)\mathrm{d}r \end{aligned} \tag{A.19}$$

where, the integrand in (2.9) can be solved using Gauss-Hermite Quadrature Integration and can written in the form,

$$\begin{aligned} R' &= \int_{-\infty}^{\infty} \frac{1}{|r|} \exp\left(-\frac{r^2}{2P_1} - \frac{z^2}{2P_2r^2}\right)\mathrm{d}r \\ &\approx \sum_{h=1}^{m} w_h f(r_h) \\ &\approx \sum_{h=1}^{m} w_h\left[\frac{1}{|r_h|} \exp\left(\frac{{r_h}^2(2P_1-1)}{2P_1} - \frac{z^2}{2P_2{r_h}^2}\right)\right] \end{aligned} \tag{A.20}$$

where, m is the approximation index. The multiplier w_h denotes the associated weights and is given by,

$$w_h = \frac{2^{m-1} m! \sqrt{\pi}}{m^2[H_{m-1}(r_h)]^2}$$

where $H_{m-1}(.)$ is the Hermite polynomial with roots r_h for $h = 1, 2, \ldots, m$. Hence, (A.19) can be rewritten as,

$$f_Z(z) = \frac{z}{P_1P_2}\ \exp\left(-K - S_h\right)\sum_{j=1}^{4} b_j D\left(z\sqrt{\frac{2K}{P_1P_2}}; S_h, \Delta\cos\frac{\pi(j-1)}{2M-1}\right)$$
$$\sum_{h=1}^{m} w_h\left[\frac{1}{|r_h|}\ \exp\left(\frac{{r_h}^2(2P_1-1)}{2P_1} - \frac{z^2}{2P_2{r_h}^2}\right)\right]. \tag{A.21}$$

Appendix B

Statistics of Composite Envelope

B.1 Moments of the Composite Envelope

In order to arrive at the final expression of the joint moments, the first integral that is needed to solved can be written as,

$$\mathcal{A} \;=\; \int_{-\infty}^{\infty} \frac{(x)^{n+1}}{P_1}\; e^{-\frac{x^2}{2P_1}-K} I_0\!\left(x\sqrt{\frac{2K}{P_1}}\right)\mathrm{d}x \tag{B.1}$$

Using infinite series expansion of the modified Bessel function, the integrand in (B.1) can be expressed as,

$$\begin{aligned}\mathcal{A} \;&=\; \int_{-\infty}^{\infty} \frac{(x)^{n+1}}{P_1}\; e^{-\frac{x^2}{2P_1}-K} \sum_{\mathsf{k}=0}^{\infty} \frac{1}{(\mathsf{k}!)^2}\left(\frac{x^2 K}{P_1}\right)^{\mathsf{k}}\mathrm{d}x\\ &= \sum_{\mathsf{k}=0}^{\infty} \frac{1}{(\mathsf{k}!)^2}\frac{K^{\mathsf{k}}}{P_1^{\mathsf{k}+1}}\; e^{-K} \int_{-\infty}^{\infty} (x)^{n+1+2\mathsf{k}}\; e^{-\frac{x^2}{2P_1}}\mathrm{d}x \end{aligned}\tag{B.2}$$

Putting $n' = n + 1 + 2\mathsf{k}$, $p' = \frac{1}{2P_1}$ and $q' = 0$, and using the integral solution from [39] (B.2) can be written as,

$$\mathcal{A} \;= (2P_1)^{n/2}\; \frac{(1+n/2)!}{(n/2)!}\; e^{-K}\; \frac{\mathrm{d}^{n/2}}{\mathrm{d}(-K)^{n/2}}\left(K^{n/2}\; e^{K}\right) \tag{B.3}$$

which can be written in terms of the Laguerre polynomial and the incomplete Gamma function as,

$$\mathcal{A} \;= (2P_1)^{n/2}\; \Gamma(1+n/2)\;\; L_{n/2}(-K) \tag{B.4}$$

The second integration can also be solved by following the same procedure as before to obtain,

$$\begin{aligned}\mathcal{B} &= \sum_{j=1}^{4} a_j \int_{-\infty}^{\infty} \mathsf{T}_j \, \frac{(y)^{n+1}}{P_2} \, e^{-\frac{y^2}{2P_2} - S_h} \mathrm{d}y \\ &= \sum_{j=1}^{4} a_j \, (2P_2)^{n/2} \, \Gamma(1+n/2) \, \big[L_{n/2}(-(1-\Delta\mathsf{M}_j)S_h) + L_{n/2}(-(1+\Delta\mathsf{M}_j)S_h)\big] \qquad \text{(B.5)}\end{aligned}$$

where,

$$\mathsf{T}_j = e^{S_h \Delta\mathsf{M}_j} \, I_0\Big(y\sqrt{2S_h(1-\Delta\mathsf{M}_j)/P_2}\Big) + e^{-S_h \Delta\mathsf{M}_j} \, I_0\Big(y\sqrt{2S_h(1+\Delta\mathsf{M}_j)/P_2}\Big)$$

B.2 CDF of the Composite Envelope

In order to derive the CDF of the JFTS distribution, the following integral is needed to be solved as,

$$\mathcal{I} = \mathcal{C}_1 \sum_{j=1}^{4} \frac{b_j}{2} \sum_{h=1}^{20} \mathcal{R} \int_{-\infty}^{z} \mathsf{u} \, e^{-\mathcal{C}_2 \mathsf{u}^2} \, \big[\mathcal{D}_3 \, I_0(2\mathsf{u}\mathcal{D}_1) \; + \; \mathcal{D}_4 \, I_0(2\mathsf{u}\mathcal{D}_2)\big] \, \mathsf{du} \qquad \text{(B.6)}$$

Using the infinite series expansion of the modified Bessel function of the first kind, (B.6) can be expressed as,

$$\mathcal{I} = \mathcal{C}_1 \sum_{j=1}^{4} \frac{b_j}{2} \sum_{h=1}^{20} \mathcal{R} \sum_{\mathsf{k}=0}^{\infty} \frac{\mathcal{D}_3 \, \mathcal{D}_1^{2\mathsf{k}} + \mathcal{D}_4 \, \mathcal{D}_2^{2\mathsf{k}}}{(\mathsf{k}!)^2} \int_{-\infty}^{z} \mathsf{u}^{2\mathsf{k}+1} \, e^{-\mathcal{C}_2 \mathsf{u}^2} \, \mathsf{du} \qquad \text{(B.7)}$$

Using the integral solution from [39] and the incomplete Gamma function given in [45], (B.7) can be written as,

$$\mathcal{I} = \mathcal{C}_1 \sum_{j=1}^{4} \frac{b_j}{2} \sum_{h=1}^{20} \mathcal{R} \sum_{\mathsf{k}=0}^{\infty} \frac{\mathcal{D}_3 \, \mathcal{D}_1^{2\mathsf{k}} + \mathcal{D}_4 \, \mathcal{D}_2^{2\mathsf{k}}}{(\mathsf{k}!)^2} \left[1 \; - \; \frac{\Gamma(\mathsf{k}+1, \mathcal{C}_2 z^2)}{2\mathcal{C}_2^{\mathsf{k}+1}}\right] \qquad \text{(B.8)}$$

Instead of using the infinite series representation, Marcum-Q function can be also be used to represent the expression in (B.8) as,

$$\mathcal{I} = \mathcal{C}_1 \sum_{j=1}^{4} \frac{b_j}{2} \sum_{h=1}^{20} \frac{\mathcal{R}}{\sqrt{2\mathcal{C}_2}} \left[\mathcal{D}_3 Q_1\bigg(\frac{\sqrt{2}\mathcal{D}_1}{\sqrt{\mathcal{C}_2}}, z\bigg) + \mathcal{D}_4 Q_1\bigg(\frac{\sqrt{2}\mathcal{D}_2}{\sqrt{\mathcal{C}_2}}, z\bigg)\right] \qquad \text{(B.9)}$$

B.3 Calculation of MGF of Instantaneous CSNR

In order to derive the expression for the MGF of the instantaneous received CSNR, γ, the integral that is needed to be solved can be expressed in the form,

$$\begin{aligned}\mathcal{I}_1 \;=\; & \int_0^\infty \Bigg[e^{S_h \Delta\mathsf{M}_j - s\gamma - \frac{2P_1\tilde{K}\tilde{S_h}\gamma}{r_h^2\overline{\gamma}}} I_0\left(8\sqrt{KS_h\tilde{K}\tilde{S_h}(1-\Delta\mathsf{M}_j)\gamma/\overline{\gamma}}\right) \\ & + \; e^{-S_h \Delta\mathsf{M}_j - s\gamma - \frac{2P_1\tilde{K}\tilde{S_h}\gamma}{r_h^2\overline{\gamma}}} I_0\left(8\sqrt{KS_h\tilde{K}\tilde{S_h}(1+\Delta\mathsf{M}_j)\gamma/\overline{\gamma}}\right)\Bigg] \mathrm{d}\gamma \end{aligned} \tag{B.10}$$

The solution to this integral can be found by using the integral solution from [48] to obtain,

$$\mathcal{I}_1 \;=\; \frac{1}{\sqrt{\mathtt{AB}_1}}\; e^{S_h\Delta\mathsf{M}_j + \frac{\mathtt{B}_1}{2\mathtt{A}}}\; \mathtt{M}_{-1/2,0}\left(\frac{\mathtt{B}_1}{\mathtt{A}}\right) \;+\; \frac{1}{\sqrt{\mathtt{AB}_2}}\; e^{S_h\Delta\mathsf{M}_j + \frac{\mathtt{B}_2}{2\mathtt{A}}}\; \mathtt{M}_{-1/2,0}\left(\frac{\mathtt{B}_2}{\mathtt{A}}\right) \tag{B.11}$$

where,

$$\begin{aligned} \mathtt{A} &= s \;+\; 2P_1\tilde{K}\tilde{S_h}/r_h^2\overline{\gamma} \\ \mathtt{B}_1 &= 16KS_h\tilde{K}\tilde{S_h}(1-\Delta\mathsf{M}_j)/\overline{\gamma} \\ \mathtt{B}_2 &= 16KS_h\tilde{K}\tilde{S_h}(1+\Delta\mathsf{M}_j)/\overline{\gamma} \end{aligned} \tag{B.12}$$

and $\mathtt{M}_{-1/2,0}(\cdot)$ is the Whittaker M-function which can be expanded as,

$$\mathtt{M}_{-1/2,0}\left(\frac{\mathtt{B}_1}{\mathtt{A}}\right) \;=\; \sqrt{\frac{\mathtt{B}_1}{\mathtt{A}}}\; e^{\frac{\mathtt{B}_1}{2\mathtt{A}}} \text{ and } \mathtt{M}_{-1/2,0}\left(\frac{\mathtt{B}_2}{\mathtt{A}}\right) \;=\; \sqrt{\frac{\mathtt{B}_2}{\mathtt{A}}}\; e^{\frac{\mathtt{B}_2}{2\mathtt{A}}} \tag{B.13}$$

Using (B.13), (B.11) can now be expressed as,

$$\begin{aligned} \mathcal{I}_1 &= \frac{1}{\mathtt{A}}\left[e^{S_h\Delta\mathsf{M}_j + \frac{\mathtt{B}_1}{\mathtt{A}}} \;+\; e^{-S_h\Delta\mathsf{M}_j + \frac{\mathtt{B}_2}{\mathtt{A}}}\right] \\ &= \frac{r_h^2\overline{\gamma}}{2P_1\tilde{K}\tilde{S_h} + sr_h^2\overline{\gamma}}\left[e^{S_h\Delta\mathsf{M}_j + \frac{16KS_h\tilde{K}\tilde{S_h}(1-\Delta\mathsf{M}_j)r_h^2}{2P_1\tilde{K}\tilde{S_h} + sr_h^2\overline{\gamma}}} \;+\; e^{-S_h\Delta\mathsf{M}_j + \frac{16KS_h\tilde{K}\tilde{S_h}(1+\Delta\mathsf{M}_j)r_h^2}{2P_1\tilde{K}\tilde{S_h} + sr_h^2\overline{\gamma}}}\right] \end{aligned} \tag{B.14}$$

Putting (B.14) back in the integral in (4.10), the final expression for the MGF, $\mathcal{M}_\gamma(s)$ can be obtained in the form of (4.10).

Appendix C

Error Probability Performance

C.1 MGF-based Error Probability Performance

Solution to $\mathcal{I}(\bar{\mathsf{x}}, \pi/2)$ **:** Substituting (4.10) in (4.16), followed by $\mathtt{t}_1 = \frac{2\mathtt{F}_3 \sin^2\theta}{2\mathtt{E}_2 \sin^2\theta + \mathtt{E}_3 \bar{\mathsf{x}}^2}$, $\mathtt{t}_2 = \frac{2\mathtt{F}_4 \sin^2\theta}{2\mathtt{E}_2 \sin^2\theta + \mathtt{E}_3 \bar{\mathsf{x}}^2}$, $\mathtt{u}_1 = \left(\frac{2\mathtt{E}_2 + \mathtt{E}_3\bar{\mathsf{x}}^2}{2\mathtt{F}_3}\right)\mathtt{t}_1$ and $\mathtt{u}_2 = \left(\frac{2\mathtt{E}_2 + \mathtt{E}_3\bar{\mathsf{x}}^2}{2\mathtt{F}_4}\right)\mathtt{t}_2$ respectively, the closed-form expression for the integral $\mathcal{I}(\bar{\mathsf{x}}, \pi/2)$ can be given by,

$$\begin{aligned}
\mathcal{I}(\bar{\mathsf{x}}, \pi/2) &= \frac{1}{\pi}\int_0^{\pi/2} \mathcal{M}_\gamma\left(\frac{\bar{\mathsf{x}}^2}{2\sin^2\theta}\right) \mathrm{d}\theta \\
&= \sum_{j=1}^{4}\sum_{h=1}^{20}\left[\frac{\bar{\mathsf{x}}\mathtt{E}_1\sqrt{\mathtt{E}_3}}{2(2\mathtt{E}_2 + \mathtt{E}_3\bar{\mathsf{x}}^2)^{3/2}}\ e^{\mathtt{F}_1 - \frac{\mathtt{F}_3}{\mathtt{E}_2}}\ \phi_1\left(\frac{3}{2}, 1; 2; \frac{2\mathtt{E}_2}{2\mathtt{E}_2 + \mathtt{E}_3\bar{\mathsf{x}}^2}, \frac{2\mathtt{F}_3}{2\mathtt{E}_2 + \mathtt{E}_3\bar{\mathsf{x}}^2}\right)\right. \\
&+ \left.\frac{\bar{\mathsf{x}}\mathtt{E}_1\sqrt{\mathtt{E}_3}}{2(2\mathtt{E}_2 + \mathtt{E}_3\bar{\mathsf{x}}^2)^{3/2}}\ e^{\mathtt{F}_2 - \frac{\mathtt{F}_4}{\mathtt{E}_2}}\ \phi_1\left(\frac{3}{2}, 1; 2; \frac{2\mathtt{E}_2}{2\mathtt{E}_2 + \mathtt{E}_3\bar{\mathsf{x}}^2}, \frac{2\mathtt{F}_4}{2\mathtt{E}_2 + \mathtt{E}_3\bar{\mathsf{x}}^2}\right)\right]
\end{aligned} \tag{C.1}$$

where,

$$\begin{aligned}
\mathtt{E}_1 &= b_j \mathcal{R}\tilde{K}\tilde{S}_h r_h^2\ e^{-K-S_h} \\
\mathtt{E}_2 &= 2P_1\tilde{K}\tilde{S}_h \\
\mathtt{E}_3 &= r_h^2\overline{\gamma} \\
\mathtt{F}_1 &= S_h \Delta\mathsf{M}_j \\
\mathtt{F}_2 &= -S_h \Delta\mathsf{M}_j \\
\mathtt{F}_3 &= 16KS_h\tilde{K}\tilde{S}_h(1 - \Delta\mathsf{M}_j)r_h^2 \\
\mathtt{F}_4 &= 16KS_h\tilde{K}\tilde{S}_h(1 + \Delta\mathsf{M}_j)r_h^2
\end{aligned} \tag{C.2}$$

and $\phi_1(\cdot)$ is a confluent hypergeometric function of two variables.

Solution to $\mathcal{I}(\bar{\mathsf{x}}, \pi/2 - \arctan(\bar{\mathsf{y}}/\bar{\mathsf{x}}))$: Substituting (4.10) in (4.16), followed by $\mathtt{t}_1 = \frac{2\mathsf{F}_3 \sin^2\theta}{2\mathsf{E}_2 \sin^2\theta + \mathsf{E}_3\bar{\mathsf{x}}^2}$, $\mathtt{t}_2 = \frac{2\mathsf{F}_4 \sin^2\theta}{2\mathsf{E}_2 \sin^2\theta + \mathsf{E}_3\bar{\mathsf{x}}^2}$, $\mathtt{u}_1 = \left(\frac{2\mathsf{E}_2\bar{\mathsf{x}}^2(\bar{\mathsf{x}}^2+\bar{\mathsf{y}}^2)+\mathsf{E}_3\bar{\mathsf{x}}^2}{2\mathsf{F}_3}\bar{\mathsf{x}}^2\right)\mathtt{t}_1$ and $\mathtt{u}_2 = \left(\frac{2\mathsf{E}_2\bar{\mathsf{x}}^2(\bar{\mathsf{x}}^2+\bar{\mathsf{y}}^2)+\mathsf{E}_3\bar{\mathsf{x}}^2}{2\mathsf{F}_4}\bar{\mathsf{x}}^2\right)\mathtt{t}_2$ respectively, the closed-form expression for the integral $\mathcal{I}(\bar{\mathsf{x}}, \pi/2 - \arctan(\bar{\mathsf{y}}/\bar{\mathsf{x}}))$ can be given by,

$$\mathcal{I}(\bar{\mathsf{x}}, \pi/2 - \arctan(\bar{\mathsf{y}}/\bar{\mathsf{x}})) \;=\; \frac{1}{\pi}\int_0^{\pi/2-\arctan(\bar{\mathsf{y}}/\bar{\mathsf{x}})} \mathcal{M}_\gamma\left(\frac{\bar{\mathsf{x}}^2}{2\sin^2\theta}\right)\mathrm{d}\theta \tag{C.3}$$

$$\begin{aligned}\mathcal{I}(\bar{\mathsf{x}}, \pi/2 - \arctan(\bar{\mathsf{y}}/\bar{\mathsf{x}})) \;=\; & \sum_{j=1}^{4}\sum_{h=1}^{20}\left[\frac{2\bar{\mathsf{x}}\mathsf{E}_1\sqrt{\mathsf{E}_3}}{3\pi(2\mathsf{E}_2+\mathsf{E}_3(\bar{\mathsf{x}}^2+\bar{\mathsf{y}}^2))^{3/2}}\; e^{\mathsf{F}_1-\frac{\mathsf{F}_3}{\mathsf{E}_2}}\right.\\ & \phi_1^{(3)}\left(\frac{3}{2},1,\frac{1}{2};\frac{5}{2};\frac{2\mathsf{E}_2}{2\mathsf{E}_2+\mathsf{E}_3(\bar{\mathsf{x}}^2+\bar{\mathsf{y}}^2)},\frac{2\mathsf{E}_2+\mathsf{E}_3\bar{\mathsf{x}}^2}{2\mathsf{E}_2+\mathsf{E}_3(\bar{\mathsf{x}}^2+\bar{\mathsf{y}}^2)},\frac{2\mathsf{F}_3}{2\mathsf{E}_2+\mathsf{E}_3(\bar{\mathsf{x}}^2+\bar{\mathsf{y}}^2)}\right)\\ & +\;\frac{2\bar{\mathsf{x}}\mathsf{E}_1\sqrt{\mathsf{E}_3}}{3\pi(2\mathsf{E}_2+\mathsf{E}_3(\bar{\mathsf{x}}^2+\bar{\mathsf{y}}^2))^{3/2}}\; e^{\mathsf{F}_2-\frac{\mathsf{F}_4}{\mathsf{E}_2}}\\ & \left.\phi_1^{(3)}\left(\frac{3}{2},1,\frac{1}{2};\frac{5}{2};\frac{2\mathsf{E}_2}{2\mathsf{E}_2+\mathsf{E}_3(\bar{\mathsf{x}}^2+\bar{\mathsf{y}}^2)},\frac{2\mathsf{E}_2+\mathsf{E}_3\bar{\mathsf{x}}^2}{2\mathsf{E}_2+\mathsf{E}_3(\bar{\mathsf{x}}^2+\bar{\mathsf{y}}^2)},\frac{2\mathsf{F}_4}{2\mathsf{E}_2+\mathsf{E}_3(\bar{\mathsf{x}}^2+\bar{\mathsf{y}}^2)}\right)\right]\end{aligned} \tag{C.4}$$

where, $\phi_1^{(3)}(\cdot)$ is a confluent Lauricella's hypergeometric function of three variables. The integral solutions from (C.1) and (C.4) can be inserted back in (4.12) to obtain the ABER expressions of (4.17) and (4.19).

C.2 CDF-based Error Probability Performance

In order to obtain the expression for ABER of binary modulation techniques, the integral that is needed to be solved can be expressed as,

$$\begin{aligned}
\mathcal{I}_2 &= \int_0^\infty \gamma^{v+\overline{\beta}-1}\, e^{-\frac{2P_1\tilde{K}\tilde{S}_h\gamma}{r_h^2\overline{\gamma}}-\overline{\alpha}\gamma} \mathrm{d}\gamma \\
&= (-1)\ (v+\overline{\beta}-1)! \left(\frac{r_h^2\overline{\gamma}}{2P_1\tilde{K}\tilde{S}_h + r_h^2\overline{\gamma\alpha}}\right)^{v+\overline{\beta}} \\
&= (-1)\ \frac{(v+\overline{\beta})!}{v+\overline{\beta}} \left(\frac{r_h^2\overline{\gamma}}{2P_1\tilde{K}\tilde{S}_h + r_h^2\overline{\gamma\alpha}}\right)^{v+\overline{\beta}} \qquad \text{(C.5)}
\end{aligned}$$

Using (4.8) and (C.5), the infinite series summation that is needed to be solved to obtain the final expression for ABER, can be given by,

$$\mathcal{S}_2 = \sum_{\mathsf{k}=0}^{\infty}\sum_{v=0}^{\mathsf{k}} \left(\frac{r_h^2\overline{\gamma}}{2P_1\tilde{K}\tilde{S}_h + r_h^2\overline{\gamma\alpha}}\right)^{\overline{\beta}} \left[(-1)\ \frac{(v+\overline{\beta}-1)!}{v!}\left(\frac{2P_1\tilde{K}\tilde{S}_h}{2P_1\tilde{K}\tilde{S}_h + r_h^2\overline{\gamma\alpha}}\right)^{v}\right] \qquad \text{(C.6)}$$

which can be solved as below,

$$\begin{aligned}
\mathcal{S}_2 = \sum_{\mathsf{k}=0}^{\infty} & \frac{(-2)^{\mathsf{k}}(\bar{\beta}+\mathsf{k})!}{(\mathsf{k}+1)!}\left(\frac{2P_1\tilde{K}\tilde{S}_h}{\bar{\alpha}r_h^2\overline{\gamma}+2P_1\tilde{K}\tilde{S}_h}\right)^{\mathsf{k}+1} \left(\frac{r_h^2\overline{\gamma}}{\bar{\alpha}r_h^2\overline{\gamma}+2P_1\tilde{K}\tilde{S}_h}\right)^{\bar{\beta}} \\
& {}_2F_1\left(1, \bar{\beta}+\mathsf{k}+1; \mathsf{k}+2; \frac{2P_1\tilde{K}\tilde{S}_h}{\bar{\alpha}r_h^2\overline{\gamma}+2P_1\tilde{K}\tilde{S}_h}\right) - \frac{(\bar{\beta}-1)!}{\bar{\alpha}^{\bar{\beta}}} \qquad \text{(C.7)}
\end{aligned}$$

Putting (C.7) back in (4.25), the final expression for ABER of binary modulation techniques can be obtained in the form of (4.26).

C.3 PEP-based Error Probability Performance

The inner integral in (4.42) can be solved using the infinite series representation of [48] as,

$$\begin{aligned}\mathcal{I}_3 &= \int_0^{\frac{\zeta_\tau}{E_s/N_0}} \zeta_\tau^{\mathsf{k}\delta_1}\; e^{-\frac{\zeta_\tau}{2P_2 r_h^2}} \mathrm{d}\zeta_\tau \\ &= \frac{\mathsf{k}\delta_1!}{(1/2P_2 r_h^2)^{\mathsf{k}\delta_1+1}}\; e^{-\frac{\mathsf{k}^2 N_0}{2E_s P_2 r_h^2}} \sum_{v=0}^{\mathsf{k}\delta_1} \frac{\mathsf{k}\delta_1!}{v!} \frac{(\mathsf{k}^2 N_0/E_s)^v}{(1/2P_2 r_h^2)^{\mathsf{k}\delta_1 - v+1}} \qquad \text{(C.8)}\end{aligned}$$

Putting (C.8) in (4.42), the outer integral can be solved as below,

$$\begin{aligned}\mathcal{I}_4 &= \int_0^{\infty} e^{\nu^2/2} \left(\int_0^{\frac{\zeta_\tau}{E_s/N_0}} \zeta_\tau^{\mathsf{k}\delta_1}\; e^{-\frac{\zeta_\tau}{2P_2 r_h^2}} \mathrm{d}\zeta_\tau \right) \mathrm{d}\nu \\ &= \frac{\mathsf{k}\delta_1!}{(1/2P_2 r_h^2)^{\mathsf{k}\delta_1+1}} \sqrt{\frac{\pi}{2}} - \sum_{v=0}^{\mathsf{k}\delta_1} \frac{\mathsf{k}\delta_1!}{2v!(E_s/N_0)^v} \frac{\Gamma(v+1/2)}{(1/2P_2 r_h^2)^{\mathsf{k}\delta_1 - v+1}(1/2 + N_0/2E_s P_2 r_h^2)^{v+1/2}} \qquad \text{(C.9)}\end{aligned}$$

where $\Gamma(\cdot)$ is the upper incomplete Gamma function. Substituting (C.9) back in (4.42), the final expression for PEP of Turbo coded BPSK over a JFTS faded/shadowed communication channel can be obtained in the form of (4.43).

C.4 GA-based Error Probability Performance

In order to obtain the expression in (4.46), the integral that is needed to be solved can be given by,

$$\begin{aligned}\mathcal{I}_5 &= \int_0^{\infty} \zeta_\tau^{\mathsf{k}}\; e^{-\frac{\zeta_\tau}{2P_2 r_h^2}} \frac{\sigma_n}{2\sqrt{2\pi\zeta_\tau}}\; e^{\frac{c}{2} - \frac{c^2\sigma_n^2}{8\zeta_\tau} - \frac{\zeta_\tau}{2\sigma_n^2}} \mathrm{d}\zeta_\tau \\ &= \frac{\sigma_n}{2\sqrt{2\pi}}\; e^{\frac{c}{2}} \int_0^{\infty} \zeta_\tau^{\mathsf{k}-1/2}\; e^{-\frac{\zeta_\tau}{2P_2 r_h^2} - \frac{c^2\sigma_n^2}{8\zeta_\tau} - \frac{\zeta_\tau}{2\sigma_n^2}} \mathrm{d}\zeta_\tau \\ &= \frac{\sigma_n}{\sqrt{2\pi}}\; e^{\frac{c}{2}} \left(\frac{c\sigma_n^2 r_h}{2} \sqrt{\frac{P_2}{\sigma_n^2 + P_2 r_h^2}} \right)^{\mathsf{k}+1/2} \mathcal{K}_{\mathsf{k}+1/2}\left(\frac{c}{2r_h} \sqrt{\frac{\sigma_n^2 + P_2 r_h^2}{P_2}} \right) \qquad \text{(C.10)}\end{aligned}$$

Putting (C.10) back, the unconditional PDF of the channel LLR can be obtained in the form of (4.46).

In order to obtain the expression in (4.47), the integral that is needed to be solved can be calculated as below,

$$
\begin{aligned}
\mathcal{I}_6 &= \int_0^\infty \mathsf{o}^{\mathsf{k}+1/2}\, e^{-\frac{\mathsf{o}^2}{4\mu_\upsilon}}\, \mathcal{K}_{\mathsf{k}+1/2}\left(\frac{\mathsf{o}}{2r_h}\sqrt{\frac{\sigma_n^2+P_2r_h^2}{P_2}}\right)\mathrm{d}\mathsf{o} \\
&= \frac{1}{2}(4\mu_\upsilon)^{\mathsf{k}/2+1/4}\left(\sqrt{\frac{4r_h^2P_2}{\sigma_n^2+P_2r_h^2}}\right)\Gamma(\mathsf{k}+1)\Gamma(1/2)\, e^{\frac{\mu_\upsilon(\sigma_n^2+P_2r_h^2)}{8r_h^2P_2}}\, \mathcal{W}_{-\mathsf{k}/2+1/4,\mathsf{k}/2+1/4}\left(\frac{\mu_\upsilon(\sigma_n^2+P_2r_h^2)}{8r_h^2P_2}\right) \\
&= \frac{\sqrt{\pi}}{2}(4\mu_\upsilon)^{\mathsf{k}/2+1/4}\left(\sqrt{\frac{4r_h^2P_2}{\sigma_n^2+P_2r_h^2}}\right)\Gamma(\mathsf{k}+1)\, e^{\frac{\mu_\upsilon(\sigma_n^2+P_2r_h^2)}{8r_h^2P_2}}\, \mathcal{W}_{-\mathsf{k}/2+1/4,\mathsf{k}/2+1/4}\left(\frac{\mu_\upsilon(\sigma_n^2+P_2r_h^2)}{8r_h^2P_2}\right)
\end{aligned}
\tag{C.11}
$$

Putting (C.11) back, the PDF of the bit node message can be obtained in the form of (4.47).

In order to obtain the expression in (4.48), the integral that is needed to be solved can be expressed as below,

$$
\begin{aligned}
\mathcal{I}_7 &= \int_0^\infty e^{\frac{c}{2}-\frac{c^2}{4\mu_\upsilon^{\delta_2+1}}}\mathrm{d}c \\
&= \sqrt{\pi\mu_\upsilon^{\delta_2+1}}\, e^{\frac{\mu_\upsilon^{\delta_2+1}}{4}}\left[1-\phi_1\left(-\frac{\sqrt{\mu_\upsilon^{\delta_2+1}}}{2}\right)\right] = \sqrt{\pi\mu_\upsilon^{\delta_2+1}}\,\left(\mu_\upsilon^{\delta_2+1}\right)^{\frac{\mathsf{k}+1}{2}}
\end{aligned}
\tag{C.12}
$$

Putting (C.12) back, the final expression for BER of LDPC coded BPSK over a JFTS faded/shadowed communication channel can be obtained in the form of (4.48).

Bibliography

[1] A. Algans, K. Pedersen, and P. Morgensen, “Experimental analysis of the joint properties of azimuth spread, delay spread and shadowing fading”, in *IEEE journal on selected areas in communication*, vol. 20, no. 3, Apr. 2002, pp. 523–531.

[2] A. Mawira, “Models for the spatial correlation functions of the log-normal component of the variability of the VHF/UHF eld strength in urban environment”, in *Proc. IEEE PIMRC*, pp. 436440, 1992.

[3] N. Jalden, P. Zetterberg, B. Ottersten, A. Hong, and R. Thomas, “Correlation Properties of Large Scale Fading Based on Indoor Measurements,” in *Proc. IEEE Wireless Communications and Networking Conference (WCNC)*, pp. 1894–1899, Mar. 2007.

[4] A. Abdi, W. C. Lau, M. S. Alouini, and M. Kaveh, “A new simple model for land mobile satellite channels: First- and second-order statistics,” in *IEEE Trans. Wireless Commun.*, vol. 2, no. 3, pp. 519–528, 2003.

[5] C. Loo, “A statistical model for a land mobile satellite link,” in *IEEE Trans. Veh. Technol.*, vol. 34, no. 3, pp. 122–127, 1985.

[6] G. E. Corazza and F. Vatalaro, “A statistical model for land mobile satellite channels and its application to non-geostationary orbit systems,” in *IEEE Trans. Veh. Technol.*, vol. 43, no. 3, pp. 738–741, 1994.

[7] S. H. Hwang, K. J. Kim, J. Y. Ahn, and K. C. Whang, “A channel model for non-geostationary orbiting satellite system,” in *Proc. IEEE Vehicular Technology Conf.*, Phoenix, AZ, 1997, pp. 41–45.

[8] F. Vatalaro, "Generalized Rice-lognormal channel model for wireless communications," in *Electron. Lett.*, vol. 31, pp. 1899–1900, 1995.

[9] E. Lutz, D. Cygan, M. Dippold, F. Dolainsky, and W. Papke, "The land mobile satellite communication channel - Recording, statistics, and channel model," in *IEEE Trans. Veh. Technol.*, vol. 40, pp. 375–386, May 1991.

[10] Y. Karasawa, K. Kimura, and K. Minamisono, "Analysis of availability improvement in LMSS by means of satellite diversity based on threestate propagation channel model," in *IEEE Trans. Veh. Technol.*, vol. 46, pp. 1047–1056, Nov. 1997.

[11] S. X. Ng, O. Alamri, Y. Li, J. Kliewer, and L. Hanzo, "Near-capacity turbo trellis coded modulation design based on EXIT charts and union bounds," in *IEEE Transactions on Communications*, vol. 56, no. 12, pp. 2030–2039, December 2008.

[12] M. S. Alouini and A. J. Goldsmith, "Comparison of fading channel capacity under different CSI assumptions," in *Proc. IEEE Veh. Tech. Conf. VTC-Fall 2000*, pp. 1844–1849, Sep. 2000.

[13] H. Suzuki, "A statistical model for urban radio propagation," in *IEEE Trans. Commun.*, vol. COM-25, no. 7, pp. 673–680, Jul. 1977.

[14] A. Abdi and M. Kaveh, "K-distribution: an appropriate substitute for Rayleigh-log-normal distribution in fading-shadowing wireless channels," in *Electron. Lett.*, vol. 34, pp. 851–852, April 30, 1998.

[15] G. D. Durgin, T. S. Rappaport, and D. A. de Wolf, "New analytical models and probability density functions for fading in wireless communications," in *IEEE Trans. Commun.*, pp. 1005–1015, Jun. 2002.

[16] X. Tang, M. S. Alouini and A. Goldsmith, "Effect of channel estimation error on M-QAM BER performance in Rayleigh fading," in *IEEE Trans. Commun.*, vol. 47, no. 12, pp. 1856–1864, Dec. 1999.

[17] H. Holm, "Adaptive Coded Modulation Performance and Channel Estimation Tools for Flat Fading Channels," Ph.D. dissertation, Norwegian Univ. Sci. Technol., Trondheim, Norway, Mar. 2002.

[18] T. T. Tjhung, and C. C. Chai, "Fade statistics in Nakagami-lognormal channels," in *IEEE Trans. Commun.*, vol. 47, no. 12, pp. 1769–1772, 1999.

[19] R. Esposito and L. R. Wilson, "Statistical properties of two sine waves in Gaussian noise," in *IEEE Trans. Inform. Theory*, vol. IT-19, pp. 176–183, Mar. 1973.

[20] A. A. M. Saleh, and R. A. Valenzuela, "A statistical model for indoor multipath propagation," in *IEEE Journal on Selected Areas in Communications*, vol. SAC-5, pp. 128–137, Feb. 1987.

[21] R. Ganesh, and K. Pahlavan, "On arrival of paths in fading multipath indoor radio channels," in *IEEE Electronic Letters*, vol. 25, pp. 763–765, Jun. 1989.

[22] A. K. Jagannatham, and V. Erceg, "MIMO indoor WLAN channel measurements and parameter modeling at 5.25 GHz," in *Proc. IEEE VTC2004 - Fall*, Sep. 2004, pp. 106–110.

[23] R. Tahri, V. Guillet, J. Y. Thiriet, and P. Pajusco, "Measurements and Calibration Method for WLAN Indoor Path Loss Modelling," in *Proc. IEEE International Conference on 3G and Beyond*, Nov. 2005, pp. 1–4.

[24] N. Jalden, P. Zetterberg, B. Ottersten, A. Hong, and R. Thomas, "Correlation Properties of Large Scale Fading Based on Indoor Measurements," in *Proc. IEEE Wireless Communications*

and Networking Conference (WCNC), pp. 1894–1899, Mar. 2007.

[25] E. Tanghe, W. Joseph, L. Verloock, L. Martens, H. Capoen, K. V. Herwegen, and W. Vantomme, "The Industrial Indoor Channel: Large-Scale and Temporal Fading at 900, 2400, and 5200 MHz," in *IEEE Trans. on Wireless Comms.* vol. 7, no. 7, Jul. 2008, pp. 2740–2751.

[26] S. Zvanovec, M. Valek, and P. Pechac, "Results of indoor propagation measurement campaign for WLAN systems operating in 2.4 GHz ISM band," in *Proc. IEEE Twelfth ICAP*, Apr. 2003, pp. 63–66.

[27] V. Degli-Eposti, C. Passerini, and G. Riva, "Wide-band measurement and ray-tracing simulation of the 1900-MHz indoor propagation channel: comparison criteria and results," in *Proc. IEEE Trans. on Antennas and Propagation*, vol. 49, no. 7, Jul. 2001, pp. 1101–1110.

[28] Shoa-Yei Yeong, W. Al-Salihy, and Wan Tat-Chee, "Indoor WLAN Monitoring and Planning Using Empirical and Theoretical Propagation Models," in *Proc. IEEE Second International Conference on NETAPPS*, Sep. 2010, pp. 165–169.

[29] B. Sklar, "Digital Communications: Fundamentals and Applications," Prentice Hall, Jan. 2001.

[30] G. G. Messier, and J. A. Hartwell, "A stochastic model for non-stationary outdoor K-factor variation," in *Proc. IEEE Vehicular Technology Conference (VTC)*, Sep. 2008, pp. 1–5.

[31] S. Y. Seidel and T. S. Rappaport, "Site-specific propagation prediction for wireless in-building personal communication system design," in *IEEE Trans. Veh. Technol.*, vol. 43, no. 4, pp. 879–891, 1994.

[32] Y. Wang, S. Safavi-Naeini, and S. K. Chaudhuri, “A combined ray tracing and FDTD method for modeling indoor radio wave propagation,” in *Proc. Antennas and Propagation Society Int. Symp.*, 1998, vol. 3, pp. 1668–1671.

[33] A. Alighanbari and C. D. Sarris, “Rigorous and Efficient Time-Domain Modeling of Electromagnetic Wave Propagation and Fading Statistics in Indoor Wireless Channels”, in *IEEE Trans. Antenna and Propagation*, vol. 55, no. 8, pp. 2373–2381, 2007.

[34] A. O. Kaya, L. Greenstein and W. Trappe, “Modeling temporal channel variations in indoor wireless environments,” in *Proc. IEEE MILCOM 2008*, pp. 1–7, 16-19 Nov. 2008.

[35] T. E. Truman, and R. W. Brodersen, “A measurement-based characterization of the time variation of an indoor wireless channel,” in *Proc. IEEE 6th Int. Conf. on Universal Personal Communications Record, 1997*, Oct. 1997, vol. 1, pp. 25–32.

[36] S. Salahuddin, C. Thompson and K. Chandra, “A New Nonstationary Gaussian Noise Model for Indoor Wireless Channels”, in *Proc. IEEE MILCOM 2006*, pp. 1–4, 23-25 Oct. 2006.

[37] F. J. Lopez-Martinez, D. Morales-Jimenez, E. Martos-Naya, and J. F. Paris, “On the Bivariate Nakagami-m Cumulative Distribution Function: Closed-Form Expression and Applications,” in *IEEE Trans. Commun.*, vol. 61, no. 4, pp. 1404–1413, Apr. 2013.

[38] M. K. Simon and M. -S. Alouini, “Digital Communication Over Fading Channels,” 2nd edition. New Jersey : John Wiley and Sons, 2005.

[39] *Handbook of Mathematical Functions with Formulas, Graphs, and Mathematical Tables*, 1972. Ninth printing. New York: Dover, M. Abramowitz and I. A. Stegun, Eds..

[40] A. Dogandzic', and J. Jin, "Maximum likelihood estimation of statistical properties of composite gamma - lognormal fading channels," in *IEEE Trans. Signal Processing*, vol. 52, no. 10, pp. 2490–2495, Oct. 2004.

[41] W. H. Press, S. A. Teukolsky, W. T. Vetterling and B. P. Flannery, "Numerical recipes in C - The art of scientific computing," Cambridge University Press, 1996.

[42] A. Dogandzic, and J. Jinghua, "Maximum likelihood estimation of statistical properties of composite gamma-lognormal fading channels," in *IEEE Trans. Signal Processing*, vol. 52, no. 10, pp. 2940–2945, 2004.

[43] A. Papoulis and S. U. Pillai, "Probability, Random Variables and Stochastic Processes," Fourth Edition. Mcgraw Hill, 2002.

[44] A. Erde'lyi, et al., "Higher Transcendental Functions," in vol. II, McGraw Hill, New York, 1935–1955.

[45] A. Erde'lyi, et al., "Higher Transcendental Functions," in vol. I, McGraw Hill, New York, 1935–1955.

[46] A. H. Nuttall, "Some Integrals Involving the Q_M function," in *IEEE Trans. Info. Theory*, vol. 21, no. 1, pp. 95–96.

[47] G. K. Karagiannidis, N. C. Sagias, and P. T. Mathiopoulus, "The N*Nakagami fading channel model," in *Proc. IEEE 2nd International Symposium on Wireless Communication Systems*, pp. 185–189, 5 - 7 Sept. 2005.

[48] *Table of Integrals, Series and Products*, Elsevier Academic Press publications, Seventh Edition. USA, I. S. Gradshteyn and I. M. Ryzhik.

[49] J. G. Smith, "Odd-bit quadrature amplitude shift keying," in *IEEE Trans. Commun.*, vol. 23, no. 3, pp. 1235–1239, Apr. 2007.

[50] S. Abrar, and I. Qureshi, "Blind equalization of cross-QAM signals", in *IEEE Signal Process. Lett.*, vol. 13, no. 12, pp. 745–748, 2006.

[51] S. Panigrahi, and T. Le-Ngoct, "Fine-granularity loading schemes using adaptive Reed-Solomon coding for discrete multitone modulation systems," in *Proc. IEEE ICC 2005*, vol. 2, pp. 1352–1356.

[52] M. Zwingestein-Colin, M. Gazalet, and M. Gharbi, "Non-iterative bit-loading algorithm for ADSL-type DMT applications," in *Proc. IEE Commun.*, vol. 150, no. 6, pp. 414–418, 2003.

[53] N. C. Beaulieu, "A useful integral for wireless communication theory and its application to rectangular signaling constellation error rates," in *IEEE Trans. Commun.*, vol. 54, no. 5, pp. 802–805, May 2006.

[54] H. Yu, G. Wei, F. Ji and X. Zhang, "On the error probability of cross-QAM with MRC reception over generalized η-μ fading channels," in *IEEE Trans. Veh. Technol.*, vol. 60, no. 6, pp. 2631–2643, Jul. 2011.

[55] W. Jeong, J. Lee and D. Yoon, "New BER expression of MPSK," in *IEEE Trans. Veh. Technol.*, vol. 60, no. 4, pp. 1916–1924, May 2011.

[56] N. Y. Ermolova, "Average symbol error probability of arbitrary rectangular quadrature amplitude modulation in generalized shadowed fading channels," in *IET Commun.*, 2008, vol. 2, no. 7, pp. 903–908.

[57] G. P. Efthymoglou, N. Y. Ermolova and V. A. Aalo, “Channel capacity and average error rates in generalised-K fading channels,” in *IET Communications*, vol. 4, no. 11, pp. 1364–1372, Jul. 2010.

[58] H. Jin, A. Khandekar, and R. McEliece, “Irregular repeat- accumulate codes,” in *Proc. 2nd International Symposium on Turbo Codes*, pp. 1–8, 2000.

[59] U. Haccoun and G. Be'gin, “High-rate punctured convolutional codes for Viterbi and sequential decoding,” in *IEEE Trans. Commun.*, vol. 37, pp. 1113–1125, Nov. 1989.

[60] C. E. Shannon, “A mathematical theory of communication,” in *Bell System Technical Journal*, pp. 379–427, 1948.

[61] R. W. Hamming, “Coding and Information Theory,” 2nd edition, Prentice Hall, 1986.

[62] M. Golay, “Notes on digital coding,” in *Proceedings of the IEEE*, vol. 37, pp. 657, 1949.

[63] P. Elias, “Coding for noisy channels,” in *IRE Conv. Rec. pt. 4*, pp. 37–47, 1955.

[64] A. Viterbi, “Error bounds for convolutional codes and an asymptotically optimum decoding algorithm,” in *IEEE Trans. Info. Theory*, vol. IT-13, pp. 260–269, Apr. 1967.

[65] L. Bahl , J. Cocke , F. Jelinek, and J. Raviv, “Optimal decoding of linear codes for minimizing symbol error rate,” in *IEEE Trans. Info. Theory*, vol. 20, pp. 284–287, 1974.

[66] C. Berrou , A. Glavieux, and P. Thitimajshima, “Near Shannon limit error-correcting coding and decoding: Turbo-codes”, in *Proc. IEEE Int. Conf. Commun. (ICC)*, pp. 1064–1070, 1993.

[67] R. G. Gallager, “Low-density parity-check codes”, in *IRE Trans. Inf. Theory*, vol. 8, no. 1, pp. 21–28, 1962.

[68] D. J. C. MacKay, “Good error-correcting codes based on very sparse matrices”, in *IEEE Trans. Inf. Theory*, vol. 45, no. 2, pp. 399–431, 1999.

[69] R. Steele and L. Hanzo, eds., “Mobile Radio Communications : Second and Third Generation Cellular and WATM Systems”, New York, USA : IEEE Press - John Wiley and Sons, 2nd ed., 1999.

[70] S. A. Zummo, P. Yeh and W. E. Stark, “A union bound on the error probability of binary codes over block-fading channels,” in *IEEE Trans. Veh. Tech.*, vol. 54, no. 6, pp. 2085–2093, 2005.

[71] I. Sason and S. Shamai, “On improved bounds on the decoding error probability of block codes over interleaved fading channels, with applications to Turbo-like codes,” in *IEEE Trans. Inf. Theory*, vol. 47, no. 6, pp. 2275–2299, 2001.

[72] T. J. Richardson, and R. L. Urbanke, “The capacity of low-density parity check codes under message-passing decoding”, in *IEEE Trans. Inf. Theory*, vol. 47, pp. 599–618, Feb. 2001.

[73] T. J. Richardson, M. A. Shokrollahi, and R. L. Urbanke, “Design of capacity-approaching irregular low-density parity-check codes”, in *IEEE Trans. Inf. Theory*, vol. 47, pp. 619–637, Feb. 2001.

[74] S. T. Brink, “Convergence of iterative decoding”, in *Electron. Lett.*, vol. 35, pp. 1117–1119, June 1999.

[75] S. T. Brink, “Convergence behavior of iteratively decoded parallel concatenated codes”, in *IEEE Trans. Commun.*, vol. 49, pp. 1727–1737, Oct. 2001.

[76] E. A. Ince, N. S. Kambo and S. A. Ali, "Efficient expression and bound for pairwise error probability in Rayleigh fading channels, with application to union bounds for turbo codes," in *IEEE Commun. Lett.*, vol. 9, no. 1, pp. 25–27, Jan. 2005.

[77] F. Lehmann, and G. M. Maggio, "Analysis of the iterative decoding of LDPC and product codes using the Gaussian approximation", in *IEEE Trans. Inf. Theory*, vol. 49, pp. 2993–3000, Nov. 2003.

[78] E. A. Ince, N. S. Kambo and S. A. Ali, "Exact expression and tight bound on pairwise error probability for performance analysis of turbo codes over Nakagami-m fading channel," in *IEEE Commun. Lett.*, vol. 11, no. 5, pp. 399–401, May 2007.

[79] B. S. Tan, K. H. Li, and K. C. Teh, "Performance Analysis of LDPC Codes with Maximum-Ratio Combining Cascaded with Selection Combining over Nakagami-m Fading", in *IEEE Trans. Wireless Commun.*, vol. 10, no. 6, pp. 1886–1894, Jun. 2011.

[80] A. P. Prudnikov, Y. A. Brychkov, and O. I. Marichev, "Integrals and Series", Vol. 3. Gordon and Breach Science Publishers, 1986.

[81] A. P. Prudnikov, Y. A. Brychkov, and O. I. Marichev, "Integrals and Series", Vol. 1. Gordon and Breach Science Publishers, 1986.

[82] W. Jeong, J. Lee and D. Yoon, "New BER expression of MPSK," in *IEEE Trans. Veh. Technol.*, vol. 60, no. 4, pp. 1916–1924, May 2011.

[83] Y. Zhao, P. Adve and T. J. Lim, "Symbol error rate of selection amplify-and-forward relay systems," in *IEEE Commun. Letters*, vol. 10, no. 11, pp. 757–759, 2006.

[84] J. Lu, K. B. Letaief, J. C. Chuang and M. L. Liou, "M-PSK and M-QAM BER computation using signal-space concepts," in *IEEE Trans. Commun.*, vol. 47, no. 2, pp. 181–184, Aug. 2002.

[85] E. K. Hall and S. G. Wilson, "Design and analysis of turbo codes on Rayleigh fading channels," in *IEEE J. Sel. Areas Communs.,*, pp. 160–174, Feb. 1998.

[86] S. Benedetto and G. Montorsi, "Unveiling turbo codes : Some results on parallel concatenated coding schemes," in *IEEE Trans. Inf. Theory*, vol. 42, pp. 409–429, Mar. 1996.

[87] S. -Y. Chung, T. J.'Richardson, and R. L. Urbanke, "Analysis of sum-product decoding of low-density parity-check codes using a Gaussian approximation," in *IEEE Trans. Inf. Theory*, vol. 47, pp. 657–670, Feb. 2001.

[88] F. Lehmann, and G. M. Maggio, "Analysis of the iterative decoding of LDPC and product codes using the Gaussian approximation," in *IEEE Trans. Inf. Theory*, vol. 49, pp. 2993–3000, Nov. 2003.

[89] J. Hou, P. H.Siegel, and L. B. Milstein, "Performance analysis and code optimization of low density parity-check codes on Rayleigh fading channels," in *IEEE J. Sel. Areas Commun.*, vol. 19, pp. 924–934, May 2001.

[90] P. E. MacIllree, "Channel capacity calculations for M-ary n-dimensional signal sets," M.Eng thesis, The University of South Australia, 1995.

[91] G. J. Foschini, and M. J. Gans, "On limits of wireless communications in a fading environment when using multiple antennas," in *Wireless Personal Communications*, vol. 6, pp. 311–335, Mar. 1998.

[92] D. Divsalar, and M. K. Simon, "Trellis coded modulation for 4800-9600 bits/s transmission over a fading mobile satellite channel", in *IEEE J. Select. Areas Commun.*, vol. SAC-5, pp. 162–177, 1987.

[93] D. Divsalar, and M. K. Simon, "The design of trellis coded MPSK for fading channels: Performance criteria", in *IEEE Trans. Commun.*, vol. 36, pp. 1004–1012, 1988.

[94] J. K. Cavers, "Variable-rate transmission for Rayleigh fading channels," in *IEEE Trans. Commun.*, vol. COM-20, pp. 15–22, Feb. 1972.

[95] T. Ue, S. Sampei, and N. Morinaga, "Symbol rate and modulation level controlled adaptive modulation / TDMA / TDD for personal communication systems," in *Proc. IEEE VTC95*, July 1995, pp. 306–310.

[96] W. T. Webb and R. Steele, "Variable rate QAM for mobile radio," in *IEEE Trans. Commun.*, vol. 43, pp. 2223–2230, July 1995.

[97] H. Matsuoka, S. Sampei, N. Morinaga, and Y. Kamio, "Adaptive modulation system with variable coding rate concatenated code for high quality multi-media communication systems," in *IEICE Trans. Commun.*, vol. E79-B, pp. 328–334, Mar. 1996.

[98] C. Kse and D. L. Goeckel, "On power adaptation in adaptive signaling systems," in *IEEE Trans. Commun.*, vol. 48, pp. 1769–1773, Nov. 2000.

[99] A. J. Goldsmith and P. Varaiya, "Capacity of fading channels with channel side information," in *IEEE Trans. Inform. Theory*, vol. 43, pp. 1986–1992, Nov. 1997.

[100] A. J. Goldsmith and S. Chua, "Variable-rate variable-power MQAM for fading channels," in *IEEE Trans. Commun.*, vol. 45, pp. 1218–1230, Oct. 1997.

[101] A. J. Goldsmith and L. Greenstein, "Effect of average power estimation error on adaptive MQAM modulation," in *Proc. IEEE ICC97*, June 1997, pp. 1105–1109.

[102] D. L. Goeckel, "Adaptive coding for time-varying channels using outdated fading estimates," in *IEEE Trans. Commun.*, vol. 47, pp. 844–855, June 1999.

[103] J. G. Proakis, *Digital Communications*, 2nd ed. New York: McGraw - Hill, 1989.

[104] I. Korn, *Digital Communications*. New York: Van Nostrand Reinhold, 1985.

[105] P. J. Lee, "Computation of the bit error rate of coherent M-ary PSK with Gray code bit mapping," in *IEEE Trans. Commun.*, vol. COM-34, pp. 488–491, May 1986.

[106] D. L. Goeckel, "Robust adaptive coded modulation for time-varying channels with delayed feedback," in *Proc. 35th Annu. Allerton Conf. Commun., Control and Comput.*, Sept. 1997, pp. 370–379.

[107] G. Caire and S. Shamai, "On the capacity of some channels with channel state information," in *IEEE Trans. Inform. Theory*, vol. 45, pp. 2007–2019, Sept. 1999.

[108] G. Caire, G. Taricco and E. Biglieri, "Optimum power control over fading channels" in *IEEE Trans. Info. Theory*, vol. IT-45, pp. 1468–1489, Jul. 1999.

[109] A. J. Goldsmith and S. Chua, "Adaptive coded modulation for fading channels," in *IEEE Trans. Commun.*, vol. 46, pp. 595–602, May 1998.

[110] A. Svensson, "An Introduction to Adaptive QAM Modulation Schemes for Known and Predicted Channels," in *Proc. IEEE*, vol. 95 (12), pp. 2322–2336, Dec. 2007.

[111] S T. Chung and A. J. Goldsmith, "Degrees of freedom in adaptive modulation: A unified view," in *IEEE Trans. Commun.*, vol. 49, no. 9, pp. 1561–1571, Sep. 2001.

[112] E. Biglieri, J. Proakis and S. Shamai (Shitz), "Fading channels : Information-theoretic and communications aspects," in *IEEE Trans. Info. Theory*, vol. 44, no. 6, pp. 2619–2692, Oct. 1998.

[113] M. S. Alouini and A. J. Goldsmith, "Capacity of Rayleigh fading channels under different adaptive transmission and diversity techniques," in *IEEE Trans. Veh. Tech.*, vol. VT-48, pp. 1165–1181, Jul. 1999.

[114] K. J. Hole, H. Holm, and G. E. ien, "Adaptive multidimensional coded modulation over flat fading channels," in *IEEE Journal on Selected Areas in Communications*, vol. 18, no. 7, pp. 1153–1158, July 2000.

[115] M. S. Alouini and A. J. Goldsmith, "Capacity of Nakagami Multipath Fading Channels," in *Proc. IEEE Veh. Tech. Conf. VTC97*, pp. 358–362, May. 1997.

[116] X. Lei, Z. Zhangdui, A. Bo and Q. Jinlong, "Ergodic and outage capacity for Ricean fading channel with shadow fading on high-speed railway," in *Proc. IEEE 4th IET International Conference on Wireless, Mobile and Multimedia Networks (ICWMMN 2011)*, pp. 325–328, Nov. 2011.

[117] X. Tang, M. S. Alouini and A. Goldsmith, "Effect of channel estimation error on M-QAM BER performance in Rayleigh fading," in *IEEE Trans. Commun.*, vol. 47, no. 12, pp. 1856–1864, Dec. 1999.